

**Mobile Fission and Activation Products  
in Nuclear Waste Disposal**

**Workshop Proceedings  
La Baule, France  
16-19 January 2007**

OECD 2009  
NEA No. 6310

NUCLEAR ENERGY AGENCY  
ORGANISATION FOR ECONOMIC CO-OPERATION AND DEVELOPMENT

## ORGANISATION DE COOPÉRATION ET DE DÉVELOPPEMENT ÉCONOMIQUES

L'OCDE est un forum unique en son genre où les gouvernements de 30 démocraties œuvrent ensemble pour relever les défis économiques, sociaux et environnementaux que pose la mondialisation. L'OCDE est aussi à l'avant-garde des efforts entrepris pour comprendre les évolutions du monde actuel et les préoccupations qu'elles font naître. Elle aide les gouvernements à faire face à des situations nouvelles en examinant des thèmes tels que le gouvernement d'entreprise, l'économie de l'information et les défis posés par le vieillissement de la population. L'Organisation offre aux gouvernements un cadre leur permettant de comparer leurs expériences en matière de politiques, de chercher des réponses à des problèmes communs, d'identifier les bonnes pratiques et de travailler à la coordination des politiques nationales et internationales.

Les pays membres de l'OCDE sont : l'Allemagne, l'Australie, l'Autriche, la Belgique, le Canada, la Corée, le Danemark, l'Espagne, les États-Unis, la Finlande, la France, la Grèce, la Hongrie, l'Irlande, l'Islande, l'Italie, le Japon, le Luxembourg, le Mexique, la Norvège, la Nouvelle-Zélande, les Pays-Bas, la Pologne, le Portugal, la République slovaque, la République tchèque, le Royaume-Uni, la Suède, la Suisse et la Turquie. La Commission des Communautés européennes participe aux travaux de l'OCDE.

Les Éditions de l'OCDE assurent une large diffusion aux travaux de l'Organisation. Ces derniers comprennent les résultats de l'activité de collecte de statistiques, les travaux de recherche menés sur des questions économiques, sociales et environnementales, ainsi que les conventions, les principes directeurs et les modèles développés par les pays membres.

*Cet ouvrage est publié sous la responsabilité du Secrétaire général de l'OCDE. Les opinions et les interprétations exprimées ne reflètent pas nécessairement les vues de l'OCDE ou des gouvernements de ses pays membres.*

### L'AGENCE POUR L'ÉNERGIE NUCLÉAIRE

L'Agence de l'OCDE pour l'énergie nucléaire (AEN) a été créée le 1<sup>er</sup> février 1958 sous le nom d'Agence européenne pour l'énergie nucléaire de l'OECE. Elle a pris sa dénomination actuelle le 20 avril 1972, lorsque le Japon est devenu son premier pays membre de plein exercice non européen. L'Agence compte actuellement 28 pays membres de l'OCDE : l'Allemagne, l'Australie, l'Autriche, la Belgique, le Canada, le Danemark, l'Espagne, les États-Unis, la Finlande, la France, la Grèce, la Hongrie, l'Irlande, l'Islande, l'Italie, le Japon, le Luxembourg, le Mexique, la Norvège, les Pays-Bas, le Portugal, la République de Corée, la République slovaque, la République tchèque, le Royaume-Uni, la Suède, la Suisse et la Turquie. La Commission des Communautés européennes participe également à ses travaux.

La mission de l'AEN est :

- d'aider ses pays membres à maintenir et à approfondir, par l'intermédiaire de la coopération internationale, les bases scientifiques, technologiques et juridiques indispensables à une utilisation sûre, respectueuse de l'environnement et économique de l'énergie nucléaire à des fins pacifiques ; et
- de fournir des évaluations faisant autorité et de dégager des convergences de vues sur des questions importantes qui serviront aux gouvernements à définir leur politique nucléaire, et contribueront aux analyses plus générales des politiques réalisées par l'OCDE concernant des aspects tels que l'énergie et le développement durable.

Les domaines de compétence de l'AEN comprennent la sûreté nucléaire et le régime des autorisations, la gestion des déchets radioactifs, la radioprotection, les sciences nucléaires, les aspects économiques et technologiques du cycle du combustible, le droit et la responsabilité nucléaires et l'information du public. La Banque de données de l'AEN procure aux pays participants des services scientifiques concernant les données nucléaires et les programmes de calcul.

Pour ces activités, ainsi que pour d'autres travaux connexes, l'AEN collabore étroitement avec l'Agence internationale de l'énergie atomique à Vienne, avec laquelle un Accord de coopération est en vigueur, ainsi qu'avec d'autres organisations internationales opérant dans le domaine de l'énergie nucléaire.

#### © OCDE 2009

Toute reproduction, copie, transmission ou traduction de cette publication doit faire l'objet d'une autorisation écrite. Les demandes doivent être adressées aux Éditions de l'OCDE [rights@oecd.org](mailto:rights@oecd.org) ou par fax (+33-1) 45 24 99 30. Les demandes d'autorisation de photocopie partielle doivent être adressées au Centre français d'exploitation du droit de copie (CFC), 20 rue des Grands-Augustins, 75006 Paris, France, fax (+33-1) 46 34 67 19, ([contact@cfcopies.com](mailto:contact@cfcopies.com)) ou (pour les États-Unis exclusivement) au Copyright Clearance Center (CCC), 222 Rosewood Drive Danvers, MA 01923, USA, fax +1 978 646 8600, [info@copyright.com](mailto:info@copyright.com).

## FOREWORD

According to international safety evaluations of radioactive waste disposal concepts, only a few radionuclides contribute to their long-term exposure risks, mainly  $^{129}\text{I}$ ,  $^{36}\text{Cl}$ ,  $^{79}\text{Se}$  and in some cases  $^{14}\text{C}$  and  $^{99}\text{Tc}$ , whatever the scenarios considered. Performance assessment is then directly concerned with the mobility of these fission and activation products in the geosphere.

An international workshop on Mobile Fission and Activation Products in Nuclear Waste Disposal, MOFAP07, was organised by the French nuclear waste agency ANDRA and by SUBATECH (École des Mines de Nantes, Université de Nantes, IN2P3/CNRS) at La Baule, France on 16 to 19 January 2007. The workshop was cosponsored by the OECD Nuclear Energy Agency (NEA), the Swiss National Co-operative for the Disposal of Radioactive Waste (NAGRA), the Belgian Agency for Radioactive Waste and Enriched Fissile Materials (ONDRAF/NIRAS). Some 90 experts from Belgium, China, the Czech Republic, Finland, France, Germany, Hungary, Japan, Korea, the Netherlands, South Africa, Spain, Sweden, Switzerland, the United Kingdom and the United States participated.

The workshop focused on the transport and chemical behaviour of the above-mentioned radionuclides, thereby helping to stimulate international radionuclide migration research on mobile fission and activation products. Key issues were:

- Engineered barrier system (EBS)/geosphere/additives to reduce mobility/analogues.
- Performance assessment (PA) view on mobile fission and activation products.
- Inventories/release properties in/from waste matrices.
- Chemical thermodynamics/co-precipitation/databases.
- Speciation/interaction (organic/inorganic) in aqueous media.
- Redox reactions/kinetics/micro-organism mediation processes.
- Sorption/reversibility.
- Diffusion-driven mass transfer properties in nano-porous media.
- Geochemical cycles and natural tracers.

Keynote lectures, oral and poster sessions were combined with sufficient discussion time to debate with key experts the current state of knowledge, recent developments and future research needs, attempting to increase the reliability of performance assessment. The workshop was guided by an International Steering Committee. Members were: Jordi Bruno (Enviros, Spain), Horst Geckeis (INE-FZK, Germany), Pedro Hernan (Enresa, Spain), André Maes (K.U. Leuven, Belgium), Federico Mompean (OECD/NEA), Ake Olin (Uppsala University, Sweden), Christophe Poinssot (CEA, France), Joseph Rard (LLNL, United States), Kastriot Spahium (SKB, Sweden), Pierre Van Iseghem (SCK-CEN, Belgium), Lawrence Johnson (Nagra, Switzerland), Susan Stipp (Copenhagen University, Denmark), Pierre Toulhoat (CEA-CNRS, France), and Hiroyuki Umeki (JAEA, Japan). A selection of papers is presented covering most research items presented at the workshop. The papers were reviewed by international experts in the field.

## TABLE OF CONTENTS

Foreword .....	3
Introductory Remarks .....	7
<i>H. Umeki</i>	
Holistic assessment to put mobile radionuclides in perspective.....	11
<i>E. Leclerc, G. Smith and P. Lloyd</i>	
Review of Cl-36 behaviour in the biosphere and implications for long-term dose assessment .....	21
<i>J. Marivoet and E. Weetjens</i>	
The importance of mobile fission products for long-term safety in the case of disposal of vitrified high-level waste and spent fuel in a clay formation .....	31
<i>I. Rojo, M. Rovira, V. Martí, J. de Pablo, L. Duro, X. Gaona, E. Colàs, M. Grivé</i>	
Uptake of selenate on hydrated and degraded cement: batch and dynamic experiments .....	43
<i>J. Giménez, M. Rovira, J. de Pablo, I. Casas, A. Martínez-Esparza, X. Martínez-Lladó</i>	
Sorption of cesium on freshly precipitated studtite (UO <sub>4</sub> .4H <sub>2</sub> O). Kinetics of sorption and sorption isotherm .....	55
<i>N. Jordan, C. Lomenech, N. Marmier, E. Giffaut, J-J. Ehrhardt</i>	
Sorption of selenium (IV) in the presence of aqueous silicates species on iron corrosion product in underground radwaste repository conditions .....	65
<i>B. Kienzler, D. Schild, J. Römer, M. Jansson</i>	
Retention of <sup>99</sup> Tc onto fractures of crystalline rock .....	77
<i>T. Kikuchi, Y. Seida and K. Suzuki</i>	
Sorption behaviour of granite for radionuclides in groundwater condition .....	87
<i>X. Liu, M. Fattahi, G. Montavon and B. Grambow</i>	
Sorption of Se(-II) onto pyrite under redox potential conditions .....	95
<i>C. Tournassat, E.C. Gaucher, M. Fattahi, A. Vinsot, B. Grambow</i>	
Evaluating the potential retention of iodine in the clayey host-rocks .....	105

<i>J. Muller, A. Abdelouas, B. Grambow</i> Sorption of selenite ions on solid soil components using dialysis membranes .....	113
<i>F. Poineau, A. Sattelberger, K. Czerwinski, M. Fattahi and B. Grambow</i> Synthesis and characterisation of technetium polymers.....	125
<i>Y. Iida, T. Yamaguchi, T. Tanaka, A. Kitamura and S. Nakayama</i> Determination of the solubility limiting solid of the selenium in the presence of iron under anoxic conditions.....	135
<i>B. Rotenberg, V. Marry, N. Malikova, R. Vuilleumier, J-F. Dufrêche, E. Giffaut and P. Turq</i> Ions at clay particle surfaces and ionic exchange: A molecular dynamics study .....	147
<i>H. Sato</i> Activation energies of diffusion for I and Cs in interlayer of smectite .....	157
<i>H. Sato</i> Thermodynamic data of water on smectite surface and those applications to swelling pressure of compacted bentonite .....	173
<i>P. Hölttä, M. Siitari-Kauppi, A. Poteri</i> The importance of Matrix diffusion for the transport of mobile radionuclides in granitic rock – summary of laboratory – scale experiments .....	185
<i>S. Suzuki, Y. Seida and K. Suzuki</i> Sorption and diffusion of Cs in compacted bentonite saturated with saline water under temperature range of 30-60°C .....	197
<i>H. Tanabe, T. Nishimura, M. Kaneko, T. Sakuragi, Y. Nasu, H. Asano</i> Characterisation of hull waste in underground condition.....	207
<i>T. Nishimura, T. Sakuragi, Y. Nasu, H. Asano, H. Tanabe</i> Development of immobilisation techniques for radioactive iodine for geological disposal.....	221
<i>J. Quiñones, J. Cobos, E. Iglesias, S. van Winckel, A. Martínez-Esparza, J.P. Glatz</i> Burn-up effect on instant release from an initial corrosion of UO <sub>2</sub> and MOX fuel under anoxic conditions .....	235
<i>P. Van Iseghem, K. Lemmens, V. Pirlet</i> The leaching of Se, Sn, Zr, Pd from vitrified high-level waste in clay slurries .....	247
List of participants.....	259

## INTRODUCTORY REMARKS

### **B. Grambow, SUBATECH, Nantes, France**

The concept of isolation and immobilisation of nuclear waste in deep geological repositories is a cornerstone in making full use of nuclear energy to contribute to an energy policy allowing that we and a future multi billion world population can live in a rich, prosperous, resource conserving, clean and healthy environment. All safety analyses have shown that this concept promises almost absolute safety for the next 1000 years if inadvertent human intrusion can be ruled out. The safety margin may even better be appreciated if we look for much longer times into future, an effort not endeavoured for any other human activity. Radioactive waste invites to such look into a future of millions of years by its build-in clock, the radioactive decay period, even though that we have no guarantee that humans will still live on earth at that time. This puts the concept of isolation to its extreme. Will the radionuclides still remain fixed?

It has been shown very convincingly for most scenarios since long time, and without ignoring certain still open questions for various repository concepts, that the most toxic elements like Pu, Np or Am do move only few centimetres to meters before they decay, provided reducing conditions are assured and colloids migration is limited.

Nevertheless, the much less toxic nuclides like I129, C14, Tc99, Se79 or Cl36 may move over such long times much farther and some of these isotopes may reach biosphere after hundreds of thousands of years. Even in this case, due to their comparatively low toxicity, it is expected that dose thresholds become never exceeded. But more evidence must be collected to quantify the safety margins. The mobility of these nuclides under geological disposal conditions therefore was the theme of the international MOFAP07 workshop. The use of the term “mobility” to such long time period shall nevertheless not be misunderstood. In normal language context, iodine and chlorine are for example in clay rock extremely immobile.

Important research themes were addressed, such as how to translate molecular level information on speciation of radionuclides and a nano-porous medium or surface properties of rock fracture to detailed diffusion mechanism and to large migration distances facing mineralogical heterogeneities over tens to hundreds of meters. The large volume of traversed rock will provide so many retention sites that despite their weak retention, even these nuclides may show significant retardation. Redox chemistry of radionuclides might change along the migration path. Comparison between the retention behaviour of radionuclides and homologue natural elements present in the host rock provides important insight into potential retention mechanism. Additionally, the radioactivity of some of the nuclides in the waste is so low that sophisticated techniques have been employed to measure them and to identify the speciation of release.

But in all of this focus on very long migration times it shall not be forgotten that “time” has a quite different meaning for us as nuclear waste scientists and for our families, neighbours or other average people. They are concerned with a much closer future. For the close future, no harm is expected from the repository. Why then, do we have to look for these much longer time and space scales: because time and space are not just variables, they are for mobile fission products much more than for the actinides the problem and the solution, they are the only forms in which any reason, understanding and confidence can develop.

## **H. Umeki, Japan Atomic Energy Agency**

### **Impressions and suggestions**

A sound scientific and technical basis is essential for developing (implementers) or reviewing (regulators) the post-closure safety case for a radwaste repository. The repository will be developed in a step-wise manner, and it may take many decades – to more than a century – from initial concept development and siting to final closure. At each step of the development process, the safety case will be iteratively reviewed and improved to increase the confidence of interested stakeholders, taking account of the evolving state-of-the-art science and technology.

At this workshop, it was observed that advanced analytical techniques (e.g. XANES, XAS, etc.) and new modelling methods, (e.g. MD) have been widely applied to understand in detail the sorption and transport mechanisms of mobile fission and activation products. Such scientific challenges can provide good evidence of a close linkage between fundamental science and the applied waste management business. It is also clear that overall performance assessments have been used, in some cases, to guide basic scientific studies - by identifying key radionuclides and relevant safety issues. The workshop has successfully provided a useful platform for communication between performance assessors and more specialist scientific researchers.

This framework should, however, be extended to involve a more holistic approach – e.g. by including repository design studies which can assess different approaches to solve some of the key issues associated with the significance of mobile elements. The tools for performance assessments should also be developed further, aiming to be as realistic as possible, in order to reflect improved design features and more detailed mechanistic understanding. More specifically, increased understanding of the behaviour of potentially mobile elements under the geochemical conditions to be realistically expected in a repository – taking account of its evolution with time – should be prioritised, involving, for example, focused experiments in underground research laboratories, possibly supported by relevant natural analogue studies. There is also a clear need for studies on the kinetics of key reactions within the system of engineered barrier materials, groundwater and surrounding rock formation. In this regard, microbiological effects are commonly observed to play a critical role in low temperature (<100°C) environments. There were, however, very few papers at this workshop that considered this issue.

The continuation of such workshops, e.g. every three years, is thus strongly recommended, especially if they could be better focused on the key requirements of developing (and reviewing) post-closure safety cases for geological repositories for long-lived wastes.



# **HOLISTIC ASSESSMENT TO PUT MOBILE RADIONUCLIDES IN PERSPECTIVE**

**Hiroyuki Umeki**

Japan Atomic Energy Agency (JAEA), Japan

## **Abstract**

Some radionuclides are inherently more mobile than others in the near- and far-field of repository systems and hence, if long-lived, tend to dominate the calculated doses in normal evolution scenarios. High mobility – generally a consequence of high solubility coupled to low sorption – does not, however, necessarily mean that a particular radionuclide is problematic in terms of repository safety. A more holistic approach, considering the entire safety case, gives a better indication of the critical nuclides and the R&D required to strengthen the assurance of safety.

## Introduction

The fact that a few mobile fission and activation products tend to dominate the calculated doses from repositories for a wide range of radioactive wastes can actually be attributed to the robustness of the disposal concepts involved. Even when conservative assessments are carried out, most radionuclides decay to insignificance within the engineered barrier system. It is inevitable, however, that some releases will eventually occur and, over assessment periods in the Ma timescale, these tend to be dominated by the most mobile of the long-lived radionuclides.

Before concentrating further R&D effort on such radionuclides, which often have relatively low radiotoxicity, it is important to determine:

- if such releases have any radiological significance ;
- whether the calculated releases are realistic, or result from great over-conservatism in the assessment process ;
- to what extent releases can be reduced by simple design modifications.

Such an assessment is inevitably dependant on the type of waste considered and the disposal concept involved. For deep geological disposal in Japan, effort is currently concentrated on vitrified high-level waste (HLW) from the reprocessing of spent fuel and the higher activity, longer-lived intermediate waste streams containing high concentrations of alpha-emitters (termed “transuranic (TRU)” waste in Japan). These examples will be used to illustrate the use of a holistic assessment approach to identify the safety-critical radionuclides and determine how R&D can most effectively strengthen the safety case for such elements. The procedures are, however, general and can be applied to any other waste or disposal option.

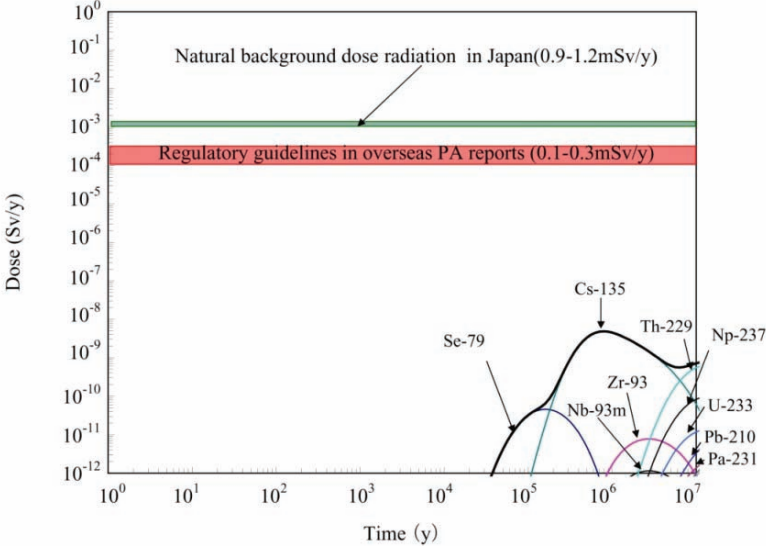
## Doses in perspective

Figure 1 shows the calculated doses from HLW for the reference case of H12 generic performance assessment (PA) study [1]. First releases are dominated by  $^{79}\text{Se}$  up to about 100ka and then  $^{135}\text{Cs}$  completely dominates until the actinide decay series finally break through after several millions of years. Does this mean that Se and Cs are safety-critical and should be a special focus for future R&D? It is important to emphasise, when interpreting Figure 1, that these doses are orders of magnitude below the already insignificant regulatory limits specified for geological repositories. Indeed, it is known that the models and databases used for the PA calculations are very conservative, ignoring some key barrier processes (e.g. transport resistance within the corroding glass block/failed overpack, co-precipitation processes – especially at the redox front within the overpack) and taking very pessimistic values for some uncertain data (e.g. solubility limits, sorption distribution coefficients).

The reference case depicted in Figure 1 is, of course, only a single model representation of a particular scenario. The safety case is built on consideration of a wide range of such model results and identification of key uncertainties that may lead to a reduction in performance of the

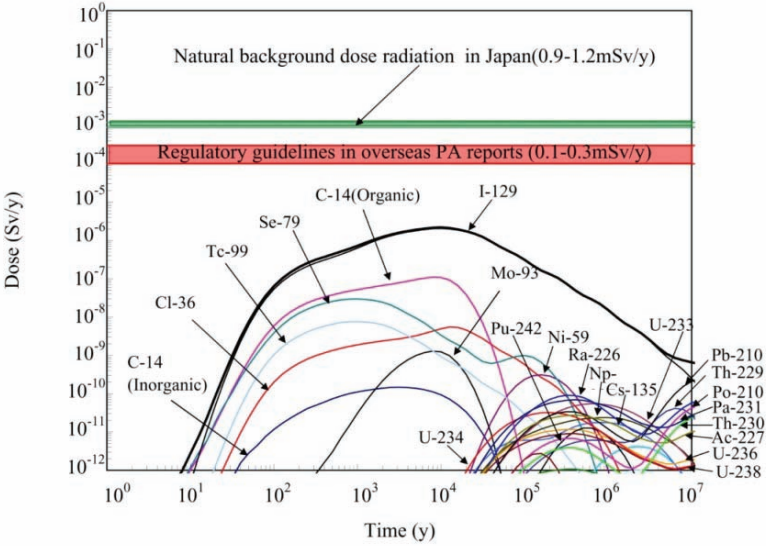
repository system. The fact that  $^{79}\text{Se}$  and  $^{135}\text{Cs}$  are very mobile, however, means that the doses calculated for such radionuclides tend to be less sensitive to geochemical perturbations. On the other hand, scenarios involving the roles of colloids, microbes, organic complexation etc. can result in mobilisation of more toxic, low mobility radionuclides (e.g. actinides like Pu) – considerably increasing calculated doses. It may also be noted that such nuclides also tend to be of most concern to many stakeholders.

**Figure 1. Reference case calculated doses from HLW repository (after [1])**



Admittedly, making the safety case for HLW in H12 is rather simple, due to the very robust engineered barrier system (EBS) design – in which most radionuclides decay to insignificance within the near field. The situation is more complex for TRU waste – as indicated in the reference case dose curves presented in Figure 2 [2].

**Figure 2. Reference case calculated doses from TRU waste repository [2]**



In this case it is clear that doses are completely dominated by  $^{129}\text{I}$  up to times in the order of 10Ma, when the actinide decay chains begin to break through. Nevertheless, there are a number of other mobile radionuclides that significantly contribute to doses in the most sensitive period of 100ka, when the stability of the geosphere can be generally relied on. Even here, calculated doses are well below the typical regulatory guidelines used in other countries.

In the case of TRU waste, however, it is more challenging to argue that the assessment is clearly conservative, due to the much greater complexity of the waste and the engineered barrier system. In particular, it is assumed that a bentonite diffusion barrier around the concrete waste disposal caverns maintains its critical properties over the timescale of interest and the effects of plumes of high pH leachate on the surrounding geological barrier are treated very simplistically.

When evaluating Figures 1 and 2, it is important to realise that any repository in Japan is likely to be in an area of net uplift and, within periods in the order of Ma, erosion is likely. Although there has not yet been clear regulatory guidance on how such erosion scenarios should be treated, it is probable that formally calculated doses from both HLW and TRU waste will be significantly above those for the reference groundwater case. Here, the peak dose will be very site-specific but, clearly, the more effective the EBS, the higher the dose will be. The dispersion of the  $^{129}\text{I}$  indicated in Figure 2 may thus be favourable – as compared to the case with efficient containment until the EBS gets very close to the surface.

### **Improving models and supporting system understanding**

Erosion scenarios need to be borne in mind, but focus in the post closure safety case will be on variants of the groundwater-release scenario which result in doses in the period of greatest concern – up to about 100 ka or so, particularly if these approach regulatory limits. In such cases, it should be emphasised that such high doses arise only when conservative assumptions of radionuclides mobility characteristics are made – e.g. instant release into a mixing tank, no solubility limit, no sorption, no other retardation mechanisms, etc. Such assumptions were often originally introduced when models and system understanding were less developed than at present and are carried forward over generations of assessments without reconsideration. By simply using the knowledge that is available now, doses may be reduced by orders of magnitude – moving them into the category where safety margins are sufficiently large that further supporting evidence is not needed. Such an investment in knowledge management provides better gains and identifies future direction of R&D actually needed.

For example, Figure 3 shows the sensitivity of releases from the HLW EBS to various data and model uncertainties [1]. Releases are clearly dominated by  $^{135}\text{Cs}$ , which are relatively insensitive to the variants considered. This conclusion is, however, inherently limited by the simplicity of the calculational model used, which greatly simplifies some of the key safety features of the design (Figure 4). Simply assuming dissolving glass (represented as spheres) within a vanishing overpack ignores many physical and chemical processes that will limit releases of even rather mobile radionuclides. Indeed, there is a lot of evidence from natural analogue systems suggesting that many trace elements are effectively immobilised at redox fronts – of the type that will inevitably exist at the interface between the oxidising glass leachate and the huge redox buffer provided by the iron corrosion products of the overpack. More

realistic models might lead to both longer complete isolation and decreases in maximum release rates of orders of magnitude. In fact, isolation within the EBS may be so effective that erosion scenarios become potentially problematic.

**Figure 3. Comparison of maximum release rates per waste package from the EBS for Np-237, Se-79 and Cs-135 (data and model uncertainty cases) [1]**

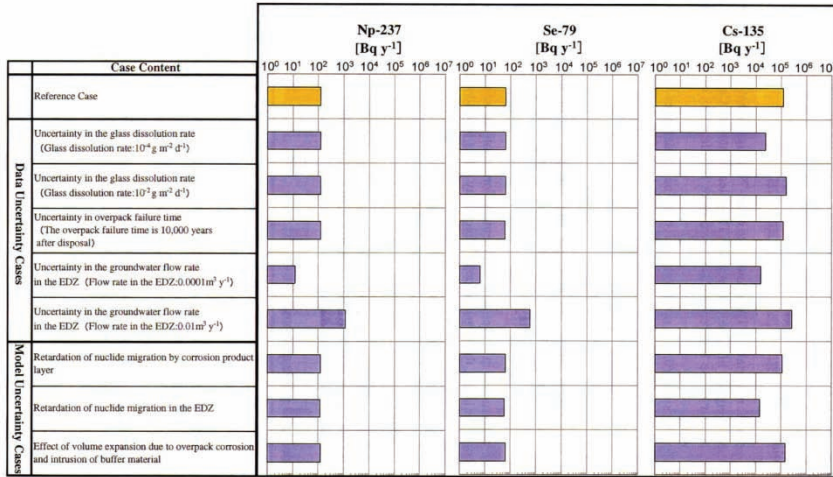
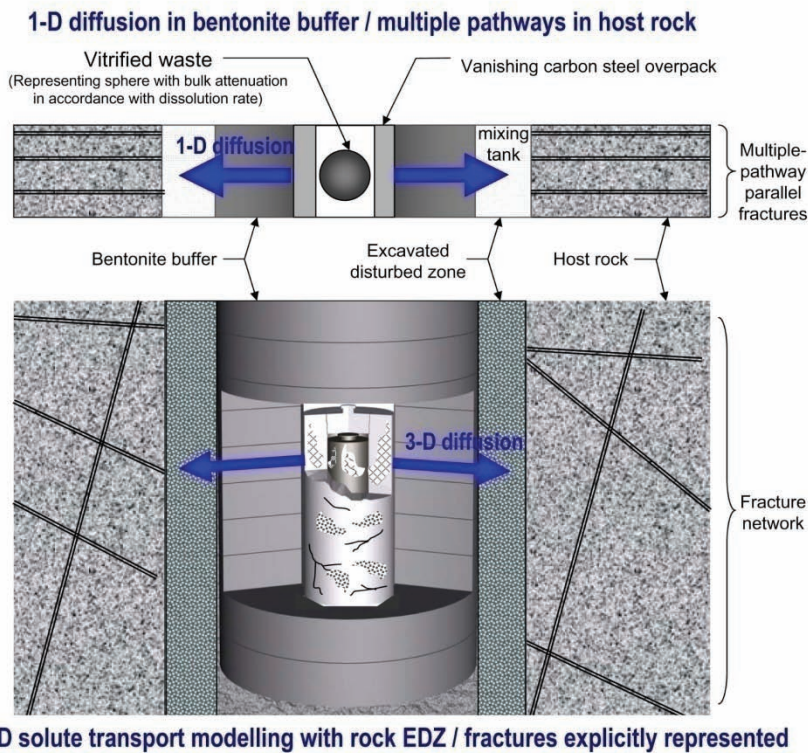
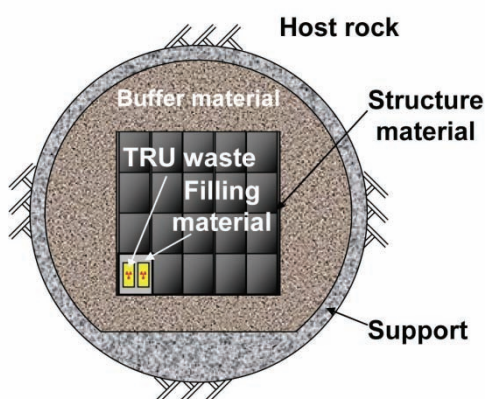


**Figure 4. Comparison of H12 NF model [1] with a more realistic representation of the safety barriers for HLW disposal**



For TRU waste, again, the situation is more complex. Current models which represent the near-field as a mixing tank are clearly simplistic and, in terms of physical transport of radionuclides, could be greatly improved on by 3-dimensional (3-D) advection/diffusion models which include direct representation of leaching from the waste matrix and the barrier roles of the waste package, grouts, concrete walls/liners, bentonite layers, etc. (Figure 5). Although, initially, a pure diffusive transport model may be appropriate, the physical evolution of the system needs careful consideration to determine the possible effects of gas pressurisation, swelling of corrosion products, alteration of bentonite, etc.

**Figure 5. Sketch of possible TRU waste emplacement cavern layout; standardised packages contain conditioned TRU waste and filled with grout. These, in turn are grouted into emplacement pits with concrete walls (structure material). The pit is surrounded by a thick layer of bentonite-based buffer and the entire EBS is placed within concrete-lined tunnels.**



Improving representation of geochemical retardation processes, particularly for the most mobile radionuclides, is greatly complicated by the heterogeneity and time dependence of the chemistry of porewaters – which are not only highly alkaline, but may also contain significant quantities of dissolved organics, colloids and microbes. First priority is therefore developing a more realistic representation of chemical evolution within the near-field as a function of space and time. Only when such background information is available, would it be valuable to consider improvement of the representation of the behaviour of key elements in this system.

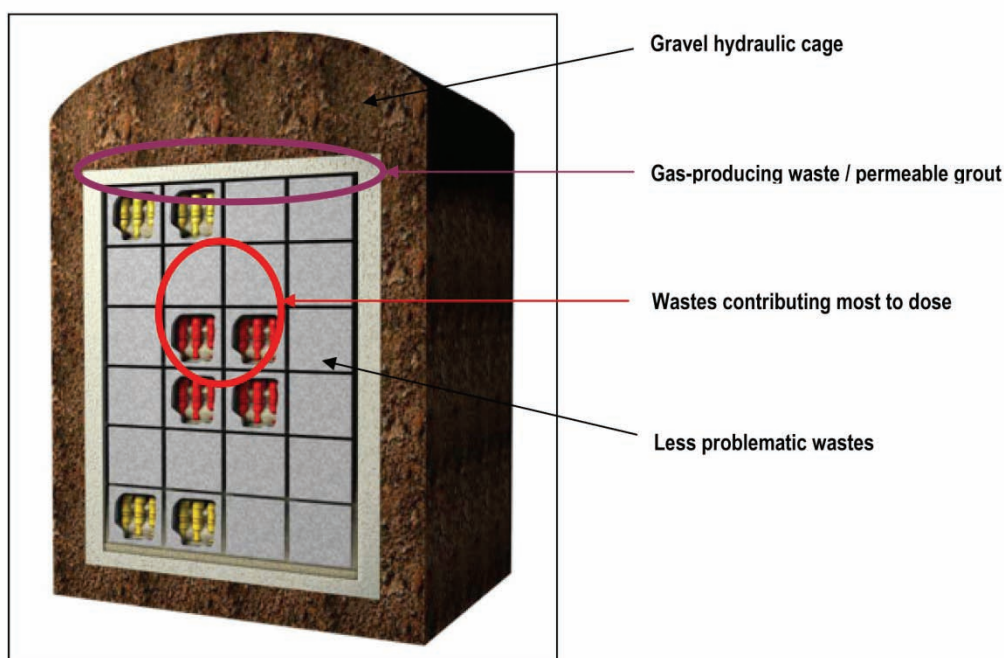
### **Improving repository design**

The generic assessments carried out to date are based on the assumption of reasonably favourable natural barrier characteristics. In Japan, however, siting is proceeding on the basis of a volunteering approach [3] and hence assessments may need to be applied to potential host sites that meet minimum stability criteria but, especially at early stages of site characterisation, have less potent geosphere barriers than previously assumed [4, 5]. In such cases, if calculated doses remain of concern on the basis of best available system understanding, before effort is invested elsewhere, it should be examined if simple design modifications can provide major performance gains. This is less likely to be the case for HLW where, as indicated above, the very robust EBS places very minor requirements on the geology. Indeed, the main concern here

is the practicality of safe emplacement with assured quality and hence optimisation with regards to operational aspects is the key priority for this type of waste [4].

For TRU waste, an obvious option which could improve performance involves optimised waste positioning within the repository. In the past, waste partitioning in many LLW/ILW/TRU waste repository designs has generally concentrated on locating wastes with similar characteristics together – which simplifies the performance assessment process [2]. By taking into account that “problem” radionuclides are usually restricted to a small fraction of the total inventory, however, designs can be developed that surround such packages with other wastes (Figure 6), which act as additional barriers – achieving significant spatial and temporal dilution of even completely mobile species.

**Figure 6. Optimisation scheme in which more problematic wastes are located in the centre of waste emplacement caverns**



Although designs such as indicated in Figure 6 increase operational complexity, they can be implemented rather cheaply, particularly if standardised sizes of waste emplacement packages are used. In terms of developing a robust EBS model, it is noticeable also that, for such designs, the porewater chemistry will evolve more slowly in the centre of the tunnels and that some potential disruptions can be minimised by design (e.g. placing wastes with higher potential gas production above the problem wastes and using more gas-permeable mortar in such zones to encourage gas release through the roof of the cavern). As the main emphasis is, however, on maintaining a diffusion-dominated system, the outer bentonite layer might usefully be replaced by gravel – which is much less vulnerable to physical or chemical perturbation.

## Optimising R&D

Given the limited resources available, it is important that R&D is focused on the areas where it can contribute most towards making a defensible safety case. From the considerations above, it is evident that the most important mobile radionuclide in the case of HLW is  $^{135}\text{Cs}$  and the determination of EBS performance is rather insensitive to the assumed chemical characteristics of this radionuclide. If higher safety reserves are desired, improved realism in the near-field model using existing system understanding offers the potential to gain orders of magnitude (which would also be reflected for other mobile elements such as Se). If such an improved model was developed, it might indicate areas where even greater performance could be demonstrated – e.g. in the consideration of immobilisation processes associated with redox fronts within the near-field – rather than further measurements of negligibly low  $K_d$  values, which have less potential to significantly strengthen the safety case. Nevertheless, it may transpire that the drive to improve realism of assessing HLW EBS performance is driven by erosion scenarios, which become more important when containment is extremely efficient (e.g. [1]).

For TRU waste, because doses are dominated by a relatively small fraction of the total waste inventory, there has been considerable effort invested in improving the performance of the conditioning process. Although many different matrices have been considered which could increase immobilisation of key radionuclides (especially  $^{129}\text{I}$ , but also  $^{14}\text{C}$ ) (e.g. [6]), their cost, operational doses to workers and secondary waste production have to be balanced against any assured long-term performance (NB this assurance has to be robust for expected long-term hyperalkaline conditions). As noted above, strategies based on chemical immobilisation / retardation of normally mobile radionuclides have to be balanced against those which depend on physical processes of dilution and dispersion – as the latter may be easier to justify in a safety case.

For example, “high tech” options for incineration of nuclear graphite and immobilisation of  $^{14}\text{C}$  in special matrices have been studied (e.g. [7]). These should be balanced against a “low tech” approach of crushing the graphite and using it in mortar used to fill packages of other types of waste (e.g. [8]). The latter is clearly much cheaper and, due to the known stability of graphite under hyperalkaline conditions (including analogue evidence [9]) coupled to the physical dispersion of this waste throughout the repository, may provide a more robust contribution to the safety case than a very high performance matrix that involves novel materials and is planned to be concentrated in specific parts of a repository.

In terms of improving models of the performance of TRU waste repositories, it is likely that improvements of system understanding will be needed – especially if such facilities need to be located in volunteer communities that are less than optimal in terms of geological barrier performance. The top priority is developing the models and data that allow the repository system to be characterised in detail (in 3-D, as a function of time on a site-specific basis). Such input will allow the needs in terms of mobile radionuclides to be defined. It would be expected that the emphasis would be on behaviour under hyperalkaline conditions and also on the influence of reaction fronts – where strong gradients in pH and/ or redox conditions may occur. For TRU waste, such fronts will occur in environments where concentrations of organic materials may be high, microbial activity may catalyse many key reactions and colloidal

material may be produced. Thus, even if some development work is carried out on ideal systems, it must be constantly assessed in terms of its applicability to relevant systems – and validated wherever possible. This last aspect is particularly tricky, but may be a particular focus for work planned in the next generation of projects in underground test facilities and be a special target for natural analogue work.

## **Conclusions**

In this paper, some issues associated with identifying future R&D needs related to mobile fission & activation products have been discussed in the context of the safety case for geological repositories, with reference to relevant studies carried out for HLW and TRU waste in Japan. Over the decades until such repositories are licensed, greatly improved system understanding will be required, which will certainly include more realistic models of the release and transport of mobile radionuclides. Emphasis is on realism; the greatly simplified, generic approaches typical of the 20<sup>th</sup> century need to be replaced by site-specific models, which account for 3-D distributions of key structures and incorporate system evolution with time. For HLW, indeed, it may well be that rather than the contribution of mobile radionuclides to groundwater scenario doses, the efficient isolation of most long-lived isotopes within the EBS focuses concerns on erosion scenarios.

The situation with regard to TRU waste is more complex and here, in particular, a holistic approach to strengthening the safety case is valuable – combining improved assessment of repository performance with utilisation of opportunities to improve such performance by simple design improvements. Although the advantages of holistic assessment are clear, this is not easy and, indeed, maintaining an overview is becoming increasingly difficult as the information base associated with repository projects expands with time. For this purpose, a formal Knowledge Management System utilising state-of-the-art IT tools can provide essential support and hence this is now identified as a key goal in the present JAEA R&D programme [10].

## **Acknowledgements**

The author wishes to thank Drs. M. Yui, M. Naito, G. Kamei, A. Honda and M. Mihara of JAEA and Dr. I.G. McKinley of McKinley Consulting for their useful input to this manuscript.

## REFERENCES

- [1] JNC (2000): H12: Project to Establish the Scientific and Technical Basis for HLW Disposal in Japan, Project Overview Report, Japan Nuclear Cycle Development Institute (now Japan Atomic Energy Agency), JNC TN1400 2000-001, Tokai, Japan.
- [2] FEPC and JAEA (2007): Second Progress Report on Research and Development for TRU Waste Disposal in Japan, “Repository Design, Safety Assessment and Means of Implementation in the Generic Phase”, Federation of Electric Power Companies and Japan Atomic Energy Agency, FEPC TRU-TR2-2006-01 (in press).
- [3] NUMO (2002): “Information Package” for open solicitation of volunteers for areas to explore the feasibility of constructing a final repository for high-level radioactive waste, Nuclear Waste Management Organization of Japan ([www.numo.or.jp/english/index.html](http://www.numo.or.jp/english/index.html)).
- [4] NUMO (2004): Development of Repository Concepts for Volunteer Siting Environment, Nuclear Waste Management Organization of Japan, NUMO-TR-04-03.
- [5] NUMO (2004): Evaluating Site Suitability for a HLW Repository, Scientific Background and Practical Application of NUMO’s Siting Factors, Nuclear Waste Management Organization of Japan, NUMO-TR-04-04.
- [6] H. Kato, O. Kato and H. Tanabe (2001): Review of Immobilization Techniques of Radioactive Iodine for Geological Disposal, NUCEF 2001, PW-13, 31 October – 2 November 2001, Japan Atomic Energy Research Institute, Tokai, Japan.
- [7] I.A. Sobolev, S.A. Dmitriev, F.A. Lifanov, A.P. Kobelev, V.N. Popkov, M.A. Polkanov, A.E. Savkin, A.P. Varlakov, S.V. Karlin, S.V. Stefanovsky, O.K. Karlina and K.N. Semenov (2003): High Temperature Treatment of Intermediate-level Radioactive wastes – Sia Radon Experience, WM ’03 Conference, February 23-24, 2003, Tucson, AZ, USA.
- [8] G. Tress, L. Doehring, H. Pauli and H.-F. Beer (2002): Optimised Conditioning of Activated Reactor Graohite, WM ’02 Conference, February 24-28, 2002, Tucson, AZ, USA.
- [9] I.G. McKinley: Personal communication.
- [10] JNC (2005): H17: Development and management of the technical knowledge base for the geological disposal of HLW – Knowledge Management Report – , Japan Nuclear Cycle Development Institute (now Japan Atomic Energy Agency), JNC TN1400 2005-022, Tokai, Japan.

# REVIEW OF CL-36 BEHAVIOUR IN THE BIOSPHERE AND IMPLICATIONS FOR LONG-TERM DOSE ASSESSMENT

Elisabeth Leclerc<sup>1</sup>, Graham Smith<sup>2</sup> and Pamela Lloyd<sup>2</sup>

<sup>1</sup> ANDRA, France

<sup>2</sup> Enviro Consulting Ltd, United Kingdom

## Abstract

Cl-36 is an important contributor to potential radiation doses in the long term, arising from release into the biosphere from radioactive waste disposal facilities. Its special attributes include its long half-life, high mobility in many environmental conditions, and potentially high uptake into plants and hence accumulation in the food-chain. Review has shown very wide ranges of Cl-36 values of parameters commonly employed in models used for long term doses. Accordingly, a workshop was held recently within the aegis of the international collaboration project BIOPROTA, to consider the causes of such variation, and in particular:

- to provide an open forum for presentation and discussion of environmental processes involved in Cl-36 migration and accumulation, and on how to model them, and
- to develop recommendations for the direction of continuing research as input to long-term radiological assessment .

Participation in the workshop included specialists and contributions from North America, Europe and Japan in environmental behaviour of chlorine, radioecology of Cl-36 and long term dose assessment. This paper will present the output from that workshop in the context of the wider aspects of performance assessment, taking into account information about:

- waste types for which Cl-36 is a significant component of the total Cl-36 inventory;
- data requirements for the dose assessment models, notably concerning uptake from soils into food crops which may lead to higher doses than direct consumption of contaminated drinking water;
- critical data weaknesses which may lead to overly pessimistic dose estimates;

- time dependent factors within a single growing season which can affect final concentrations in food crops for animals and humans;
- alternative conceptual models for the behaviour of Cl-36 in the environment, notably models structured as other trace radionuclide dose assessment models as opposed to models which are based specifically on chlorine behaviour which should take account explicitly of processes of isotopic dilution; and
- the interface with the geosphere transport models for Cl-36 migration and accumulation, especially in the geosphere-biosphere interface zone.

Proposals for further work are considered, designed to reduce uncertainties in the dose assessments.

## **Introduction**

Twenty-nine participants from nine countries, representing a range of operators, regulatory bodies, research laboratories and technical support organisations attended the workshop. A workshop report was prepared [1] and workshop presentations are being made available at [www.bioprota.com](http://www.bioprota.com). During the presentations, several common themes and issues arose. These included:

- Distinguishing organic and inorganic chlorine and Cl-36 in samples.
- Understanding of the system so as to resolve modelling/data issues.
- Integrated understanding of the plant-soil-hydrological interaction and making distinctions between oxidising and reducing zones, which may affect chlorine speciation.

From discussion, it was proposed to develop a working group with the objective of updating Cl-36 dose assessment models, taking account of alternative basic theoretical assumptions about the behaviour of chlorine in the environment and new and/or collated information from field and experimental measurements.

## **Why is Cl-36 of interest?**

From the information presented at the workshop, the main sources of Cl-36 in radioactive waste are activated metals and graphite following activation of Cl-35 and other stable elements contained in metal and graphite reactor components. However, there are major uncertainties in the initial stable element contents of activated materials and in the release rate from disposed wastes, dependent upon the rates of degradation of these materials in the near field of the repository.

Examples of the above include:

- Cl-36 inventories in low and intermediate level waste stores are of interest to ANDRA because Cl-36 contributes 77% ( $5.7E-3$  mSv/y) of the peak dose at Centre de l'Aube.
- The JGC Corporation in Japan are concerned with Cl-36 issues in Low and Intermediate Level Waste because Cl-36 is assessed to be the major contributor to dose following disposal of this waste, assumed to arise due to use of river water for irrigation.

Cl-36 is generally assumed to be mobile in the near field and geosphere, and is too long lived to decay during transport with water through the geosphere, and so the remaining major uncertainties in the overall dose assessment concern the degree of dilution that occurs as groundwater passes from the geosphere into the biosphere (in the geosphere-biosphere interface zone, GBIZ), and the accumulation of Cl-36 in food crops, as a result of irrigation and root uptake.

### **Distinguishing organic and inorganic chlorine and Cl-36 in samples**

It was noted that one of the main characteristics of Cl-36 include its speciation in soils and because of the different mobilities and roles in plant growth etc, it is of interest to be able to distinguish inorganic and organic chlorine. Some models do not currently include chlorine speciation. The general assumption is that the predominant chemical species is anionic chloride (Cl<sup>-</sup>). However, Gunilla Oberg (Institute of Resources, Environment and Sustainability) has concluded that Cl<sup>-</sup> in soils can be converted into various organic forms due to microbial activity and that this clearly impacts upon the biochemical cycling of chlorine.

SCK•CEN are studying the radio-element-biomass-water cycling at a forest site to improve their understanding of the processes taking place and thus their ability to model different scenarios. Yves Thiry mentioned that the conclusions so far indicate that the forest area (especially in wet zones) is a possible interim sink and vector of chlorine recycling in the long term due to environmental changes and the rate of turnover of chlorine is associated with the turnover of organic matter in the soil.

Mike Thorne noted that, based on experiments undertaken at Imperial College, London, there is some evidence for the organic partitioning of Cl-36 in lysimeter studies and this may affect the uptake into crops and the level of activity in the crop at the time of harvesting. Experiments specifically designed to look at isotopic exchange processes of Cl-36 in soil-plant systems have also been undertaken at Imperial College. Cl-36 was added to soils with different organic matter contents and samples were taken at various stages of the experiment. Almost immediately, less than 100% of the Cl-36 added could be recovered, suggesting that there is rapid exchange of the Cl-36 with the organic matter.

Gunilla Oberg has studied the terrestrial chlorine cycle in the Stubbetorp catchment (Sweden) and noted that during analysis, the organic chloride cannot be removed first because

the process will break the organic matter down. Chloride analysis must be done first, followed by organic chlorine. She also noted that in the top layer of soil storage there is about double the quantity of organic chlorine to inorganic chlorine. In vegetation there is an order of magnitude more inorganic chlorine compared to organic. Based on the inorganic and organic chlorine contents of system inputs and that found in the outputs there must be a conversion from inorganic to organic chlorine in or on plants. However, from the samples they have taken, it appears that the variability across 1 m<sup>2</sup> of forest matches the variability across Sweden. The variation is very large due to the heterogeneous nature of the vegetation and uptake in forests. There may be less variation in pastureland.

Gunilla suggested a theoretical framework for the chlorine cycle in soil. According to this, a considerable part of the chloride brought to the system through deposition is transformed to organic chlorine due to exo-enzymes that enable degradation of organic matter by formation of reactive chlorine. The reactive chlorine oxidizes, depolymerizes and chlorinates the organic matter. As a result, the chlorinated organic matter more easily follows the movement of water but eventually it precipitates at lower levels in the soil and is slowly degraded, thus releasing chloride. A considerable part of chloride in surface water originates from decomposing organic matter, not rain.

### **Understanding of the system so as to resolve modelling/data issues**

In 2000, ANDRA began studying Cl-36 and conclude that are 2 or 3 orders of magnitude uncertainty surrounding the possible impact of Cl-36 on human health while site-specific data is not taken into account. This uncertainty needs to be reduced through site characterisations and taking account of site-specific data such as stable chlorine content. However, such matters will be subject to change, both before the release to the biosphere occurs, and during the period of significant release. Different authorities take different approaches as to how the operator is supposed to take account of environmental change [2].

Yves Thiry noted that Cl-36 is an important potential contributor to radiation doses. However, there are data gaps in process description and understanding for Cl-36 which need to be understood before it can be simplified for use in models. Potentially, this could be based on stable chlorine studies. However, the relevant studies will depend on the important dynamic issues in chlorine accumulation and loss from soils, and the relationship to plant uptake in different hydrological conditions. In addition, not all ecological systems will be the same – e.g. coastal, non-coastal, forest and farmland. Thus, repository sites of interest and other aspects of the assessment context may influence choices of relevant studies.

These other aspects include features of the assumed geosphere-biosphere interface, the requirement or otherwise to take account of environmental and other system change, and the assessment endpoints that have to be calculated, e.g. the definition of the critical group, and the temporal averaging in the assessed dose that is acceptable.

SCK•CEN have been focussing their studies on the forest ecosystem as a study system for sink-source models, because it is an important part of the landscape everywhere and vegetation development has great effects on water and element cycling. Interactions of climate and site

vegetation are well reflected by changes in forest type. Currently SCK•CEN is acquiring data and functional information for quantitative descriptions of the radio-element-biomass-water cycling at the forest site affected by a shallow water table to provide ecosystem justification. There are data gaps in process description and understanding for Cl-36 which need to be understood before it can be simplified for use in models.

ANDRA has commissioned experiments at Imperial College, London to examine the use of isotopic exchange as a method to understand relative behaviour of stable chlorine and Cl-36, including the dynamics of evolution of soils and plants and the environmental and agricultural conditions which might influence uptake into crops were also examined. One set of experiments involved incubation in soil under controlled conditions. Small containers of soil uniformly mixed with chlorine but held under different conditions (some saturated some not, and at different temperatures, from -20°C to +20°C, and with different levels of fertilisation to alter the stable chlorine content). The evolution of stable chloride in these containers was examined. Over time there was a systematic decline in chloride concentration in soil water. This suggests that the chloride is interacting with the soil matrix.

Christian Tamponnet (IRSN) gave an overview of geochemical cycles of Cl-36 in the environment. Globally, chlorine is located in a few large reservoirs: the earth's mantle, crust and oceans. The troposphere, freshwaters and pedosphere are the main reservoirs of anthropogenic sources of Cl-36. Chlorine can transfer from the pedosphere to troposphere via two routes, mineral aerosols and biomass burning. Mineral aerosols are injected in troposphere via strong winds during dry season in deserts. Biomass contains chlorine and around 70 to 85% of this chlorine goes to atmosphere during biomass burning. The geochemical cycle of chlorine is driven by physical (wind, water, fire) and chemical forces (ion exchange, weathering, rainfall). It has been studied for decades. Therefore, there is extensive information about geochemical cycling of chlorine either in its main inorganic form of chlorides and in some organic forms. The biogeochemical cycle of chlorine is much more complex and has only been considered in detail relatively recently. It is notable that organic chlorine compounds are the product of human activity as well as of general biological origin. Human activity can therefore be an important part of the system under investigation.

Gunilla Oberg has done some studies to check if organic chlorine can be found in old deposits/carbon and found that it is present but there is no clear pattern in the quantity found. However, as long as there is carbon in the soil there will be organic chlorine, regardless of the age of the soil. George Shaw (Nottingham University) wondered how relevant old (geological) carbon stores really are, because coal, for instance, takes much longer than 100 000 years to form and so may not contain the Cl-36 we are interested in. There is a general concern that experiments are usually conducted over very short timescales and so scaling the results up may be problematic. The evolution of forest and European agricultural systems is well known but the evolution of mires, deserts, agricultural systems outside of Europe, coastal systems, tropical and subtropical ecosystems are less well known and so should possibly be considered.

## **Integrated understanding of the plant-soil-hydrological interaction and making distinctions between oxidising and reducing zones**

It was noted that the plant – soil – hydrological interaction should include the interaction with soil organic matter, and that changes can occur through the year, so different seasons need to be considered in appropriate sequences. However, there may also be changes from year to year, which can be relevant for longer-term continuous releases.

During the 1980s lysimeter studies were set up at Imperial College. The lysimeters contained plants growing in soil with the water table fixed at 40 or 65 cm. The lysimeters were based outside so natural environmental processes could continue. Cl-36 was added to the bottom of the lysimeters whence it rapidly redistributed through the soil. Activity balance calculations using a systems model tend to work better when some organic partitioning is assumed. Soil profiles of Cl-36 appear to develop rapidly, but differently under different moisture stress regimes and the degree of uptake by the plants varies dramatically; from negligible under wet conditions, generally reducing conditions to more than 70% of the total added to soil in dry, more oxidising, conditions. Thus, understanding of water flow and water status is fundamental to assessing Cl-36 uptake by plants. They also reported some evidence for organic partitioning of Cl-36.

Overall, plant-soil transfer factors are high but depending on the season they can sometimes be low. These seasonal changes cause the reported transfer factors to differ by 5 orders of magnitude (0.01 to 10,000). Part of the explanation could be that soil can be depleted of chlorine during a growing season, so measured transfer factors are very high if the concentration ratios are measured when the soil has been depleted and all the chlorine is in the growing plants.

In other available literature, chlorine uptake by plants varies by three orders of magnitude, see presentation for details and also show that concentration ratios are not time or soil dependent but the  $[Cl-36]/[Cl]$  in the plant does not equal the  $[Cl-36]/[Cl]$  in the soil. This relationship is time dependent and so the specific activity approach for modelling cannot be used without consideration of the relevant temporal scale issues inherent in any assessment question. Mike Thorne commented that there could be a relationship between chlorine uptake and water uptake or it may be between chlorine uptake and the biomass dry rate production. However, both appear correlated and so it can be argued either way.

In the more recent experiments at Imperial College they aimed to follow the dynamics of chlorine and Cl-36 in the soil plant system when two types of contamination (irrigation from above and the water table from below) are present. Two types of soil (colluvial and garden) and two types of plant – *Lolium perenne* (Ryegrass) and *Beta vulgaris* were tested. Surface irrigation produced a better yield of crop biomass than water from beneath. Only around 1 or 2% of the Cl-36 was removed from the system by the plant. However, there tended to be more removal of Cl-36 following irrigation. This is thought to be because the Cl-36 is more or less directly available for root uptake due to the roots being near the surface. The opposite is true for the contaminated water table experiment. For the contaminated water table experiment, the evolution of Cl-36 in the soil column shows that close to the water table the concentration of chlorine rises rapidly and reaches a steady state, while the top 5 cm of the soil contains hardly

any Cl-36. In conclusion, migration of chlorine appears to be less in the colluvial soil than in garden soil; however due to the organic content of the soils, one might expect it to be the other way round. For stable chloride, there was generally a reduction with time in chloride in soil solution, probably due to the formation of organic complexes.

Further Benefit could be gained by performing assessments at different temporal and spatial scales and testing when and under what conditions the results can be extrapolated. The testing would need to be conducted under different hydrological and redox conditions to allow the significance of different assumptions to be determined, based on current understanding.

It was noted that although chlorine is very mobile, organic recycling means that the chlorine is released but then taken up by plants again before it has time to migrate. This gives an appearance of mobility and accumulation at the same time.

### **Modelling task group to look at model development and comparison of equilibrium (CR) specific activity (SA) and kinetic approaches to model structure**

The model comparisons should allow for the scientific issues associated with Cl-36 behaviour but also include the radiological endpoint, bearing in mind that the dynamical issues will depend on what we mean by the average dose to a critical group.

The SA approach assumes no isotopic discrimination, constant stable chlorine contents in environmental media and speciation between chloride and organic chlorine. The main pathway of interest follows from irrigation with contaminated water. This approach leads to data problems, as the data required for the model are not always available. It is more applicable to long-term safety assessments than short-term assessments, due to the seasonal variation of chlorine content in soils and the need to take account of all stable chlorine inputs into each compartment in the system including chemical and organic amendment such as fertilisers. However, the SA approach does allow chlorine speciation and environmental processes to be taken into account along with adaptation to varying environmental conditions. It can be thought to provide a more realistic estimate of Cl-36 concentrations.

Mike Thorne presented a simple soil plant model used for assessment purposes. It is a water balance model for soils with a kinetic model of stable chloride flows. It assumes non-linear binding of chloride in soil and both active and passive uptake of chloride by plants. Passive, diffusive loss of chloride from plant roots is included. Mike suggested that there were few concerns about assessing Cl-36 transfer to animal products. For inhalation, which is a minor route of exposure, he uses the ICRP Publication 66 model for humans, with compounds of chlorine treated as Class F or Class M for modelling the respiratory system in animals. A four compartment model is used for the gastrointestinal tract, with very little faecal excretion, so as to give rapid and complete uptake of chloride from the stomach(s) and small intestine. Systemic circulation is modelled assuming a well-mixed single compartment.

NRI is currently undertaking dose assessments for those radionuclides which enter the biosphere. Four situations are under consideration: release to farmland, a well; highlands and a small lake. Each situation has different ecology, irrigation and foodchain pathways. The

important pathways for radiation exposure for Cl-36 are the consumption of milk, meat and vegetables. The key issue is that, according to NRI model assumptions, the main loss from soil is uptake to plants and removal by harvesting. This process is more important than percolation. NRI use a very high assumption for root uptake, similar to the data seen in earlier presentations. However, uptake is different for different systems. In a natural environment, crops die and their constituent elements are returned to the ground but in an agricultural system crops are harvested and the contaminants are assumed to be removed with the crop.

The probabilistic compartment model, OURSON (EdF) incorporates a specific activity model for Cl-36 migration. For Cl-36 modelling, transfers are governed by the stable chlorine concentration in each of the compartments. Chlorine is essential for life so the concentration in each compartment must be greater than the minimum necessary for life but below toxic levels. The model ensures that the content of stable chlorine in each part of the system is appropriate for the levels essential for life.

There are currently two types of model, simple equilibrium and sophisticated, e.g. flux based. However, data are missing for some parameters in both models, reflecting that we do not completely understand the system we are trying to model. The more sophisticated models may be useful to provide parameters for simple models. In addition, there was consensus towards using dynamic models, and deriving those models on complete system descriptions. A comparison of these descriptions would ensure that all potentially important pathways are included.

## **Conclusions**

It was concluded that a lot of information had been exchanged among participants with different backgrounds and technical contributions to make to waste disposal safety assessment. In addition, much had been learnt over the course of the forum, which has implications for long term Cl-36 dose assessment.

It was decided to set up a further Bioprotia international working group to test and improve models for long-term Cl-36 dose assessment, with the specific objectives to compare and contrast alternative models for long-term Cl-36 accumulation in soil and uptake into food crops. This will include:-

- standard models for radionuclide accumulation in soil and the assumption of equilibrium concentration ratios (CRs) for crop uptake,
- specific activity (SA) models special for Cl-36, and
- more detailed dynamic models which take fuller account of relevant mixing in the soil-plant-hydro system as well as chlorine chemistry.

The comparison will be structured so as to identify relevant features for inclusion in future long-term assessment models, making best use of data available and maximising confidence in

the result of related dose assessments. It may be possible to develop specific recommendations on future model use, but these may in turn depend on local assessment contexts: e.g. the definition of the quantity which has to be calculated; the way in which evolution of the environment has to be taken into account; and local climate and other local geographical features. So there may be different conclusions for different situations, both concerning the migration and accumulation models and the related dose calculation for human exposure. To the extent that significant uncertainties remain, recommendations will be made for how to address them.

### **Acknowledgement**

Thanks are given to the BIOPROTA sponsoring organisations and especially to ANDRA for hosting the workshop.

### **REFERENCES**

- [1] BIOPROTA (2006). Report of an International Forum on Cl-36 in the Biosphere. ANDRA, Chatenay-Malabry, available at [www.bioprota.com](http://www.bioprota.com)
- [2] IAEA (2003). “Reference Biospheres” for Solid Radioactive Waste Disposal. Report of BIOMASS Theme 1 of the International Atomic Energy Agency’s Coordinated Research Programme on Biosphere Modelling and Assessment (BIOMASS). IAEA-BIOMASS-6, Vienna.



# THE IMPORTANCE OF MOBILE FISSION PRODUCTS FOR LONG-TERM SAFETY IN THE CASE OF DISPOSAL OF VITRIFIED HIGH-LEVEL WASTE AND SPENT FUEL IN A CLAY FORMATION

**Jan Marivoet and Eef Weetjens**  
SCK•CEN, Boeretang 200, 2400 Mol, Belgium

## Abstract

In Belgium, the possibility to dispose of high-level radioactive waste in clay formations is studied since 1976. In the PAGIS report, which was the first performance assessment of the disposal of vitrified high-level waste in a clay formation and which was published in 1988, the most important contributors to the total dose via a water well pathway were  $^{237}\text{Np}$ ,  $^{135}\text{Cs}$  and  $^{99}\text{Tc}$ .

Since 1988, several elements that strongly influence the calculated doses have evolved:

- the inventory of long-lived mobile fission and activation products in vitrified high-level waste has been improved;
- the half-life of  $^{79}\text{Se}$  has been re-estimated;
- substantial progress has been made in the determination of migration parameters of the main fission and activation products and actinides.

In recent performance assessments, the actinides and  $^{135}\text{Cs}$  do not significantly contribute to the total dose, as they remain confined in the host clay formation during several millions of years due to sorption on clay minerals. Consequently, the total dose resulting from the disposal of vitrified high-level waste or spent fuel is essentially due to releases of mobile fission and activation products. On the basis of recent waste inventory data and parameter values, the most important contributors to the total dose via a water well are:

- in the case of disposal of spent fuel:  $^{79}\text{Se}$ ,  $^{129}\text{I}$ ,  $^{126}\text{Sn}$ ,  $^{36}\text{Cl}$ , and  $^{99}\text{Tc}$ ;
- in the case of disposal of vitrified HLW:  $^{79}\text{Se}$ ,  $^{126}\text{Sn}$ ,  $^{36}\text{Cl}$ ,  $^{129}\text{I}$ , and  $^{99}\text{Tc}$ .

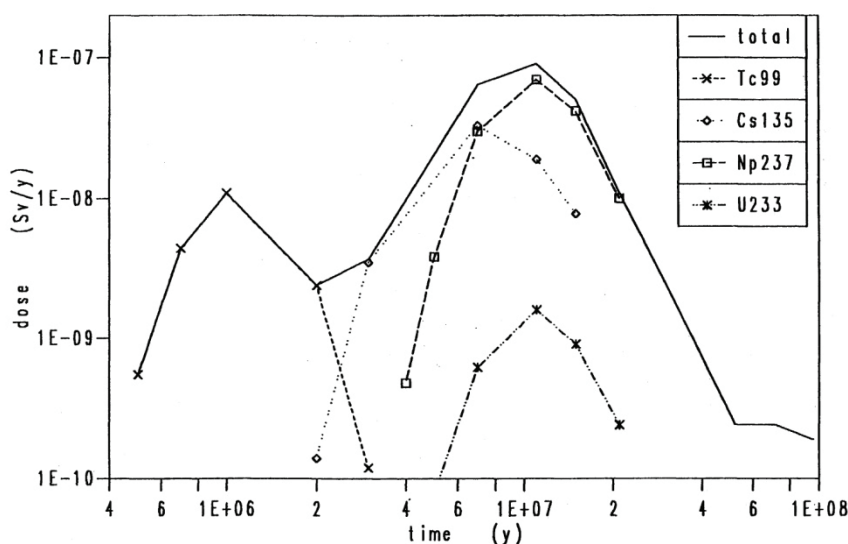
Important remaining uncertainties are the transfer factors of volatile fission and activation products into the vitrified waste during reprocessing and migration parameters of Se.

## Introduction

In Belgium, the possibility to dispose of high-level radioactive waste in clay formations is studied since 1976. From a European Catalogue of “Geological Formations Having Favourable Characteristics for the Disposal of Solidified High-Level and/or Long-Lived Radioactive Wastes” [1] it appeared that the Boom Clay Formation is one of the most promising potential host formations in Belgium. It was decided in 1980 to construct an underground research laboratory (URL), called HADES, in the Boom Clay under the site of the Belgian Nuclear Research Centre SCK•CEN at Mol. This URL became operational in 1984 and since then it has been extended at several times. A large amount of geoscientific data [2] became available from the site characterisation programme that was carried out *insitu* or in surface laboratories on cores taken from the URL or from boreholes.

The safety assessments of the possible geological disposal of high-level radioactive waste in the Boom Clay started in 1983 in the framework of the PAGIS (Performance Assessment of Geological Isolation Systems) project of the European Commission (EC). The resulting report [3] was the first performance assessment of the disposal of vitrified high-level waste (HLW) in a clay formation. At that time, the studies on the migration of radionuclides in clay formations were still in a very preliminary phase. As a consequence, the migration parameters were largely based on generic data, e.g. [4] and [5]. The calculated total doses via a water well pathway are shown in Figure 1. The most important contributors to the total dose were  $^{237}\text{Np}$ ,  $^{135}\text{Cs}$  and  $^{99}\text{Tc}$ . Somewhat surprisingly, only one radionuclide ( $^{99}\text{Tc}$ ) of those that are now considered as mobile fission products appeared in the PAGIS list of important radionuclides.

**Figure 1. Total doses via a water well pathway calculated in the PAGIS study [3]**



## Evolution of the assessment basis

Since 1988, several elements that may strongly influence the calculated doses have evolved:

- the inventory of long-lived mobile fission and activation products in vitrified high-level waste has been improved;
- the half-life of  $^{79}\text{Se}$  has been re-estimated;
- substantial progress has been made in the determination of migration parameters of the main fission and activation products and actinides.

### ***Inventory of activation and volatile fission products***

Old inventories of vitrified HLW (e.g. [6]) did not contain activation or volatile (during reprocessing) fission products. At the end of the eighties it became clear that the activity of a number of activation products in vitrified HLW is not negligible and that they have to be considered as well in safety evaluations of high-level waste disposal. Moreover, it appeared that a small fraction of the volatile fission and activation products present in the spent fuel is transferred into the vitrified high-level waste. The lack of accurate data on the fraction of volatile fission and activation products in vitrified high-level waste sometimes led to a rather surprising evolution of the amount of these products in vitrified high-level waste; for example, in the Belgian waste management programme, the assumed fraction of  $^{129}\text{I}$  remaining in the vitrified high-level waste evolved as follows: 0% [6], 0.1% [7], 10% [2] and 1% in the inventory of ONDRAF/NIRAS of 2003.

Within the Red-Impact project [8], information collected from various sources has been used to re-estimate the fraction of volatile fission and activation products going into vitrified high-level waste. This led to the following estimation of the remaining fractions:  $^{14}\text{C}$ : 10%,  $^{36}\text{Cl}$ : 1%,  $^{129}\text{I}$ : 1%. However, one can observe considerable differences between the thus estimated amounts of  $^{14}\text{C}$  and  $^{36}\text{Cl}$  in the vitrified HLW and the values used by waste agencies; the latter are especially for  $^{36}\text{Cl}$  much higher.

### ***Half-life of $^{79}\text{Se}$***

Until 1990, most radionuclide tables mentioned a half-life of 65 000 years for  $^{79}\text{Se}$ . Around 1992 the half-life was increased to 650 000 years and around 1998 it was even increased to 1.1 million years. Since 2003, a value of 295 000 years is used within the Belgian waste management programme on the basis of measurements published by Jiang Song-Sheng *et al.* [9]. The Laboratoire National Henry Becquerel from CEA also recommended in 2005 a value of 300 000 years for the half-life of  $^{79}\text{Se}$  [10]; however, in October 2006 this value was increased to 356 000 ( $\pm$  40 000) years [11].

### ***Migration parameters***

In 1985 the values of the migration parameters used in the safety evaluations were mainly based on databases in which sorption data of various origins, and consequently measured in different chemical conditions, had been collected. During the last half of the eighties it became

clear that speciation and chemical conditions (pH and Eh) strongly influence the solubility and the migration parameters of many radionuclides in the Boom Clay. Since then, extensive formation-specific migration research programmes have been set up in many countries that are considering geological disposal. These programmes presently provide much more reliable migration parameters, e.g. [12].

Table I illustrates the evolution of the values used for the solubility limit and apparent diffusion coefficient of C, Cl, Se, Tc, I, Pd, Sn, Cs and Np within the Belgian programme for geological disposal of high-level waste; it gives the data that was used for the PAGIS calculations [3], for which solubility limits were not yet applied, and the data used in 2006.

**Table I. Values of solubility limit ( $C_{sol}$ ) and apparent diffusion coefficient ( $D_a$ ) of selected radionuclides used in PAGIS [3] and in recent performance assessment calculations**

	PAGIS (1985)	New data (2006)	
	$D_a$ (m <sup>2</sup> /s)	$D_a$ (m <sup>2</sup> /s)	$C_{sol}$ (mol/l)
<b>C-14</b>	-	7.0E-11	-
<b>Cl-36</b>	-	1.4E-10	-
<b>Se-79 (VI)</b>	1.0E-12	3.0E-11	-
<b>Se-79 (0, -II)</b>	1.0E-12	1.4E-10	5.0E-08
<b>Tc-99</b>	3.0E-12	2.0E-10	3.0E-08
<b>I-129</b>	-	1.4E-10	-
<b>Pd-107</b>	1.0E-12	1.0E-11	1.0E-07
<b>Sn-126</b>	1.0E-12	1.0E-11	5.5E-07
<b>Cs-135</b>	8.0E-13	1.0E-13	-
<b>Np-237</b>	3.0E-13	2.0E-13	1.0E-06

Table I gives two sets of migration parameters for Se. It has been observed that selenate (Se VI) is very stable and that it is not reduced in Boom Clay conditions at the laboratory timescale; selenate is not solubility limited and, as it is a relatively big anion and very weakly retarded, it diffuses somewhat slower than, e.g. I-, through the clay [13]. Selenite (Se IV) can be reduced in Boom Clay conditions; if sorbed and reduced it becomes Se (0), it precipitates and is solubility limited; if it is reduced to HSe<sup>-</sup> (Se -II), it is solubility limited in the presence of Fe<sup>++</sup>, but as it is a small ion, it is expected to diffuse at about the same rate as I-. In 1985, Se was assumed to be sorbed on clay minerals.

The migration parameters for Tc were drastically changed between 1985 and 2006; high K<sub>d</sub> values were sometimes reported from batch experiments; these high values were probably due to precipitation and not to sorption. The apparent diffusion coefficient used for Pd and Sn is now a factor 10 higher than it was in 1985, and a solubility limit is now also applied. For Cs, the updated apparent diffusion coefficient is 8 times lower than in 1985; this slower diffusion rate makes that the amount of <sup>135</sup>Cs that is released from the host clay layer is negligible. For Np, the apparent diffusion coefficient is somewhat lower than it was in 1985, and a solubility limit is now applied as well.

The migration parameters of I, Cl and C in the Boom Clay are considered to be well known. Especially for I a large number of results are available from experiments carried out at scales ranging from a few centimetres to a few decimetres. For another mobile element, HTO, it is demonstrated with a large scale *insitu* experiment that diffusion parameters measured on a 5-cm clay core can be used to forecast the migration of HTO over a distance of a few metres in the Boom Clay.

### **Recent assessments of disposal of vitrified HLW and spent fuel**

In the performance assessment calculations, of which results are given hereafter, we have simulated the dissolution of the waste matrix, the migration of radionuclides through the host clay layer, the transport and dilution of radionuclides in the aquifer overlying the host formation and transfers of radionuclides in the biosphere to man [2]. The doses were calculated for the expected evolution scenario of the repository system; this means that it is assumed that the essential repository components will function as expected. A water well is considered as geosphere-biosphere interface; in the dose calculations it is assumed that water from this well is used by a small self-sustaining community as drinking water for men and cattle and as irrigation water. Another possible geosphere-biosphere interface is a local river draining the overlying aquifer. The doses calculated for this last pathway are more than 2 orders of magnitude lower than the doses via the water well pathway because of the considerable dilution of the radionuclide concentrations by the river water. Complementary indicators that are also calculated are released radiotoxicity flux and cumulative released radiotoxicity.

### ***Vitrified HLW***

We consider the amount of vitrified high-level waste that arises if all the spent fuel irradiated in the 7 Belgian nuclear power plants should be reprocessed; this corresponds to 3915 vitrified HLW canisters. The designed lifetime of the overpack is 2 000 years and the waste matrix is assumed to dissolve at a constant rate over 70 000 years. The considered repository design is based on the supercontainer concept [14].

**Figure 2. Evolution of the total dose and its main contributors via a water well pathway (vitrified HLW, expected evolution scenario)**

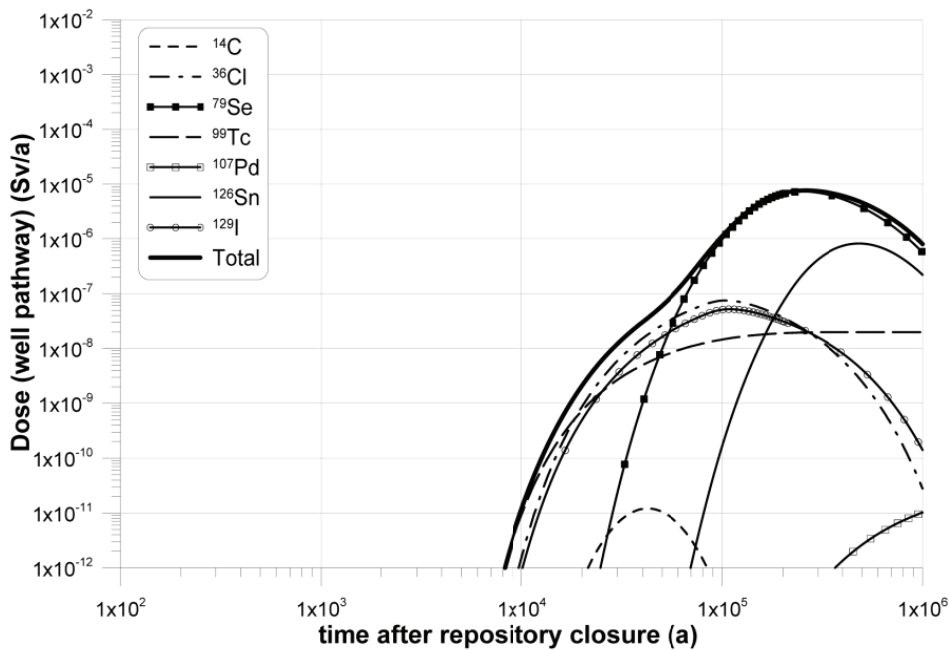


Figure 2 shows that in case of disposal of vitrified HLW the main contributor to the total dose is  $^{79}\text{Se}$  (by applying the migration parameters of Se(VI)). Other significant contributions are due to  $^{126}\text{Sn}$ ,  $^{36}\text{Cl}$ ,  $^{129}\text{I}$ , and  $^{99}\text{Tc}$ . Because of its relatively short half-life, the contribution of  $^{14}\text{C}$  to the total dose is nearly negligible. A similar ranking of the radionuclides is obtained for the river doses. However, for the indicators radiotoxicity flux and cumulative radiotoxicity, the rankings are somewhat different:

- radiotoxicity flux:  $^{129}\text{I}$ ,  $^{79}\text{Se}$ ,  $^{36}\text{Cl}$ ,  $^{126}\text{Sn}$ , and  $^{99}\text{Tc}$ ;
- cumulative radiotoxicity:  $^{79}\text{Se}$ ,  $^{129}\text{I}$ ,  $^{126}\text{Sn}$ ,  $^{99}\text{Tc}$ , and  $^{36}\text{Cl}$ .

### ***Spent fuel***

We consider an amount of spent fuel with a burn-up of 50 GWd/tHM (initial enrichment 4.2%  $^{235}\text{U}$ ) that is equivalent to the amount of spent fuel (with burn-ups increasing from 36 to 55 GWd/tHM) irradiated in the 7 Belgian nuclear power plants; this amount is 4 235 tHM. The designed lifetime of the overpack is 2 000 years and the uranium oxide matrix is assumed to dissolve at a constant rate over 500 000 years; 5% of the  $^{129}\text{I}$  is assumed to occur on the surface of the spent fuel pellets and to dissolve instantaneously in the groundwater after corrosion of the container. The considered repository design is also based on the supercontainer concept.

**Figure 3. Evolution of the total dose and its main contributors via a water well pathway (spent fuel, expected evolution scenario)**

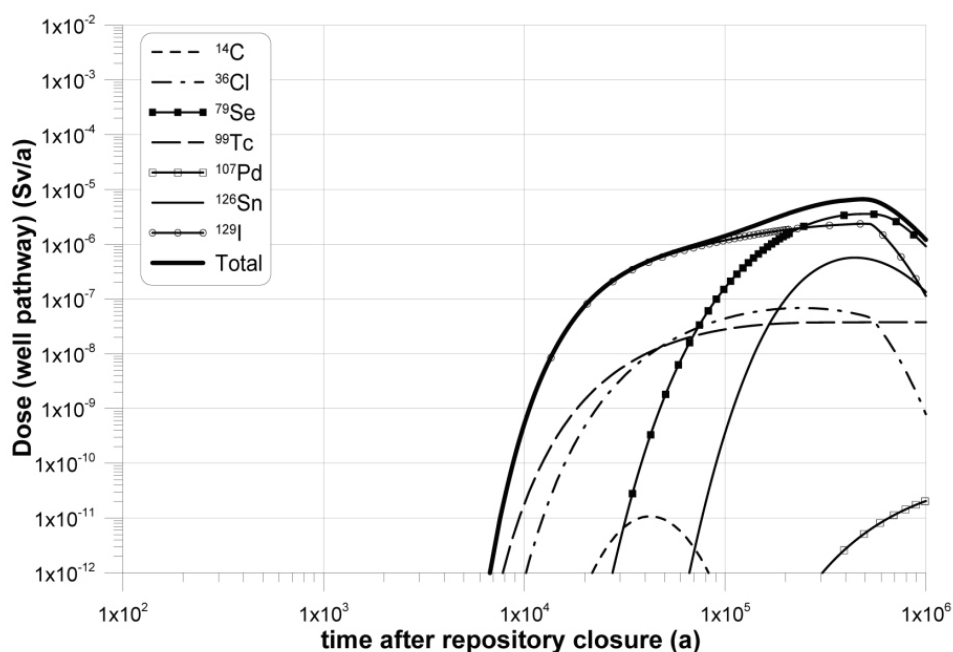


Figure 3 shows that in the case of disposal of spent fuel the main contributors to the total dose are  $^{79}\text{Se}$  and  $^{129}\text{I}$ ; other significant contributions are due to  $^{126}\text{Sn}$ ,  $^{36}\text{Cl}$ , and  $^{99}\text{Tc}$ . Because of its relatively short half-life, the contribution of  $^{14}\text{C}$  to the total dose is about negligible. A similar ranking of the radionuclides is obtained for the river doses. However, for the indicators radiotoxicity flux and cumulative radiotoxicity, the rankings are somewhat different:

- radiotoxicity flux:  $^{129}\text{I}$ ,  $^{79}\text{Se}$ ,  $^{36}\text{Cl}$ ,  $^{99}\text{Tc}$ , and  $^{126}\text{Sn}$ ;
- cumulative radiotoxicity:  $^{129}\text{I}$ ,  $^{99}\text{Tc}$ ,  $^{79}\text{Se}$ ,  $^{126}\text{Sn}$ , and  $^{36}\text{Cl}$ .

The long-living waste matrix makes that the dose curves of  $^{129}\text{I}$  and  $^{36}\text{Cl}$  have a relatively flat top; on the other hand, the flat peak of  $^{99}\text{Tc}$  is due to its solubility limit. The fast rising curve of  $^{129}\text{I}$  around 10 000 years can be attributed to the 5% of its inventory that is directly soluble.

The most striking difference between the HLW and spent fuel doses is the much lower contribution of  $^{129}\text{I}$  in the case of vitrified HLW, clearly linked to the inventory, since the remaining fraction of  $^{129}\text{I}$  in the vitrified HLW is only 1%. This is not the case for  $^{36}\text{Cl}$  because of the high amount of  $^{36}\text{Cl}$  in the inventory used for vitrified HLW.

## Sensitivity studies

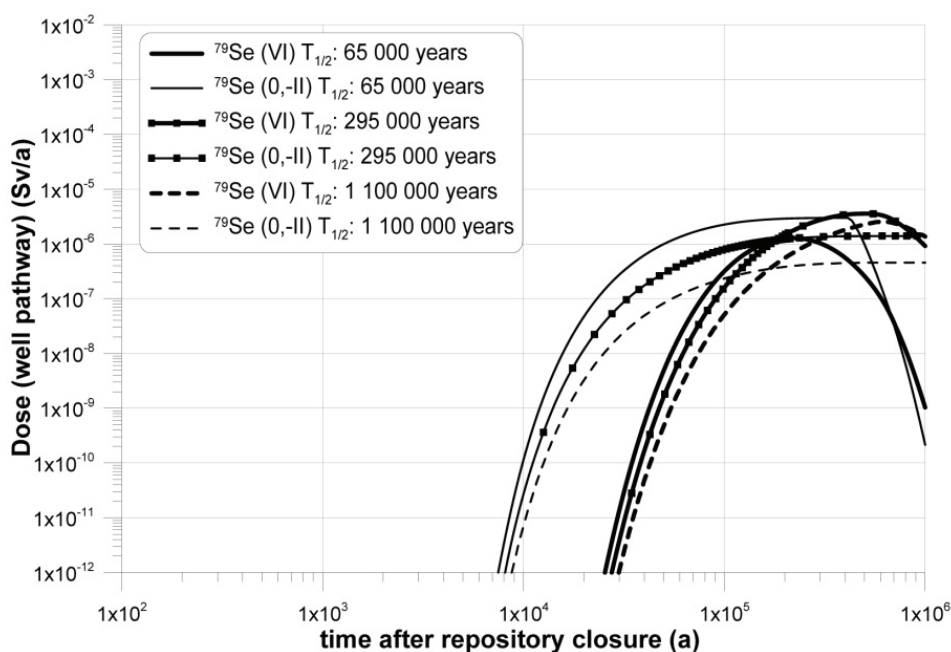
### Migration parameters of Se

As reference migration parameters for Se we have used the Se (VI) values (Figures 2 and 3). Because it is not clear what will be the speciation of Se (Se(VI), Se (IV) or Se(0)) when it is released from the waste matrix (vitrified HLW or spent fuel), we will make a scoping calculation to check which one of the two possible Se migration data sets is the most conservative one.

### Half-life of $^{79}\text{Se}$

As the value of the half-life of  $^{79}\text{Se}$  has been changed several times during the last decade, we will make sensitivity calculations for half-life values of 65 000, 295 000 and 1 100 000 years to illustrate the effect of the half-life on the calculated doses.

**Figure 4. Sensitivity of the  $^{79}\text{Se}$  dose to its migration parameters and half-life (water well pathway, spent fuel, expected evolution scenario)**



## Results

The results of the sensitivity calculations for the case of spent fuel disposal are given in Figure 4. This figure clearly illustrates the effect of the higher value of the apparent diffusion coefficient of Se for the Se(0, -II) data set;  $^{79}\text{Se}$  fluxes are leaving the clay layer after about 10 000 years whereas this takes about 30 000 years for the Se(VI) data set. However, the curves calculated with the Se(0, -II) data show a flat top which is due to the solubility limit.

When the shortest half-life (65 000 years) of  $^{79}\text{Se}$  is considered, higher doses are calculated up to a few hundreds of thousands of years because of the high molar activity; after about 500 000 years the effect of radioactive decay becomes clearly visible. The value that is considered at present (295 000 years) yields the highest dose for the Se(VI) migration data set because around 500 000 years the effect of decay is still limited but the molar activity is higher than for a half-life of 1 100 000 years.

## Conclusions

Results of recent performance assessment calculations for a repository in clay show that mobile fission and activation products, mainly  $^{79}\text{Se}$ ,  $^{129}\text{I}$  and  $^{126}\text{Sn}$  and to a lesser extent  $^{36}\text{Cl}$  and  $^{99}\text{Tc}$ , are the main contributors to the total dose or released radiotoxicity in case of the expected evolution scenario for the disposal of vitrified high-level waste as well as spent fuel. The other fission and activation products and all the actinides are sorbed by the clay and/or are solubility limited what makes that they are efficiently confined within the host clay formation during very long times and that they do not give any significant contribution to the total dose.

In case of disposal of vitrified high-level waste, important remaining uncertainties in the assessment of the contributions of mobile fission and activation products to the total dose are the fractions of volatile fission and activation products, i.e.  $^{14}\text{C}$ ,  $^{36}\text{Cl}$  and  $^{129}\text{I}$ , that are transferred into the vitrified high-level waste during reprocessing. In case of disposal of spent fuel, the considerable fraction of mobile activation and fission products that can dissolve instantaneously when the waste comes in contact with groundwater has a substantial impact on the resulting dose curve and strongly limits the contribution of the long-lived  $\text{UO}_2$  matrix. During the last decade the value of the half-life of  $^{79}\text{Se}$  has been changed at several occasions, what obviously influences the resulting  $^{79}\text{Se}$  doses; the recently measured value of 356 000 years, in combination with the high mobility of Se, makes that a large fraction of the disposed  $^{79}\text{Se}$  can diffuse out of the host clay formation. The speciation of Se in the waste form can have a strong influence on the values of its migration parameters, and hence on the eventual dose. In this respect, it might be interesting to re-evaluate the values of the migration parameters used for Sn, because the presently used values might be excessively conservative. The migration parameters of the other mobile fission and activation products are considered to be well known.

From a long-term safety point of view, one of the essential differences between the disposal of vitrified high-level waste and of spent fuel is that in case of reprocessing a large fraction of the fission product  $^{129}\text{I}$  is not remaining in the high-level waste, but is directly discharged into the sea, whereas in case of direct disposal of spent fuel its whole inventory is going into the geological repository.

## **Acknowledgements**

The results presented in this paper were obtained in the framework of the long-term safety studies on geological disposal of high-level and long-lived radioactive waste in clay formations carried out by SCK•CEN for the Belgian agency for the management of radioactive waste ONDRAF/NIRAS. Other results were obtained in the frame of the PAGIS project of the European Commission.

## REFERENCES

- [1] EC (1979), European Catalogue of Geological Formations Having Favourable Characteristics for the Disposal of Solidified High-Level and/or Long-Lived Radioactive Wastes; Volume 2: Belgium. EC, Luxembourg.
- [2] ONDRAF/NIRAS (2001), SAFIR-2, Second Safety Assessment and Interim Report. NIRON, Brussels, Report NIRON 2001-06 E.
- [3] Marivoet J. and A. Bonne (1988), PAGIS: Performance Assessment of Geological Isolation Systems, Disposal in Clay Formations. EC, Luxembourg, Report EUR 11776 EN.
- [4] Sheppard M.I, D.I Beals, D.H. Thibault and P. O'Connor (1984), Soil Nuclide Distribution Coefficients and their Statistical Distribution. AECL, Pinawa, Report AECL-8364.
- [5] Andersson K. and B. Allard (1983), Sorption of Radionuclides on Geologic Media: A Literature Survey. Chalmers university of Technology, Göteborg, KBS Report TR 83-07.
- [6] Cadelli N., G. Cottone, G. Bertozzi and F. Girardi (1984), PAGIS, Summary Report of Phase 1: A Common Methodological Approach Based on European Data and Models. EC, Luxembourg, Report EUR 9220 EN.
- [7] NAGRA (1985) Project Gewähr 1985, Nuclear Waste Management in Switzerland: Feasibility Studies and Safety Analyses. NAGRA, Baden, Report NGB 85-09.
- [8] Gudowski W., E. Gonzales, D. Greneche, L. Boucher, J. Marivoet, C. Zimmerman, W. von Lenza, A. Vokal (2006), Impact of Partitioning, Transmutation and Waste Reduction Technologies on the Final Nuclear Waste Disposal. Proc. FISA 2006 Conference, Luxembourg, March 13-16, 2006, European Commission (in preparation).
- [9] Jiang Song-Sheng, He Ming, Diao Li-Jun, Guo Jing-Ru and Wu Shao-Yong (2001) Remeasurement of the Half-Life of <sup>79</sup>Se with the Projectile X-Ray Detection Method. Chinese Phys. Lett. **18** 746-749.
- [10] Bé M.M, V. Chisté and C. Dulieu (2005) Half-lives: Table of Recommended Values. CEA, Saclay, Note Technique DETECS/LHNB/2005-08.
- [11] Bé M.M, V. Chisté and C. Dulieu (2006) Half-lives: Table of Recommended Values. CEA, Saclay, Note Technique DETECS/LHNB/2006-58.
- [12] Maes N., Wang L., Delécaut G., Beauwens T., Van Geet M., Put M., Weetjens E., Marivoet J., van der Lee J., Warwick P., Hall A., Walker G., Maes A., Bruggeman C.,

Bennett D., Hicks T., Higgs J., and Galson D. (2004), Migration Case Study: Transport of Radionuclides in a Reducing Clay Sediment (TRANCOM-II). Final scientific and technical report of the EC TRANCOM-II project. SCK•CEN, Mol, Report BLG-988.

- [13] De Cannière P. and Maes N. (2007), Transport Properties of Selenium in Boom Clay for Long-Term Safety Assessment of <sup>79</sup>Se. International Workshop Mobile fission and Activation Products in Nuclear Waste Disposal, La Baule, France, 16-19 January 2007.
- [14] ONDRAF/NIRAS (2004), Multi-Criteria Analysis on the Selection of a Reference EBS Design for Vitrified High-Level Waste. NIRONDD, Brussels, Report NIRONDD 2004-03 E.

## **UPTAKE OF SELENATE ON HYDRATED AND DEGRADED CEMENT: BATCH AND DYNAMIC EXPERIMENTS**

<sup>1,2</sup>Isabel Rojo, <sup>1,2</sup>Miquel Rovira, <sup>1,2</sup>Vicens Martí, <sup>1,2</sup>Joan de Pablo, <sup>3</sup>Lara Duro, <sup>3</sup>Xavier Gaona,  
<sup>3</sup>Eli Colàs, <sup>3</sup>Mireia Grivé

<sup>1</sup>CTM Centre Tecnològic, Avinguda de les Bases de Manresa 1, 08242 Manresa (Spain)

<sup>2</sup>Chemical Engineering Department, Universitat Politècnica de Catalunya, Barcelona (Spain)

<sup>3</sup>Enviros Spain S.L., Passeig de Rubí 29-31, 08197 Valldoreix (Spain)

### **Abstract**

The evaluation of selenate sorption and retardation in batch and dynamic experiments on hydrated and degraded cement has been studied. Desorption studies have also been carried in order to assess the reversibility of the sorption process. Sorption data onto degraded cement have been treated assuming the formation of surface complexes, whereas sorption kinetics has been fitted by using a pseudo-first order kinetic equation. Dynamic flow experiments have also been modelled.

## Introduction

Cement-based materials play an important role in the multibarrier concept developed worldwide for the safe disposal of low- and intermediate-level radioactive wastes in underground repositories as well as for the temporary storage of high level nuclear wastes. The near-field of a cementitious repository acts as chemical barrier for radionuclides, retarding their migration to the far-field [1].

The retardation of selenium species by hardened cement paste (HCP) and concrete is of major interest in nuclear waste management due to the long half life of  $^{79}\text{Se}$  ( $t_{1/2} \sim 7.10^4$  years). In this study, the results of the study of the sorption of selenate on hydrated and altered cement by means of batch and dynamic experiments are presented.

## Experimental Section

### *Preparation of the cement materials*

The cement used in this work was a type I Portland cement sulphate resistant (CEM I 42.5 HS) obtained from the El Cabril, the Spanish low- and intermediate-level radioactive waste disposal located in Córdoba (Spain). This cement type is commonly used in the Spanish waste management programme in standard formulations of concrete for underground repositories, as it has been reported elsewhere [2].

The hydrated cement paste (HCP) was prepared adding Milli-Q water to the cement to produce a paste of water/cement ratio of 0.40. The paste was allowed to settle for 24 h at 25°C. After that, the cement monoliths were demolded and cured immersed in Milli-Q water (according to [3]) for 28 days at 25°C. The cement specimens were afterwards dried, crushed and sieved to obtain the fractions between 0.25-0.5 mm. All manipulations were performed in an open air atmosphere.

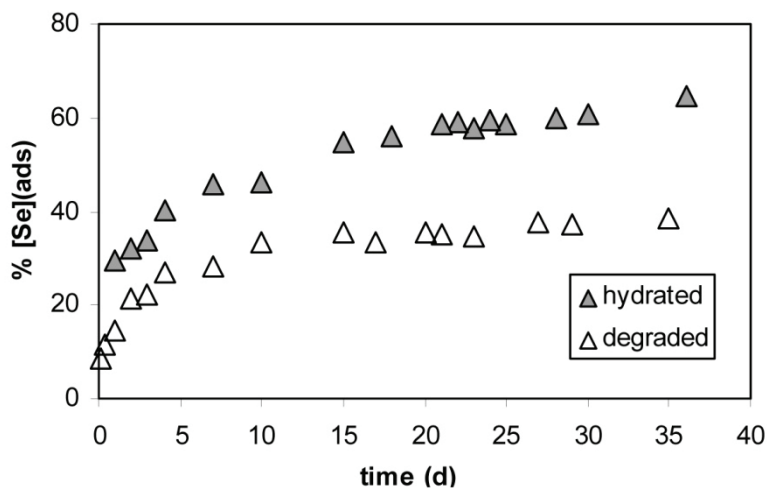
To obtain degraded HCPs, crushed hydrated cement (0.25-0.5 mm) was packed in a column and artificial groundwater (AGW) was passed through the system during 15 days at a flow rate of 0.4 mL/min to reproduce the same leaching conditions reported in the literature [4,5]. Details on groundwater preparation are reported elsewhere [6]. The outlet of the column was collected periodically and the pH and Ca concentration (analyzed by atomic absorption spectroscopy (AA-6200 Shimadzu)) were measured for each fraction. Latest fractions were mixed to produce the aged cement pore water (ACPW). The pH of ACPW was 12.5, that corresponds to the cement degradation step II. Concentration of Ca considered in the experiment (655ppm) is in agreement with portlandite equilibrium. The resulting degraded cement was dried and stored in the desiccator.

The specific surface area was determined by the BET methodology (Micromeritics Flowsorb II 2300). Values of 6.35 and  $10.97 \pm 0.01$  m<sup>2</sup>/g were obtained for hydrated and degraded cement, respectively.

### Batch sorption experiments

In order to ensure that equilibrium was reached in the experiments, preliminary kinetic data was obtained in batch experiments with both hydrated and degraded cement at 10g/L and selenium concentration  $1 \cdot 10^{-6}$  M (see Figure 1). These results indicated that 18 days were necessary to reach equilibrium.

**Figure 1. Results obtained from kinetic experiments conducted with hydrated and degraded cement at 10 g/L and selenium concentration  $1 \cdot 10^{-6}$  M**



Batch sorption experiments with Se(VI) on both hydrated and degraded cement were carried out at 25°C using 14 mL polystyrene centrifuge tubs. Two batch sorption procedures were followed for each solid: A) batch sorption experiments at constant initial selenium concentration ( $1 \cdot 10^{-6}$  M) and variable solid to liquid (S/L) ratio (5 to 400g/L) and B) batch sorption experiments at constant S/L ratio (50g/L) and variable initial selenium concentration ( $6 \cdot 10^{-8}$  M to  $6 \cdot 10^{-5}$  M). In both cases, crushed, size-fractionated (0.25-0.5 mm) hydrated or degraded cement was contacted with 10 mL of the corresponding initial concentration solution. Se(VI) stock solutions ( $2.5 \cdot 10^{-3}$  M) were prepared dissolving 47.4 mg of  $\text{Na}_2\text{SeO}_4$  in 100 mL of Milli-Q water, in case of experiments with hydrated cement, or directly in ACPW, in case of degraded cement experiments. Successive dilutions (with Milli-Q and ACPW water, respectively) of these stock solutions were done to obtain the desired initial concentration of selenium.

The temperature was held constant at 25°C. After equilibration in a rotatory shaker, the tubes were centrifuged at 3 000 rpm for 30 min. After removing the aqueous phase of each tube, a 4.5 mL-aliquot was used to measure the final pH and electrical conductivity. The larger fraction of the aqueous phase was acidified with 1% (v/v) 65%  $\text{HNO}_3$  and analyzed by ICP-MS (Perkin-Elmer, Elan 6 000 spectrometer) to determine Se. Additional centrifugation and filtration steps (through 0.45  $\mu\text{m}$  membrane nylon filters), lead to similar Se aqueous concentration.

Desorption studies were also conducted in order to assess the reversibility of the sorption process. After centrifugation in the type A and B experiments, the solution was removed from

the tube, and replaced by the same volume of ACPW or Milli-Q water for degraded and hydrated cement experiments, respectively. The tubes were shaken for 18 days. The reaction mixture was centrifuged and the supernatant used to determine the Se concentration after desorption.

### ***Dynamic flow experiments***

Simultaneously to the batch experiments, a dynamic experiment was performed at 25°C by means of a continuous flow-through system with a column packed with degraded cement. A  $1 \cdot 10^{-6}$  M Se(VI) solution was continuously pumped through the column by means of a peristaltic pump. Samples were taken at the column outlet at regular time intervals, and Se concentration was determined by ICP-MS. Additionally, one of each three samples were used to measure pH, electrical conductivity and Ca concentration. The three parameters were found to be approximately constant during the experiment at values of  $12.45 \pm 0.05$ ,  $7.8 \pm 0.4$  mS/cm and  $623 \pm 52$  ppm respectively. The porosity and the darcian flux of the column were obtained from the modelling of a conservative tracer breakthrough curve (15% acetone).

In order to compare the results of the dynamic flow experiment with batch data, an additional batch experiment with degraded cement was performed by triplicate. The initial selenate concentration considered in the experiment was  $1 \cdot 10^{-6}$  M, whereas the ratio S/L varied from 5 to 400g/L. This experiment lasted 25 min, which corresponds to the calculated residence time in the column.

## **Results**

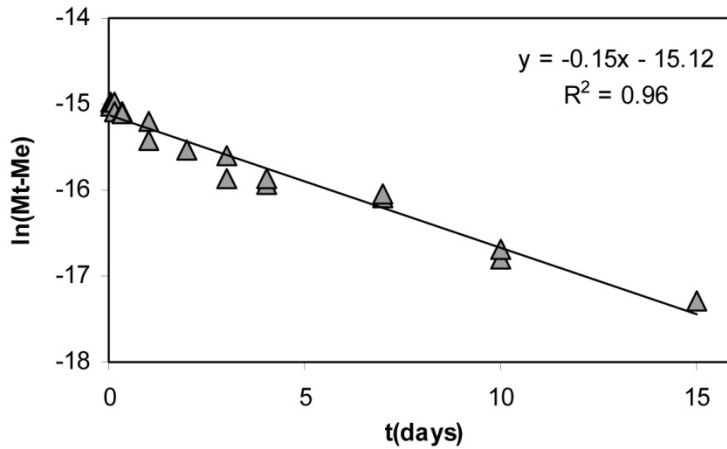
### ***Kinetic experiments***

Kinetic batch experiments performed at  $S/L = 10$  g/L and  $[Se]_0 = 1 \cdot 10^{-6}$  M show that 18 days are necessary to reach the equilibrium between degraded cement and selenate (see Figure 1). As shown in Figure 2, experimental data for degraded cement can be fitted by considering a pseudo-first order equation [7], [8] (eq.1).

$$\ln(M_t - M_{(e)}) = \ln(M_0 - M_{(e)}) - k_t t \quad (\text{eq.1})$$

In eq. 1,  $M_t$  (mol/L) is the concentration of aqueous selenate at a time  $t$  (days),  $M_0$  (mol/L) is the initial selenate concentration, and  $M_{(e)}$  (mol/L) is the concentration of aqueous selenate at equilibrium. The later ( $M_{(e)} = 6.40 \cdot 10^{-7}$  M) has been obtained from batch experiments carried out at  $t = 18$  days. Fitting the experimental data at  $t < 15$  days with eq. 1 leads to a value of  $k_t = -0.15 \text{ d}^{-1}$ .

**Figure 2. Results of the kinetic batch experiments at different times for degraded cement (triangles). Solid line has been calculated according to eq. 1**



### *Sorption Isotherms*

The results from batch experiments show that selenate sorption by hydrated and degraded cement amounted up to 82% uptake from solution.  $R_d$  calculated values, obtained for selenium concentrations between  $6 \cdot 10^{-8}$  M to  $6 \cdot 10^{-5}$  M and S/L ratios between 5 to 400g/L, were in the range 0.05-0.15  $\text{m}^3/\text{kg}$  for both hydrated and degraded cement.

These distribution ratios are higher than those described in the literature. [5] reported a weak sorption of  $\text{SeO}_4^{2-}$  on leached cement with  $R_d$  values of  $\approx 0.01$   $\text{m}^3/\text{kg}$  for  $[\text{Se}] \approx 1 \cdot 10^{-5}$  M and S/L 5-50 g/L. In the present work,  $R_d \approx 0.1$   $\text{m}^3/\text{kg}$  are obtained under similar conditions for degraded cement. However, the cement employed in [5] has an initial content of  $\text{C}_3\text{A} + \text{C}_4\text{AF}$  (aluminates and ferrite phases) of 7.1%. The cement employed in the present work has an initial  $\text{C}_3\text{A} + \text{C}_4\text{AF}$  content of 16.05%. Ettringite and monosulphoaluminate, in principle playing a key role in Se(VI) immobilization (see below), are formed mainly from these  $\text{C}_3\text{A}$  and  $\text{C}_4\text{AF}$  phases. Then, the lower  $R_d$  values obtained in [5] may be due to the lower amount of ettringite and monosulphoaluminate present in the cement employed.

In addition, [9] reported  $R_d$  values of 0.002-0.02  $\text{m}^3/\text{kg}$  for hydrated cement. In these cases, the artificial cement pore waters employed in [9], characteristic of the initial stage of cement degradation ( $\text{pH}=13.3$ ), are different from the ones employed in the present work, which may explain the differences observed.

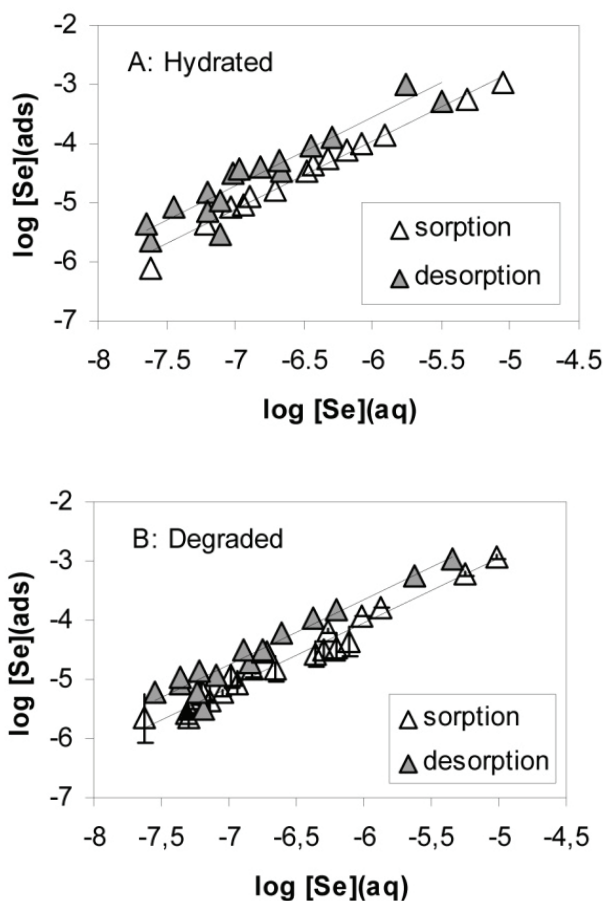
The Freundlich adsorption isotherm of selenate on hydrated and degraded cement can be written as in eq. 2, where  $A_i$  is the amount of selenate adsorbed per kg of cement,  $C_i$  is the concentration of selenate (mol/L) in the aqueous phase,  $n$  is a constant and  $R_F$  is the Freundlich adsorption constant.

$$\log A_i = \log R_F + 1/n \log C_i \quad (\text{eq.2})$$

In Figure 3, the measured values of  $\log[\text{Se}](\text{ads})$  in front of the corresponding  $\log[\text{Se}](\text{aq})$  are shown. The lines correspond to the fit obtained by using eq. 2. The  $R_F$  values in sorption experiments were  $1.1 \pm 0.7 \text{ m}^3/\text{kg}$  for hydrated cement and  $0.3 \pm 0.2 \text{ m}^3/\text{kg}$  for degraded cement. The values of  $n$  were  $0.86 \pm 0.03$  for hydrated cement and  $0.92 \pm 0.03$  for degraded cement, indicating the possibility of some surface heterogeneities.

In addition to the sorption isotherms, desorption isotherms originating from each of the initial points are also shown in Figure 3. These results indicate a reversible selenate sorption, as similar slope values have been obtained in both sorption and desorption experiments.

**Figure 3. Sorption and desorption isotherms of selenate on cement after 18 days of equilibration (A: hydrated cement; B: degraded cement). The solid lines represent the adjusted Freundlich isotherm. The error bars express the 2-fold standard deviation**



### *Mechanistic model*

Literature regarding selenate uptake onto Portland cement is scarce. [5] developed a simple solid-solution model, to estimate  $K_d$  values in terms of an exchange of sulphate by selenate in the ettringite structure. A later publication [9], based on X-ray absorption spectroscopy measurements, suggested that either i) non-specific interactions of selenium species with the

surface of the cement or ii) incorporation of Se anions into the structure of the minerals, presumably into channels and interlayers, could also explain Se(VI) uptake by cement. Based on these assumptions, an attempt has been made to obtain a mechanistic adsorption model that can explain the experimental data obtained for degraded cement.

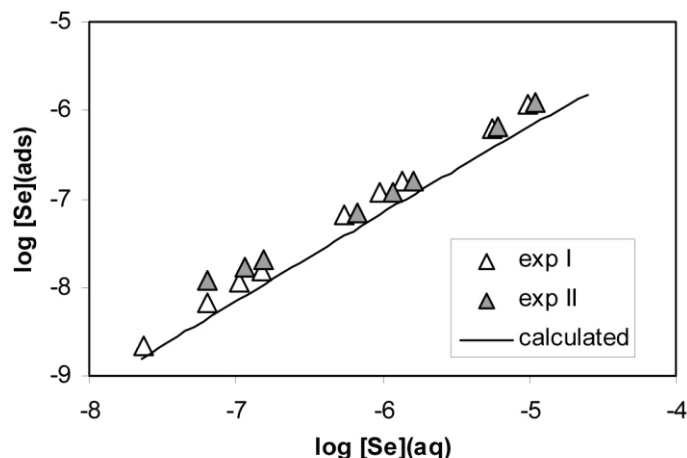
In agreement with the first hypothesis mentioned in [9] (non-specific interactions), sorption of selenate to the degraded cement may be described by the reaction shown in eq. 3. Batch experiments with degraded cement at a constant selenium concentration ( $1 \cdot 10^{-6}$  M) and low S/L ratios (5-50 g/L) have been used to obtain an apparent equilibrium constant for this equation.



[10] have shown strong uptake of selenate onto Al-bearing cement phases, namely ettringite and monosulfoaluminate, whereas in the same study no significant uptake on CSH phases was observed. In [10], the authors also provide a rough estimation of the concentration of the amount of Al and Ca sites at the surface of either ettringite or monosulfoaluminate ( $\approx 0.1$  mol sites/kg in each case). Using these values and the amount of ettringite and monosulfoaluminate present in a typical Portland cement [11], it is possible to calculate an approximate value of  $1.08 \cdot 10^{-5}$  mol of sites per gram of cement. Taking into account this value, and the results from the batch sorption experiments for degraded cement, an apparent equilibrium constant  $\log K(\text{eq.3}) = 3.7 \pm 0.1$  has been obtained.

This apparent equilibrium constant has been afterwards used to calculate the sorption of increasing concentrations of Se ( $1 \cdot 10^{-7}$ - $7 \cdot 10^{-5}$  M) onto degraded cement at a constant S/L ratio (50 g/L). The calculated values agree well with the experimental data (see Figure 4), although the concentration of adsorbed Se is slightly underestimated. The lineal trend indicates that, under these conditions, the concentration of free sites is much larger than the concentration of Se, and therefore the former remains almost constant and no saturation of sites is observed.

**Figure 4. Results of batch experiments with increasing concentrations of Se ( $1 \cdot 10^{-7}$ - $7 \cdot 10^{-5}$  M) onto degraded cement at a constant S/L ratio (50 g/l) (triangles). I and II stand for two different duplicates. Calculated data according to eq. 3 is also plotted (solid line)**



As shown in Figure 4, the proposed non-electrostatic model is able to properly explain Se(VI) uptake onto degraded cement.

The slow kinetics observed (see above) may suggest that additional processes are taking place. According to [12], slow uptake behaviour may be related with surface precipitation, diffusion to internal sites or even solid solution formation.

The precipitation of species such as  $\text{CaSeO}_4(\text{s})$  in the degraded cement surface is not expected, due to the high solubility of these selenate-bearing phases. Slow diffusion of selenate to the internal sites and later non-specific sorption of the anion would be in better agreement with the incorporation of Se anions into channels and interlayers suggested by [9].

[5] also proposed a solid-solution formation based on a sulphate-selenate exchange in the structure of ettringite. As sulphate concentration was not measured in the present work, this possibility cannot be ruled out. However, [5] reported this exchange to be especially important when a fast precipitation of secondary ettringite occurred. In the case of degraded cement contacted with ACPW, only primary (pre-formed) ettringite is expected. According to [5], the incorporation of selenate by a solid-solution formation in this pre-formed ettringite is less extensive.

None of these possibilities can be completely disregarded without additional data. Then, further experimental and modelling work will be conducted.

### ***Dynamic flow experiments***

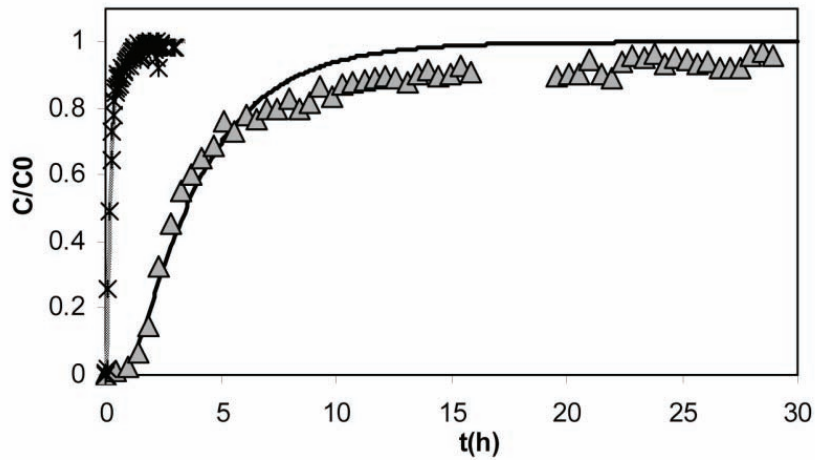
In addition to batch experiments, a dynamic experiment was also performed in a continuous flow-through system with a column packed with degraded cement.

Experimental data was modelled by using the analytical solution of the 1D advection-dispersion equation [13] for a semi-infinite column with a constant mass flux at  $x=0$ . The hydrodynamic parameters were obtained from the experiment performed with the conservative tracer (acetone).

The results shows that selenium presents a considerable retardation with respect to the tracer ( $R=17.4$ ), which results on a distribution ratio of  $R_d=0.009 \text{ m}^3/\text{kg}$ . This value agrees with the  $R_d$  values obtained in batch sorption experiments with short time interactions between the solid phase and the selenium solution:  $R_d=0.006 \text{ m}^3/\text{kg}$  after  $t=25 \text{ min}$  and  $R_d=0.009 \text{ m}^3/\text{kg}$  after  $t=1 \text{ hour}$ .

As shown in Figure 5, calculated values agree with experimental data.

**Figure 5. Results of transport flow experiments (crosses: acetone tracer, triangles: selenium data) and calculated data (lines)**



## Conclusions

The adsorption of selenate on sulphate-resistant Portland cement has been studied both from batch and dynamic experiments. Further kinetic experiments show that 18 days are needed to reach equilibrium between cement and selenate, and that sorption kinetics follow a pseudo-first order trend.

Experimental data can be fitted using Freundlich isotherms with  $n \neq 1$ , which indicates the existence of some surface heterogeneity.

A preliminary mechanistic approach has been also developed by considering the formation of the surface complex  $>X--SeO_4^{2-}$ . The estimated equilibrium constant has permitted to properly reproduce sorption experimental data obtained at constant S/L and increasing Se concentrations. However, it does not explain the surface heterogeneity or the slow kinetics observed for selenate uptake already mentioned.

Dynamic flow experiments have been modelled after adjusting the hydrodynamic parameters by using conservative tracer data. The distribution ratio obtained in the column agrees with the  $R_d$  values obtained in batch experiments at short contact times.

Further work will be conducted to improve the proposed the mechanistic model. Diffusion experiments are also scheduled, as diffusion is expected to be a key mechanism for Se transport through cementitious environments.

## **Acknowledgements**

The authors gratefully acknowledge Pedro Hernán and the financial support by ENRESA (Spain). I.R. and V.M. acknowledge the Spanish Ministerio de Ciencia y Tecnología for the research contracts (“Juan de la Cierva” and “Ramón y Cajal” programs). Dr. Cristina Domènech and an anonymous reviewer are acknowledged for fruitful comments to the document.

## REFERENCES

- [1] Bonhoure, I., Scheidegger, A. M., Wieland, E., Dähn R.(2002), *Radiochim. Acta*, 90, 647.
- [2] De la Cruz, B., Villar, M.V., Turrero, M.J., Peña, J., Fernández, A.M., Carlsson, T., Herbert, H.J., Meyer, T., Vokal, A. and Arcos, D. (2004), *State-of-the-art-report: Critical review and incorporation of information of EC, national and international programmes in RTD component 2. NF-PRO D.2.1.1.*
- [3] American Society for Testing and Materials (ASTM). Practice for making and curing concrete test specimens in the laboratory (ASTM Standard C190-90a. In: 1994 Annual book of ASTM standards, Vol. 4.02. Philadelphia (PA): ASTM, 1990.
- [4] Ochs, M., Hager, D., Helfer, S., Lothenbach, B. (1998), *Mat. Res. Soc. Symp. Proc.* 506, 773.
- [5] Ochs, M., Lothenbach, B., Giffaut, E. (2002), *Radiochim. Acta* 90, 639-646.
- [6] Cera, E. (1996) PhD thesis, UAB.
- [7] Tebes-Stevens, C., Valocchi, A.J, VanBriesen, J.M., Rittmann, B.E. (1998), *J. Hydrol.* 209, 8.
- [8] Rudzinski, W., Plazinski, W. (2006), *J. Phys. Chem. B*, 110, 16514.
- [9] Bonhoure, I., Baur, I., Wieland, E., Johnson, C. A., Scheidegger, A. M. (2006), *Cem. Concr. Res.*, 36, 91.
- [10] Baur, I., Johnson, C.A. (2003), *Environ. Sci. Technol.*, 37, 3442.
- [11] Taylor, H.F.W. (1997), *Cement Chemistry*. Thomas Thelford publishing.
- [12] Davis, J.A., Kent, D.B., (1990), in *Mineral-Water interface geochemistry* (Hochella, M.F.Jr., White, A.F., Eds.) *Reviews in Mineralogy* Vol. 23 Mineralogical Society of America.
- [13] Bear, J. (1972), *Dynamics of fluids in porous media*. Dover publications, Inc.



## **SORPTION OF CESIUM ON FRESHLY PRECIPITATED STUDDTITE (UO<sub>4</sub>·4H<sub>2</sub>O). KINETICS OF SORPTION AND SORPTION ISOTHERM**

**Javier Giménez<sup>1</sup>, Miquel Rovira<sup>1,2</sup>, Joan de Pablo<sup>1,2</sup>, Ignasi Casas<sup>1</sup>,  
Aurora Martínez-Esparza<sup>3</sup>, Xavier Martínez-Lladó<sup>2</sup>**

<sup>1</sup> Department of Chemical Engineering (ETSEIB-UPC), Av. Diagonal 647, 08028 Barcelona, Spain

<sup>2</sup> CTM Centre Tecnològic, Av. Bases de Manresa 1, 08240 Manresa, Spain

<sup>3</sup> ENRESA, Emilio Vargas 7, Madrid, Spain

### **Abstract**

One of the mechanisms that may increase the retention of different fission products and actinide elements is their sorption onto uranyl-containing secondary solid phases formed onto the surface of the spent nuclear fuel. Among these phases, studdtite (UO<sub>4</sub>·4H<sub>2</sub>O) has received increasing attention because it was identified on the surface of the spent fuel in leaching experiments in deionized water, due to the radiolytic formation of hydrogen peroxide.

In this work, we study the sorption of cesium onto studdtite through two series of experiments: (1) kinetics of cesium sorption, and (2) sorption isotherms. The results obtained have shown that cesium sorption is a very fast process, cesium in solution (an almost 40% of a 10<sup>-5</sup> mol·dm<sup>-3</sup> solution) is sorbed in less than one hour at pH around 5. On the other hand, the cesium sorption as a function of initial cesium in solution has been studied between initial cesium concentrations of 7.6·10<sup>-9</sup> mol·dm<sup>-3</sup> and 1.0·10<sup>-3</sup> mol·dm<sup>-3</sup>. The data have been modelled considering a Langmuir isotherm and a Freundlich isotherm. The best results have been obtained with a Freundlich isotherm with KF and n values of 10±1, and 1.4±0.1, respectively, with r<sup>2</sup>=0.998. The results show that the Freundlich isotherm is a good model for the cesium sorption onto studdtite ( $\chi^2=8\cdot 10^{-3}$ ), especially at cesium concentrations in the range between 7.6·10<sup>-9</sup> mol·dm<sup>-3</sup>, and 10<sup>-4</sup> mol·dm<sup>-3</sup>. Langmuir isotherm would better fit the experimental data at cesium concentrations at equilibrium higher than 5·10<sup>-4</sup> mol·dm<sup>-3</sup>.

## Introduction

During the long-term storage of the spent nuclear fuel in a high-level nuclear waste deep repository, the formation of secondary solid phases on the spent fuel should be considered because they might influence the radionuclides release by two different mechanisms [1,2]:

- blocking the fuel corrosion process;
- retaining/sorbing the radionuclides.

Different uranyl secondary phases have been identified on  $\text{UO}_2$  spent nuclear fuel. Wilson [3-5] identified uranophane ( $\text{Ca}(\text{UO}_2)_2(\text{SiO}_3\text{OH})_2 \cdot 5\text{H}_2\text{O}$ ), and soddyite ( $\text{U}_5\text{Si}_2\text{O}_{19} \cdot 6\text{H}_2\text{O}$ ); Sunder and Miller [6] schoepite ( $\text{UO}_3 \cdot 2\text{H}_2\text{O}$ ) and soddyite; Forsyth and Werme [7] dehydrated schoepite ( $\text{UO}_3 \cdot 0.8\text{H}_2\text{O}$ ); Stroes-Gascoyne *et al.* [8] schoepite; Finn *et al.* [9] and Finch *et al.* [10] schoepite, soddyite, Na-boltwoodite ( $\text{Na}(\text{H}_3\text{O})\text{UO}_2(\text{SiO}_4) \cdot n\text{H}_2\text{O}$ ) and uranophane; and McNamara *et al.* [11] identified schoepite, studtite ( $\text{UO}_4 \cdot 4\text{H}_2\text{O}$ ), and metastudtite ( $\text{UO}_4 \cdot 2\text{H}_2\text{O}$ ).

On the other hand, different studies based on crystal chemistry considerations have been carried out in order to establish the retention capacity of these solid phases for different radionuclides. Burns *et al.* [12] deduced the possible incorporation of actinides into the structure of different uranyl phases, Chen *et al.* [13,14] studied the incorporation of selenium and technetium to schoepite, soddyite, uranophane, and boltwoodite. The incorporation of radionuclides on the uranium-containing secondary solid phases has also been experimentally studied in some cases [15-19], especially the incorporation of neptunium [20-22].

Cesium has several radioactive isotopes, and due to their long half lives both  $^{135}\text{Cs}$  and  $^{137}\text{Cs}$  are main radiocontaminants. The  $\text{Cs}^+$  ion can be highly mobile in aqueous media due to its low hydration energy as compared to elements of larger oxidation state or smaller size, for which the hydration energies can rise up to several thousands of kilojoules per mole [23], facilitating its involvement with the hydrological cycle.

Sorption of cesium onto different soils and geologic formations has been already studied [24] but few data about its sorption on uranyl phases might be found in literature. An almost complete ion exchange  $\text{Cs}^+ - \text{K}^+$  in boltwoodite was observed by Burns [15] while the incorporation of caesium to compregnacite and uranophane was demonstrated by Hoskin and Burns [19] and Douglas *et al.* [25], respectively. In particular, the sorption of radionuclides onto the uranium peroxides has not been studied in detail, yet. Only Friese *et al.* [20], and Douglas *et al.* [18] studied the potential incorporation of neptunium into these phases, being the main result that studtite (or metastudtite,  $\text{UO}_4 \cdot 2\text{H}_2\text{O}$ ) are able to sorb most of the neptunium in solution.

Considering the potential role of uranyl secondary phases (e.g. uranium peroxides) in the sorption/retention of different radionuclides released from the spent nuclear fuel, we study in this work the sorption of cesium onto studtite through two series of experiments: (1) sorption kinetics, and (2) sorption isotherms.

## Experimental

Studtite was precipitated by mixing a uranium nitrate solution with a hydrogen peroxide solution in the presence of some  $\text{UO}_2$  particles (10-50 $\mu\text{m}$ ). The yellow solid obtained was dried and characterized by X-ray diffraction. The surface area of the solid was determined by the BET method, the value obtained was  $1.01 \pm 0.01 \text{ m}^2/\text{g}$ .

The cesium solutions used in the experiments were prepared dissolving  $\text{CsCl}$ . The pH of the solutions was adjusted by the addition of  $\text{NaHCO}_3$  to give a final concentration in solution of  $10^{-3} \text{ mol}\cdot\text{dm}^{-3}$ . The ionic medium was  $0.01 \text{ mol}\cdot\text{dm}^{-3} \text{ NaClO}_4$ .

Solutions with different initial cesium concentrations (between  $7.6 \cdot 10^{-9} \text{ mol}\cdot\text{dm}^{-3}$  and  $1.0 \cdot 10^{-3} \text{ mol}\cdot\text{dm}^{-3}$ ) were put in contact with studtite at pH around 7 during 24 hours (initial cesium concentrations and weights of studtite are shown in the two first columns of Table 1).

The study was carried out by means of sorption batch experiments at  $25.0 \pm 0.1 \text{ }^\circ\text{C}$  in a thermostatic cabinet. A known amount of the solid (0.05 g) was put in contact with 20  $\text{cm}^3$  of cesium solution in stoppered polystyrene tubes. The tubes were continuously stirred until equilibrium was reached, in less than one day, as it can be seen in Figure 1, where the variation of cesium sorbed onto studtite as a function of contact time is shown.

Once the equilibrium was reached, samples were taken and filtered through 0.45  $\mu\text{m}$  pore size filters. Cesium concentration in solution was determined by ICP-MS. The concentration of cesium attached to the solid in units of moles of Cs per  $\text{m}^2$  of dry solid was calculated by subtracting the final metal concentration,  $[\text{Cs}]$  in  $\text{mol}\cdot\text{dm}^{-3}$ , to the initial concentration of metal added to the solution,  $[\text{Cs}]_0$  in  $\text{mol}\cdot\text{dm}^{-3}$ , and normalising with the surface area (SA) to volume (V) ratio:

$$\Gamma = \frac{([\text{Cs}]_0 - [\text{Cs}]) \cdot V}{SA} \quad (\text{eq.1})$$

**Table 1. Caesium concentrations in solution at equilibrium and concentration of caesium sorbed on studtite at pH=7**

Studtite weight (g)	$[\text{Cs}]_0$ ( $\text{mol}\cdot\text{dm}^{-3}$ )	$[\text{Cs}]$ ( $\text{mol}\cdot\text{dm}^{-3}$ )	q ( $\text{mol}\cdot\text{kg}^{-1}$ )	$\Gamma$ ( $\text{mol}/\text{m}^2$ )
0,0501	$1.02 \cdot 10^{-3}$	$(9.10 \pm 0.07) \cdot 10^{-4}$	$(4.4 \pm 0.1) \cdot 10^{-2}$	$3.29 \cdot 10^{-5}$
0,0502	$8.00 \cdot 10^{-4}$	$(7.05 \pm 0.09) \cdot 10^{-4}$	$(3.97 \pm 0.06) \cdot 10^{-2}$	$2.97 \cdot 10^{-5}$
0,0501	$6.00 \cdot 10^{-4}$	$(5.08 \pm 0.01) \cdot 10^{-4}$	$(3.7 \pm 0.1) \cdot 10^{-2}$	$2.76 \cdot 10^{-5}$
0,0501	$4.02 \cdot 10^{-4}$	$(3.38 \pm 0.02) \cdot 10^{-4}$	$(2.54 \pm 0.03) \cdot 10^{-2}$	$1.90 \cdot 10^{-5}$
0,0502	$1.99 \cdot 10^{-4}$	$(1.57 \pm 0.01) \cdot 10^{-4}$	$(1.66 \pm 0.07) \cdot 10^{-2}$	$1.24 \cdot 10^{-5}$
0,0500	$9.73 \cdot 10^{-5}$	$(7.14 \pm 0.04) \cdot 10^{-5}$	$(1.04 \pm 0.01) \cdot 10^{-2}$	$7.78 \cdot 10^{-6}$
0,0501	$6.64 \cdot 10^{-5}$	$(4.76 \pm 0.04) \cdot 10^{-5}$	$(7.49 \pm 0.06) \cdot 10^{-3}$	$5.60 \cdot 10^{-6}$
0,0498	$5.22 \cdot 10^{-5}$	$(3.68 \pm 0.04) \cdot 10^{-5}$	$(6.20 \pm 0.08) \cdot 10^{-3}$	$4.64 \cdot 10^{-6}$
0,0499	$5.09 \cdot 10^{-5}$	$(3.15 \pm 0.05) \cdot 10^{-5}$	$(7.8 \pm 0.1) \cdot 10^{-3}$	$5.84 \cdot 10^{-6}$
0,0500	$2.61 \cdot 10^{-5}$	$(1.68 \pm 0.01) \cdot 10^{-5}$	$(3.74 \pm 0.04) \cdot 10^{-3}$	$2.80 \cdot 10^{-6}$
0,0502	$8.77 \cdot 10^{-6}$	$(5.12 \pm 0.03) \cdot 10^{-6}$	$(1.45 \pm 0.01) \cdot 10^{-3}$	$1.08 \cdot 10^{-6}$
0,0502	$3.45 \cdot 10^{-6}$	$(1.84 \pm 0.01) \cdot 10^{-6}$	$(6.44 \pm 0.07) \cdot 10^{-4}$	$4.81 \cdot 10^{-7}$

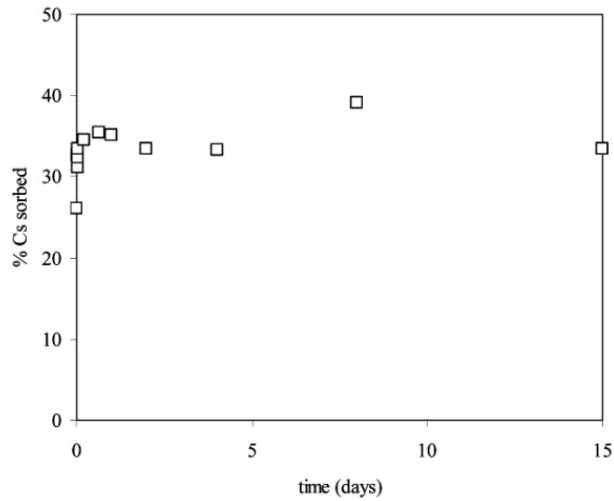
0,0500	$8.83 \cdot 10^{-7}$	$(3.71 \pm 0.02) \cdot 10^{-7}$	$(2.04 \pm 0.04) \cdot 10^{-4}$	$1.52 \cdot 10^{-7}$
0,0505	$3.86 \cdot 10^{-7}$	$(1.38 \pm 0.01) \cdot 10^{-7}$	$(9.82 \pm 0.05) \cdot 10^{-5}$	$7.30 \cdot 10^{-8}$
0,0500	$7.08 \cdot 10^{-8}$	$(1.91 \pm 0.02) \cdot 10^{-8}$	$(2.07 \pm 0.01) \cdot 10^{-5}$	$1.51 \cdot 10^{-8}$
0,0499	$3.60 \cdot 10^{-8}$	$(8.0 \pm 0.1) \cdot 10^{-9}$	$(1.12 \pm 0.01) \cdot 10^{-5}$	$8.38 \cdot 10^{-9}$
0,0505	$7.65 \cdot 10^{-9}$	$(1.27 \pm 0.05) \cdot 10^{-9}$	$(2.52 \pm 0.04) \cdot 10^{-6}$	$1.88 \cdot 10^{-9}$

## Results and Discussion

### *Sorption of Cs as a function of initial Cs concentration*

The final cesium concentrations in solution are shown in Table 1. The values of cesium concentration sorbed on the studtite,  $q$  in  $\text{mol} \cdot \text{kg}^{-1}$ , have been calculated considering the loss of cesium in solution, while the parameter gamma,  $\Gamma$  in  $\text{mol} \cdot \text{m}^{-2}$ , is the cesium sorbed on studtite normalized with the surface area of the solid.

**Figure 1. Variation of cesium sorbed onto studtite with contact time at pH 5**



Equilibrium isotherm equations are used in order to describe the experimental sorption data [26, and references therein]. Two different isotherms are mostly used for describing solid-liquid sorption systems, Langmuir isotherm, and Freundlich isotherm.

The Langmuir isotherm describes sorption of a solute from a liquid solution as:

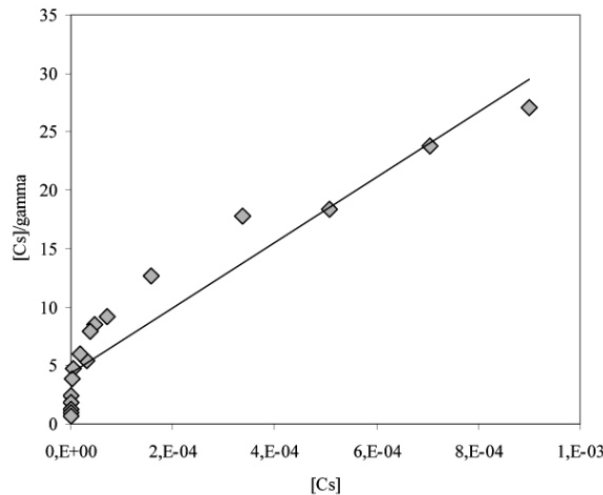
$$\Gamma = \Gamma_{\max} \frac{K_L \cdot [Cs]}{1 + K_L \cdot [Cs]} \quad (\text{eq.2})$$

where  $K_L$  is the Langmuir constant ( $\text{dm}^3 \cdot \text{mol}^{-1}$ ), gamma,  $\Gamma$ , is defined as the cesium concentration sorbed on the studtite in  $\text{mol} \cdot \text{m}^{-2}$ , and  $\Gamma_{\max}$  is the maximum caesium sorption ( $\text{mol} \cdot \text{m}^{-2}$ ). To obtain the values of the parameters  $\Gamma_{\max}$ , and  $K_L$ , we have used the linear form of the equation:

$$\frac{[Cs]}{\Gamma} = \frac{[Cs]}{\Gamma_{\max}} + \frac{1}{\Gamma_{\max} \cdot K_L} \quad (\text{eq.3})$$

From the plot of  $[Cs]/\Gamma$  against  $[Cs]$  the values of the parameters  $K_L$  and  $\Gamma_{\max}$  are obtained. However, as it can be seen in Figure 2, where the fitting of the model to the experimental data is shown, the Langmuir isotherm seems not to be a good model for the cesium sorption onto studtite, at least for cesium concentrations in solution lower than  $5 \cdot 10^{-4} \text{ mol} \cdot \text{dm}^{-3}$ .

**Figure 2. Fitting of the linearised form of the Langmuir isotherm (eq. 3) to the experimental data.**



The Freundlich isotherm is considered to be appropriate for describing both multilayer sorption and sorption on heterogeneous surfaces [27,28]. It can be used for non-ideal sorption that involves heterogeneous sorption, and it is expressed by the following equation:

$$q = K_F \cdot [Cs]^{1/n} \quad (\text{eq.4})$$

where  $K_F$ , and  $n$  are empirical constants dependent on several environmental factors, these parameters have no exact meaning, however, correlations with molecular properties of adsorbate and adsorbent have been studied [29,30], and the parameter  $1/n$  has been related to the affinity adsorbent-adsorbate [31] or to the solid-state properties of the adsorbent [32].

To obtain these parameters, equation 4 may be linearized by taking the logarithm on both sides:

$$\log q = 1/n \log [Cs] + \log K_F \quad (\text{eq.5})$$

The application of equation 5 to our data is shown in Figure 3. The  $K_F$ , and  $n$  values obtained are  $10 \pm 1$ , and  $1.4 \pm 0.1$ , respectively ( $r^2=0.998$ ).

Considering these values, the fitting of the Freundlich isotherm to the experimental data is shown in Figure 4. The examination of the plot suggests that the Freundlich isotherm is a good

model for the cesium sorption onto studdite ( $\chi^2=8\cdot 10^{-3}$ ) at cesium concentrations lower than  $5\cdot 10^{-4} \text{ mol}\cdot\text{dm}^{-3}$ .

As it can be seen in Figure 5, where the data are shown in a logarithmic form, the Langmuir isotherm seems to better fit the data at the highest cesium concentrations ( $>5\cdot 10^{-4} \text{ mol}\cdot\text{dm}^{-3}$ ) while the Freundlich isotherm seems to better fit the experimental data at lower cesium concentrations ( $<5\cdot 10^{-4} \text{ mol}\cdot\text{dm}^{-3}$ ).

**Figure 3. Fitting of equation 3 (linearized form of the Freundlich isotherm) to the experimental results obtained in this work**

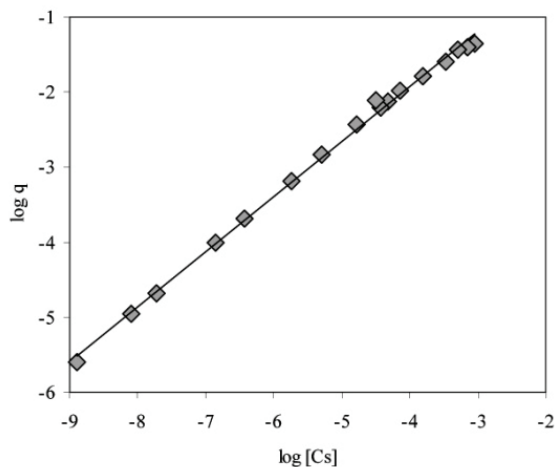


**Figure 4. Cesium sorption isotherm onto studdite at pH=7.**

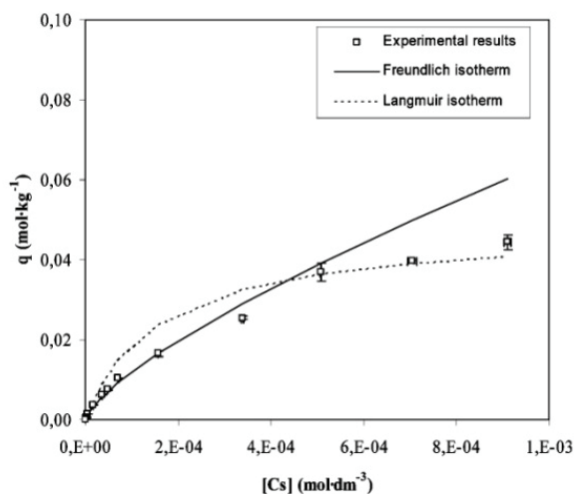
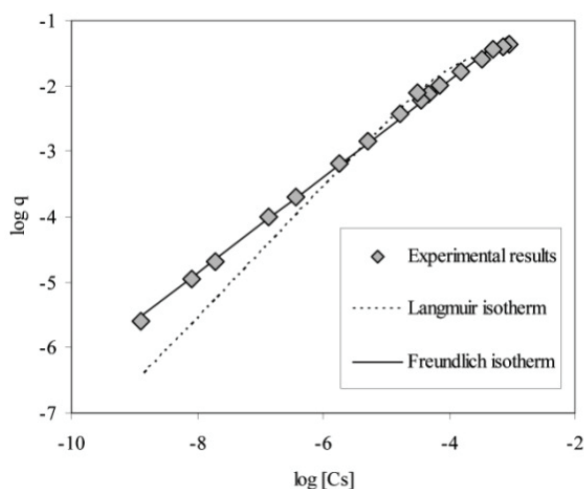


**Figure 5. Cesium sorption as a function of cesium concentration in solution at equilibrium**



The Freundlich isotherm parameter  $K_F$  indicates the adsorption capacity when the concentration of the ion is unitary, and it is useful in the evaluation of the sorption capacity of the solid. However, no data in literature was found related neither to the sorption isotherms of other ions on studtite, nor to the sorption of caesium on other uranyl solid phases. Since units for  $K_F$  depend on the value of  $1/n$ ,  $K_F$  parameters are only comparable when their  $1/n$  parameters are the same, therefore,  $K_F$  is not analogous to the distribution coefficient [28,33].

It is interesting to note that at cesium concentrations higher than  $10^{-3} \text{ mol}\cdot\text{dm}^{-3}$ , studtite seems to still increase its sorption capacity, what would point to the large ability of studtite to sorb cesium and, potentially, other radionuclides which would be released from the spent fuel. However, the studtite sorption capacity should be studied as a function of different parameters related to the solution composition such as pH or carbonate concentration in solution.

### Acknowledgements

This work was financially supported by ENRESA (Spanish Radioactive Waste Management Co), the European Commission, the Spanish *Ministerio de Educación y Ciencia* (MEC) by means of the Ramón y Cajal programme and the Catalan *Departament d'Universitats, Recerca i Societats de la Informació* (DURSI) by means of a “FI” grant.

## REFERENCES

- [1] J. Giménez, I. Casas, J. de Pablo, A. Martínez-Esparza (2005), Secondary-phase formation on UO<sub>2</sub> fuel. State-of-the-Art Report. NF PRO Project Deliverable 1.5.8.
- [2] D.W. Shoesmith (2000), Fuel corrosion processes under waste disposal conditions. *J. Nucl. Mater.* 282, 1-31
- [3] C.N. Wilson (1988), Summary of results from the series 2 and series 3 NNWSI bare fuel dissolution tests. *Mater. Res. Soc. Symp. Proc.* 112, 473-483.
- [4] C.N. Wilson (1990)a, Results from NNWSI Series 3 spent fuel dissolution tests. Pacific Northwest Laboratory Report PNL-7170, June 1990. Richland, Washington, USA.
- [5] C.N. Wilson (1990)b, Results from NNWSI Series 2 bare fuel dissolution tests. Pacific Northwest Laboratory Report PNL-7169, September 1990. Richland, Washington, USA.
- [6] S. Sunder, N.H. Miller (1996), Oxidation of CANDU uranium oxide fuel by air in gamma radiation at 150°C. *J. Nucl. Mater.* 231, 121-131.
- [7] R.S. Forsyth, L.O. Werme (1992), Spent fuel corrosion and dissolution. *J. Nucl. Mater.* 190, 3-19.
- [8] S. Stroes-Gascoyne, L.H. Johnson, J.C. Tait, J.L. McConnell, R.J. Porth (1997), Leaching of used CANDU fuel: results from a 19-year leach test under oxidizing conditions. *Mater. Res. Soc. Symp. Proc.* 465, 511-518.
- [9] P.A. Finn, R.J. Finch, E.C. Buck, J.K. Bates (1998), Corrosion mechanisms of spent fuel under oxidizing conditions. *Mater. Res. Soc. Symp. Proc.* 506, 123-131.
- [10] R.J. Finch, E.C. Buck, P.A. Finn, J.K. Bates (1999), Oxidative corrosion of spent UO<sub>2</sub> fuel in vapour and dripping groundwater at 90°C. *Mater. Res. Soc. Symp. Proc.* 556, 431-438.
- [11] B. McNamara, E. Buck, B. Hanson (2003), Observation of studtite and metastudtite on spent fuel. *Mater. Res. Soc. Symp. Proc.* 757, 401-406.
- [12] P.C. Burns, R.C. Ewing, M.L. Miller (1997), Incorporation mechanisms of actinide elements into the structures of U<sup>6+</sup> phases formed during the oxidation of spent nuclear fuel. *J. Nucl. Mater.* 245, 1-9.
- [13] F. Chen, P.C. Burns, R.C. Ewing (1999), <sup>79</sup>Se: geochemical and crystallo-chemical retardation mechanisms. *J. Nucl. Mater.* 275, 81-94.

- [14] F. Chen, P.C. Burns, R.C. Ewing (2000), Near-field behavior of  $^{99}\text{Tc}$  during the oxidative alteration of spent nuclear fuel. *J. Nucl. Mater.* 278, 225-232.
- [15] P.C. Burns (1999), Cs boltwoodite obtained by ion exchange from single crystals: implications for radionuclide release in a nuclear repository. *J. Nucl. Mater.* 265, 218-223.
- [16] C.W. Kim, D.J. Wronkiewicz, E.C. Buck (1999), Incorporation of radionuclides in the alteration phases of spent nuclear fuel. Argonne National Laboratory Report ANL/CMT/CP-99894. USA.
- [17] C.W. Kim, D.J. Wronkiewicz, E.C. Buck (2000), Potential incorporation of transuranics into uranium phases. Argonne National Laboratory Report ANL/CMT/CP-100657. USA.
- [18] M. Douglas, S.B. Clark, J.I. Friese, B.W. Arey, E.C. Buck, B.D. Hanson (2005), Neptunium(V) partitioning in uranium(VI) oxide and peroxide solids. *Environ. Sci. Technol.* 39, 4117-4124.
- [19] P.W.O. Hoskin, P.C. Burns (2003) Ion exchange between aqueous fluid and spent nuclear fuel alteration products: implications for the mobility of Cs in the probable repository at Yucca Mountain. *Mineral. Mag.* 67, 689-696.
- [20] J.I. Friese, M. Douglas, B.K. McNamara, S.B. Clark, B.D. Hanson (2004), Np behavior in synthesized uranyl phases: results of initial tests. Pacific Northwest National Laboratory Report PNNL-14856, USA.
- [21] P.C. Burns, K.M. Deely, S. Skanthakumar (2004), Neptunium incorporation into uranyl compounds that form as alteration products of spent nuclear fuel: Implications for geologic repository performance. *Radiochim. Acta* 92, 151-159.
- [22] J.A. Fortner, R.J. Finch, A.J. Kropf, J.C. Cunnane (2004), Re-evaluating neptunium in uranyl phases derived from corroded spent fuel. *Nucl. Technol.* 148, 174-180.
- [23] T. Shahwan, D. Akar, A.E. Eroğlu (2005), Physicochemical characterization of the retardation of aqueous  $\text{Cs}^+$  ions by natural kaolinite and clinoptilolite minerals. *J. Colloid. Interface Sci.* 285, 9-17.
- [24] J. Kónya, N.M. Nagy, Z. Nemes (2005), The effect of mineral composition on the sorption of cesium ions on geological formation. *J. Colloid Interface Sci.* 290, 350-356.
- [25] M. Douglas, S.B. Clark, S. Utsunomiya, R.C. Ewing (2002), Cesium and strontium incorporation into uranophane,  $\text{Ca}[(\text{UO}_2)(\text{SiO}_3\text{OH})]_2 \cdot 5\text{H}_2\text{O}$ . *J. Nucl. Sci. Technol.* Supplement 3, 504-507.
- [26] Y.-S. Ho, W.-T. Chiu, Ch.-Ch. Wang (2005), Regression analysis for the sorption isotherms of basic dyes on sugarcane dust. *Bioresource Technol.* 96, 1285-1291.
- [27] Y.-S. Ho, J.F. Porter, G. McKay (2002), Equilibrium isotherm studies for the sorption of divalent metal ions onto peat: copper, nickel, and lead single component systems. *Water Air Soil Pollut.* 141, 1-33.

- [28] C.A. Coles, R.N. Young (2006), Use of equilibrium and initial metal concentration in determining Freundlich isotherms for soils and sediments. *Eng. Geol.* 85, 19-25.
- [29] Y. Otake, N. Kalili, T.H. Chang, E. Furuya (2004), Relationship between Freundlich-type equation constants and molecular orbital properties. *Sep. Purif. Technol.* 39, 67-72.
- [30] A.K. Oskouie, Y. Miura, E.G. Furuya, K.E. Noll (2002), Relationship between the highest occupied molecular orbital (HOMO) electron density of adsorption sites on carbon and the Freundlich exponent. *Carbon* 40, 1199-1202.
- [31] E.G. Furuya, H.T. Chang, Y. Miura, K.E. Noll (1997), A fundamental analysis of the isotherm for the adsorption of phenolic compounds on activated carbon. *Sep. Purif. Technol.* 11, 69-78.
- [32] P. Baláž, A. Aláčova, J. Briančin (2005), Sensitivity of Freundlich equation constant  $1/n$  for zinc sorption on changes induced in calcite by mechanical activation. *Chem. Eng. J.* 114, 115-121.
- [33] Z. Chen, B. Xing, W.B. McGill (1999), A unified sorption variable for environmental applications of the Freundlich isotherm. *J. Environ. Qual.* 28, 1422-1428.

# **SORPTION OF SELENIUM (IV) IN THE PRESENCE OF AQUEOUS SILICATES SPECIES ON IRON CORROSION PRODUCT IN UNDERGROUND RADWASTE REPOSITORY CONDITIONS**

**Norbert Jordan <sup>a,b</sup>, Claire Lomenech <sup>a</sup>, Nicolas Marmier <sup>a</sup>  
Eric Giffaut <sup>b</sup>, Jean-Jacques Ehrhardt <sup>c</sup>**

<sup>a</sup> Université de Nice-Sophia-Antipolis, Laboratoire de Radiochimie, Sciences analytiques et Environnement, 28 avenue Valrose, 06108 Nice Cedex 2, France ; phone: (+33) 4 92 07 63 77, fax: (+33) 4 92 07 63 64, e-mail: [jordan@unice.fr](mailto:jordan@unice.fr).

<sup>b</sup> Agence nationale pour la gestion des déchets radioactifs, Châtenay-Malabry, F-92298, France.

<sup>c</sup> Centre national de la recherche scientifique, UMR7564 – Université de Nancy, Laboratoire de Chimie-Physique et Microbiologie pour l'Environnement, Villers-lès-Nancy, F-54600, France.

## **Abstract**

Sorption of selenium (IV) and aqueous silicates onto Magnetite (Fe<sub>3</sub>O<sub>4</sub>) has been investigated, with initial concentration of aqueous silicates under solubility limit of amorphous silica. By using the double diffuse layer model (DDLDM), the adsorption constants for selenium (IV) and H<sub>4</sub>SiO<sub>4</sub> onto Magnetite have been determined from those experimental observations.

Then, by using those surface complexation constants, prediction curves of the sorption of selenium (IV) in the presence of aqueous silicates onto Magnetite have been calculated.

Finally, laboratory experiments were performed, confirming the ability of the DDLDM to predict the competition effect observed experimentally between selenium (IV) and aqueous silicates for the surface sites of Magnetite.

## Introduction

In the context of an underground repository for nuclear wastes, silicates would be one of the major species found in interstitial water. Aqueous silicates would come from clays and silica (present as an impurity in many minerals) as well as from the degradation of glass canisters. However studies of their sorbing properties are rather scarce in the literature although their presence on solid surfaces can modify the availability of surface sites, and also surface charge, which can influence global surface reactivity of solids [1,2].

Indeed, presence of these aqueous silicates may have several consequences on the sorption of radionuclides:

- they may compete with the studied element and then lead to a decrease of retention capacities of studied materials;
- and also may modify the surface affinity for the ionic and neutral species by modifying the electrical double layer or by forming chemical bonds with surface groups [1,2]. For example, it has already been demonstrated that the presence of aqueous silicates could enhance significantly the sorption of cesium onto the surface of Magnetite [1].

Furthermore, sorption of aqueous silicates on corrosion products formed on the metallic containers used in the underground repository, could increase the dissolution of the glass canisters by a displacement of equilibria [1,3]. In deep geological conditions such as those found in Callovo-Oxfordian clays of the underground repository in the site of Bure (France) (Table 1), corrosion of metallic surcontainers would lead mainly to the formation of Magnetite  $\text{Fe}_3\text{O}_4$  and Siderite  $\text{FeCO}_3$  [4,5].

**Table 1: Characteristic conditions found in Callovo-Oxfordian clays in Bure (France) [6]**

pH	7.32
Eh (V)	-0.185
$[\text{SiO}_2]_{\text{aq}} (\text{mol.L}^{-1})$	$9.44 \times 10^{-5}$
$[\text{HCO}_3^-] (\text{mol.L}^{-1})$	$1.44 \times 10^{-3}$

Selenium-79, a long-lived radionuclide which will be the most contributing radioisotope to the selenium radioactivity after a long time storage, could be released from the radioactive wastes of the French underground repository located in Bure (east of France). In the context of an underground laboratory, the migration of the mobile species of Selenium is limited by sorption on corrosion products. Using laboratory experiments, this work is basically aiming at a deeper insight in the role of the aqueous silicates, by studying their influence on the sorption of selenium (IV) on Magnetite. Surface complexation models have been used to model experimental observations and predict the behavior of this ternary system.

## Experiments

### *Solid phase*

Magnetite ( $\text{Fe}_3\text{O}_4$ ) is a commercial powder purchased from Alfa Aesar. The surface acidity constants of the solid used in this study have been determined by fitting potentiometric titrations using the Fiteql 4.0 code [7] in previous published works [8].

Specific surface area of Magnetite was determined by applying the Brunauer-Emmet-Teller (BET) equation with nitrogen adsorption isotherms at 77K. Results are given in Table 2.

**Table 2: Surface characteristics of Magnetite**

Specific surface area ( $\text{m}^2\cdot\text{g}^{-1}$ )	1.6
Concentration of surface sites ( $\text{sites}\cdot\text{g}^{-1}$ )	$5.70 \times 10^{-6}$
pKa <sub>1</sub> (DDL) $\equiv\text{FeOH}_2^+ \leftrightarrow \equiv\text{FeOH} + \text{H}^+$	4.60
pKa <sub>2</sub> (DDL) $\equiv\text{FeOH} \leftrightarrow \equiv\text{FeO}^- + \text{H}^+$	8.20

Magnetite has also been characterized by X-ray diffraction (XRD). XRD pattern showed the presence of well-crystallized  $\text{Fe}_3\text{O}_4$ , with no trace of other crystallized solids.

Some additional structural informations have been obtained for Magnetite using  $^{57}\text{Fe}$  Mössbauer spectroscopy: the ratio Fe(II)/Fe(III) has been measured and showed a slight non-stoichiometry with a percentage of vacant sites less than 1%.

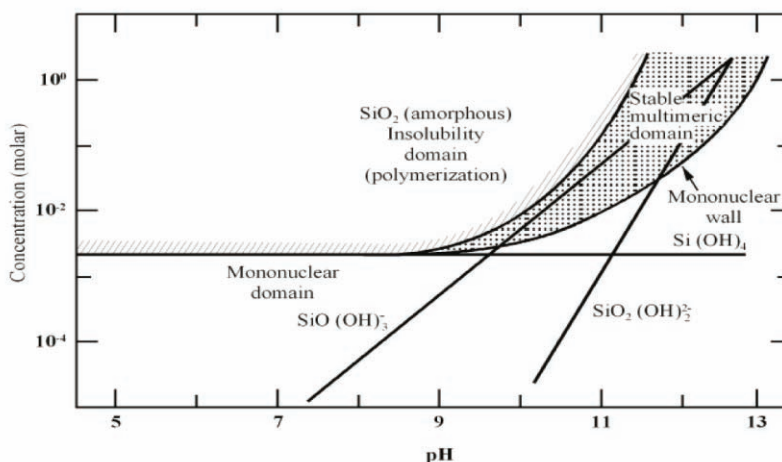
### **Solutions**

The master selenium (IV) solution was prepared by dissolving  $\text{Na}_2\text{SeO}_3$  (from Alfa Aesar) in deionized water. The concentration of this master solution was determined by inductively coupled plasma mass spectrometry (ICP-MS ELAN DRC, Perkin Elmer).

The master silicate solution has been obtained by partial dissolution of silica gel (mean particle size 15  $\mu\text{m}$ ) purchased from Merck. Silica was stirred in a NaOH solution ( $1.00 \times 10^{-2}$   $\text{mol}\cdot\text{L}^{-1}$ ) for three days and then filtered through a Millipore cell (0.45  $\mu\text{m}$ ) [1].

The amount of total silicates in solution was determined by inductively coupled plasma atomic emission spectrometry (ICP-AES OPTIMA 2000 DV, Perkin Elmer). All experiments were then carried out using diluted fractions of this solution.

**Figure 1: Speciation curve of silicates species in equilibrium with amorphous silica [9]**



For concentrations of aqueous silicates under the solubility limit ( $2 \cdot 10^{-3} \text{ mol.L}^{-1}$ ) of amorphous silica (Figure 1), only monomeric species will be encountered into the solution. Although, for initial concentration of aqueous silicates over the solubility limit of amorphous silica, polymeric species can be found for pH less than 10.

Silicate concentrations used in the experiments ( $1.00 \times 10^{-5}$  to  $1.12 \times 10^{-4} \text{ mol.L}^{-1}$ ) have been chosen in order to avoid precipitation of silicates and to minimize polymerisation in solution.

Deionised water was used in all experiments. The background electrolyte was a  $\text{NaNO}_3$  solution prepared from a Prolabo powder. In order to avoid possible contamination of the solutions by glass, polypropylene or polycarbonate flasks were used for all experiments.

### ***Sorption experiments***

Sorption studies have been carried out in polycarbonate batches. All experiments have been performed at room temperature, into a glove box and under an argon atmosphere in order to exclude  $\text{CO}_2$  from sorption experiments.

After stirring, the pH was recorded and suspensions were filtered through a Millipore cell ( $0.45 \mu\text{m}$ ). Then, the total concentrations of remaining selenium (IV) and aqueous silicates in the supernatants were determined by ICP-MS and ICP-AES, respectively. Concentration of sorbed selenium (IV) and silicates was determined by subtracting the remaining concentration in the supernatant from the initial concentration.

Two different protocols were applied for kinetics and sorption edge experiments, both with  $\text{NaNO}_3$  as the background electrolyte with a concentration of  $1.00 \times 10^{-1} \text{ mol.L}^{-1}$ . The total volume of solution was  $40 \text{ cm}^3$  in both cases.

### *Experiments as a function of time*

Magnetite was added separately to a solution of selenite ions or aqueous silicates with the background electrolyte. The pH has been adjusted with  $1.00 \times 10^{-2}$  mol.L<sup>-1</sup> HNO<sub>3</sub> or NaOH aqueous solutions to 4.0 for selenium (IV) and 7.0 for aqueous silicates. These pH values correspond to the experimental maximal sorption rates for both species, respectively. Experiments with increasing oxide-solution contact times were performed, until the sorption rates of Se(IV) and H<sub>4</sub>SiO<sub>4</sub> reached a plateau corresponding to the time necessary to reach equilibrium. Results of this time dependence study have been used for all further experiments.

### *Sorption edges*

Sorption of selenium (IV) and aqueous silicates onto Magnetite as a function of pH has also been studied, separately. A solid to solution ratio (m/v) of 5 g.L<sup>-1</sup> and 6 g.L<sup>-1</sup> has been used for selenium (IV) and aqueous silicates, respectively. In order to check the existence of an equilibrium, reversibility of the sorption of selenium (IV) and silicates onto Magnetite has been tested. Following sorption experiments, and after separation of the solid and the supernatant, the solid has been reintroduced in a NaNO<sub>3</sub> background electrolyte solution. The pH of the suspension and the stirring time were the same than those used for sorption experiments but with no selenium (IV) or aqueous silicates initially present. The concentration of selenium (IV) and aqueous silicates in solution coming from the solid has then been measured, and confirmed the existence of an equilibrium during sorption experiments.

### *Competition experiments*

Sorption experiments of selenium (IV) onto Magnetite as a function of the pH, in the presence of aqueous silicates have been performed. Selenium (IV) and aqueous silicates have been introduced simultaneously in the suspension. The effect of aqueous silicates on the adsorption of selenium (IV) onto Magnetite was determined for total Si to Fe mole ratios, i.e. Si(T)/Fe ratios between 0.0002 and 0.0016. Si(T) also represents initial concentrations of aqueous silicates, which were ranging from approximately  $1.00 \times 10^{-5}$  to  $1.01 \times 10^{-4}$  mol.L<sup>-1</sup>.

## **Results and discussion**

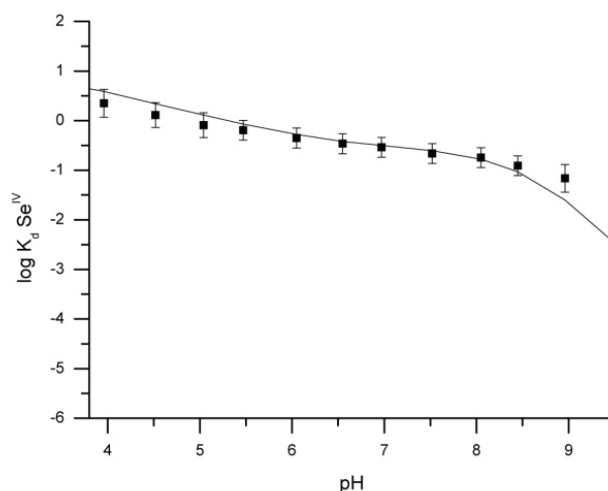
### *Experiments as a function of time*

Results show that the amount of adsorbed selenium (IV) and adsorbed silicates onto Magnetite depends on the time of reaction, reaching respectively a plateau after stirring times of 30 hours and 7 days. Thus, those stirring times have been chosen for all further sorption experiments on Magnetite.

## Sorption edges

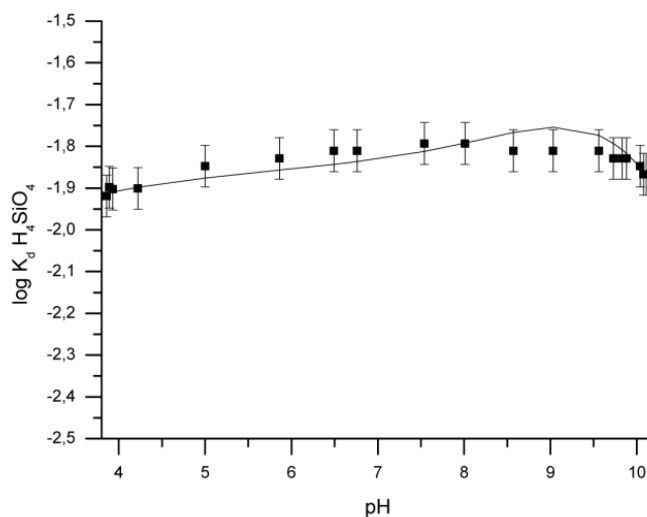
Sorption of selenium (IV) onto Magnetite decreases when the pH increases [10] (Figure 2), as expected for anions. Data are plotted in term of  $K_d$ , (= amount of Se adsorbed in mole/g divided by amount of Se in solution in mole/l) coefficient distribution of selenium (IV) between the solid and the solution. Experimental uncertainties shown in Figures 2, 3 and 4 come from statistical calculations on the analytic ICP-AES and ICP-MS results (measurements being usually done in triplicates). The total concentrations of surface sites,  $[≡FeOH]$ , were calculated using sites densities determined by potentiometric titrations in a previous study.

**Figure 2: Sorption of Selenium (IV) onto Magnetite as a function of the pH solid/solution ratio  $m/v = 5$  g/L,  $I = 10^{-1}$  M ( $NaNO_3$ )  $[SeO_3^{2-}]_i = 1.06 \times 10^{-5}$  mol.L $^{-1}$ , 30 hours of stirring. Solid line: DDLM calculation,  $[≡FeOH] = 2.85 \times 10^{-5}$  mol.L $^{-1}$**



Concerning aqueous silicates, experimental data show that silicates can bind on the surface of Magnetite over a wide pH range (Figure 3).

**Figure 3: Sorption of  $H_4SiO_4$  onto Magnetite as a function of the pH solid/solution ratio  $m/v = 6$  g/L,  $I = 10^{-1}$  M ( $NaNO_3$ )  $[H_4SiO_4]_i = 1.12 \times 10^{-4}$  mol.L $^{-1}$ , 7 days of stirring Solid line: DDLM calculation,  $[≡FeOH] = 3.41 \times 10^{-5}$  mol.L $^{-1}$**



This differs from the sorption edge observed for anions, for which sorption decreases from 100 to 0% within a sharper pH range. The bell-shaped curve (Figure 3) obtained is characteristic of the sorption of weak acids like  $H_4SiO_4$  [1,3,11]. Maximal sorption occurs between pH 8 and 10, close to the first pKa of  $H_4SiO_4$  (9.86).

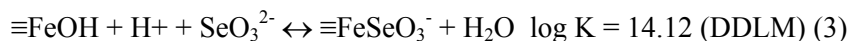
### ***Modelling results for Se(IV)/Fe<sub>3</sub>O<sub>4</sub> and H<sub>4</sub>SiO<sub>4</sub>/Fe<sub>3</sub>O<sub>4</sub> systems***

During the modelling stage, the first step was to extract surface complexation constants of selenium (IV) and aqueous silicates using sorption edge data.

The acidity constants of the selenium (IV) from the NEA database [12] are defined as follows:



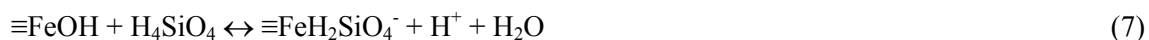
Several stoichiometries including the formation of two monodentate complexes and one bidentate complex were tested to describe the experimental observations. The stoichiometry involving the formation of the monodentate species  $\equiv FeSeO_3^-$  allowed us to obtain the best fit (quality of the fit defined as WSOS/DF (Weighted Sum Of Squares divided by Degrees of Freedom) less than 1).



The acidity constants of the silicates used for the calculations are defined as follows in the Mineql database [13] :



Two surface complexes for the binding of silicates onto Magnetite have been used and are defined as follows:



Stoichiometries and surface complexation constants for all these surface complexes have been extracted with the Fiteql 4.0 code. Neither the surface acidity constants nor the surface site concentration ( $[\equiv FeOH]$ ) have been adjusted. Three electrostatics models (Non Electrostatic Model (NEM), Constant Capacitance Model ( $C = 1.2 \text{ F.m}^{-2}$ ) (CCM) and DDLMM) have been tested for Magnetite in order to fit sorption edges.

Results for all these modelling are presented in Table 3. Best fits for these sorption experiments have been obtained by using the DDLM model.

**Table 3: Surface complexation constants for binding of selenium (IV) and aqueous silicates onto Magnetite for sorption experiments**

Electrostatic model	NEM	CCM	DDLM
Log K $\equiv\text{FeSeO}_3^-$	13.60	14.04	14.12
Log K $\equiv\text{FeH}_3\text{SiO}_4$	3.58	3.53	3.50
Log K $\equiv\text{FeH}_2\text{SiO}_4^-$	-5.54	-4.00	-3.56

The stoichiometries used in this work to describe the binding of selenium (IV) and aqueous silicates onto Magnetite are similar to those already given by several authors for this iron oxide [1,10,14-17]. The surface complexation constant used in this work have been calculated in order to obtain a consistent modeling of the experimental data. The log K values obtained in this study are four orders of magnitude higher than those found by Martinez et al [10].

### Prediction curves

The stoichiometries and surface complexation constants determined by DDLM modelling (Equilibria 3, 6 and 7), have then been used to obtain prediction curves for the sorption of selenium (IV) onto Magnetite in the presence of silicates (Figure 4).

**Figure 4: Prediction curves and experimental results for the sorption of selenium (IV) in the presence of aqueous silicates on Magnetite as a function of pH**

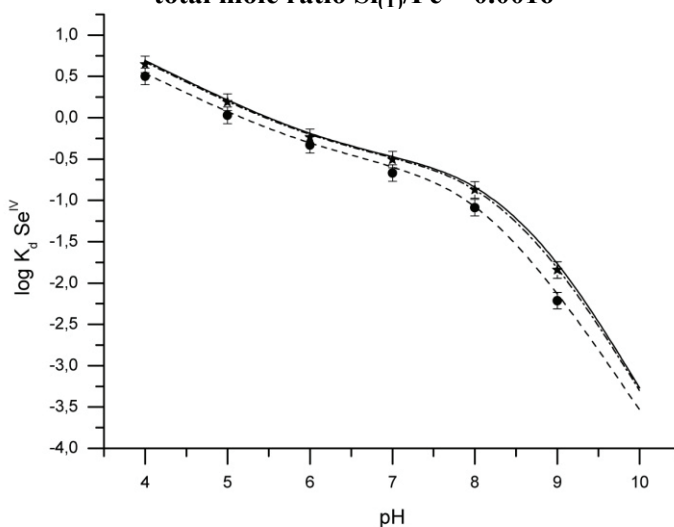
solid/solution ratio  $m/v = 5 \text{ g/L}$ ,  $I = 10^{-1} \text{ M (NaNO}_3)$   $[\text{SeO}_3^{2-}]_i = 9.86 \times 10^{-6} \text{ mol.L}^{-1}$

★  $[\text{H}_4\text{SiO}_4]_i = 1.00 \times 10^{-5} \text{ mol.L}^{-1}$

●  $[\text{H}_4\text{SiO}_4]_i = 1.01 \times 10^{-4} \text{ mol.L}^{-1}$

Lines: DDLM predictions,  $[\equiv\text{FeOH}] = 2.85 \times 10^{-5} \text{ mol.L}^{-1}$ .

————  $[\text{SeO}_3^{2-}]_i = 9.86 \times 10^{-6} \text{ mol.L}^{-1}$ ,  $[\text{H}_4\text{SiO}_4]_i = 0.00 \text{ mol.L}^{-1}$   
 - - - - -  $[\text{SeO}_3^{2-}]_i = 9.86 \times 10^{-6} \text{ mol.L}^{-1}$ ,  $[\text{H}_4\text{SiO}_4]_i = 1.00 \times 10^{-5} \text{ mol.L}^{-1}$ ,  
 total mole ratio  $\text{Si}_{(T)}/\text{Fe} = 0.0002$   
 .....  $[\text{SeO}_3^{2-}]_i = 9.86 \times 10^{-6} \text{ mol.L}^{-1}$ ,  $[\text{H}_4\text{SiO}_4]_i = 1.01 \times 10^{-4} \text{ mol.L}^{-1}$ ,  
 total mole ratio  $\text{Si}_{(T)}/\text{Fe} = 0.0016$



For the lowest initial concentration, aqueous silicates have a very small effect on the sorption of selenium (IV) onto Magnetite. Indeed,  $[\text{Se}]_i + [\text{H}_4\text{SiO}_4]_i < [\equiv\text{FeOH}]$ , which means that there is no competition between the two studied species for the surface sites of Magnetite.

For the highest initial concentration of aqueous silicates, prediction curves show that the sorption of selenium (IV) onto Magnetite should decrease when the ratio  $\text{Si}_{(\text{T})}/\text{Fe}$  increases, i.e. when initial concentration of aqueous silicates increases. This phenomenon could be explained by a competition between selenium (IV) and aqueous silicates for the surface sites of Magnetite, where  $[\text{Se}]_i + [\text{H}_4\text{SiO}_4]_i \gg [\equiv\text{FeOH}]$ .

### ***Comparison between prediction curves and experimental results***

Finally, sorption experiments of selenium (IV) onto Magnetite have been performed in the presence of aqueous silicates (for different ratios  $\text{Si}_{(\text{T})}/\text{Fe}$ ), and have been compared to the prediction curves. As it can be seen, prediction curves were able to account well for the behavior of the sorption of selenium (IV) onto Magnetite in the presence of aqueous silicates, for initial concentration of aqueous silicates of  $1.00 \times 10^{-5}$  and  $1.01 \times 10^{-4} \text{ mol.L}^{-1}$ .

The adsorption of selenium (IV) onto Magnetite appears to be affected by the presence of aqueous silicates for a wide pH range from 4 to 10 and decreases when the ratio  $\text{Si}_{(\text{T})}/\text{Fe}$  increases.

For low values of  $\text{Si}_{(\text{T})}/\text{Fe}$  ratios, aqueous silicates could sorb onto the surface of Magnetite only as monomeric species. The competition between selenium (IV) and aqueous silicates for the surface of Magnetite can be accurately predicted by using the DDLM. The fact that the DDLM model account for this competition suggest that the process inhibiting the adsorption of selenium (IV) onto the surface of Magnetite is the adsorption of monomeric species, which presence can modify surface charge potential of Magnetite.

For higher values of  $\text{Si}_{(\text{T})}/\text{Fe}$  ratios, polymerisation of  $\text{H}_4\text{SiO}_4$  onto the Magnetite surface should occur. In this case, the polymerisation of  $\text{H}_4\text{SiO}_4$  onto the surface of Magnetite could inhibit the adsorption of selenium (IV) by steric effects or by modifying the surface charge of Magnetite. Swedlund *et al.* [19] were able to accurately predict the competing effect for the adsorption of As(III) and As(V) onto Ferrihydrite in the presence of aqueous silicates using the DDLM even in the case of polymerisation of  $\text{H}_4\text{SiO}_4$  which was supposed to occur for values of  $\text{Si}_{(\text{T})}/\text{Fe}$  higher than 0.1.

However, a spectroscopic study should be done in order to elucidate the mechanisms of the sorption of aqueous silicates onto Magnetite, mostly for high ratios  $\text{Si}_{(\text{T})}/\text{Fe}$  in order to confirm the probable surface precipitation of silica. This will be presented in a next paper.

## Conclusion

In this study, we have shown that aqueous silicates have an influence on the fixation of selenium (IV) onto the surface of Magnetite. Indeed, it seems that aqueous silicates compete with selenium for surface sites of  $\text{Fe}_3\text{O}_4$ .

To achieve a better understanding of this type of systems, a structural study, combining XPS measurements, Infrared and Raman spectroscopy is under progress, aiming to elucidate the mechanism of  $\text{Se(IV)}$  and  $\text{H}_4\text{SiO}_4$  adsorption onto Magnetite and to confirm macroscopic observations obtained in this study.

## Acknowledgements

The authors would like to thank Andra for its financial support, as well as Mr. Jean-Marie Couret, from the University of Nice-Sophia Antipolis for his help during ICP-AES measurement and also Mr. Mustapha Abdelmoula for Mössbauer measurements.

## REFERENCES

- [1] N. Marmier, F. Fromage, J. Colloid Interface Sci. 223 (2000) 83.
- [2] N. Marmier, J. Dumonceau, J. Chupeau, F. Fromage, C. R. Acad. Sci. Paris 318 (2) (1994) 177.
- [3] V. Philippini, A. Naveau, H. Catalette, S. Leclerq, J. Nucl. Mater. 348 (2006) 60.
- [4] D. Neff, S. Reuger, L. Bellot-Gurlet, P. Dillmann, R. Bertholon, J. Raman Spectrosc. 35 (2004) 739.
- [5] D. Neff, S. Reuger, L. Bellot-Gurlet, G. Beranger, Corros. Sci. 47 (2005) 515.
- [6] E. Jacquot, Technical Report D NT ASTR 02.041, ANDRA, France (2002).
- [7] A.L. Herbelin, J.C. Westall, FITEQL 4.0, Department of Chemistry, Oregon State University Report 99-01, 1999.
- [8] N. Marmier, A. Delisée, F. Fromage, J. Colloid Interface Sci. 211 (1999) 54.
- [9] L. Sigg, P. Behra, W. Stumm, Chimie des Milieux Aquatiques 4<sup>th</sup> edition, Dunod, 2006, p. 247.

- [10] M. Martinez, J. Gimenez, J .de Pablo, M. Rovira, L. Duro, *Appl. Surf. Sci.* 252 (10) (2005) 3767.
- [11] L. Sigg, W. Stumm, *Colloids Surf.* 2 (1981) 101.
- [12] OECD/NEA, *Chemical Thermodynamics of Selenium*, Elsevier, Volume 7, 2005, p 142.
- [13] J.C. Westall, J.L. Zachary, F.M.M. Morel, "MINEQL, a Computer Program for Calculation of Chemical Equilibrium Composition of Aqueous Systems," Technical note 18. Department of Civil Engineering, MIT, 1976.
- [14] H.C. Bruun Hansen, B. Raben-Lange, K. Raulund-Rasmussen, O.K. Borggaard, *Soil Sci.* 158 (1) (1994) 40.
- [15] S. Goldberg, *Soil Sci. Soc. Am. J.* 49 (1985) 851.
- [16] M. Dietzel, *Water Sci. Technol.* 40 (2002) 207.
- [17] P.J. Swedlund, J.G. Webster, *Water Res.* 33 (16) (1999) 3413.



## RETENTION OF <sup>99</sup>Tc ONTO FRACTURES OF CRYSTALLINE ROCK

**Bernhard Kienzler, Dieter Schild, Jürgen Römer, Mats Jansson\***

Forschungszentrum Karlsruhe, Institut für Nukleare Entsorgung (INE), Germany

\*KTH, Stockholm, Sweden

### Abstract

A series of migration experiment with actinides and technetium(VII) were performed at the Äspö Hard Rock Laboratory in Sweden. The migration experiments were complemented by batch sorption experiments using flat natural samples of weathered fractures. In the batch experiments, Tc showed pronounced sorption kinetics. The retention mechanism of <sup>99</sup>Tc was investigated mainly by X-ray photoelectron spectroscopy (XPS). XPS analyses showed a clear shift of Tc binding energy to a reduced redox state which means that Tc is retained controlled by reduction processes. Tc underwent reduction in the solution which was facilitated by the low redox potential of the groundwater. Tc retention was not necessarily correlated to high Fe concentrations of the mineral phases at the surfaces. In a long-term migration experiment, an initial breakthrough of <sup>99</sup>Tc was observed simultaneously with an inert tracer (HTO). Observed Tc recovery after 280 days was found in the range of about 1%. After termination of the experiment, the fracture was analyzed with respect to the sorbed <sup>99</sup>Tc by abrasive techniques. Only at some particular locations along the migration path <sup>99</sup>Tc could be found in significant concentrations.

## Introduction

The yield of  $^{99}\text{Tc}$  from thermal fission of  $^{235}\text{U}$  amounts to  $\sim 2.3$  mass%. In spent fuel  $\text{UO}_2$  fuel, Tc exists mainly in metallic inclusions distributed in the fuel matrix. During reprocessing, Tc will be dissolved and separated with the high-level radioactive waste stream. In the aquatic waste stream, Tc exists as  $\text{Tc(VII)}$  which shows a high volatility during the vitrification process. As a consequence,  $\text{Tc(VII)}$  has to be disposed off not only as part of vitrified high-level waste forms but also in technology wastes which include components of the vitrification cells and the off-gas treatment.

In the case of direct disposal of spent fuel, the metallic inclusions in the  $\text{UO}_2$  matrix are exposed to the  $\alpha$ -radiation field of the minor actinides and decay chain elements of the spent fuel. If groundwater interacts with spent fuel, oxidizing radiolytic species may oxidize the surface of solid  $\text{UO}_2$  and uranium may be mobilized in the hexavalent redox state. An oxidation of metallic inclusions might occur by the same oxidizing species forming  $\text{TcO}_4^-$  in the solution in contact with the spent fuel.

These information shows that at the waste form where Tc is released, the  $\text{Tc(VII)}$  is the prominent species. Investigation of the retention behavior of  $\text{Tc(VII)}$  in reducing disposal environments and its retention onto different components in the surrounding of the wastes is of interest for the safety cases of the various disposal concepts. Within the scope of a bilateral cooperation, a series of *insitu* migration experiment were performed by Forschungszentrum Karlsruhe, Institute of Nuclear Waste Disposal (INE) at the Äspö Hard Rock Laboratory in Sweden. The migration experiments were complemented by batch sorption experiments with actinides and technetium(VII) using flat natural samples of weathered fracture surfaces.

## Materials

### *Groundwater*

For laboratory investigations, Äspö groundwater was used, which was extracted from the drill hole SA 2600. The groundwater composition is given in ref. [1]. Major cations were  $\text{Na}^+$  and  $\text{Ca}_2^+$ , the dominant anion was  $\text{Cl}^-$  (0.09, 0.04 and  $0.2 \text{ mol dm}^{-3}$ ). Ionic strength was 0.24 molal. The laboratory experiments were performed in a glove box under a 99%  $\text{Ar}$ , 1%  $\text{CO}_2$  atmosphere at room temperature ( $22 \pm 1^\circ\text{C}$ ). The pH was 7.2 and Eh was found in the experiments between 112 to -50 mV (Ingold Pt4805 against  $\text{Ag/AgCl}$ , corrected with respect to hydrogen electrode). Fe could not be measured in the groundwater used in laboratory (SA 2600). Fe-hydroxides had been precipitated during the transport to Germany.

### *Rock samples from Äspö*

In order to do the experiments with relevant materials, drill cores were provided by SKB. The drill cores showed natural fractures. The fracture surfaces consisted of layers of weathered/altered material. These materials are characterised as *Fracture Type 2* using the definition of a recent SKB report [2]. Under this definition, the chlorite layer is  $< 1$  mm with an

average porosity of 5%. Sorption experiments in laboratory were performed onto samples provided as slices (1.5cm × 1.5cm, grinded and polished) of freshly broken Äspö rock and of altered material (weathered fracture filling, untreated, selected planar samples). The solids were characterised and analysed by scanning electron microscopy (SEM/EDX) and XRD. Element mappings of granite and altered material in a fracture are presented in ref. [5]. The granite showed fine grained Fe-oxides/oxyhydroxides. X-ray diffraction showed that chlorite is a main constituent in the altered fracture material.

### ***Radionuclides***

For the *insitu* migration experiment with core #7, a cocktail was applied consisting of groundwater SA 2600 spiked by 370 Bq ml<sup>-1</sup> HTO, 1.35x10<sup>-6</sup> mol l<sup>-1</sup> <sup>233</sup>U, <sup>99</sup>Tc 7.0x10<sup>-7</sup> mol l<sup>-1</sup> (aqueous NaTcO<sub>4</sub> stock solution) for migration tests and 2.6x10<sup>-5</sup> mol l<sup>-1</sup> for XPS investigations. The pH of the cocktail was 7.3. The cocktail was prepared under anoxic conditions in a glovebox.

## **Methods**

### ***Batch experiments***

Sorption experiments were conducted in batch mode with a granite slice cut from drill core material. One side of the slice was polished the other side was left as cut. Sorption coefficient of technetium onto flat samples of Äspö materials was determined after 14 days of immersion. The samples used for Tc tests were prepared from unaltered granite.

### ***Specific analytical methods for determination of Tc redox state***

Determination of redox states of sorbed Tc and iron at the mineral surfaces was performed mainly by X-ray photoelectron spectroscopy (XPS). Samples were mounted on sample holders within a glovebox at anoxic conditions (99% Ar, 1% CO<sub>2</sub>, O<sub>2</sub> < 10 ppm), introduced into a transfer vessel and moved to the spectrometer (PHI model 5600ci, Physical Electronics Inc.) without air contact. XPS spectra were acquired by use of Mg K<sub>α</sub> (1253.6 eV), Al K<sub>α</sub> (1486.6 eV) or monochromatic Al K<sub>α</sub> X-ray excitation. Narrow scans of elemental lines were recorded at 11.75 eV pass energy of the hemispherical capacitor analyzer which yields a full-width-at-half-maximum (FWHM) of the Ag 3d<sub>5/2</sub> line of 0.85 eV, 1.02 eV or 0.60 eV, respectively.

### ***Preparation of cores for migration experiments***

Migration experiments required naturally fractured core samples. In total, 7 cores were prepared for the migration experiments. Cores #1 to #4 were drilled at the KA 2195A 01-05 borehole in the HRL, cores #5, #6, and #7 originate from drill hole KOV 01 778.50-779.25. Selected parts of the drill cores were placed into stainless steel cylinders. The design of these autoclaves is shown in ref. [1]. The length of cores was 150 mm and the diameter 52 mm. The

periphery between cores and steel cylinder wall was filled with epoxy resin. Top and bottom ends were closed with acrylic glass covers. Sealing between the top/bottom ends and the stainless steel cylinder was achieved by O-rings. The lids were provided with fittings for feeding and extracting the groundwater. Tightness of the autoclaves was tested in subsequent laboratory experiments, indicating leak tightness up to 60 bar groundwater pressure. The maximum fluid pressure in the *insitu* experiments was about 27 bar.

## Results and discussion

### *Sorption coefficients for Tc*

For the batch and migration experiments Tc(VII) was used. A sorption coefficient of  $0.210 \pm 0.013$  (surface related) was found onto the flat rock samples. In this sample shown in Figure 1, black areas indicate mainly epidote or chlorite which is in correspondence with the measured Fe distribution. For Tc a strong correlation is observed with the Fe distribution pattern. In batch experiments, Tc shows pronounced sorption kinetics. The kinetics of the retention process within the period under investigation is relatively slow (> 50% of total retention within 9 days), in comparison to the actinides (Am and Pu (> 50% of total retention within 3 days, for U(VI) more than 50% of total retention is obtained after 5 days).

Tc retention is not correlated exclusively to high Fe concentrations in the mineral phases. XPS analyses show a clear shift of Tc 3d binding energy to a reduced redox state. This is explained by the fact that Tc undergoes reduction in the solution. A solid surface - as in the case of redox sensitive Np - is not a requirement for the reduction of Tc(VII) to Tc(IV).

### *Redox speciation of Tc by XPS*

After interaction with pertechnetate spiked solution for 25 days, XPS spectra were acquired by use of monochromatic Al K $\alpha$  X-rays excitation. Figure 2 shows detailed scans of Tc 3d spectra (raw data) taken at 4 different areas on the solid surface where Tc was detected. Slightly different line widths are presumably caused by differential surface charging of the lateral heterogeneous sample surface.

**Figure 1: Optical scan (a), Fe distribution (b), and  $\alpha$ -autoradiography (c) of freshly broken granite exposed to  $^{99}\text{Tc}$  spiked solution.**

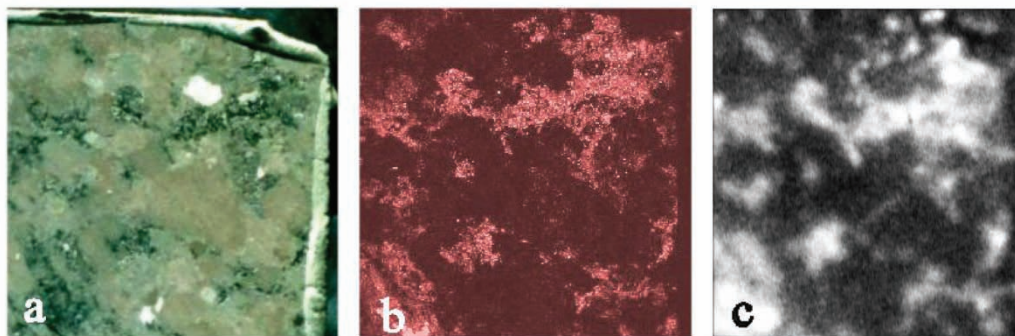
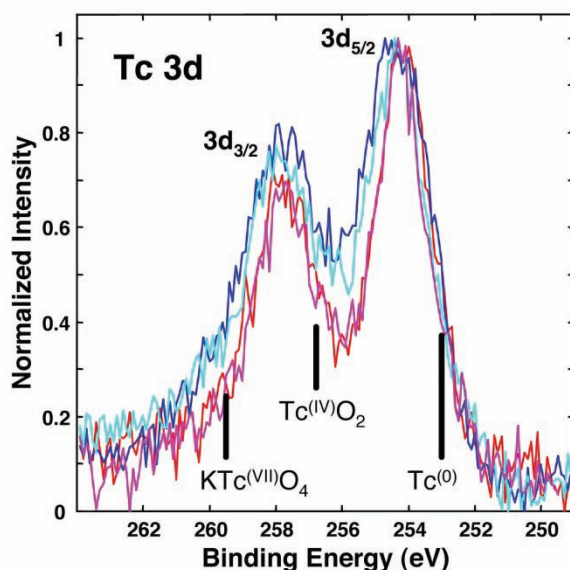


**Figure 2: Narrow scans of Tc 3d spectra (raw data) taken at 4 different areas on the hard rock surface where Tc was detected. Tc 3d<sub>5/2</sub> binding energies of reference compounds (NIST database) are included for comparison**



Significant Tc sorption is observed both onto iron containing areas and onto areas free of Fe. Even if reduction of TcO<sub>4</sub><sup>-</sup> is expected from thermodynamics in solution [7], the process is kinetically hindered [8]. However, in the presence of reducing solids, reduced Tc solids such as TcO(OH)<sub>2</sub>(aq) may be formed and be sorbed onto the surfaces. The average mineralogical composition of the Tc sorbing phases could be calculated to be M(II)M(III)<sub>2</sub>(SiO<sub>4</sub>)<sub>2</sub> which is typical for a feldspar, such as anorthite (CaAl<sub>2</sub>(SiO<sub>4</sub>)<sub>2</sub>). This means that Tc retention is not necessarily correlated to high Fe concentrations in the mineral phases.

XPS analyses show a clear shift of Tc 3d spectra to lower binding energy, characteristic for a reduced valence state. The Tc 3d XPS spectrum shows one single specie with binding energy of the Tc 3d<sub>5/2</sub> line in the range of (254.2 – 254.4) eV. The presence Tc redox states below (IV) cannot be excluded from the observed low binding energy of the Tc 3d<sub>5/2</sub> line. However, under the prevailing groundwater conditions and rock minerals, the formation of Tc(III)/Tc(II) oxides onto the surfaces is not expected because of the harsh conditions required. A solid Tc(III) phase, such as NaTcO<sub>2</sub>(s) can be formed by reacting TcO<sub>2</sub>(cr), technetium metal, and Na<sub>2</sub>O in vacuum at about 873 K [3]. Recent investigations show that the reduction of Tc(VII) may show a position of the absorption edge in agreement with the presence of a Tc(IV)/Tc(III) mixture [4]. These experiments were performed under an electrochemical potential at low pH and the solid Tc(IV)/Tc(III) compound was deposited on the working electrode. For Tc(II), complexes, such as nitrido, nitrosyl and thionitrosyl complexes are reported [3] which are not relevant in the system under consideration. Also under microbial reduction of Tc(VII), TcO<sub>2</sub> was found to be the stable end product [5].

A shift of the binding energy of Tc 3d<sub>5/2</sub> (IV) for TcO<sub>2</sub> (256.8 eV) [6] to lower values is also expected, if less electronegative (Pauling) elements are present in the second shell (first

shell oxygen), for example alkaline or earth-alkaline elements. Due to the fact that the Tc reduction takes place in a natural multi component environment at pH = 7.2, the shift of the binding energy caused by the influence of alkaline or earth-alkaline elements seems to be most probable.

### *In situ migration experiments with Tc*

Core #7 and the cocktail were transferred to Äspö HRL, inserted into the Chemlab 2 probe and a pre-equilibration phase was started in March 2004. After 6 weeks, the flow rate was adjusted to 0.03 to

0.05 ml h<sup>-1</sup>. In total 10.6 ml of cocktail were injected within a period of 342 hours (14.3 days). Sampling of eluted groundwater was performed by an automatic sampler, changing vials after each 30 hour interval. The vials were sealed to avoid evaporation. Within the first few days, an operating error of the sampler occurred and several sampled volumes have to be united for analysis. The first phase of the experiment lasted from May 13 to July 30, 2004, delivering 62 samples. After the restart of Chemlab 2 in September 3, additional 110 groundwater samples were collected until January 19, 2005. The samples were transported to Forschungszentrum Karlsruhe and analysed with respect to the sampled groundwater volume, the radionuclide concentrations and the groundwater constituents.

Redox potentials were recorded after termination of the experiment, when Chemlab was still in the drillhole (undisturbed conditions). Measurements were performed in 10 minutes intervals for more than 16 hours. Mean redox potential of 4.2 ±1.1 mV was obtained which corresponds to E<sub>h</sub> = +248±1 mV (SHE). The performance of the electrode was controlled by a second measurement.

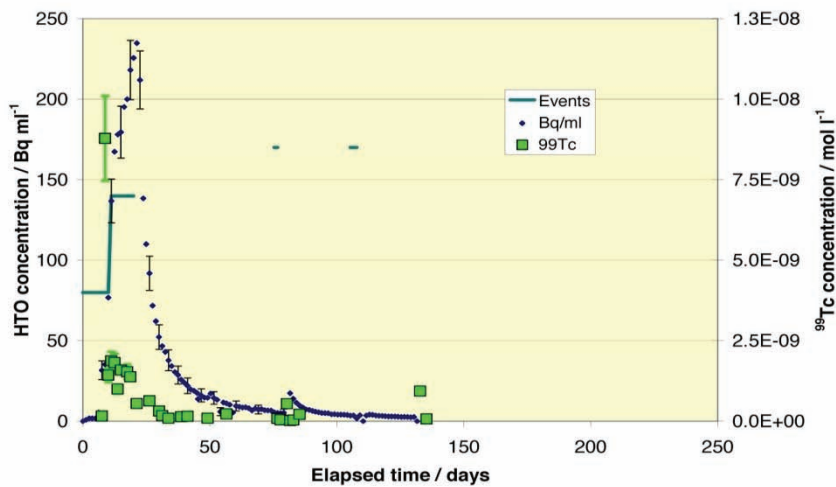
<sup>99</sup>Tc was eluted simultaneously with the inert tracer HTO (Figure 3). In contrast to the uranium tracer, after the initial peak, the concentration dropped and remained close to the detection limit of 1×10<sup>-10</sup> mol L<sup>-1</sup> during the whole experiment. After an interruption of the experiment after the elapsed time of 75 days for duration of 37 days, a small Tc peak was found in the eluted groundwater. This peak was also detected in the HTO and the uranium elution curve. In total, recovery of Tc amounted to ~1% of the injected quantity.

A discussion of the peak after 75 days with respect to the HTO and uranium tracer was presented elsewhere[7]. This HTO peak – and some other peaks in connection with interruptions of the experiment – are the result of a depletion of HTO in the fracture with respect to the concentration in the pore system. During interruption period, HTO concentration in the fracture increased controlled by diffusion. For natural uranium which showed the same elution characteristics than <sup>233</sup>U tracer, it was concluded, that oxygen which was adsorbed to the inner surfaces of the granite matrix could diffuse towards the fracture leading to a remobilization of sorbed Tc. Specific model calculations are in preparation to test assumptions that the extend of O<sub>2</sub> diffusion and the resulting increase of mobilized U and Tc is related to the HTO peak [7, 8].

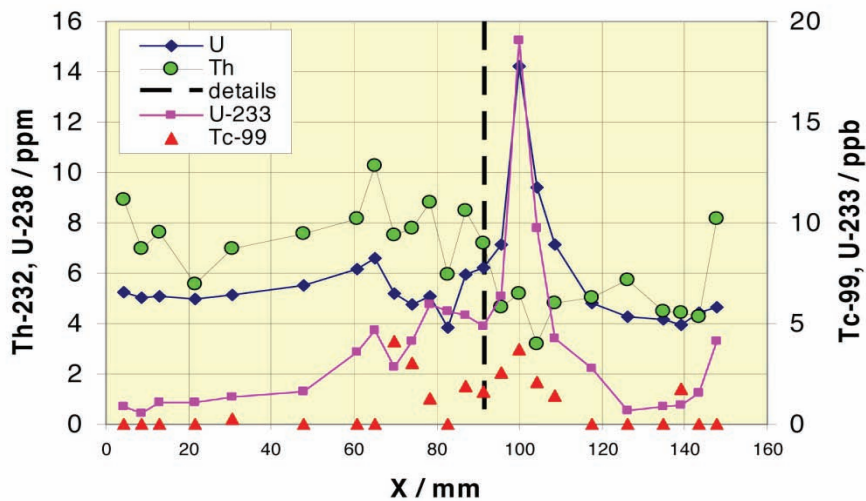
After termination of the migration experiment, the core was cut and the fracture was investigated with respect to element distributions [8, 9]. The abraded material from cutting the core was analysed by ICP-MS.

Figure 4 shows the  $^{99}\text{Tc}$  and  $^{233}\text{U}$  distributions along flow path as well as the distribution of natural uranium. In a distance of  $\sim 100$  mm from injection, significant concentrations of natural U and  $^{233}\text{U}$  tracer are found. Also the  $^{99}\text{Tc}$  concentration is increased in this region. In contrast to U, a decrease of the Th concentration (from  $\sim 8$  ppm to  $\sim 4$  ppm) is found in this region. In this region, matrix elements show also deviations from the average values of the whole core: Mg concentration is decreased by a factor  $\sim 5$ , Ca is increased by about 2. Fe and K show also deviations from average values.

**Figure 3: Breakthrough of HTO and  $^{99}\text{Tc}$  tracers as function of elapsed time in the core #7 *insitu* experiment**



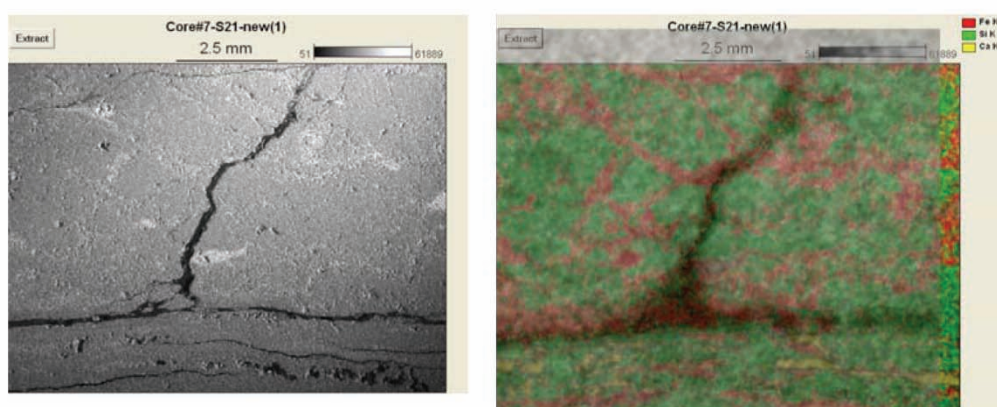
**Figure 4: Concentrations of  $^{99}\text{Tc}$  and  $^{233}\text{U}$  tracers as well as of natural U and Th of the abraded material obtained by slice cutting of a core. (Dashed line: Part of the fracture for detailed analysis)**



Potential sites for reduction processes might be pyrite and Fe(II) containing clay minerals which are detected in the Äspö granite fracture. As described previously, Tc was detected by XPS onto iron rich and onto  $\text{CaAl}_2(\text{SiO}_4)_2$  phases. Significant sorption is observed also onto areas free of Fe.

Figure 5a shows a SEM back-scattering image which is sensitive to differences of the atomic number of the elements, present. White areas represent Ti containing phases. The element mapping (Figure 5a) shows the distributions of the elements Ca (yellow), Si (green) and Fe (red) adjacent to the surfaces of the fracture in slice #21 shown in Figure 4. In total Ca, Al, Si, K, Ca, Ti, Fe were analysed. By combination of the element compositions, some characteristic mineral compositions can be deduced

**Figure 5: Evaluation of element distributions, radioactivity and fracture geometry at a location in the fracture (indicated in Figure 4) by SEM, EDX and  $\alpha$ -autoradiography**



**a. SEM image of slice #21**

**b. Superposition of  $\alpha$ -autoradiogram and the element distribution**

In Figure 5b the superposition of the  $\alpha$ -activity and the element composition is shown. Combination of information of Figure 2a and 6 indicates that especially at the bifurcation of the fracture, the fracture surfaces consist of Fe phases. It is obvious that the surface area at this region is significantly higher than elsewhere in the fracture. Unfortunately, the concentrations of Th, U and Tc were below the detection limit, even if small part of the fracture surfaces were investigated.

The total  $\beta$ -activity injected into the fracture during the experiment amounted to  $\sim 100$  Bq. For this reason, it was not possible to discriminate between the two tracers by radiography.

## Conclusions

The conclusions drawn from batch experiments and elution tests with  $^{99}\text{Tc(VII)}$  are corroborated by the study of the flow path in a natural fracture. Retention takes place on a multitude of minerals, preferentially Fe containing phases. The internal surfaces of the fracture exposed to the tracer play the dominant role for retaining redox sensitive  $^{99}\text{Tc}$ .

The migration experiments show an initial breakthrough of  $^{99}\text{Tc}$ . After this peak, Tc concentration decreases to values close to the detection limit. Measurement of the sorbed Tc distribution in core #7 gave  $R_s = 331$  for this specific experiment. However, from investigations of the retention reactions it is concluded, that the desorption process is based on solid Tc(IV) species and is therefore not in an equilibrium with the sorption reaction of Tc(VII). Desorption of Tc(VII) will take place only, if  $\text{O}_2$  is available. As long as reducing conditions in a deep underground repository persist, desorption of Tc(IV) can be expected only in an equilibrium reaction with solid Tc(IV) phases, such as  $\text{TcO}_2 \times 2\text{H}_2\text{O}$  or even lower soluble mixed Tc(IV) phases or solid solutions.

For safety analysis of a repository in granite host rock, it can be concluded that 99% of  $^{99}\text{Tc}$  tracer was retained within a migration distance of 15 cm during an experimental duration of 280 days. Due to the fact that Tc is reduced, the upper limit of dissolved Tc concentration will be below the solubility of a relevant Tc(IV) phase. This assumption is corroborated by the migration experiments. After the initial breakthrough the maximum concentration of Tc in the eluted groundwater was measured to  $9.4 \times 10^{-10} \text{ mol l}^{-1}$  which is by a factor of 30 below the calculated solubility of  $\text{TcO}_2 \times \text{H}_2\text{O}$  at  $\text{pH} = 7.2$  (reducing conditions of  $E_h < 0. \text{V}$  (SHE)).

## REFERENCES

- [1] Kienzler, B., *et al.*, Swedish-German actinide migration experiment at ÄSPÖ hard rock laboratory. *Journal of Contaminant Hydrology*, 2003. 61: p. 219-233.
- [2] Widestrand, H., *et al.*, Strategy for the use of laboratory methods in the site investigations programme for the transport properties of the rock. 2003, Svensk Kärnbränslehantering AB (SKB): Stockholm Sweden.
- [3] Rard, J.A., *et al.*, Chemical Thermodynamics of Technetium. Chemical Thermodynamics Series, ed. OECD/NEA. 1999: Elsevier Science.
- [4] Poineau, F., *et al.*, Speciation of technetium and rhenium complexes by *in situ* XAS-electrochemistry. *Radiochim. Acta*, 2006. 94: p. 283-289
- [5] Lloyd, J.R., *et al.*, Direct and Fe(II)-mediated reduction of technetium by Fe(III)-reducing bacteria. *Applied and Environmental Microbiology*, 2000. 66(9): p. 3743-3749
- [6] NIST. Standard Reference Database 2.0 Version 3.4 (Web Version). 2006 [cited; Available from: <http://srdata.nist.gov/xps>.
- [7] Kienzler, B., *et al.*, Actinide Migration Experiment in the ÄSPÖ HRL in Sweden: Results for Uranium and Technetium with Core #7 (Part IV). 2005, Forschungszentrum Karlsruhe.

- [8] Kienzler, B., *et al.* Experiences with underground laboratory experiments. in Internat. High Level Radioactive Waste Management Conf. (IHLWM). 2006. Las Vegas, Nev., April 30 May 4 2006.
- [9] Kienzler, B., *et al.*, Actinide Migration Experiment in the ÄSPÖ HRL in Sweden: Analysis of retained uranium and technetium in core #7 (Part V). 2006, Forschungszentrum Karlsruhe.

## **SORPTION BEHAVIOUR OF GRANITE FOR RADIONUCLIDES IN GROUNDWATER CONDITION**

**Takahiro Kikuchi\*, Yoshimi Seida and Kazunori Suzuki**

Institute of Research and Innovation, 1201, Takada, Kashiwa, Chiba, 277-0861, Japan

\* [tkikuchi@iri.or.jp](mailto:tkikuchi@iri.or.jp)

### **Abstract**

The sorption behavior of granite for Cs and Nd in the underground water condition was investigated as the function of mineralogical alteration of granite and particle size. The physicochemical characterization of the granite samples was carried out in terms of mineral phase, pore structure and elements eluted by soft acid treatment as the function of alteration of the granite. The increase of porosity of granite, and phase change of biotite and plagioclase into chlorite and illite, respectively were observed with the increase of alteration degree. The sorption capacities of the series of granites slightly increased with the increase of alteration degree.

## Introduction

Deep geological repository of high level radioactive waste (HLW) in the form of borosilicate glass has been considered in Japan [1]. Although the borosilicate glass is sealed in engineering barriers, the radionuclides may be released to geologic environment after 1000 or 10000 years. We must select sites where the radionuclides in groundwater hardly reach the biosphere. Thus, understanding of radionuclide migration and sorption behaviors on natural rocks in underground environment is important for the safety assessment of the geologic disposal of radioactive wastes. The geological rock containing granite is one of the important disposal sites of HLW. Alteration by water-rock interaction with groundwater is widely observed in fractured granites [2]. Illite, the secondary-fracture-filling materials, showed high sorption abilities for Cs, Pm, Am and Sr [3]. The illitic clay has a greater sorption capacity for Cs than does the montmorillonitic clay [4]. Thus, studying the sorption behaviour of alteration minerals is important. The influence of granite alteration on nuclides retardation is discussed in this study.

## Experimental

### *Materials*

Three series of mineralogical alteration granites occurring in Okayama prefecture designated as sample No.1-3 were used in this study. Table 1 shows physicochemical characteristics for the series of samples such as density and pore structure. The alteration granite samples, collected from close to a fracture, were influenced under hydrothermal conditions. Sample No.1 is the granite sample without alteration. Sample No.2 is the granite with a middle degree of alteration. The alteration of last granite has been most proceeding (sample No.3). Both illite and chlorite that were formed by the hydrothermal alteration were also used for the sorption experiment to elucidate the influence of the minerals on the sorption using standard samples of them supplied from elsewhere. All samples ground into powders with diameters 0.1mm-2.4 mm (granular rock) and 1  $\mu$ m-100  $\mu$ m (fine powder) to investigate an influence of particle size on the sorption.

**Table 1: Pore structure of the series of granite samples**

Sample No.	Density /g cm <sup>-3</sup>	Porosity /%	Specific surface area/m <sup>2</sup> g <sup>-1</sup>	Average of pore diameter /nm
1	2.58	0.7	0.064	10.9
2	2.55	1.6	0.50	12.7
3	2.55	1.8	1.3	12.7

## Characterisation of granite

Mineralogical composition in the granites was analyzed by means of X-ray diffraction (XRD). Specific surface area and pore size distribution of each sample were measured by N<sub>2</sub> adsorption method at 77K. The specific surface area and the pore size distribution were calculated by BET and BJH methods, respectively. We assumed that the deposits on the surface of alteration granites contain some soluble foreign elements or soluble elements of granite mineral origin caused by the hydrothermal alteration. To elucidate the influence of deposits on the sorption property of the granites, we simply carried out the soft acid treatment to remove the soluble elements but not dissolve main minerals of granite. The granite samples were washed with 0.01M HNO<sub>3</sub> followed by analysis of elution elements. The fractures in each sample were also observed by means of fluorescent microscopy for polished thin plates of the samples with an embedded fluorescent reagent.

## Sorption test

The distribution coefficients (K<sub>d</sub>) for Cs on each granite sample was measured by batch adsorption experiments under atmospheric condition. We used vessels which are made of the polypropylene in the sorption test. 2g of the series of granite samples, illite and chlorite were added to 20cm<sup>3</sup> of synthetic ground water solutions containing a predetermined concentration of Cs, respectively. The blank test was also carried out to determine sorption on the walls of the vessel. The slurries were shaken at 298K for 7days in a temperature controlled water bath. The initial concentration of Cs in the synthetic groundwater was adjusted to 0.01mM.

**Table 2: Chemical composition of synthetic groundwater**

	Concentration
Na <sup>+</sup>	3.6
Ca <sup>2+</sup>	0.11
K <sup>+</sup>	0.062
Mg <sup>2+</sup>	0.05
HCO <sup>3-</sup>	3.6
SO <sub>4</sub> <sup>2-</sup>	0.16
Cl <sup>-</sup>	0.062
pH	8.5

Table 2 lists the chemical composition of the synthetic groundwater. The pHs of solution before and after the sorption test were 8.5 and 8.5-9.0, respectively. After the sorption test, the sample solutions were separated from the granite powder samples by filtration using 0.45 μm PTFE membrane. The concentrations of Cs in the solutions were measured by inductively coupled plasma with mass spectrometer (ICP-MS). Duplicate sorption tests were carried out for all the samples to confirm reproducibility of the sorption. The distribution coefficient, K<sub>d</sub>, was calculated based on mass balance using the following equation.

$$Kd = \frac{C_i - C_e}{C_e} \cdot \frac{V_s}{W_e} (m^3 / kg)$$

where  $C_i$ ,  $C_e$ ,  $V_s$  and  $W_e$  are initial concentration of Cs in the solution, equilibrium concentration of Cs in the solution, volume of solution, weight of granite, respectively. Sorption behavior for Nd was also examined by a similar batch method using the same synthetic groundwater with a mixture of Cs and Nd. The initial concentration of Cs and Nd was adjusted to 0.01mM and 0.5  $\mu$ M, respectively.

## RESULTS AND DISCUSSION

### *Composition of granite*

Figure 1 shows XRD patterns for the series of granite samples. Compared with sample No.1 (the granite sample without alteration), a decrease of diffraction peak at  $2\theta=8.6^\circ$  which assigned (001) plane of biotite was observed in sample No.2. The (001) peak disappeared in sample No.3. These results indicate biotite alteration into chlorite [2]. The diffraction pattern of plagioclase that appeared around  $2\theta=22^\circ$  to  $28^\circ$  also changed with the increase of alteration of granite.

**Figure 1: XRD patterns of mineralogically alternated granites**

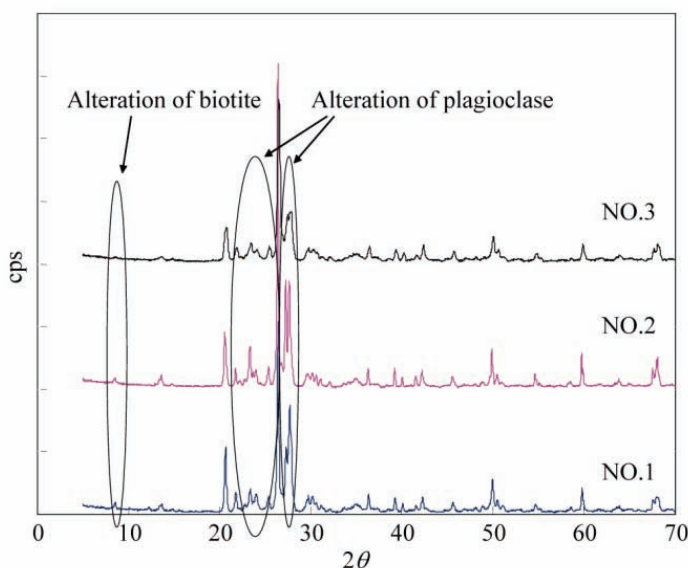
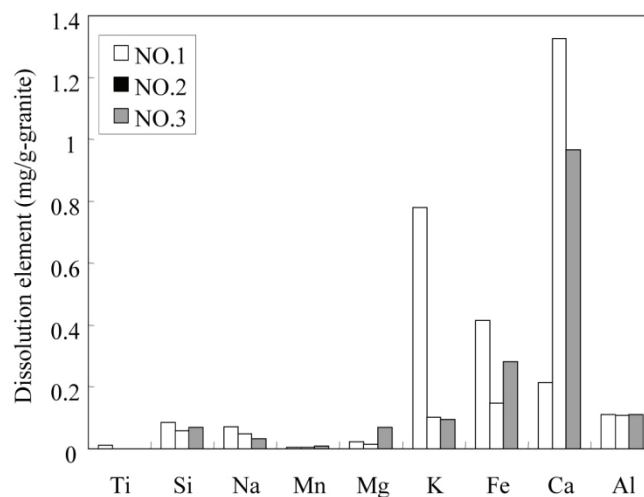


Figure 2 shows chemical composition in the eluate obtained from the acid treatment of granite samples. Dissolved amount of K from Sample No.1 granite is larger than that from the altered granites. A large amount of Ca was dissolved from sample No.2. Increase of Fe and K and decrease of Ca contents with the alteration were also observed by the elemental analysis SEM/EDX in the plagioclase [2]. So, excessive elements will be dissolved by the flush acid treatment. These results suggest that K ion has incorporated into granite, and Ca ion has been released from granite by the alteration. We considered that plagioclase altered mineralogically to illite from the result shown in Figure 2 as discussed in [3].

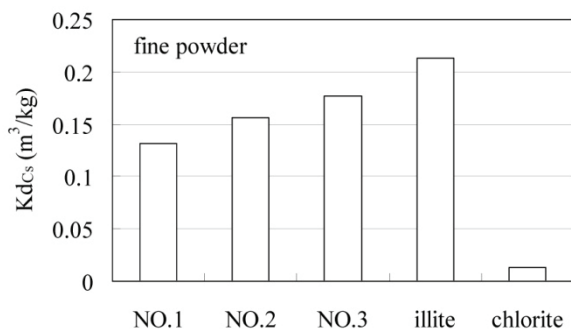
**Figure 2: Chemical composition of eluate obtained from the acid treatment of granites**



***Sorption behaviour of Cs on fine powder***

Figure 3 shows distribution coefficients for Cs for the series of granite fine powder samples as well as for pure illite and chlorite with diameters 1  $\mu\text{m}$ -100 $\mu\text{m}$ . The distribution coefficient for Cs ( $K_{dCs}$ ) increased in the alteration granite depending on the increase of degree of alteration. The specific surface area and the porosity also increased with increasing the degree of alteration. The  $K_{dCs}$  increased with increasing the specific surface area and the porosity of samples (see Table 1). The  $K_d$  of biotite for Cs is much larger than that of quartz and plagioclase according to the reported  $K_d$ s of each mineral in the granite. The  $K_d$  of granite obtained in the present study was comparable to the reported  $K_d$  values. Illite revealed sorption capacity for Cs but chlorite did not as shown in Figure 3, which indicates that the hydrothermal alteration will produce extra sorption capacity for Cs in granite.

**Figure 3: Sorption behaviour of Cs on altered granite samples**



***Effect of particle size on sorption of Cs***

Figure 4 shows influence of particle size of the samples on the sorption of Cs. The sorption capacities for Cs in the case of fine powders are much larger than those in the case of granular

rocks. This result will be reasonable due to the increase in the contact area to the solution in the case of fine powder. The order of  $K_d$  was not a simple function of the particle size in the case of granular rock. That is,  $K_{dCs}$  on No.2 granite is the largest among the samples. We also analyzed the relationship between the Ca content in synthetic ground water and Cs sorption after the sorption test. The increase of Cs sorption was observed in the system with large Ca content. That was granite No.2.

**Figure 4: Influence of particle size on sorption of Cs**

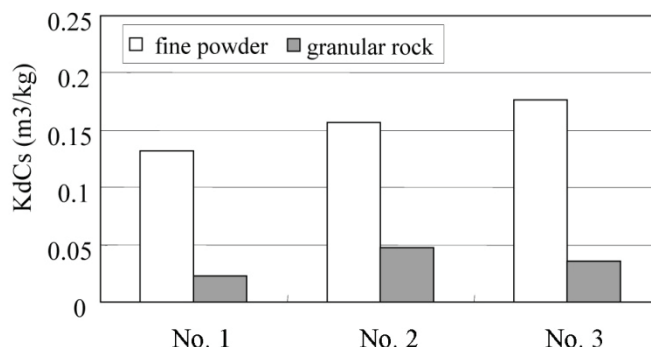
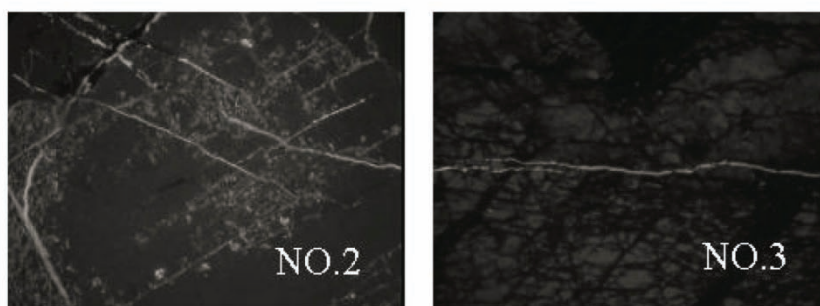


Figure 5 shows fluorescent micrograph of polished thin-sections of alteration granites. The bright areas in the micrograph indicate fractures that were embedded by the fluorescent reagent. Since the fluoresce reagent permeated into most of the fractures of granite No.2, it means that the fractures in granite No.2 will be accessible ones for Cs. On the other hand, the fluorescent reagent permeated into a few of fractures in granite No.3. This indicates that the many of the fractures in granite No.3 are not accessible and Cs does not reach the sorption site in the case of granular rock. Then,  $K_{dCs}$  on No.3 is smaller than that on No.2. In the case of fine powders, Cs will be rather easy to access to the sorption site in the fractures due to the small particle size.

**Figure 5: Fluorescent micrograph of alteration granites**



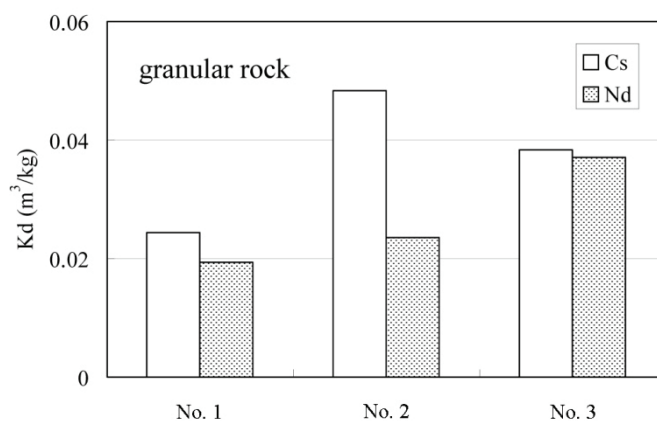
***Sorption behaviour of Nd***

Figure 6 shows sorption behavior for Cs and Nd in the solution with mixture of Cs and Nd in contact with granular granite. The  $K_{dCs}$  in the mixture of Cs and Nd is almost the same with the  $K_{dCs}$  obtained from the single Cs solution (see Figure 4). Then, Nd does not influence the sorption of Cs. The distribution coefficient for Nd ( $K_{dNd}$ ) increased in the alteration granite. We considered that these results suggest that sorption site for Cs is different from the sites for Nd.

## Conclusions

The sorption behaviour of granite for Cs and Nd in the underground water condition was investigated as the function of mineralogical alteration of granite and particle size. The alteration of biotite to chlorite and also plasioclase to illite were observed with the increase of specific surface area and porosity of the granite depending on the degree of alteration. The Kds of the granite samples for Cs and Nd in the ground water condition were slightly increased with increasing the degree of alteration of the granite. The sorption of Cs onto the granites was not disturbed by the co-existence of Nd in the system. The results obtained in the present study indicate that the alteration of granite will not affect the sorption capacity of granite for Cs and Nd from the viewpoint of static sorption.

**Figure 6: Sorption behaviour of Cs and Nd on alteration granite**



## Acknowledgements

This study was supported by the Ministry of Economy, Trade and Industry of Japan. The granite samples were provided from Assoc. Prof. Yoshida of Nagoya University of Japan.

## REFERENCES

- [1] JNC, TN1410 2000-001. JNC, TOKAI, JAPAN, 2000.
- [2] S. Hamasaki, *et. al.*, Sci Basis Nucl Waste Manag 18 Part 2 pp1275-1282 (1995).
- [3] D.C. Kamineni, *et. al.*, Clay Minerals, 21 pp.909-924 (1986).
- [4] D.W. Oscarson, *et. al.*, Applied Clay Science, 2 pp.29-39 (1987).



## **RETENTION OF Se(-II) ONTO PYRITE UNDER REDOX POTENTIAL CONDITIONS**

**Xiaolan Liu, Massoud Fattahi, Gilles Montavon and Bernd Grambow**

SUBATECH UMR 6457 (Université de Nantes, École des Mines de Nantes, IN2P3/CNRS),  
4 rue Alfred Kastler, BP 20722, 44307 Nantes cedex 03, France

### **Abstract**

Pyrite ( $\text{FeS}_2$ ) is a mineral phase often present as inclusions in temperate soils. Moreover, it constitutes an indirect corrosion product of steel, a containment material that is candidate to confine radionuclides in deep geological disposals. The present study was thus initiated to determine the capacity of pyrite to immobilise selenide ( $\text{Se}(-\text{II})$ ). A freshly synthesised pyrite was used in NaCl electrolyte solution to carry out the sorption experiments. After 8 hours, at least 97% of  $\text{Se}(-\text{II})$  initially present in solution were disappeared. This study demonstrates that  $\text{Se}(-\text{II})$  can be immobilised by pyrite via surface reaction.

## Introduction

The storage of high-level nuclear wastes in geological disposal is based on the concept of confinement by a multibarrier system in order to prevent radionuclides from entering the biosphere until radioactive toxicity has decreased to a harmless level. Transport by groundwater is the most likely mechanism for radionuclides to migrate through the engineered and geological barriers and sorption of radionuclides onto mineral surfaces is expected to delay these migrations. Studying sorption processes is therefore fundamental to understand and predict the migration behaviour of radionuclides in the near field geological disposal. Since each component of the barrier will contribute to its sorbing capacity, one needs to know the sorbing properties of each component to understand the sorbing properties of the barrier. Pyrite,  $\text{FeS}_2$ , constitutes one of the components that should receive attention. Under anaerobic conditions, pyrite is a stable mineral phase that is often present as inclusions in temperate soils, as demonstrated by its presence in the argillaceous geological barrier of the site of Bure (Haute-Marne, France).

The sorbing properties of pyrite and its surface chemistry has been well studied, especially towards cationic species. On the contrary, anion adsorption on sulfide minerals has received less attention. Anion adsorption to sulfide minerals is typically modelled as an exchange reaction with surface hydroxyl and sulfhydryl group. Disproportionation or other redox transformations may also couple with anion sorption on sulfide surfaces; however, the extend of oxidation and reduction during anion sorption is not well documented.

Concerning selenium, it is an element of great interest, not only because it is an essential micronutrient for life, but toxic in large doses; but also because one of its isotopes,  $^{79}\text{Se}$ , has a very long half-life:  $3.77 \cdot 10^5$  years [1]. Moreover, in anionic forms, Se(IV) is very mobile in nuclear waste storage background. The chemistry of selenium (Se) resembles that of sulfur (s) because of its proximity to it with group VIA. Se, like S, can exist in four different oxidation states: selenide (Se(-II)), elemental selenium (Se(0)), selenite (Se(IV)), and selenate (Se(VI)).

Sulfide minerals or dissolved sulfide appear to regulate Se levels in anoxic environments. Numerous macroscopic studies of selenite sorption have been performed on pyrite. However, the mechanism of selenide retention, has not been described. Accordingly, we characterized selenide sorption on pyrite ( $\text{FeS}_2$ ) using both traditional solution-phase methods and spectroscopic techniques. Solution-phase data provide information about the variable that control Se sorption to pyrite. Spectroscopic techniques, such as X-ray absorption spectroscopy (XAS) and X-ray photoelectron spectroscopy (XPS) were used to identify the structure and oxidation state of sorbed Se. In combination, the importance of pyrite on Se regulation in the environment is established.

## Material and methods

### *Materials*

#### *Pyrite synthesis*

All chemicals used were of analytical grade except for pyrite and selenide solution. Nitrogen ( $\text{CO}_2 < 1$  ppm) was used to maintain anaerobic conditions. The  $\text{O}_2$  concentration in the glove box was continuously controlled electronically and maintained under 1 ppm by a purification unit.

The pyrite used was synthesized using the method of D. Wei *et al.* [2]. The procedure is described briefly as follows: A batch of pyrite samples was made in 50 ml vials in a glove box filled with nitrogen. Each vial contained a mixture of 10 ml 0.1M  $\text{FeCl}_3$  and 20 ml 0.1M NaHS solutions at pH 4.9. These were allowed to age for 5 days, after which pyrite was well formed and precipitate in the bottom of the vials. The pyrite particles were separated from the solution by decanting the liquid; the solids were washed with  $\text{O}_2$ -free water several times, and dried in a vacuum oven at room temperature. The pyrite sample synthesized using this method contained elemental sulfur, thus requiring further purification. This was done by solvent extraction at  $47^\circ\text{C}$  in a Soxhlet apparatus using  $\text{CS}_2$ . After solid/liquid separation, the purified pyrite particles were washed first with carbon disulfide, then with acetone, and finally with oxygen-free water. To prevent oxidation of the sample, all processes were conducted in nitrogen atmosphere. The particles had an average diameter of 1  $\mu\text{m}$ .

A scanning electron microscopy (SEM) micrograph, a X-ray diffraction and a  $^{57}\text{Fe}$  Mössbauer spectroscopy were used to characterised the pyrite particles. Surface area was determined with a three-point Brunauer-Emmel-Teller (BET) isotherm using  $\text{N}_2$  as the adsorbate. A value of 4.8  $\text{m}^2/\text{g}$  was found for  $\text{FeS}_2$  particles.

As we know, pyrite oxidizes readily. Therefore, care must be taken to prevent oxidation and preserve as best as possible, the integrity of the sulfide surface. So before every use, oxides and other surface coatings were removed by washing the pyrite surface with nitric acid (10%) and then rinsing with deoxygenated deionised water, drying and storing under  $\text{N}_2$ . No oxidation products were found by XPS.

#### *Selenide speciation*

Selenide solution was prepared using an electrochemical method developed by Lingane *et al.* [3]. Generally, there are two means to prepare selenide solution: 1. electrochemical method: a powerful mercury pool electrode is necessary to reduce  $\text{Se(IV)}$  or  $\text{Se(0)}$  in  $\text{NH}_4\text{Cl}$  or  $\text{NaOH}$  media. 2. Hydrolysis of commercial metal sulfides under inert gas controlled conditions. In this study, we opt for the first one because this method is safer, quicker and easier to control than the second one. Moreover, with this method, we can get higher and more repeatable selenide concentration. The maximum concentration that we can get is  $5 \times 10^{-3}$  mol/l within 2-3 hours.

### ***X-ray photoelectron spectroscopy (XPS)***

Pyrite surfaces before and after sorption were characterized by X-ray photoelectron spectroscopy (XPS) at the *Institut des Matériaux Jean Rouxel de Nantes* (France) using a multidetection electron energy analyser (Leybold 30). Samples were analysed using an unmonochromatized MgK $\alpha$  source (1253.6 eV) operated at 120 W (12kV, 10mA). The analyser chamber pressure was in the low  $10^{-7}$  Pa range. Survey spectra were recorded for each sample using a fixed pass energy of 126 eV, while high-resolution spectra were recorded using a pass energy of 37.8 eV. A small charging effect (0.1-0.5 eV) was observed and correction for binding energy was made based on C1s level from contamination at 284.6 eV.

### ***X-ray absorption spectroscopy (XAS)***

X-ray absorption spectroscopy was performed at the European Synchrotron Radiation Facility on beamline 30B. The storage ring operated at 3.0 GeV and at currents between 50 and 100 mA. Spectra was taken with a Si (220) double crystal monochromator with an unfocused beam. Sample fluorescence was measured with a detuned 30-element Ge detector.

*In situ* Se k-edge XAFS measurements were carried out in an electrochemical cell specially designed for this usage in collaboration with CEA (Saclay, France). The working electrode is made of reticulated glassy carbon. The element (Z), coordination number (CN), distance (R), and the Debye-Waller factor ( $\delta$ ) for each shell were determined by fitting the experimental spectra using phase and amplitude functions derived using FEFF 8.

### ***Potentiometric titrations***

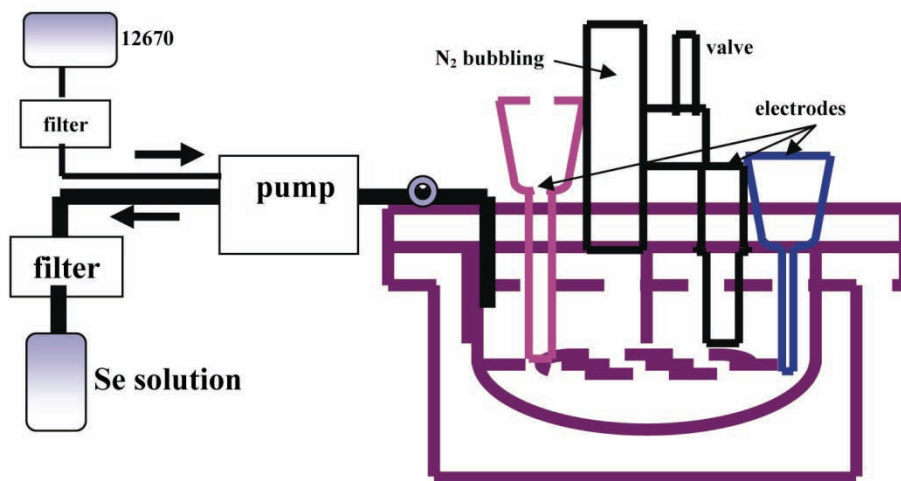
Potentiometric titrations of aqueous pyrite suspensions (4g/L) were carried out under nitrogen atmosphere with a Metrohm 716 titrator equipped with two combined electrodes, a glass electrode associated to a reference electrode Ag/AgCl/NaCl 3 mol/L and a Pt electrode associated to the same reference electrode. The glass electrode was calibrated in concentration using standard calibration solutions. The suspensions of pyrite/NaCl were magnetically stirred for 24h. The latter were then performed by adding small aliquots (50  $\mu$ l) of either NaOH or HCl every 3 min. All titrations were also conducted without solid, under strictly similar conditions to account for potential adsorption of ions on cell walls, and the amount of acid (or base) introduced were calculated from these blank titrations.

### ***Sorption experiments***

Sorption studies were performed in a glass electrochemical cell. A suspension of FeS<sub>2</sub> in 0.1 M of NaCl was prepared and pH adjusted in the glove box under nitrogen atmosphere. The suspension was under agitation for 24 hours. Then, the suspension was transferred as quickly as possible into the cell under N<sub>2</sub> protection. And an aliquot of Se(-II) solution was introduced to the suspension.

A sorption set-up (Figure 1) was developed for sorption experiments to ensure anoxic conditions. Se(-II) addition and sample uptakes were carried out through a peristaltic pump and a 0.22  $\mu\text{m}$  filter. pH was immediately measured after filtration and solution was then acidified with 2%  $\text{HNO}_3$  before ICP/MS (Thermo) analysis or by gamma counting ( $^{75}\text{Se}$ ). The quantity of selenide sorbed onto pyrite was calculated by difference.

**Figure 1: Set-up for adsorption experiments**



## Results and discussion

### *Surface density determination*

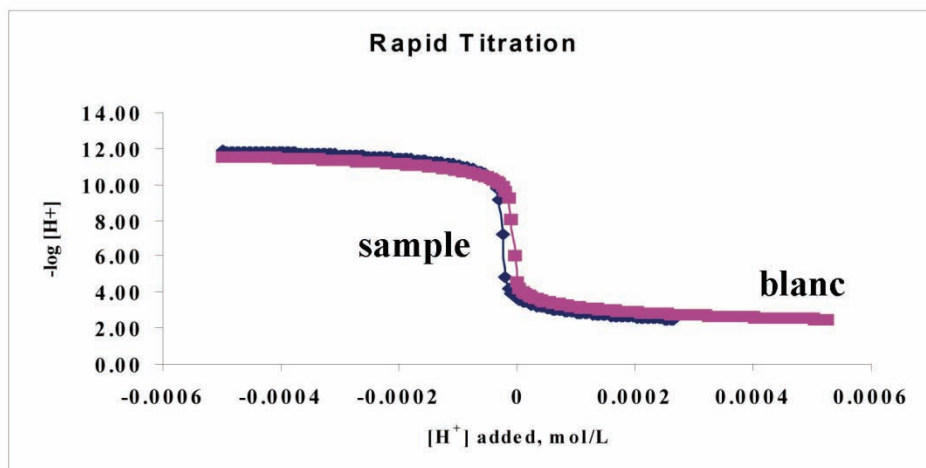
Prior to model sorption of ions on a solid surface using surface complexation model, the density of surface sites and the corresponding acidity constants must be carefully determined. One method to determine site density consists in using acid-base titration [4]. Assuming that surface sites ( $\equiv\text{SH}$ ) are amphoteric, i.e., can either be protonated to form ( $\equiv\text{SH}_2^+$ ) or deprotonated to form ( $\equiv\text{S}^-$ ), concentration of protonated and deprotonated sites, and hence site density, can be estimated from acid-base titrations.

The titration curve (Figure 2) of the pyrite suspension was modelled with FITEQL v3.2 code. Although multiple surface sites with different surface acidity constants may be expected for metallic sulfide surfaces, one surface site was sufficient to fit the experimental curves. The first acidity was too strong to be observed by this method so that only one deprotonation equilibrium could be determined,



which is coherent with the negative surface charge reported in literature. The concentration of this site was calculated by fitting and was found equal to  $2.9 \cdot 10^{-5}$  mol/g synthesized pyrite.

**Figure 2:** Example of an acid-base titration of pyrite suspension (4g/L) in 0.1 M NaCl.



### *Macroscopic sorption characteristics*

Sorption isotherms provide information about the interactions of the mineral and adsorbed species. At low concentrations, sorption resembled a Langmuir isotherm (Figure 3), typical of anion adsorption in which a finite number of sites of similar energy react until all of the sites are occupied (the monolayer capacity). And the pH edges (Figure 4) obtained shows a slight pH dependence.

**Figure 3:** Constant pH isotherm (pH 6.6) of  $1 \cdot 10^{-4}$  M Se(-II) on  $FeS_2$  (2 → 8 g/L)

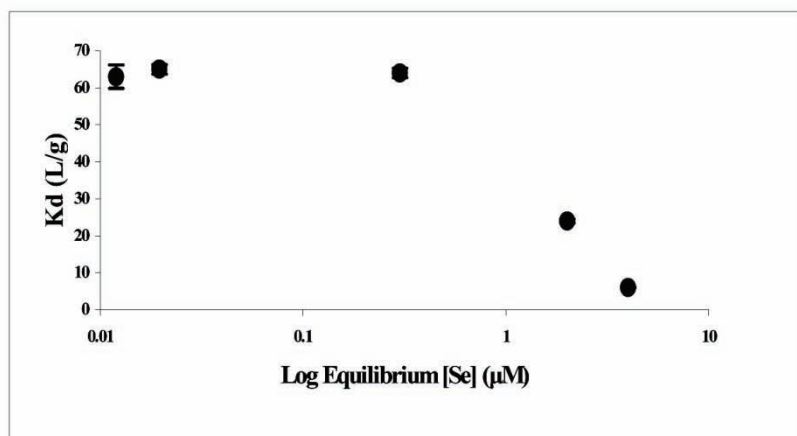
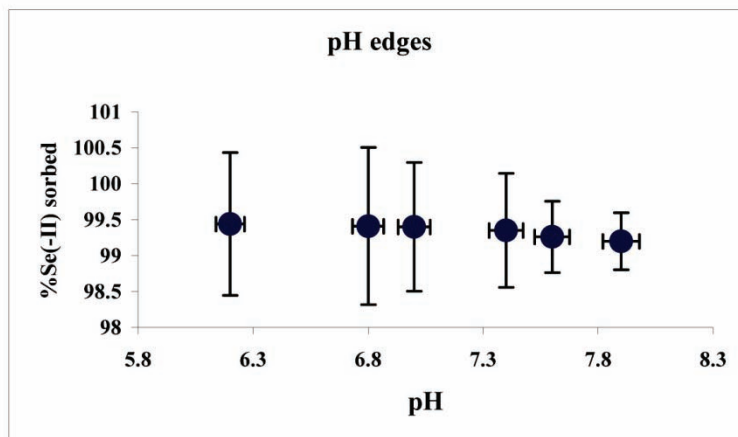


**Figure 4: pH edges sorption of  $5 \times 10^{-5}$  M of Se(-II) on 4g/L of FeS<sub>2</sub>**



### ***Selenium speciation***

To better understand the reaction mechanism, we used an *insitu* Se K-edge XAS technique to follow the reaction processes. Figure 5 shows an example of XANES spectra thus recorded. The Se(0) and ferroselite were prepared *insitu* via electrochemical reductions. XANES represents a rapid, accurate method to investigate the kinetics and the mechanisms of redox reactions. It allows not only to determine the redox state of selenium but also to derive specific structural information on local environment around selenium ions [5]. Another example of XAFS spectrum recorded on a Se(-II)-reacted pyrite suspension (Figure 6). Because the data analyses are still in progress, it is regretful that we cannot show more results.

**Figure 5: The XANES spectra of different Se references**

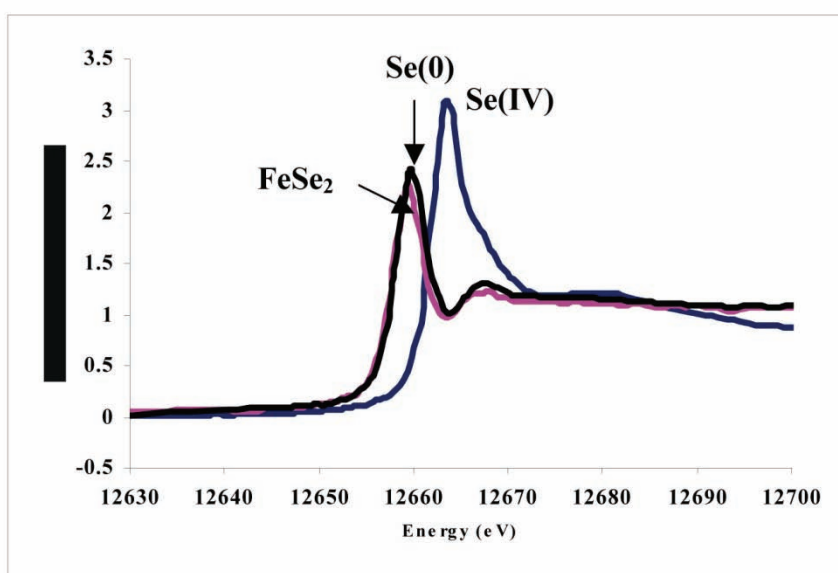
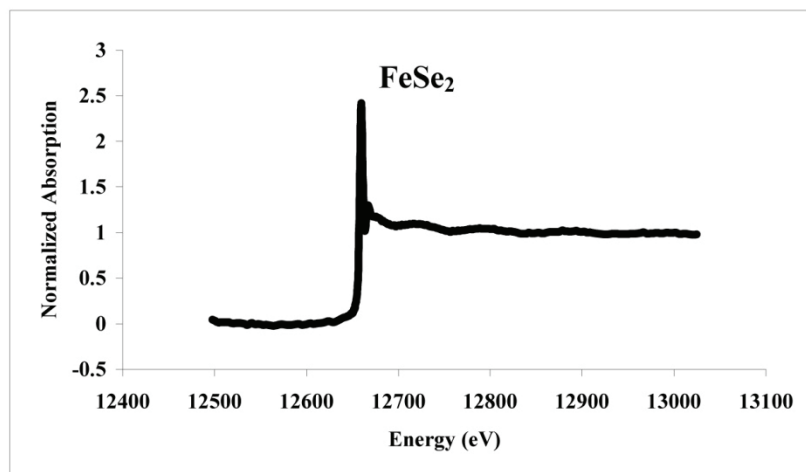


**Figure 6: Se k-edge XAFS spectrum of a Se-reacted FeS<sub>2</sub> suspension**



### *Solid-phase characterisation*

In addition to *insitu* experiments, solid-phase characterization was also carried out in order to investigate structural information on the Se adsorbed on pyrite surface. In this study, we opted for XPS because it is a surface-sensitive technique. And it can also offer information on oxidation states and chemical environment of surface products. A Se3d spectra ( $2.5 \cdot 10^{-4}$  mol/g of selenide/pyrite) was shown in Figure 7. The 3d<sub>5/2</sub> line is located at 54.6 eV, which suggests eventual presence of metal selenide. Nevertheless, the interference from Fe3p line makes this hypothesis less convincing. The same for Se3p lines (Figure 8) which are overlapped by S2p lines. To resolve these problems, we are trying to establish a relationship between Fe/S ratio and different Se coverage on the pyrite surface. Attempts are also made to analyse reference samples, like Se(0) or FeSe. Furthermore, <sup>57</sup>Fe Mössbauer spectroscopy will be employed as complementary technique to investigate the surface state of Se-reacted pyrite.

**Figure 7: The Se 3d spectrum of a cleaned and Se(-II)-reacted pyrite**

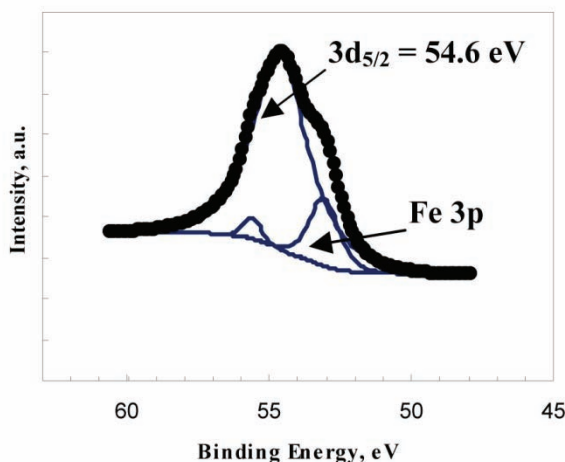
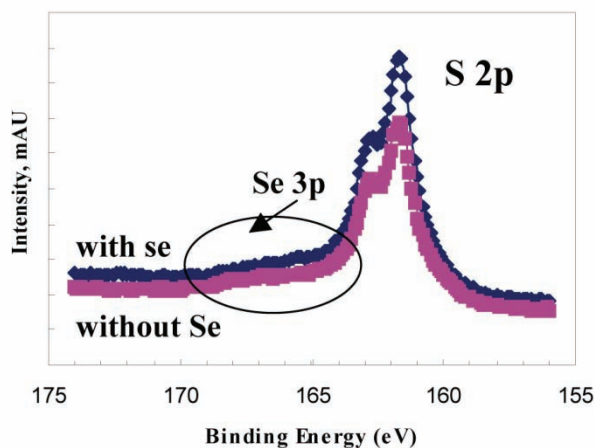


**Figure 8: The S 2p spectra of a pure pyrite and a cleaned Se(-II)-reacted pyrite**



## Conclusions

We found that Se(-II) can be immobilised by pyrite via surface reaction in the reaction system developed in this study. And the speciation methods used were proved to be reliable. Moreover, different spectroscopy *in situ* and *ex situ* experiments were conducted to characterize Se(-II)-reacted pyrite. The data treatment will be finished very soon. The same for data modelling and mechanism description.

## Acknowledgements

I would like to thank the financial support from the European Project of Funmig and technical support from the *Institute des Matériaux Jean Rouxel* (IMN) for spectroscopy experiments. For the electrochemical cell (XAS), special thanks were given to all the people who participated the Soleil project, especially to M. Shlegel from CEA, Saclay (France).

## REFERENCES

- [1] Ph. Bienvenu *et al.*, Applied Radiation and Isotopes, 65 (2007) 355-364.
- [2] D. Wei and K. Osseo-Asare, colloids and Surfaces A: Physicochemical and Engineering Aspects , 121 (1997), 27-36.
- [3] J.J. Lingane and L.W. Niedrach, Journal of the American Chemical Society, 71 (1949) 196-204.
- [4] D.A. Dzomback and F.M.M. Morel, "Surface Complxation Modeling: Hydrous Ferric Oxide" (1990) New York, Wiley-Interscience.
- [5] L. Galoisy, G. Calas *et al.*, Chemical Geology, 174 (2001) 307-319.

## EVALUATING THE POTENTIAL RETENTION OF IODINE IN THE CLAYEY HOST-ROCKS

**C. Tournassat<sup>1\*</sup>, E.C. Gaucher<sup>1</sup>, M. Fattahi<sup>2</sup>, A. Vinsot<sup>3</sup>, B. Grambow<sup>2</sup>**

<sup>1</sup>BRGM, Environment and Process Division, 3 avenue Claude Guillemin,  
F-45060 Orléans Cedex 2, France

<sup>2</sup>SUBATECH, École des Mines de Nantes, UMR 6457, F-44307 Nantes Cedex, France

<sup>3</sup>ANDRA, Laboratoire de Recherche Souterrain de Meuse/Haute-Marne, Service Scientifique,  
RD 960 F- 55290 Bure, France

### Abstract

This paper is an overview of recent works carried out on iodine retention properties of clayey compacted rocks. We show that concerning  $^{129}\text{I}$  diffusive transport in the far-field of a nuclear waste deep disposal, the only relevant mechanism for iodide retention is isotopic exchange with naturally occurring iodine ( $^{127}\text{I}$ ) on the solid or the organic phase (2-3 mg  $\text{kg}^{-1}_{\text{rock}}$ ) of the Callovian-Oxfordian clayey formation where porewater iodine solute concentration has been determined to be 30  $\mu\text{mol L}^{-1}$  as  $\text{I}^-$ . Given the natural distribution coefficient of iodine in the formation, the  $K_d$  applicable to radio iodide in the far-field cannot exceed  $\sim 0.6 \text{ L kg}^{-1}$ . The remaining problem is now to know whether natural  $^{127}\text{I}$  on the solid or organic phase is totally, partially or not at all exchangeable with  $^{129}\text{I}$ .

## Introduction

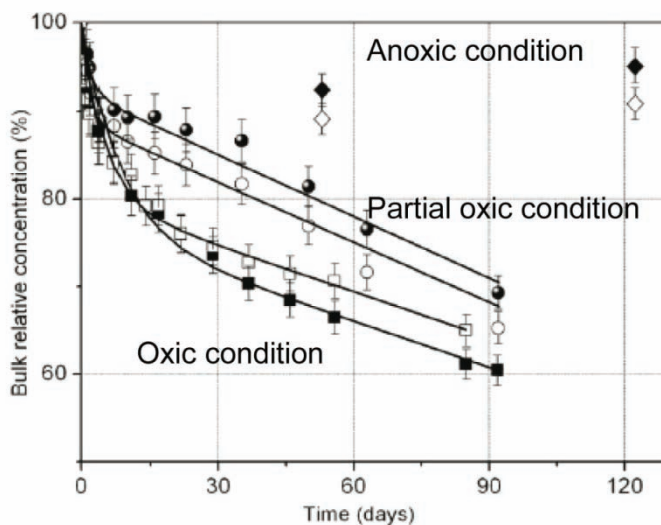
Iodine 129 is an important radioactive pollutant, contributing to potential future radiation doses resulting from radioactive waste disposal in deep host-rock formations, due to its ubiquity in these wastes, its long half-life period (approximately 16 million years) and its high mobility in most rocks and sediments. This high mobility is linked to the anionic nature of dissolved iodine species and its consequently low affinity for sorption on typically negatively charged mineral surfaces.

This paper should be seen as a short synthesis of recent works carried out on iodine retention properties of compacted clayey rocks. A possible mechanism for radio iodide uptake by clayey formations is proposed.

## Background from experiments with labelled iodide

Several studies have been recently published describing diffusive transport experiments on Opalinus Clay (Van Loon *et al.*, 2003a; Van Loon *et al.*, 2003b; Van Loon *et al.*, 2004), Callovian-Oxfordian (Bazer-Bachi *et al.*, 2006) and Tournemire (Savoie *et al.*, 2006) rock samples. Iodide through diffusion experiments have shown a weak retardation of iodide as compared to chloride and a different rock capacity factor, being interpreted as a retention process with very low  $K_d$ , typically between 0.02 and 0.1 L/kg. These values are about one order of magnitude below the  $K_d$  values obtained in batch experiments when different from 0 (see e.g. Bazer-Bachi *et al.*, 2006; Tournassat *et al.*, 2007). However, it has been also shown that different diffusion experiment set up led to different results especially for out and in-diffusion methods as compared to through diffusion (Savoie *et al.*, 2007) pointing out the questions (1) of the relevance of the derivation of very low  $K_d$  values from diffusion experiments and (2) of the mechanism responsible for the observed retention. By the way, *insitu* iodide diffusion profiles in Mont-Terri laboratory have been successfully reproduced considering that iodide was a non-sorbing species (Van Loon *et al.*, 2004). The oxidation of the iodide tracer into iodate tracer has been recognized as a possible reason for iodine retention observation on minerals and sediments (Fuhrmann *et al.*, 1998; Tournassat *et al.*, 2007 and references therein). This possible oxidation effect has been enlightened by the experiments of Bazer-Bachi *et al.*, 2006, showing the great positive effect for retention of oxic atmosphere conditions as compared to anoxic ones (Figure 1). However, this oxidation hypothesis for diffusive transport studies has been partially disproved by laboratory studies coupling through diffusion experiments with iodide tracer speciation measurements using semi-preparative fractionation of the eluent and subsequently measuring the activity of the isotope  $^{125}\text{I}$  in the fractions by  $\gamma$ -counting (Glaus *et al.*, 2007). These authors have shown that iodide was not transformed into iodate in their Opalinus clay sample for which they observed a slight retention of iodide. Moreover they also performed iodate diffusion experiments in which they observed a slow conversion of iodate to iodide. However, they also showed that in the iodide diffusion experiment, the iodine concentration signal given by  $\gamma$ -counting was 90% iodide and 10% of an unidentified iodine species, meaning that iodide has reacted with part of the media. It is then necessary to understand the mechanism of this interaction in order to know if it is applicable to the clayey rock in *insitu* conditions.

**Figure 1: Temporal evolution of  $^{125}\text{I}^-$  relative concentration, at a total iodine concentration of  $7 \times 10^{-7} \text{ mol L}^{-1}$ , in contact with  $200 \text{ g L}^{-1}$  suspensions of EST10425 (black symbols) and EST10577 (open symbols) argillite samples, varying oxic/anoxic conditions. Data from Bazer-Bachi *et al.*, 2006.**

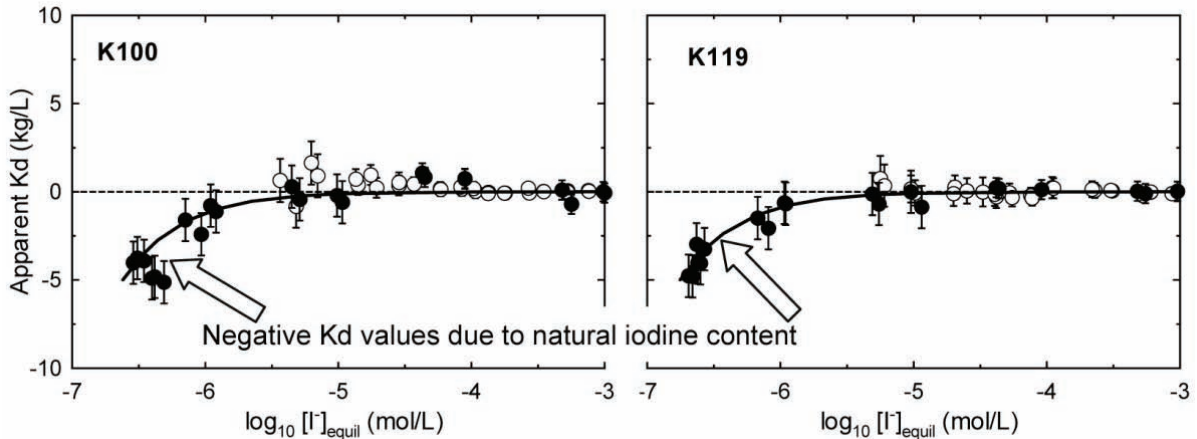


### Information from experiments with stable iodine measurements

Insitu conditions are characterised by the fact that stable  $^{127}\text{I}$  is already present in the porewater of formation (Tournassat *et al.*, 2007). By performing iodine batch sorption experiments on Callovian-Oxfordian rock samples, Tournassat *et al.* have shown that no sorption could be observed given the extent of the error bands for concentration ranging from  $10^{-5.5}$  to  $10^{-3} \text{ mol L}^{-1}$  (Figure 2,  $K_d = 0.21 \pm 0.48$  for K100 sample and  $K_d = -0.02 \pm 0.27$ ). Below this concentration range, they measured iodide concentrations higher than the concentration added to the system, leading to negative  $K_d$  values. This result means that iodide originally present in the rock samples (sorbed or just present in the remaining porewater) was leached during the “sorption” experiment. Considering that leached iodide was present only in the porewater, they could calculate a range for solute iodide in the porewater of the formation of approximately  $10$  to  $40 \mu\text{mol L}^{-1}$  depending on the sample and on the volume of water considered to be accessible to anions as compared to the total water content of the rock (see e.g. Pearson, 1999; Gaucher *et al.*, 2006). This range of values has been now confirmed by *insitu* measurements in the PAC experiments at the Bure URL, France, with a value of  $31 \pm 2 \mu\text{mol L}^{-1}$  (Vinsot and Mettler, 2007).

The total iodine content in the formation as a function of depth is very constant,  $\sim 20 \mu\text{mol kg}^{-1}_{\text{rock}}$ . The distribution ratio of iodine between solution and solid/organic phase is calculated to be  $0.6 \text{ L kg}^{-1}$ . This value is lower than the  $4.2 \text{ L kg}^{-1}$  one previously estimated in Tournassat *et al.*, 2007 based on iodide leached concentrations. The  $0.6 \text{ L kg}^{-1}$  value is likely to be a better estimate since it relies on iodide concentrations that were measured *insitu*.

**Figure 2: Iodide sorption experiment results on K100 (left) and K119 (right) samples at 25°C and after 24 h equilibrium, using non-radioactive iodide. Solid content: 200 g/L. The solid line is the modelling result by considering a  $K_d$  value of 0, and an iodide porewater concentration of 10  $\mu\text{mol/L}$  and 20  $\mu\text{mol/L}$  for K100 and K119 samples, respectively. From Tournassat *et al.*, 2007.**



### Discussion on the potential iodide retention in clayey formations

We now discuss iodide diffusion in the far-field of a nuclear waste deep disposal. Given the concentration of stable iodide in the porewater of the clayey formations porewater ( $\sim 30 \mu\text{mol L}^{-1}$ ), it is obvious that radio-iodide ( $^{129}\text{I}$ ) will represent a very minor fraction of the solute iodide in “equilibrium” with the solid or organic phases of the clayey formation. As a consequence, a complete isotopic exchange with natural iodine represents an upper limit for radioiodine retention whatever the iodine retention mechanism (sorption on organic/mineral surface sites, incorporation in organic matter...). On a pragmatic point of view, the question is then to know the extent of isotopically exchangeable iodine in the solid or organic phase of the formation.

From the natural distribution ratio of iodine in the formation, it can be inferred that the  $K_d$  for  $^{129}\text{I}$  in the far-field should be limited by the  $0.6 \text{ L kg}^{-1}$  value in the case of the Callovian-Oxfordian formation. Surprisingly, this value is about the same than the one derived in most of batch experiments using low concentration of radio labelled iodine in anoxic conditions: Bazer-Bachi *et al.*, 2006 found a value of  $\sim 0.5 \text{ L kg}^{-1}$ , with a spiked iodide concentration of  $0.7 \mu\text{mol L}^{-1}$  and a solid to liquid ratio of  $200 \text{ g L}^{-1}$ . The difference between the  $K_d$  derived from these batch sorption studies and the  $K_d$  values derived from diffusive transport studies ( $\sim 0.1 \text{ L kg}^{-1}$ ) was explained by these authors by a difference of retention sites accessibility between compacted and dispersed systems. However, only four experimental points support this finding of a  $0.5 \text{ L kg}^{-1}$   $K_d$  value (see Figure 1, anoxic conditions). When considering the data from Tournassat *et al.*, 2007, with added iodide concentrations ranging from  $0.01$  to  $10 \mu\text{mol L}^{-1}$  and a solid to liquid ratio of  $50 \text{ g L}^{-1}$ , one obtains a similar mean  $K_d$  value of  $0.4 \text{ L kg}^{-1}$  for a dataset of 54 experimental points. However, the data are scattered and the extent of the error band is  $\pm 1.1 \text{ L kg}^{-1}$ , that is to say larger than the  $K_d$  value, then preventing the drawing of any definitive

conclusion towards the retention level (end even its existence) on the Callovian-Oxfordian rock samples.

From the data analyses above, it appears that published sorption data do not enable to state definitely whether the clayey host-rock formations present an iodide retention capacity as high as  $0.5 \text{ L kg}^{-1}$ , or not. New sorption experimental setups enabling a better precision and resolution on  $K_d$  measurement is then needed to clarify this point. Amongst others, experimental setups derived from the capillary methods described by Montavon *et al.*, 2006 are promising because they enable to measure a  $K_d$ , independently of diffusion transport parameters, at very high solid to liquid ratio, leading to a great resolution for determination of low  $K_d$  values. The effects of temperature on the exchange kinetics and of perturbation such as alkaline plumes degrading the organic matter should also be investigated.

## Conclusion

Radioiodide retention in the far field of a nuclear waste deep disposal can not exceed the natural distribution ratio of iodide in this environment. Radio-iodine retention, if effective, should occur by isotopic exchange with naturally occurring iodine ( $^{127}\text{I}$ ) on the solid or the organic phase of the clayey formation. Given the natural distribution coefficient of iodine in the Callovian-Oxfordian formation, the  $K_d$  applicable to radio iodide in the far-field could not exceed  $\sim 0.6 \text{ L kg}^{-1}$ . The remaining problem is now to know whether natural  $^{127}\text{I}$  on the solid or organic phase is exchangeable totally, partially or not at all with  $^{129}\text{I}$ . From mass balance calculations and literature review, Tournassat *et al.*, 2007 have inferred that natural iodine should be concentrated in the organic matter of the Callovian-Oxfordian formation. From spectroscopic evidences (XANES, EXAFS), Schlegel *et al.*, 2006 have shown that the main part of iodine associated to natural organic matter in various sediments and clayey rocks (e.g. Boom clay but not Callovian-Oxfordian samples) is covalently bound and is present in the redox  $\text{I}^0$  form, i.e. a redox form different than that found in the porewater,  $\text{I}^{-1}$ . If isotopic exchange occurs between organic  $\text{I}^0$  and solute  $\text{I}^{-1}$ , it must be hindered by redox reactions that are usually kinetically controlled. In non perturbed systems (temperature, pH), long time equilibration experiments would then be probably necessary to observe the isotopic exchange phenomenon.

## Acknowledgements

This research was partly funded by the French National Radioactive Waste Management Agency (ANDRA, Dr. Eric Giffaut).

## REFERENCES

- [1] Bazer-Bachi F., Tevissen E., Descostes M., Grenut B., Meier P., Simonnot M.-O., and Sardin M. (2006), Characterization of iodide retention on Callovo-Oxfordian argillites and its influence on iodide migration. *Physics and Chemistry of the Earth, Parts A/B/C* 31, 517-522.
- [2] Fuhrmann M., Bajt S. and Schoonen M.A.A. (1998), Sorption of iodine on minerals investigated by X-ray absorption near edge structure (XANES) and <sup>125</sup>I tracer sorption experiment. *Appl. Geochem.* 13, 127-141.
- [3] Gaucher E. C., Blanc P., Bardot F., Braibant G., Buschaert S., Crouzet C., Gautier A., Girard J.-P., Jacquot E., Lassin A., Negrel G., Tournassat C., Vinsot A. and Altmann S. (2006), Modelling the porewater chemistry of the Callovian-Oxfordian formation at a regional scale. *C.R. Geosci.* 338, 917-930.
- [4] Glaus M., Müller W. and Van Loon L.R. (2007), Diffusion of iodide and iodate through Opalinus Clay: monitoring of the redox state using an anion chromatographic technique. This issue.
- [5] Montavon G., Alhajji E. and Grambow B. (2006), Study of the interaction of Ni<sup>2+</sup> and Cs<sup>+</sup> on MX-80 bentonite; Effect of compaction using the “capillary method”. *Environ. Sci. Technol.* 40, 4672-4679.
- [6] Pearson F.J. (1999), What is the porosity of a mudrock. In *Physical properties of muds and mudstones*, Vol. 158 (ed. A. C. Aplin, A. F. Fleet, and J. Macquaker), pp. 9-21. Geological Society Special Publication.
- [7] Savoye S., Michelot J.L. and Wittebroodt C. (2006), Evaluation of the reversibility of iodide uptake by argillaceous rocks by the radial diffusion method. *Radiochim. Acta* 94, 669-704.
- [8] Savoye S., Wittebroodt C. and Motellier S. (2007), Inter-comparison of radial- and through-diffusion methods used for studying iodide behaviour with regards to the Tournemire argillite (Aveyron, France). This issue.
- [9] Schlegel M.L., Reiller P., Mercier-Bion F., Barre N. and Moulin V. (2006), Molecular environment of iodine in naturally iodinated humic substances: Insight from X-ray absorption spectroscopy. *Geochim. Cosmochim. Acta* 70, 5536-5551.
- [10] Tournassat C., Gaucher E.C., Fattahi M. and Grambow B. (2007), On the mobility and potential retention of iodine in the Callovian-Oxfordian formation. *Physics and Chemistry of the Earth, Parts A/B/C* 32, 539-551.

- [11] Van Loon L.R., Soler J.M. and Bradbury M.H. (2003a) Diffusion of HTO,  $^{36}\text{Cl}$  and  $^{125}\text{I}$  in Opalinus Clay samples from Mont Terri: Effect of confining pressure. *J. Contam. Hydrol.* 61, 73-83.
- [12] Van Loon L.R., Soler J.M., Jakob A. and Bradbury M.H. (2003b) Effect of confining pressure on the diffusion of HTO,  $^{36}\text{Cl}$  and  $^{125}\text{I}$  in a layered argillaceous rock (Opalinus Clay): diffusion perpendicular to the fabric. *Appl. Geochem.* 18, 1653-1662.
- [13] Van Loon L.R., Wersin P., Soler J.M., Eikenberg J., Gimmi T., Hernan P., Dewonck S. and Savoye S. (2004), Insitu diffusion of HTO,  $^{22}\text{Na}^+$ ,  $\text{Cs}^+$  and  $\text{I}^-$  in Opalinus Clay at the Mont Terri underground rock laboratory. *Radiochim. Acta* 92, 757-763.
- [14] Vinsot A. and Mettler S. (2007), Callovo-Oxfordian porewater geochemical characterization. PAC experiment, Report No. ANDRA D RP ALS 07 0008.1.



## **SORPTION OF SELENITE IONS ON SOLID SOIL COMPONENTS USING DIALYSIS MEMBRANES**

**J. Muller, A. Abdelouas, B. Grambow**

SUBATECH, EMN-CNRS/IN2P3-Université de Nantes, 4 rue Alfred-Kastler, F-44300 Nantes

### **Abstract**

Selenium-79 is a radionuclide that is produced in nuclear reactors with a yield of about 0.04%. According to the French concept of deep geological high-level waste disposal selenium can have a significant effect on the cumulative radioactive dose if it is transported through the geosphere without retardation. Once in the biosphere, selenium may be retarded via sorption onto soil components including clays, calcite and Fe-oxides. The aim of this work is to develop a new method, an alternative of batch experiments, to determine the influence of chemical interactions on selenium sorption onto solid phases commonly present in soils.

A method using a dialysis membrane was used. Five millilitres of a solid/synthesized water suspension in a dialysis bag was placed in 100 mL of synthesized water containing selenium in known concentration. We first studied the effect of the dialysis membrane on the equilibrium time for each soil components. The sorption of selenite ions onto bentonite, goethite and calcite was characterized by sorption kinetics. Also, the effects of pH and selenium concentration in solution on the sorption were investigated. To establish the contribution of the different solids to the sorption, experiments with one component (bentonite, calcite, goethite) were carried out and a value of  $K_d$  was calculated. The preliminary experimental  $K_d$  obtained were between 0–58 L.kg<sup>-1</sup> for calcite and between 0-70 L.kg<sup>-1</sup> for bentonite.

Preliminary results with two solid phases at pH 7 (bentonite + calcite and goethite + calcite) show that the  $K_d$  of bentonite and goethite decrease in comparison with the single system. The retention behaviour of calcite remains the same one in a system with one component and in a system with two components at pH 7.

## Introduction

Selenium (Se) is a naturally occurring trace element found in most soils. It is an essential element for animals and human being because it is required for normal enzyme function but Se becomes toxic depending on its concentration and chemical form. Moreover, radioactive selenium is produced in fission reactors in the form of several isotopes including  $^{79}\text{Se}$ , which is a long-lived fission product with a half-life of  $1 \times 10^6$  years. Performance assessment analysis of a deep geological repository for nuclear waste done by ANDRA (*Agence nationale pour la gestion des déchets radioactifs*) has shown that  $^{79}\text{Se}$  is one of the most mobile radionuclides with a dominant contribution to the final dose. Thus, its behaviour is considered critical in safety analyses of deep geological repository of radioactive wastes. Determination of the factors governing selenium migration and speciation should improve the precision of performance assessment of a geological repository. So, it is important to study the selenium release from nuclear waste to the groundwater and its mobility through the geosphere.

This study was focused on the selenite anion ( $\text{SeO}_3^{2-}$ ) sorption on several soil components (bentonite, goethite, calcite), since it is expected that this form is very mobile and commonly found in groundwater near the repository. Experiments were conducted using dialysis membranes to better determine the interactions between sorbing phases with regard selenite. Selenite movement through soils is mainly related to the fluid dynamics and to the sorption on the solid phase, the later being in turn controlled by the composition of both solid and liquid phase. So, the aim of this study was to determine the liquid phase influence between soil components. Thus, we physically separated soil components in order to determine the influence of the matrix elements. For that, we have, in a first time, determined the equilibrium time and realise sorption isotherms for bentonite and calcite. A  $K_d$  was also measured for each component in order to compare this value with these obtain in a system with several component. Sorption behaviour of radionuclides is usually determined by calculating a distribution coefficient,  $K_d$ , which represents the distribution of radionuclides between solid and aqueous phase.

Bentonite was used because this clay was selected as a potential buffer in the French disposal program for high-level waste. Sorption on bentonite will play a key role in retarding the migration of many radionuclides from a waste repository. Boulton *et al.* (1998) [1] showed that the sorption of Se(IV) on purified bentonite is significant only below pH 7. Goethite was chosen because of its ubiquity and because Fe oxides are important scavengers of certain elements in soils and sediments. Thus, they will play an important role in the retention of radionuclides in underground water. Several authors [2-5] showed that selenite adsorption by Fe oxides is extensive, rapid, and decreasing with pH between pH 3 and 8. We also decided to study the sorption behaviour of selenite onto calcite, which is the most abundant mineral in the Earth after quartz. Singh *et al.* (1981) [6] found that a calcareous soil sorbs more selenite and selenate than a normal, saline or alkaline soil. Neal *et al.* (1987) [7] indicated that, in the range of 0 to 3%  $\text{CaCO}_3$  content was not a major factor in determining selenite sorption for five soils. Goldberg and Glaubig (1988) [8] found that selenite sorption on calcite increased from pH 6 to 8, peaked between pH 8 and 9, and decreased above pH 9. They also showed that the sorption plateau of a soil composed of montmorillonite, kaolinite and calcite virtually disappeared above pH 7 after removal of calcite, indicating that calcite plays an important role in selenite sorption of calcareous soils.

To understand the effect of physical interactions on the sorption of Se(IV) onto several soil components (goethite, bentonite, calcite), we first studied simple system (soil component/selenite ion). We then investigated systems with two soil components/selenite ion and compared the latter results to those obtained in the simpler systems.

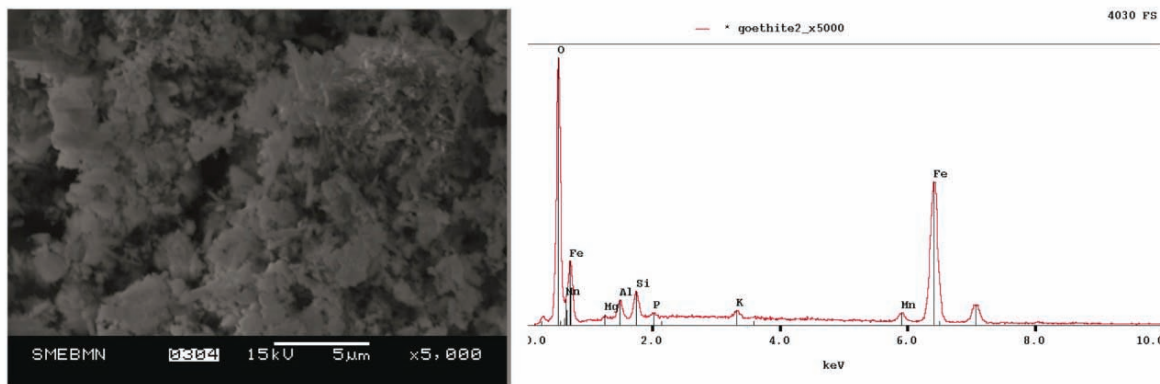
## Materials and Methods

### Sorbents

We used electronic scan microscopy (MEB JEOL 6400) to obtain pictures of our mineral phases. Pictures were obtained by applying an accelerating tension of 15 kV for an enlargement of 5000. To make a quantitative analysis of our mineral samples, we used MEB JEOL 5800. This apparatus was equipped with an electron gun and allow, using a filament carried at high temperature, to obtain an energy electron beam which passes through lenses and arrive on the sample. The interaction electron/matter gives various radiative emissions, making possible to collect information on the object from which they result.

The goethite (Figure 1) used in this study was provided by Sigma-Aldrich (Fluka 71063). A specific surface area of  $11 \text{ m}^2 \cdot \text{g}^{-1}$  was measured by B.E.T  $\text{N}_2$  adsorption [9] with an apparatus Micromeritics ASAP 2010.

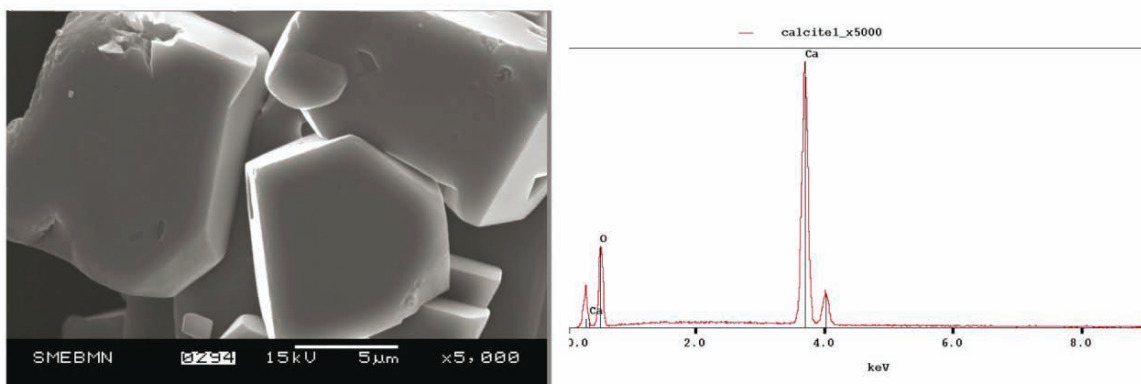
**Figure 1: Picture and qualitative analysis of goethite**



Quantitative analysis showed that goethite contains on average of O (52.44%), Fe (38.01%), Si (3.26%), Al (2.79%), Mn (1.72%), Mg(0.75%), K(0.67%) and P (0.38%).

Calcite (Figure 2) was purchased from VWR Prolabo. A specific surface area of  $0.74 \text{ m}^2 \cdot \text{g}^{-1}$  was measured by B.E.T Ar-adsorption (Micromeritics ASAP 2010).

**Figure 2: Picture and qualitative analysis of calcite**



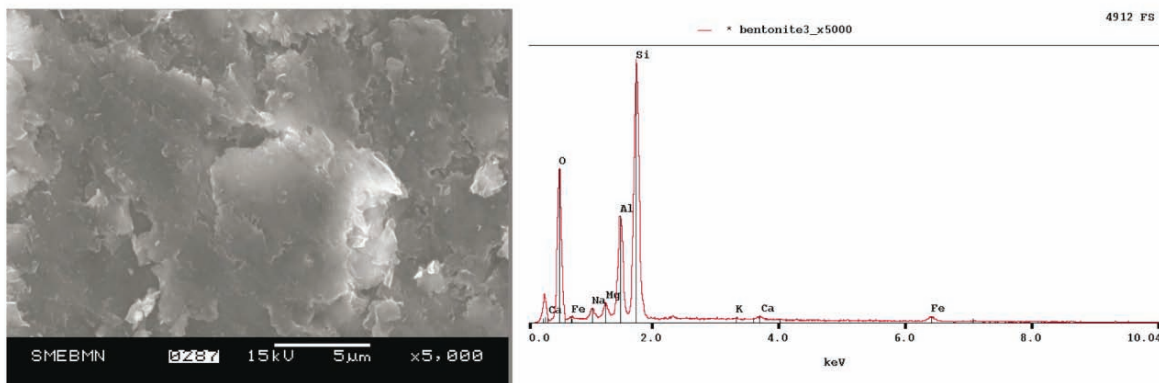
Quantitative analysis showed that calcite contains on average of O (76.65%) and Ca (23.35%).

Bentonite MX 80 (figure 3) studied was not purified and its mineralogical composition detailed in Table 3. We chose to work with a not purified bentonite because the mineral phases (except for montmorillonite) are additional phases and are thus supposed to have a weak influence on the retention of selenium. Moreover, Neal *et al.* (1987) [7] showed that for contents from 0 to 3% of  $\text{CaCO}_3$  in soils, calcite did not have an influence on the behaviour of selenium. A specific surface area of  $17 \text{ m}^2\cdot\text{g}^{-1}$  was measured by B.E.T  $\text{N}_2$  adsorption (Micromeritics ASAP 2010). Le Hécho *et al.* (2001) [9] have determined the cationic exchange capacity (CEC) of this clay according to two methods. They found a CEC of  $80 \pm 2$  and  $70 \pm 3$  meq/100g by cobaltihexamine chloride and ammonium oxalate, respectively.

**Table 3: Mineralogical composition of bentonite**

Composition of bentonite (%)									
Montmorillonite	Carbonates	Titan oxide	Phosphates	Pyrite	Na-Feldspath	K-Feldspath	Biotite	Quartz	Water
71 to 76	0.5 to 1.4	0.1	0.3	0.5	3	1	2 to 3.8	5 to 6	10

**Figure 3: Picture and qualitative analysis of bentonite**



Quantitative analysis showed that bentonite contains on average of O (63.38%), Si (23.14%), Al (8.97%), Na (1.62%), Ca (0.25%), Fe (1.06%), Mg (1.47%), and K (0.13%).

### ***Experimental conditions***

Sorption experiments were conducted in dialysis membranes, at room temperature, in contact with air to simulate the behaviour of selenite in aerated soils. We used an aerated water in order to simulate the behaviour of selenium after its migration towards surface. The water used for the various experiments is synthetic water whose composition is given by using the average values of the ratios of concentrations of the major cations in “référentiel géologique du site de l’Est” of January 1999 (A RP ADS 99-005, Figure 6.1.11). Water is then equilibrated with air under agitation during one week and the small final deviations of pH are corrected by addition of NaOH or HCl. After equilibration with ambient CO<sub>2</sub> and addition of base or acid, water is filtered with 0.2µm silver filters in order to avoid any organic matter contamination of our synthetic water. The nominal composition of water is [Ca] = 4.742 e-3 mol.L<sup>-1</sup>, [Cl] = 4.282 e-2 mol.L<sup>-1</sup>, [K] = 1.423 e-4 mol.L<sup>-1</sup>, [Mg] = 3.557 e-3 mol.L<sup>-1</sup>, [Na] = 2.640 e-2 mol.L<sup>-1</sup> and [HCO<sub>3</sub>] = 3.218 e-4 mol.L<sup>-1</sup>. The initial pH and the ionic strength of synthetic water are 7.7 and 0.05, respectively. The preparation of synthetic water with the different pH is obtained by adding NaOH or HCl.

Suspensions of bentonite/synthetic water with a ratio of 10 g.L<sup>-1</sup> were prepared. Four washing cycles of bentonite with fresh synthetic water of 24 hours each were necessary to obtain equilibrium between bentonite and synthetic water. During the washing cycles the pH was adjusted continuously. For the other suspension materials (calcite, goethite)/synthetic water, washings were not necessary; we thus directly adjusted the pH by addition of acid or base.

### ***Dialysis Sorption experiments***

This method consists of the use of two dialysis membranes of different porosities (Spectra/Por MWCO 1000 Da and MWCO 10000 Da). This method prevents from the dispersion of the components in the outer solution and does not allow colloidal dispersion of the soil components. The membranes were closed with Spectra/Por Weighed Closures (55mm) polypropylene grips. The membranes were stored at 4°C and rinsed three times with deionised water to remove traces of organic carbon. Measurements of total organic carbon were performed with a TOC-meter Shimadzu 5000A. Blank sorption experiments with selenite and polypropylene flask/grips and the membrane did not show any sorption.

**Figure 4: experimental design**



Experiments undertaken with stable selenium can be described as follow: each dialysis bag filling with 5 mL of suspension solid/ synthetic water were placed in 100 mL of synthesized water containing selenium in known concentration (Figure 4). Selenium solutions were prepared from analytical reagent grade  $\text{Na}_2\text{SeO}_3$  (Sigma S-1382). The pH was immediately measured after filtration at 0.2  $\mu\text{m}$  with inorganic membrane filter (Whatman  $\text{\textcircled{R}}$  Anotop 25) and the selenium content remaining in the filtrate is determined by ICP-MS. Elemental plasma standard solutions, Specpure  $\text{\textcircled{R}}$ , of Se with a concentration of  $1000 \text{ mg.L}^{-1}$  was used to prepare the calibration solutions. Calibration standards of 2.5, 5, 10, 15 and 20  $\mu\text{g.L}^{-1}$  were prepared by diluting the initial solution of  $1000 \text{ mg.L}^{-1}$ . The sorbed Se can be then calculated by subtracting the remaining Se concentration from the initial one. The results were obtained on an apparatus PQ\_EXCELL\_Marque\_VG\_Elemental with a quadrupole detector.

Experiments undertaken with radioactive  $^{75}\text{Se}$  can be described as follow: each dialysis bag containing 5 mL of suspension was placed in 100 mL of synthesized water containing an activity of about  $10 \text{ Bq.mL}^{-1}$ . Radioactive selenium in the form of acidic selenium in 0.1 M HCl was purchased at the CERCA LEA. The pH was immediately measured after ultra-centrifugation with sartorius Centrisart I cut off 10.000. We decided to ultra-centrifuged because preliminary studies have shown that there are still differences between the inner and outer Se concentrations at the end of 10 days of equilibrium for goethite. These differences may be due to colloids presence in the inner suspension. However it was shown in the literature that the equilibrium time of goethite and selenium is approximately two hours. Thus, all the suspensions were ultra-centrifuged in order to eliminate tiny and nanometric sized colloids containing sorbed Se. The activity was measured in the inner solution and suspension and in the outer solution. The results were obtained on a apparatus Packard Liquid Scintillation Analyser 2500 TR/AB.

## **Results and discussion**

### ***Comparison of results with the two membranes***

The results of experiments with the two different membranes are given in the form of Se concentration as a function of time in Figure 5.A, B and C for bentonite, calcite and goethite, respectively. The two goals of these experiments were to determine the time of equilibrium for each component and to determine the influence of the two kinds of membrane on the equilibrium time.

**Figure 5 A comparison of inner and outer concentration for two types of membranes with bentonite; B with calcite; C with goethite**

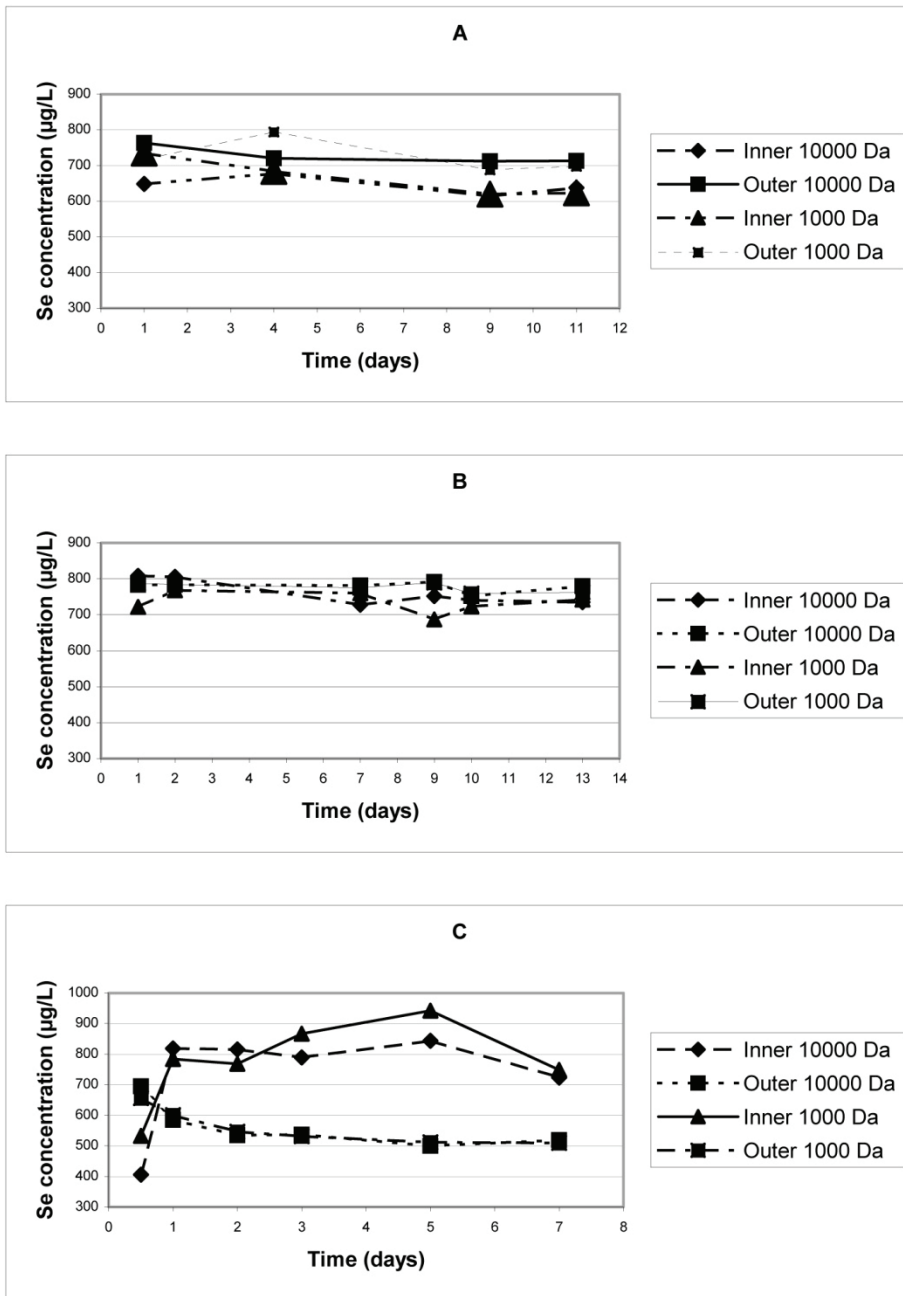


Figure 5 shows that for bentonite and calcite the equilibrium was reached within a few days and no difference between the two membranes was observed. For goethite it seems that the equilibrium was not reached within a week and more equilibrium time is need. Also, the differences in inner and outer concentrations of Se may be due to colloids presence in centrifuged inner suspension. Thus, all the suspensions will be ultra-centrifuged to eliminate tiny and nanometric sized goethite colloids containing sorbed Se. So, equilibrium time founded

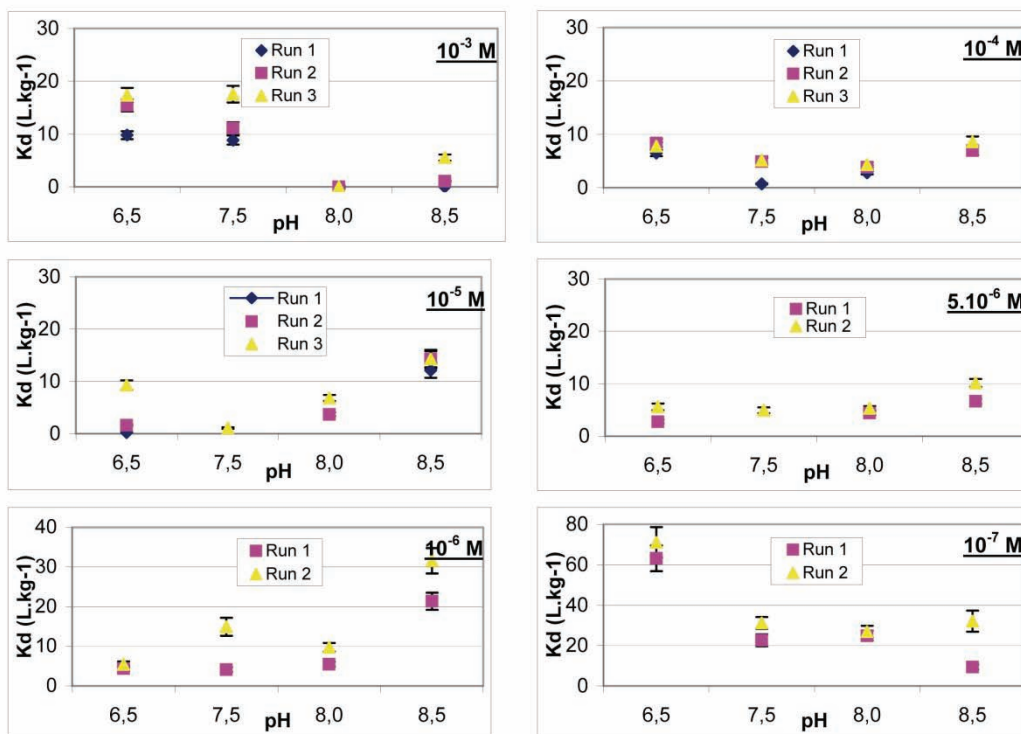
was in good agreement with these founded with batch method, except for goethite where the physical separation gives different results.

### Sorption of Se on bentonite

#### K<sub>d</sub> evolution with pH

The experimental determination of the distribution coefficient ( $K_d$ ) for bentonite at four different pH values, covering a solution concentration range of  $10^{-3}$  –  $10^{-7}$  M are presented in Fig 6. Under these experimental conditions (pH: 6.5; 7.5; 8.0 and 8.5; Se concentration:  $10^{-3}$ ;  $10^{-4}$ ;  $10^{-5}$ ;  $5.10^{-6}$ ;  $10^{-6}$  and  $10^{-7}$  M),  $K_d$  are similar. Indeed, with  $10^{-3}$ ;  $10^{-4}$ ;  $10^{-5}$ ;  $5.10^{-6}$ ;  $10^{-6}$  M concentrations, experimental  $K_d$  are between 0 and 30 L.kg<sup>-1</sup>. With a concentration of  $10^{-7}$  M, we found highest  $K_d$  values with a maximum of about 70 L.kg<sup>-1</sup> at pH 6.5 and a minimum of 20 L.kg<sup>-1</sup> at pH 8.5. The adsorption of selenite by a given concentration of bentonite is greatest at low pH and decreases with increasing pH in agreement with Howard (1972) [10] and Bar-Yosef (1987) [11] for selenite adsorption on clays. The increase in adsorption with decreasing pH is characteristic of anion adsorption. For the lowest ( $10^{-7}$  M) and the highest concentration ( $10^{-3}$  M) of Se, we notice a decrease of  $K_d$  values with increasing pH. For the four others concentrations used in this study ( $10^{-4}$ ;  $10^{-5}$ ;  $5.10^{-6}$ ; and  $10^{-6}$  M) results showed a small fluctuation of the measured  $K_d$  with pH. Except for Se concentration of  $10^{-7}$  M, experimental distribution coefficients are in the same order of magnitude, in a range of 0 to 30 L.kg<sup>-1</sup>.

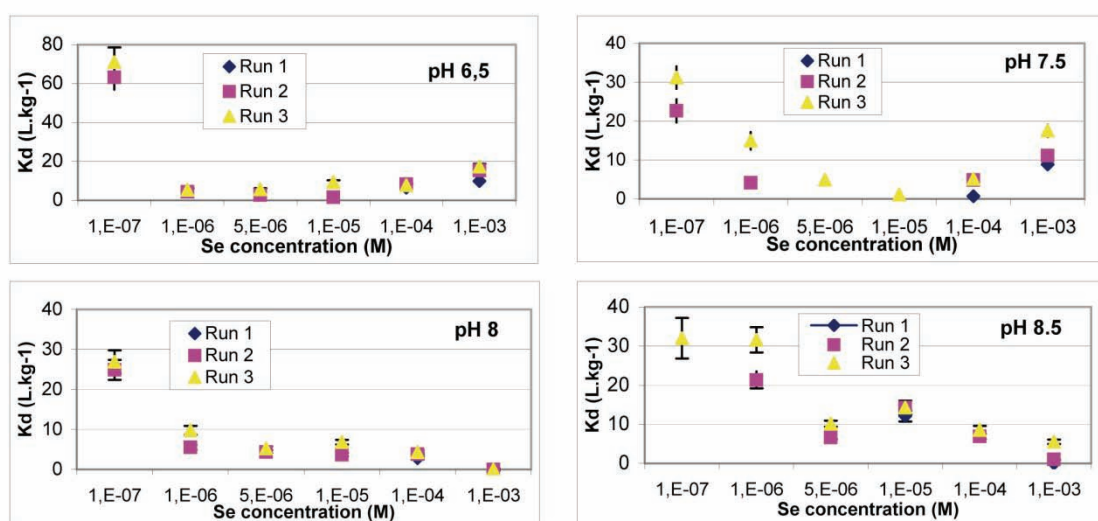
**Figure 6: Effect of pH on the distribution coefficient  $K_d$  (L.kg<sup>-1</sup>) in the range of concentration  $10^{-3}$  M –  $10^{-7}$  M (bentonite)**



### *K<sub>d</sub> evolution with Se concentration*

The evolution of  $K_d$  as a function of Se concentration at different pH values is given in Figure 7. The location of the adsorption edges for the five upper selenite concentrations ( $10^{-3}$ ;  $10^{-4}$ ;  $10^{-5}$ ;  $5 \cdot 10^{-6}$  and  $10^{-6}$  M) is the same. Indeed,  $K_d$  values are quite similar; there are only small fluctuations, for these five concentrations and pH. Figure 7 indicates that the distribution coefficient ( $K_d$ ) decreases as the total selenite concentration increases. With a concentration of  $10^{-7}$  M,  $K_d$  values are higher than for the other concentrations and this values decrease with increasing pH. As it was found by Balistreri and Chao (1987) [2], that the influence of the total selenite concentration on the  $K_d$  value is consistent with the heterogeneous site binding model. This finding is important for modelling of our experimental results with PHREEQC.

**Figure 7: The distribution coefficient of selenite  $K_d$  ( $L \cdot kg^{-1}$ ) as a function of total selenite concentration and pH (bentonite)**



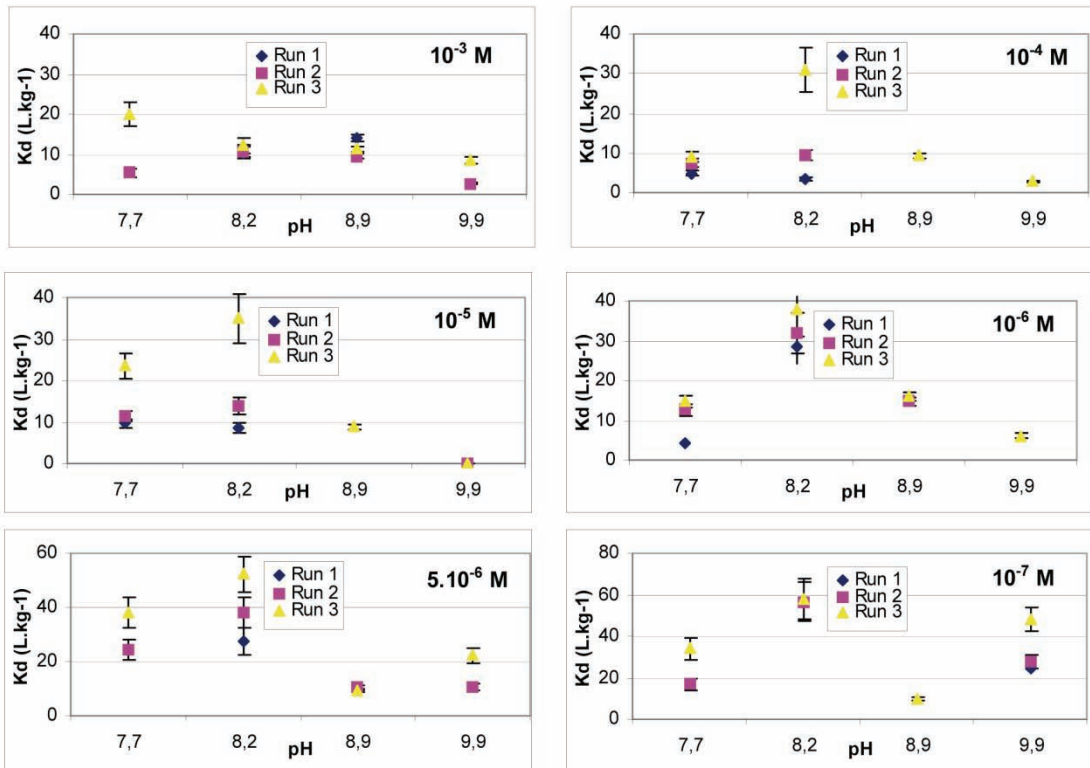
### *Sorption of Se on calcite*

#### *K<sub>d</sub> evolution with pH*

The sorption behaviour of selenite on calcite was studied on the pH range 7.7 to 9.9 in order to avoid the dissolution of calcite which occurs towards pH 7. Moreover, this pH range represents the most frequently founded pH in soils.

The experimental determination of the distribution coefficient ( $K_d$ ) for calcite at four different pH values, covering a solution concentration range of  $10^{-3}$  –  $10^{-7}$  M are presented in Figure 8.  $K_d$  values are always lower at pH 9.9 in comparison to the others pH studied, with exception of  $K_d$  values for the  $10^{-7}$  M concentration, which is highest than these obtained at pH 7.7. So, it seems that pH 9.9 is not optimal for the sorption of selenite on calcite. According to our results, it seems that the optimal pH is near 8.2.

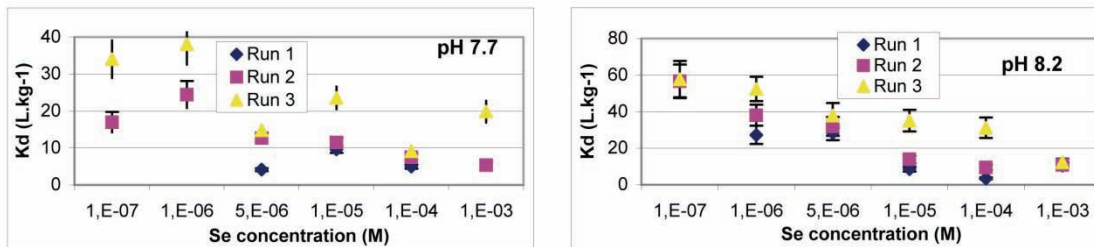
**Figure 8: Effect of pH on the distribution coefficient  $K_d$  ( $L.kg^{-1}$ ) in the range of concentration  $10^{-3} M - 10^{-7} M$  (calcite)**

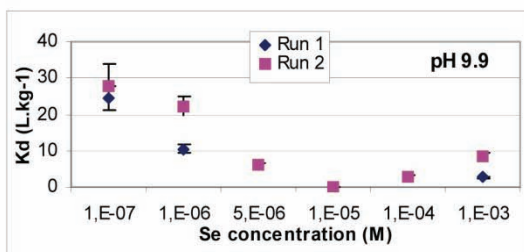
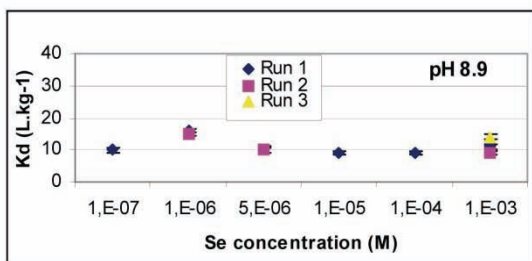


***$K_d$  evolution with Se concentration***

The  $K_d$  evolution as a function of Se concentration at various pH values is plotted in Figure 9. In the case of calcite, Figure 9 indicates that experiments with  $10^{-6}$  and  $10^{-7}$  M of Se show the highest  $K_d$  values regardless the pH, but did not an order of magnitude.

**Figure 9: The distribution coefficient of selenite  $K_d$  ( $L.kg^{-1}$ ) as a function of total selenite concentration and pH (calcite)**

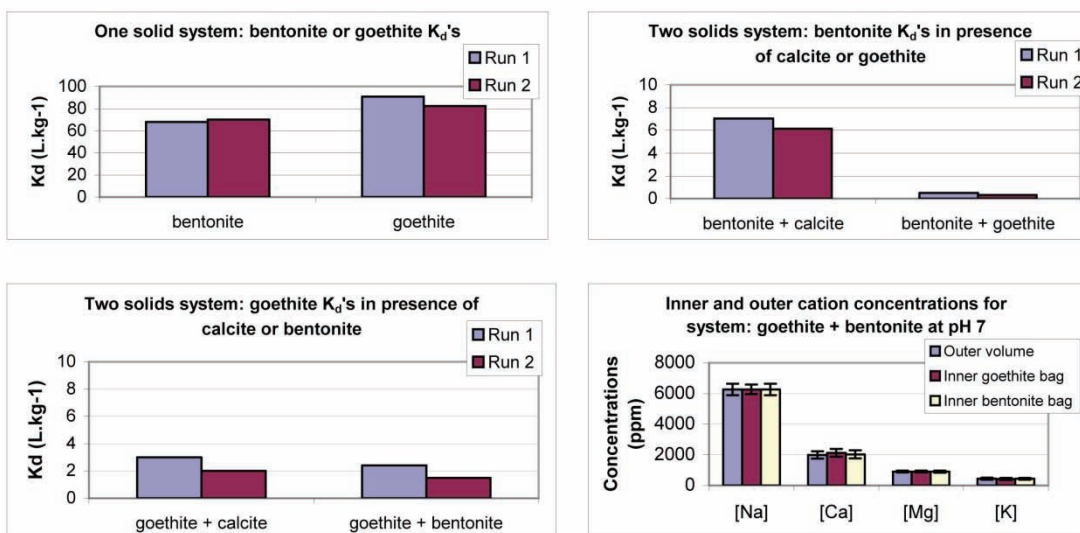




### Experiments with several components

In this part, we calculated  $K_d$  by the use of the radiotracer  $^{75}Se$ . A  $K_d$  was calculated for each component in the simplest system (one soil component) and another  $K_d$  was calculated for each component of the complex system (two soil components). For the simplest system, results of the experiments using radioactive selenium give similar values to those obtained by using stable selenium for pH near 7. Comparison of experimental  $K_d$  from the two types of system showed that goethite and bentonite  $K_d$  decreased when we added another soil component (Figure 10). So, it's means that there is a competition between cation/anion released by the component and selenite for sorption. Competition can, also, occur between cation/anion of the synthesized water and selenite for sorption on bentonite and goethite. The measure of cation concentrations in the several dialysis membrane show that the equilibrium is reached and so that this  $K_d$  decrease is not due to differences in inner and outer solution chemistry (Figure 10).

FIGURE 10: BENTONITE AND GOETHITE  $K_D$  IN SIMPLE AND COMPLEX SYSTEM



## Conclusions

We find same equilibrium time selenite-soil components and  $K_d$  as the literature but with the use of dialysis membranes. Thus we have shown that dialysis membrane does not have an effect on the sorption behaviour of selenite. Selenium concentration in solutions of bentonite and calcite suspensions in the range between  $10^{-3}$  and  $10^{-7}$  M were governed by adsorption reactions. Due to the prevalence of clays, calcite and iron oxides (like goethite), the sorption of selenite play an important role in distributing Se between solution and solid phases. This may play a significant role in Se mobility in surface and subsurface environment. Experiments with several soil components showed that the sorption behaviour of selenite on bentonite and goethite decreased. So, it is expected that the liquid phase containing ions released by soil components have an important effect on the ability of each component to sorb selenium, e.g. competition effects between ion and selenite.

## References

- [1] Boulton, K.A.; Cowper, M.M.; Heath, T.G.; Sato, H.; Shibutani, T.; Yui, M. *Journal of Contaminant Hydrology* **1998**, *35*, 141-150.
- [2] Parida, K.M.; Gorai, B.; Das, N.N.; Rao, S.B. *Journal of Colloid and Interface Science* **1997**, *185*, 355-362.
- [3] Su, C.; Suarez, D.L. *Soil Science Society of America Journal* **2000**, *64*, 101-111.
- [4] Balistrieri, L.S.; Chao, T.T. *Soil Science Society of America Journal* **1987**, *51*, 1145-1151.
- [5] Duc, M.; Lefevre, G.; Fedoroff, M.; Jeanjean, J.; Rouchaud, J.C.; Monteil-Rivera, F.; Dumonceau, J.; Milonjic, S. *Journal of Environmental Radioactivity* **2003**, *70*, 61-72.
- [6] Singh, M.; Singh, N.; Relan, P. S. *Soil Science* **1981**, *132*, 134 - 141.
- [7] Neal, R.H.; Sposito, G.; Holtzclaw, K.M.; Traina, S.J. *Soil Science Society of America Journal* **1987**, *51*, 1161-1165.
- [8] Goldberg, S.; Glaubig, R.A. *Soil Science Society of America Journal* **1988**.
- [9] Le Hécho, I.; Matera, V.; Gottelt, U.; Séby, F.; Bourg, A. "Etude de la rétention du sélénium et de l'étain par une bentonite Rapport d'avancement à l'ANDRA: étape2," LCABIE UMR 5034, 2001.
- [10] Howard, J.H. *Trace substances in environmental health* **1972**, *V*, 485 - 495.
- [11] Bar-Yosef, B.; Meek, D. *Soil Science* **1987**, *144*, 11-19.

## SYNTHESIS AND CHARACTERISATION OF TECHNETIUM POLYMERS

**F. Poineau<sup>1</sup>, A. Sattelberger<sup>2</sup>, K. Czerwinski<sup>1</sup>, M. Fattahi<sup>3</sup> and B. Grambow<sup>3</sup>**

<sup>1</sup>Harry Reid Center for Environmental Studies, UNLV, Las Vegas, United States

<sup>2</sup>Argonne National Laboratory, Lemont, USA

<sup>3</sup>Laboratoire Subatech, Nantes, France

### Abstract

The reaction between  $(n\text{-Bu}_4\text{N})_2\text{Tc}_2\text{Cl}_8$  and 1,3,4,6,7,8-Hexahydro-2H-Pyrimido[1,2-a]Pyrimidine (Hhpp) was conducted at 145°C under an argon atmosphere. The resulting product was studied by X-ray Absorption Fine Structure spectroscopy (XAFS) and cyclic voltammetry. EXAFS analysis indicate that the compound is polymeric and exhibits the core structure  $\{[\text{Tc}(\mu\text{-Cl})_2\text{Tc}](\text{hpp})_2\}$  where the Tc atoms are bridged by two chlorine atoms and two hpp ligands. In addition, a method for the synthesis of a solid containing the  $\text{Tc}_2\text{OCl}_{10}^{4-}$  anion was developed. The compound was synthesized in 3M chloride media,  $[\text{H}^+] = 0.5 \text{ M}$ , then extracted in dichloromethane and precipitated by evaporation of the solvent. The UV-vis spectrum of the compound dissolved in 3 M chloride exhibits the band at 606 nm, characteristic of the  $[\text{Tc-O-Tc}]^{6+}$  structure.

## Introduction

The co-ordination chemistry of Technetium quadruply bonded dimers is not well developed; currently, only five compounds are well-characterised. In contrast, the Rhenium dimers are much better studied. For example, fifteen dihalo-tetracarboxylato quadruply bonded Re dimers have been synthesized [1], while only three have been for Tc [2-3]. In many syntheses of Re quadruply bonded dimers,  $(n\text{-Bu}_4\text{N})_2\text{Re}_2\text{Cl}_8$  is used as a precursor. Previous studies [4-5] have shown that its reaction with Hhpp gives  $\text{Re}_2(\text{hpp})_4\text{Cl}_2$ .

The compound  $\text{Re}_2(\text{hpp})_4\text{Cl}_2$  is a typical paddlewheel quadruply bonded dimer. It exhibits one of the shortest Re-Re distances and the longest Re-Cl distance for this kind of compound. This complex was studied by UV-vis spectroscopy and cyclic voltammetry (CV) and its structure resolved by X-Ray Diffraction [4-5]. For Tc, paddlewheel complexes with the hpp ligand are still unknown. The first part of this work was to transpose to Tc the procedure used for  $\text{Re}_2(\text{hpp})_4\text{Cl}_2$  synthesis and to study the reaction product between  $(n\text{-Bu}_4\text{N})_2\text{Tc}_2\text{Cl}_8$  and Hhpp by XAFS spectroscopy and CV.

The second part of the work is related to the synthesis of a solid containing the  $\text{Tc}_2\text{OCl}_{10}^{4-}$  anion. A previous study [6] has shown that the speciation of Tc(IV) in chloride media is dominated by the species  $\text{Tc}_2\text{OCl}_{10}^{4-}$ . Crystalline compounds containing the anion  $\text{M}_2\text{OCl}_{10}^{4-}$  exist for a range of metals (M = Re, Ru, Os, W, Ta), while such compounds have until now been unknown for Tc. In the present work, a method for the synthesis of a  $\text{Tc}_2\text{OCl}_{10}^{4-}$  solid is described.

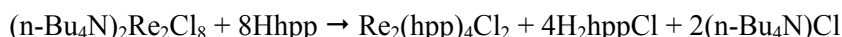
## Experimental

### *Preparation of $(n\text{-Bu}_4\text{N})_2\text{Tc}_2\text{Cl}_8$*

The compound was synthesized according to the method developed by Preetz *et al.* [7].

### *Preparation of $\text{Re}_2(\text{hpp})_4\text{Cl}_2$*

The compound was synthesized according to the method developed by Cotton *et al.* [4]. The compound was formed after ligand exchange between  $(n\text{-Bu}_4\text{N})_2\text{Re}_2\text{Cl}_8$  and melted Hhpp under Argon atmosphere according to the reaction:



### *Preparation of Tc-hpp*

The compound was obtained from the reaction between  $(n\text{-Bu}_4\text{N})_2\text{Tc}_2\text{Cl}_8$  and the melted Hhpp under Argon atmosphere. This method, involving ligand exchange, was chosen because it has been proven to be efficient for synthesis of Re paddlewheel quadruple bonded dimers [1] and then was expected to work also for Tc. A sample of 122 mg  $(n\text{-Bu}_4\text{N})_2\text{Tc}_2\text{Cl}_8$  was mixed

with 408 mg of Hhpp under an argon atmosphere. The mixture was dried under vacuum for 30 mn then heated at 145°C for 30 mn. At the end of the reaction, a brown solid was obtained; the compound was washed and centrifuged three times with acetonitrile, then washed with ether and dried under an argon atmosphere: 41 mg were obtained. Compound was insoluble in ether and acetonitrile and very soluble in acetone and CH<sub>2</sub>Cl<sub>2</sub>.

### ***Preparation of a solid containing the Tc<sub>2</sub>OCl<sub>10</sub><sup>4-</sup> anion***

The procedure developed for the synthesis of a solid containing the Tc<sub>2</sub>OCl<sub>10</sub><sup>4-</sup> anion was based on the method used by Preetz and co-workers [7] for the synthesis of (n-Bu<sub>4</sub>N)<sub>2</sub>TcCl<sub>6</sub>. A sample of 104.1 mg of (NH<sub>4</sub>)<sub>2</sub>TcCl<sub>6</sub> was dissolved in 30 ml of an aqueous solution of 3 M [Cl<sup>-</sup>] and 0.5 M [H<sup>+</sup>]. The solution was heated to 70°C for 36 hours under an argon atmosphere. The transformation was followed by UV-vis spectroscopy, and after 36 h, Tc<sub>2</sub>OCl<sub>10</sub><sup>4-</sup> was identified as the only Tc species in solution. The compound was extracted three times with 50 ml of a solution of dichloromethane containing 750 mg of (n-Bu<sub>4</sub>N)HSO<sub>4</sub>. After extraction, the green dichloromethane solution was cooled to 0°C and washed with 30 ml of ice cold water. The solution was dried over sodium sulfate and evaporated using a rotovap. After evaporation, 50 mg of a green solid were obtained. The compound was soluble in water and dichloromethane, insoluble in hexane and ether.

### ***XAFS measurements***

XAFS measurements were performed at the Advance Photon Source at the BESSRC-CAT 12 station. The sample was prepared by dilution of Tc-hpp with boron nitride (1%) and placed in special sample holder. The dilution ratio (1%) was chosen in order to minimize phenomena of self-absorption that can be observed in concentrated sample [8]. XAFS spectra were recorded at the Tc-K edge (21 044 eV) in fluorescence mode using a 13 element germanium detector. The energy was calibrated using a molybdenum foil. Four spectra were accumulated and averaged. The phase and amplitude function used for the adjustment were calculated by Feff8.2 using the atomic coordinates of Re<sub>2</sub>(hpp)<sub>4</sub>Cl<sub>2</sub><sup>+</sup> [5]. The adjustments of EXAFS spectra were performed under the constraints S<sub>0</sub><sup>2</sup> = 0.9, a single value of energy shift ΔE<sub>0</sub> was used. The uncertainty on the coordination number (C.N) was 20%, the uncertainty on the distance (R) was 0.02 Å.

### ***Other techniques***

UV-vis spectra were recorded at room temperature in 1 cm quartz cells on a Cary 6000i double beam spectrometer. Electrochemical measurements were performed on a CH 660B potentiostat from CH Instruments, Inc. Cyclic voltammetry experiments were carried out in CH<sub>2</sub>Cl<sub>2</sub> using 0.1 M (n-Bu<sub>4</sub>n)PF<sub>6</sub> as the support electrolyte. A silver wire was used as the reference electrode; platinum wire and glassy carbon were used as the counter and working electrodes, respectively.

## Results and discussion

### *Characterisation of Tc-hpp*

EXAFS study. The extracted EXAFS spectrum was  $k^2$ -weighted and the Fourier Transformation (FT) done in the  $k$ -range [3.5, 13.5]  $\text{\AA}^{-1}$ . The FT (Figure 1-1) exhibits three major peaks (A, B and C) between  $R + \Delta = [1, 3]$   $\text{\AA}$  which are characteristic of the first and second coordination shell around Tc atoms. In order to determine the contribution involved in the FT and to further characterise the core structure of the Tc-hpp compound, the fitting of the EXAFS spectra was done in two steps:

- i) The FT was decomposed in three regions: the first region between  $R + \Delta = [1; 1.7]$   $\text{\AA}$ , the second region between  $R + \Delta = [1.75; 2.18]$   $\text{\AA}$  and the third region between  $R + \Delta = [2.25; 2.80]$   $\text{\AA}$ ; each region was back transformed and independently analysed. Using the scattering previously determined in  $\text{Re}_2(\text{hpp})_4\text{Cl}_2^+$ , the EXAFS spectrum corresponding to each region was fitted in  $R$  space. Results indicate that peak A is characteristic of Tc-N scattering, peak B of Tc-Tc and Tc-Cl scattering and peak C of Tc-C scattering.
- ii) Using the contribution previously determined, the FT was fitted in  $R$  space between  $R + \Delta = [1; 3]$   $\text{\AA}$ . Adjustments of the FT and EXAFS are presented in Figure 1 and the structural parameters in Table 1. EXAFS analysis indicate that the first coordination shell around Tc consists of  $2 \pm 0.4$  nitrogen atoms at 2.02(2)  $\text{\AA}$ ,  $0.60 \pm 0.12$  Tc atoms at 2.46(2)  $\text{\AA}$ , and  $1.30 \pm 0.26$  Cl atoms at 2.36(2)  $\text{\AA}$ . While the second co-ordination shell around Tc consists of  $3.50 \pm 0.70$  carbon atoms at 3.04(2)  $\text{\AA}$ .

The presence of  $0.60 \pm 0.12$  Tc atoms at 2.46(2)  $\text{\AA}$  indicates that the Tc-hpp compound is polymeric. Since the typical metal-metal separation in Tc quadruply bonded dimmers varies between 2.147  $\text{\AA}$  and 2.192  $\text{\AA}$  [9], the Tc-Tc distance in Tc-hpp is not characteristic of a  $\text{Tc}\equiv\text{Tc}$  group but more of a  $[\text{Tc}(\mu\text{-L})_2\text{Tc}]$  ( $L = \text{Cl}$  or  $\text{O}$ ). The absence of a Tc-O bond and the presence of  $1.30 \pm 0.26$  Cl atoms at 2.36(2)  $\text{\AA}$  suggest that the chlorine atoms act as the bridging ligands. In this case, the Tc-hpp compound exhibits the  $[\text{Tc}(\mu\text{-Cl})_2\text{Tc}]$  group in its core structure. This group has already been described for  $\text{Tc}_2\text{Cl}_{10}^{2-}$  (Tc-Tc distance was not reported [10]).

EXAFS analysis also indicates the presence of two nitrogen atoms in the first co-ordination shell and 3.5 carbon atoms in the second coordination shell. This result is in accordance with the presence of two hpp ligands around the Tc atoms.

Considering the presence of the  $[\text{Tc}(\mu\text{-Cl})_2\text{Tc}]$  group and two hpp ligands around the Tc atoms, the core structure  $\{[\text{Tc}(\mu\text{-Cl})_2\text{Tc}](\text{hpp})_2\}$  is proposed. In this structure, the Tc atoms are simultaneously bridged by two chlorine atoms and two hpp ligands (Figure 2-1). This kind of geometry has already been proposed for Tc carboxylate dimers [11] where the Tc atoms are bridged by two oxygen atoms and two carboxylate ligands (figure 2-2).

Analysis of Tc-Tc and Tc-Cl distances indicate that the Tc-Cl-Tc angle ( $\sim 60^\circ$ ) is smaller than those reported for compounds with a  $[\text{M}(\mu\text{-Cl})_2\text{M}]$  structure (for  $\text{M}=\text{Re}$ ,  $\text{Re-Cl-Re} \sim 85^\circ$  [12]). This phenomenon can be due to the presence of the two hpp ligands that can influence the

Tc-Tc separation and then the Tc-Cl-Tc angle. Typically, the hpp ligand can bridge metals that are separated by  $d_{M-M} = 2.19 \text{ \AA} - 2.44 \text{ \AA}$  [13], these distances are smaller than the Tc-Tc distance usually observed in compound with a  $[\text{Tc}(\mu\text{-L})_2\text{Tc}]$  structure [14]. Then, in  $[\text{Tc}(\mu\text{-L})_2\text{Tc}]$ , a bridging of Tc atoms by hpp should lead to decrease of the Tc-Tc distance and the Tc-Cl-Tc angle.

Also, the co-ordination number of Tc and Cl around the Tc absorbing atom indicates that the compound is a small polymer but not an infinite chain constituted of  $-\{[\text{Tc}(\mu\text{-Cl})_2\text{Tc}](\text{hpp})_2\}-$  group. In the last case, the coordination number of Tc should be 2 and the CN of Cl should be 4. Nevertheless, the co-ordination numbers are slightly lower than those that should be theoretically observed for a dimer (respectively, 1 and 2). This phenomenon has already been observed for Tc dimer. Recent EXAFS measurements on  $(\text{n-Bu}_4\text{N})_2\text{Tc}_2\text{Cl}_8$  indicates that the first coordination shell around the absorbing atom is constituted by 0.6 Tc atom at  $2.16 \text{ \AA}$ . This CN is lower than the theoretical one but the reason is still not elucidated.

**Table 1: Structural parameters obtained by adjustment of the  $k^2$ -EXAFS spectra of Tc-hpp. Adjustment between  $k = [3.5, 13.5] \text{ \AA}^{-1}$**

Compound	Scattering	Structural parameter		
		C.N	R ( $\text{\AA}$ )	$\sigma^2$
Tc-hpp	Tc-N	$2 \pm 0.40$	2.02(2)	0.0020
	Tc-Tc	$0.60 \pm 0.12$	2.46(2)	0.0080
	Tc-Cl	$1.30 \pm 0.26$	2.36(2)	0.0066
	Tc-C	$3.50 \pm 0.70$	3.04(2)	0.0036

**Figure 1-1: Fourier transform of Tc-hpp  $k^2$ -EXAFS spectra.  $k = [3.5, 13.5] \text{ \AA}^{-1}$ , 1-2:  $k^2$ -EXAFS spectra, 1-3: Fitted  $k^2$ -EXAFS of Fourier Transform between  $R + \Delta = [1, 3] \text{ \AA}$  and 1-4: Fitted Fourier transform between  $R + \Delta = [1, 3] \text{ \AA}$ .**

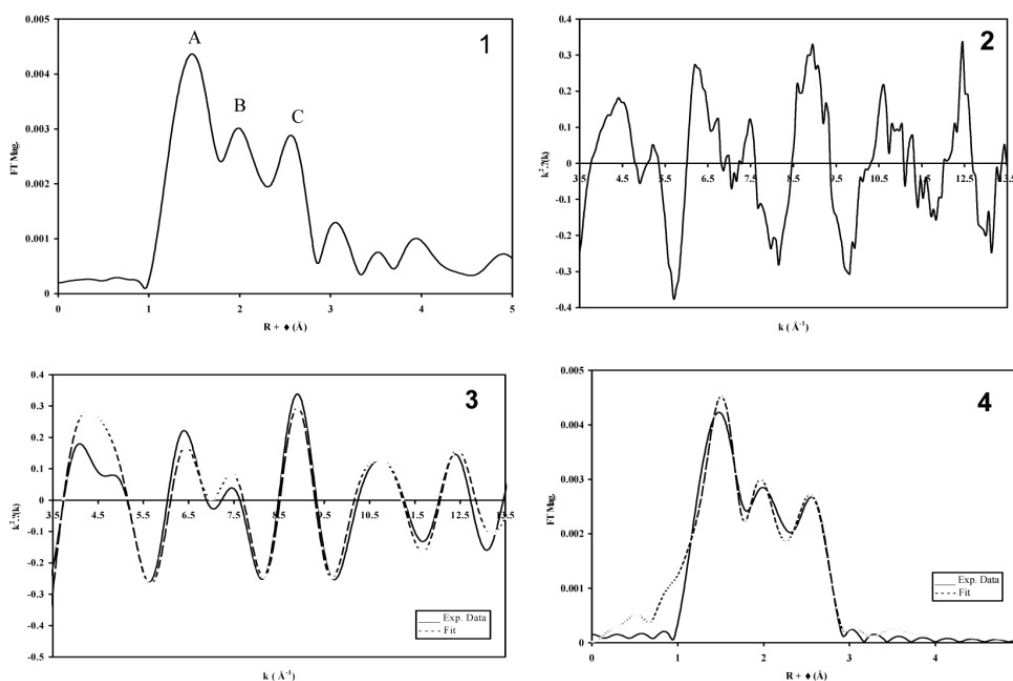
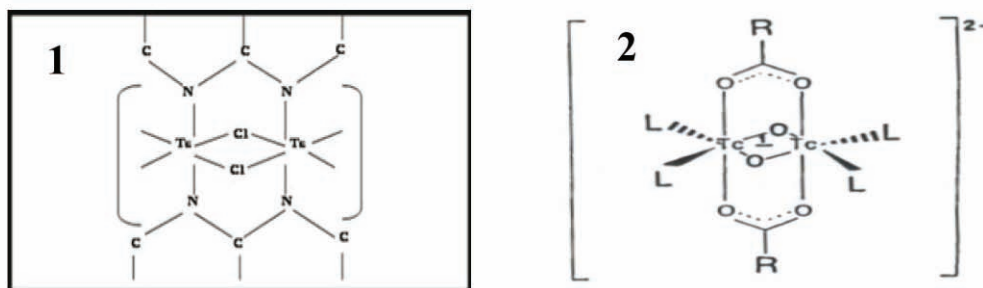


**Figure 2-1: Core structure of Tc-hpp determined from EXAFS study and 2-2: Core structure of Tc carboxylate dimer from Ref. [11]**

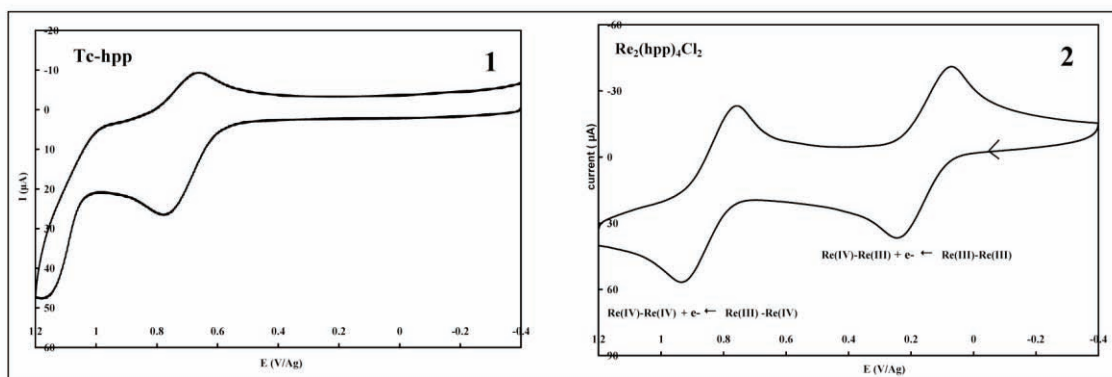


Cyclic voltammetry study. A solution of 0.005 M [Tc-hpp] in  $\text{CH}_2\text{Cl}_2$  / 0.1 M (n-Bu<sub>4</sub>N)PF<sub>6</sub> was synthesized and transferred to an electrochemical cell. The cyclic voltammetry experiment was conducted between  $E = -400$  mV and  $E = 1200$  mV at a scan rate of  $300 \text{ mV}\cdot\text{s}^{-1}$ . The cyclic voltammogram (Figure 3-1) exhibits one wave centered at 729 mV/Ag and the separation between the anodic and cathodic peak is 140 mV/Ag. In the same experimental condition, for the  $\text{Cp}_2\text{Fe}/\text{Cp}_2\text{Fe}^+$  couple, the separation is 210 mV/Ag. For  $\text{Re}_2(\text{hpp})_4\text{Cl}_2$ , the cyclic voltammetry was performed under the same conditions as for Tc-hpp.

The cyclic voltammogram of Tc-hpp is not characteristic of a  $\text{M}_2(\text{hpp})_4\text{Cl}_2$  compound ( $M = \text{Re}, \text{Ru}, \text{Os}$ ). For those compounds [4, 15-16], the cyclic voltammogram exhibits two waves, that correspond to the successive reactions:  $\text{M(III)}/\text{M(III)} \rightarrow \text{M(IV)}/\text{M(III)} \rightarrow \text{M(IV)}/\text{M(IV)}$ . For  $\text{Re}_2(\text{hpp})_4\text{Cl}_2$ , the cyclic voltammogram (figure 3-2) exhibits two waves, respectively centered at 845 mV and 156 mV. According to [4], the wave centered at 845 mV is related to the transformation  $\text{Re}^{\text{III}}\text{Re}^{\text{III}}(\text{hpp})_4\text{Cl}_2 \rightarrow \text{Re}^{\text{IV}}\text{Re}^{\text{III}}(\text{hpp})_4\text{Cl}_2^+$  and the wave at 156 mV to  $\text{Re}^{\text{III}}\text{Re}^{\text{IV}}(\text{hpp})_4\text{Cl}_2^+ \rightarrow \text{Re}^{\text{IV}}\text{Re}^{\text{IV}}(\text{hpp})_4\text{Cl}_2^{2+}$ .

Comparison of the  $\text{Re}_2(\text{hpp})_4\text{Cl}_2$  and Tc-hpp cyclic voltammogram indicates that the Tc-hpp wave and the wave relative to the  $\text{Re(IV)}/\text{Re(III)} \rightarrow \text{Re(IV)}/\text{Re(IV)}$  reaction are in the same domain of potential. Thus for Tc-hpp, the wave can be assigned to a  $\text{Tc(IV)}/\text{Tc(III)} \rightarrow \text{Tc(IV)}/\text{Tc(IV)}$  reaction; in this case, the couple involved in the reaction is  $\{[\text{Tc}(\mu\text{-Cl})_2\text{Tc}(\text{hpp})_2]^{4+} / [\text{Tc}(\mu\text{-Cl})_2\text{Tc}(\text{hpp})_2]^{3+}$ .

**Figure 3-1: Cyclic voltammogram of Tc-hpp and 3-2 of  $\text{Re}_2(\text{hpp})_4\text{Cl}_2$  in  $\text{CH}_2\text{Cl}_2$ . Referenced to Ag, scan rate  $300 \text{ mV}\cdot\text{s}^{-1}$ . Electrolyte support  $0.1 \text{ M } (\text{n-Bu}_4\text{n})\text{PF}_6$**

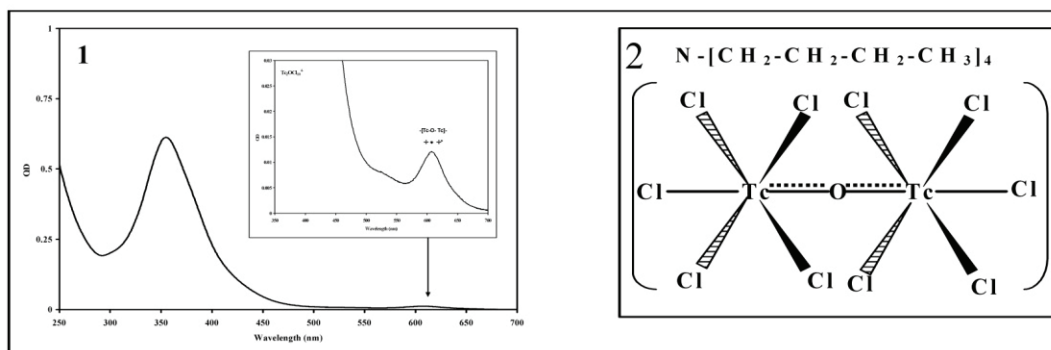


In conclusion of this first part, the reaction product between  $(\text{n-Bu}_4\text{N})_2\text{Tc}_2\text{Cl}_8$  and Hhpp was not the quadruple bonded dimer  $\text{Tc}_2(\text{hpp})_4\text{Cl}_2$  as expected by analogy with Re but a compound with a core structure  $\{[\text{Tc}(\mu\text{-Cl})_2\text{Tc}](\text{hpp})_2\}$ . The Tc-hpp compound exhibits the group  $\text{Tc}(\mu\text{-Cl})_2\text{Tc}$  which is also observed in  $\text{M}_2\text{Cl}_{10}^{2-}$  ( $\text{M} = \text{Tc, Re}$ ). Further analysis of literature indicates that many Tc(IV) and Re(IV) halogeno and oxy-halogeno compounds exhibit similar structure [17-18]. Nevertheless, for Re the compound  $\text{K}_4\text{Re}_2\text{OCl}_{10}$  is well known and characterised while for Tc a solid containing the  $\text{Tc}_2\text{OCl}_{10}^{4-}$  anion is still unknown. In the second part of this study, the compound previously synthesized and supposed to contain the  $\text{Tc}_2\text{OCl}_{10}^{4-}$  anion is characterised by UV-Vis spectroscopy.

### ***Characterisation of the solid containing the $\text{Tc}_2\text{OCl}_{10}^{4-}$ anion***

A fraction of the green solid was dissolved in  $3\text{M } [\text{Cl}^-]$ ,  $0.5\text{M } [\text{H}^+]$  and the solution analyzed by UV-vis spectroscopy. The spectrum (figure 4-1), which exhibits two bands at 354 nm and 606 nm, is identical to the UV-vis spectrum of  $\text{Tc}_2\text{OCl}_{10}^{4-}$  described in the literature [6]. Previous studies [6, 19] on  $\text{Tc}_2\text{OCl}_{10}^{4-}$  have shown that the band at 606 nm is characteristic of the  $[\text{Tc-O-Tc}]^{6+}$  structure, then during the extraction and evaporation of  $\text{Tc}_2\text{OCl}_{10}^{4-}$  in dichloromethane, the core structure is conserved. Also, during the evaporation of the solvent, only two species are present in solution:  $(\text{n-Bu}_4\text{N})^+$  and  $\text{Tc}_2\text{OCl}_{10}^{4-}$ , then the precipitation of  $(\text{n-Bu}_4\text{N})_4\text{Tc}_2\text{OCl}_{10}$  is expected (figure 4-2). Nevertheless, chemical analysis needs to be done in order to confirm the stoichiometry.

**Figure 4-1: UV-vis spectrum of the solution obtained by dissolution in 3M [Cl<sup>-</sup>], 0.5M [H<sup>+</sup>] of the solid formed after extraction and evaporation of Tc<sub>2</sub>OCl<sub>10</sub><sup>4-</sup> in CH<sub>2</sub>Cl<sub>2</sub>**  
**4-2: Representation of the (n-Bu<sub>4</sub>N)<sub>4</sub>Tc<sub>2</sub>OCl<sub>10</sub> solid.**



## Conclusions

XAFS measurements have permitted the characterization of the compound obtained from the reaction between (n-Bu<sub>4</sub>N)<sub>2</sub>Tc<sub>2</sub>Cl<sub>8</sub> and Hhpp at 145°C under an argon atmosphere. The compound was not the expected quadruply bonded dimer Tc<sub>2</sub>(hpp)<sub>4</sub>Cl<sub>2</sub>, but a polymer with the core structure {[Tc(μ-Cl)<sub>2</sub>Tc](hpp)<sub>2</sub>}; in this structure, the Tc atoms are bridged by two chlorine atoms and two hpp ligands. The cyclic voltammogram of the compound exhibits one wave centered at 729 mV/Ag that can involve the couple {[Tc(μ-Cl)<sub>2</sub>Tc](hpp)<sub>2</sub>}<sup>4+</sup>/[Tc(μ-Cl)<sub>2</sub>Tc](hpp)<sub>2</sub><sup>3+</sup>. In order to further investigate the formation of Tc<sub>2</sub>(hpp)<sub>4</sub>Cl<sub>2</sub>, the complex Tc<sub>2</sub>(O<sub>2</sub>CCH<sub>3</sub>)<sub>4</sub>Cl<sub>2</sub> can be used as precursor; its reaction with Hhpp can be performed at 145°C under an argon atmosphere and the reaction product studied by XAFS spectroscopy and cyclic voltammetry.

A method for synthesis of a solid containing the Tc<sub>2</sub>OCl<sub>10</sub><sup>4-</sup> anion has been developed. A green solid was obtained after extraction and evaporation of Tc<sub>2</sub>OCl<sub>10</sub><sup>4-</sup> in a CH<sub>2</sub>Cl<sub>2</sub>/ (n-Bu<sub>4</sub>N)HSO<sub>4</sub> solution. The UV-vis spectrum of the solution obtained by dissolution of the compound was identical to the Tc<sub>2</sub>OCl<sub>10</sub><sup>4-</sup> spectrum and (n-Bu<sub>4</sub>N)<sub>4</sub>Tc<sub>2</sub>OCl<sub>10</sub> was expected to be the reaction product. Nevertheless, the stoichiometry of the compound needs to be confirmed. In order to extend the coordination chemistry of Tc(IV) polymers, (n-Bu<sub>4</sub>N)<sub>4</sub>Tc<sub>2</sub>OCl<sub>10</sub> could be used as a precursor for the synthesis of new compounds, such as (n-Bu<sub>4</sub>N)<sub>4</sub>Tc<sub>2</sub>OBr<sub>10</sub> or (n-Bu<sub>4</sub>N)<sub>4</sub>Tc<sub>2</sub>O(SCN)<sub>10</sub>.

## Acknowledgements

Use of the Advanced Photon Source was supported by the U.S. Department of Energy, Office of Science, Office of Basic Energy Sciences, under Contract No. DE-AC02-06CH11357.

## REFERENCES

- [1] Cotton, F.A.; Oldham, C.; Robinson, W.R., *Inorganic chemistry* (1966), 5(10), 1798
- [2] Skowronek, J.; Preetz, W., *Zeitschrift fuer Naturforschung, B: Chem. Sc.* (1992), 47(4), 482
- [3] Cotton, F. A.; Gage, L. D. *Nouveau Journal de Chimie* (1977), 1(6), 441
- [4] Cotton, F. A.; Gu, J.; Murillo, C.A.; Timmons, D.J. *Journal of the Chemical Society, Dalton Transactions: Inorganic Chemistry* (1999), (21), 3741
- [5] Berry, J.F.; Cotton, F.A.; Huang, P.; Murillo, C.A. *Dalton Transactions* (2003), (7), 1218
- [6] Poineau, F.; Fattahi, M.; Montavon, G.; Grambow, B., *Radiochimica Acta* (2006), 94(5), 291
- [7] Preetz, W.; Peters, G.; Bublitz, D., *Journal of Cluster Science* (1994), 5(1), 83
- [8] Tröger, L., D. Arvanitis, K. Baberschke, H. Michaelis, U. Grimm and E. Zschech (1992). *Physical Review B* 46, 3283
- [9] Sattelberger, A.P. *Multiple Bonds between Metal Atoms* (3<sup>rd</sup> Edition) (2005), 251
- [10] Wendt, A.; Preetz, W., *Zeitschrift fuer Anorganische & Allgemeine Chem* (1994), 620(4), 655
- [11] Kennedy, C.M.; Pinkerton, T.C., *International journal of radiation applications and instrumentation. Part A, Applied radiation and isotopes* (1988,) 11, 1167
- [12] Mucker, K.D.;Smith, G.S.; Johnson, Q. *Acta Crystallographica B*.(1968), 24, 874
- [13] Clerac, R.; Cotton, F.A.; Daniels, L.M.; Donahue, J.P.; Murillo, C.A.; *Inorganic Chemistry* (2000), 39(12), 2581
- [14] Schwochau, K., *Technetium: Chemistry and Radiopharmaceutical Applications* (Wiley-VCH, Weinheim, 2000).
- [15] Bear, J.L.; Li, Y.; Han, B.; Kadish, K.M., *Inorganic Chemistry* (1996), 35(5), 1395
- [16] Cotton, F.A.; Dalal, N.S.; Huang, P.; Murillo, C.A.; Stowe, A.C.; Wang, X., *Inorganic chemistry* (2003), 42(3), 670
- [17] Rouschias, G., *Chemical Reviews* (1974), 74(5), 531
- [18] Rard, J.A., *Journal of Nuclear and Radiochemical Sciences* (2005), 6(3), 197
- [19] Poineau, F.; Fattahi, M.; Grambow, B., *Radiochimica Acta* (2006), 94(2), 91



## DETERMINATION OF THE SOLUBILITY LIMITING SOLID OF SELENIUM IN THE PRESENCE OF IRON UNDER ANOXIC CONDITIONS\*

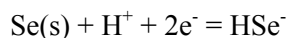
Yoshihisa Iida\*, Tetsuji Yamaguchi, Tadao Tanaka, Akira Kitamura  
and Shinichi Nakayama

Japan Atomic Energy Agency, Japan

\*This paper is a part of a study funded by the Japanese Ministry of Economy, Trade and Industry.

### Abstract

Dissolution experiments of selenium were performed from both under saturation and over saturation directions to determine the solubility limiting solid of selenium under the conditions which thermodynamically prefer the formation of ferroselite (FeSe<sub>2</sub>). X-ray diffractometry (XRD) showed that FeSe<sub>2</sub> was formed in the oversaturation experiments. However, the ion activity products for the reaction of  $0.5\text{FeSe}_2 + \text{H}^+ + \text{e}^- = 0.5\text{Fe}^{2+} + \text{HSe}^-$ ,  $a_{\text{Fe}^{2+}}^{0.5} a_{\text{HSe}^-} a_{\text{H}^+}^{-1} a_{\text{e}^-}^{-1}$ , obtained from both under saturation and over saturation directions were 3 to 4 orders of magnitude higher than the equilibrium constants calculated from existing thermodynamic data. The dependencies of the selenium concentration on pH, Eh and the iron concentration were better interpreted as a dissolution reaction of selenium solid (Se(s)) than the iron-selenium compounds. The equilibrium constant of :



was determined to be  $\log K^0 = -7.46 \pm 0.11$ . This value agrees with the value of  $\log K^0 = -7.62 \pm 0.06$  calculated from existing thermodynamic data of crystalline selenium within errors. Because crystalline selenium was not identified in the solid phases by XRD, the solubility limiting solid would be amorphous or minor amount of crystalline selenium, even if the iron-selenium compound was formed.

## Introduction

Selenium-79 ( $^{79}\text{Se}$ ) is a long-lived fission product with a half-life of  $2.95 \times 10^5$  year [1]. Performance assessment calculations [2] for a hypothetical high-level radioactive waste (HLW) repository show that  $^{79}\text{Se}$  is one of the radionuclides that dominates long-term radiological hazard. Because aqueous species of selenium are usually anionic species such as  $\text{HSe}^-$ ,  $\text{SeO}_3^{2-}$  and  $\text{SeO}_4^{2-}$ , retardation of selenium migration by sorption in the engineered and natural barrier systems is scarcely expected. Therefore, flux of  $^{79}\text{Se}$  may only be limited by solubility of its compounds. Since chemical conditions in deep underground environments are likely to be anoxic and reducing, solubility limiting solids for selenium are likely to be compounds with iron, copper or lead as can be observed from natural analogue systems. [3, 4]. In the disposal environments, ferrous ion ( $\text{Fe}^{2+}$ ) probably dissolves into groundwater from iron compounds such as pyrite ( $\text{FeS}_2$ ) in bentonite buffer materials, overpack and its corrosion products. Therefore the solubility of selenium was expected to be limited by precipitation of  $\text{FeSe}_2$  [2, 3] in the performance assessment calculations for HLW repositories, based on geochemical calculations and the chemical analogy with sulfur. Azuma *et al.* [5] showed that the aqueous concentration of selenium was decreased by several orders of magnitude by precipitation of  $\text{FeSe}_2$  compared to crystalline selenium ( $\text{Se}(\text{cr})$ ) in disposal environments. However, the low concentrations of selenium have not been observed in laboratory dissolution experiments in the presence of iron till now [6-8]. Therefore uncertainties still remain in our estimation of the solubility limiting solid of selenium.

In this study, we have performed dissolution experiments of selenium in the presence of iron under anoxic conditions to determine the solubility limiting solid of selenium. The experiments were performed under the conditions under which  $\text{FeSe}_2$  was the thermodynamically stable solid phase to examine if  $\text{FeSe}_2$  limits the concentration of selenium.

## Experimental

### *Stock solutions*

Stock solutions were prepared in a controlled atmosphere glove box under argon ( $\text{O}_2 < 1$  ppm).  $\text{Se}(\text{-II})$  stock solution was prepared by the following procedure. An appropriate amount of powdered metallic selenium (Wako Pure Chemical Ind. Ltd.) was soaked in a sodium hydroxide solution ( $\text{NaOH}$ ,  $0.01 \text{ mol dm}^{-3}$ ) for 7 days in a polypropylene test tube to remove soluble impurities such as  $\text{SeO}_2$ . Three grams of washed powdered selenium was dissolved in a  $1 \text{ cm}^3$  volume of 98 % hydrazine monohydrate ( $\text{N}_2\text{H}_4 \cdot \text{H}_2\text{O}$ ) and diluting it with a  $39 \text{ cm}^3$  volume of  $1 \text{ mol dm}^{-3}$   $\text{NaOH}$  solution [9]. The pH of the selenium solution was adjusted to 6 with a hydrochloric acid ( $\text{HCl}$ ). The selenium solution was filtered through  $0.45 \mu\text{m}$  filter (Millipore) to remove the precipitate of selenium and diluted with distilled deionized water (WT-100U, Yamato Scientific Co., Ltd) to adjust the ionic strength to  $0.1 \text{ mol dm}^{-3}$ .

$\text{Fe}(\text{II})$  stock solution was prepared by using powdered metallic iron (Rare Metallic Co., Ltd) without using a reagent of iron dichloride ( $\text{FeCl}_2$ ) to prevent a contamination of ferric ion ( $\text{Fe}^{3+}$ ) in the solution. Three grams of powdered metallic iron were dissolved in  $39 \text{ cm}^3$  of

2 mol dm<sup>-3</sup> HCl solutions. After a day, the color of the solution turned blue by the formation of ferrous ion (Fe<sup>2+</sup>), the solution was filtered through 0.45µm filter to remove the unreacted powdered iron. One cm<sup>3</sup> of 98 % N<sub>2</sub>H<sub>4</sub>•H<sub>2</sub>O was added to the solution and the pH was adjusted to the same value as the Se(-II) stock solution with a NaOH solution, to prevent precipitation of selenium solid (Se(s)) by change of pH or Eh when Se(-II) and Fe(II) stock solutions were mixed. The solution was filtered through 0.45µm filter to remove the white precipitate of ferrous hydroxide (Fe(OH)<sub>2</sub>) [10] and diluted with distilled deionized water to adjust the ionic strength to 0.1 mol dm<sup>-3</sup>.

### ***Dissolution experiments***

Dissolution experiments of selenium were performed from both undersaturation and oversaturation directions at 25°C, 45°C and 60°C. The temperatures at 45°C and 60°C were set to simulate temperature in a disposal environment [2] and to promote generation of iron-selenium compounds [7]. Sodium chloride (NaCl) was used as ionic strength adjuster and N<sub>2</sub>H<sub>4</sub>•H<sub>2</sub>O was used as a reducing agent. All the experiments were performed in 50 cm<sup>3</sup> polypropylene centrifuge tubes in the controlled atmosphere glove box under argon and the tubes were agitated once a day. The sample tubes for the experiments at 45°C and 60°C were placed in constant temperature ovens. The equilibration period was 240 days.

The oversaturation experiments were carried out by mixing 10 cm<sup>3</sup> volume of Fe(II) and Se(-II) stock solutions which had been maintained at desired temperature of 25°C, 45°C or 60°C. After a week, a part of the precipitate was removed for analysis by powder X-ray diffraction with cobalt tube (XRD, Rigaku Co., Ltd).

Two types of solids were used in the undersaturation experiments, one was a precipitate formed by the oversaturation method at 60°C (self-assembled precipitate) and the other was a commercial reagent of FeSe<sub>6</sub> (Mitsuwa Chemical Co., Ltd) (purchased reagent). Prior to the start of the experiments, 1 gram of above mentioned solids were washed with 0.1 mol dm<sup>-3</sup> N<sub>2</sub>H<sub>4</sub>•H<sub>2</sub>O solution and a part of the solid was removed for XRD analysis. The N<sub>2</sub>H<sub>4</sub>•H<sub>2</sub>O solution was then replaced by 40 cm<sup>3</sup> of a solution consisting of 0.1 mol dm<sup>-3</sup> NaCl and 0.05 mol dm<sup>-3</sup> N<sub>2</sub>H<sub>4</sub>•H<sub>2</sub>O.

### ***Analyses***

After 240-day, the pH and Eh of the sample suspensions were measured at room temperature. The pH was measured with a ROSS combination glass electrode (Thermo Fisher Scientific Inc.) calibrated with standard pH buffer solutions of 4, 7 and 10, and the Eh was measured with a platinum electrode after checking with saturated quinhydrone solutions. A 2 cm<sup>3</sup> aliquot was sampled from the suspensions and ultrafiltered through 10 000 NMWL (nominal molecular weight limit) regenerated cellulose filter (Millipore Co.) after filtering a small amount of sample solution for preconditioning. The filtration was performed at room temperature, since the available filters were not applicable for filtrations at 45°C and 60°C. One cm<sup>3</sup> was taken out of the grove box and oxidized by adding a 2 or 3 cm<sup>3</sup> volume of 30% hydrogen peroxide (H<sub>2</sub>O<sub>2</sub>) to prevent precipitation and volatilisation of selenium. After diluting

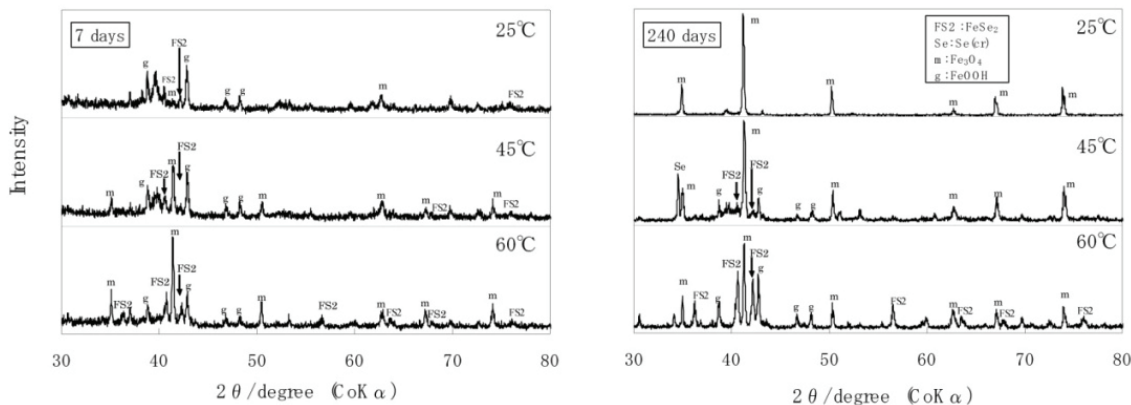
the solution with 10 cm<sup>3</sup> 3% nitric acid, the concentrations of selenium and iron were determined by inductively coupled plasma mass spectrometry (ICP-MS, JMS-PLASMAX2, JEOL Ltd.). The detection limit was 10<sup>-9</sup> mol dm<sup>-3</sup> for selenium and 10<sup>-7</sup> mol dm<sup>-3</sup> for iron. The remaining solution was used to analyse aqueous selenium species by UV-Vis spectrometry (JASCO, V-570). At the end of the equilibration period, part of the solid phase was taken and dried at 60°C in the controlled atmosphere glove box, taken out of the glove box and analysed by XRD in atmospheric condition for all the samples.

## ***Results and discussion***

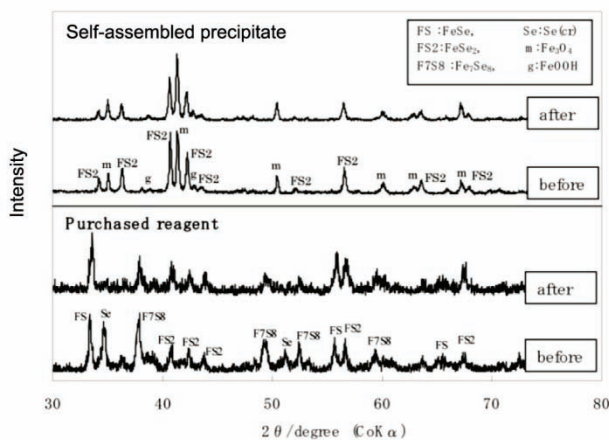
Figure 1 shows the XRD patterns of the solid phases obtained from the oversaturation experiments after 7 days and 240 days of aging. The solid phases after 7 days of aging were identified as ferroselite (FeSe<sub>2</sub>), magnetite (Fe<sub>3</sub>O<sub>4</sub>) and goethite (FeOOH) at all temperatures. Goethite would have been generated by oxidation of Fe(OH)<sub>2</sub> soon after taking the solid phase out of the glove box. After 240-day equilibration, the peaks of FeSe<sub>2</sub> grew at 60°C, Se(cr) was identified in addition to the above mentioned solid phases at 45°C, and the peaks of only Fe<sub>3</sub>O<sub>4</sub> were observed at 25°C. Therefore, FeSe<sub>2</sub> and Se(cr) were recognized as candidates of the solubility limiting solid. The difference in the solid phases with temperature might be caused by slow crystallisation kinetics of Se and FeSe<sub>2</sub>.

Figure 2 shows the XRD patterns of the solid phases obtained from the undersaturation experiments before and after the experimental period at 25°C. The same patterns were observed in the solids at 45°C and 60°C. In the systems using the self-assembled precipitates as the initial solids, the solid phases were identified as FeSe<sub>2</sub>, Fe<sub>3</sub>O<sub>4</sub> and FeOOH before and after the experimental period. In the systems using the purchased reagents as the initial solids, peaks of FeSe<sub>2</sub>, Fe<sub>7</sub>Se<sub>8</sub>, FeSe and Se(cr) were observed in the solid before the experimental period. After 240-day equilibration, the peaks of Se(cr) disappeared, the peaks of Fe<sub>7</sub>Se<sub>8</sub> weakened and the peaks of FeSe<sub>2</sub> grew. The change of these peaks indicates that Se(cr) and Fe<sub>7</sub>Se<sub>8</sub> would change to thermodynamically stable FeSe<sub>2</sub>, by the reaction of  $6\text{Se}(\text{cr}) + \text{Fe}_7\text{Se}_8 = 7\text{FeSe}_2$ . From these results, FeSe<sub>2</sub> was recognised as candidates of the solubility limiting solid.

**Figure 1: XRD patterns of the solid phases obtained from oversaturation experiments after 7 days (left) and 240 days aging (right). The solid phases after 7 days aging were identified as ferroselite (FS2: FeSe<sub>2</sub>), magnetite (m: Fe<sub>3</sub>O<sub>4</sub>) and goethite (g: FeOOH) at all temperatures. After 240-day equilibration, the peaks of FeSe<sub>2</sub> grew at 60°C, Se(cr) was identified in addition to the above mentioned solid phases at 45°C, and the peaks of only Fe<sub>3</sub>O<sub>4</sub> were observed at 25°C.**



**Figure 2: XRD patterns of the solid phases obtained from undersaturation experiments before and after equilibration. In the system using the self-assembled precipitates (upper), FeSe<sub>2</sub>, Fe<sub>3</sub>O<sub>4</sub> and FeOOH were identified before and after equilibration. In the system using the purchased reagents (lower), the peaks of FeSe<sub>2</sub>, Fe<sub>7</sub>Se<sub>8</sub>, FeSe and Se(cr) were observed before equilibration, but the peaks of Se(cr) disappeared after 240-day equilibration.**



Experimental data of the sample solutions are summarised in Table 1. Low pe values of the sample solutions show that the reducing agent was effective enough to prevent oxidation during the experimental period. The experimental conditions are plotted on pH-pe diagrams for the system Se-O-H and Se-Fe-O-H shown in Figure 3. The experimental conditions thermodynamically prefer the formation of FeSe<sub>2</sub> (Figure 3(b)). UV-Vis spectra of the sample solutions from undersaturation direction exhibit absorption bands at 247 nm and 377 nm as shown in Figure 4. These peaks were assigned to HSe<sup>-</sup> and Se<sub>4</sub><sup>2-</sup>, respectively [11, 12]. Peaks assigned to any Se species were not detected in spectra of the sample solutions from oversaturation direction because of low Se concentration.

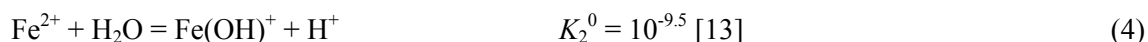
The ion activity products ( $Q$ ) were estimated for the dissolution reaction of  $\text{FeSe}_2$  which was identified in the solids by XRD. The dissolution reaction of  $\text{FeSe}_2$  can be described as,



$$K_1^0 = a_{\text{Fe}^{2+}}^{0.5} \cdot a_{\text{HSe}^-} \cdot a_{\text{H}^+}^{-1} \cdot a_{\text{e}^-}^{-1} \quad (2)$$

The activities of  $\text{Fe}^{2+}$  and  $\text{HSe}^-$ ,  $a_{\text{Fe}^{2+}}$  and  $a_{\text{HSe}^-}$ , were determined from the total concentrations of these elements and the equilibrium constants between major species by using following equations.

$$[\text{Fe}]_{\text{tot}} = [\text{Fe}^{2+}] + [\text{Fe}(\text{OH})^+] = (a_{\text{Fe}^{2+}}) / (\gamma_{\text{Fe}^{2+}}) + (a_{\text{Fe}(\text{OH})^+}) / (\gamma_{\text{Fe}(\text{OH})^+}) \quad (3)$$



$$[\text{Se}]_{\text{tot}} = [\text{HSe}^-] + 4[\text{Se}_4^{2-}] = (a_{\text{HSe}^-}) / (\gamma_{\text{HSe}^-}) + 4(a_{\text{Se}_4^{2-}}) / (\gamma_{\text{Se}_4^{2-}}) \quad (5)$$



The activity coefficient ( $\gamma$ ) was calculated by using the extended Debye-Hückel limiting law [15]. The ion activity products shown as equation (2) obtained from the experiments at 25°C were calculated to be ranging between 10-5.4 and 10-4.3 (Table 1).

**Table 1. Measured selenium and iron concentration from under- and oversaturation directions after 240-day equilibration in 0.1 mol dm<sup>-3</sup> - NaCl / 0.05 mol dm<sup>-3</sup> - N<sub>2</sub>H<sub>4</sub> solutions, and the ion activity products ( $Q$ ) for the reaction (1).**

Sample		Temp. °C	pH	pe	[Se] (mol dm <sup>-3</sup> )	[Fe] (mol dm <sup>-3</sup> )	log $Q$
Stock solution	Fe(II)		5.96	-5.1	-	2.36E-01*	
	Se(-II)		6.57	-6.3	5.38E-03	-	
Undersaturation	Purchased reagent	25	9.17	-5.3	4.68E-05	1.54E-05	-4.7
			9.61	-6.1	2.34E-04	9.43E-06	-4.3
		45	9.30	-6.8	3.81E-03	2.81E-06	-3.9
			9.41	-5.2	3.45E-05	1.12E-05	-4.9
		60	9.21	-5.2	7.09E-05	6.15E-05	-4.4
	9.11		-5.2	2.44E-05	4.64E-05	-4.6	
	Self-assembled precipitate	25	9.52	-5.1	1.18E-05	9.83E-05	-4.6
			9.54	-5.2	1.38E-05	2.39E-06	-5.4
		45	9.40	-5.1	7.62E-06	1.18E-06	-5.6
			9.45	-5.1	1.12E-04	8.32E-05	-4.4
60		9.15	-4.9	2.88E-05	4.58E-06	-5.3	
	9.16	-4.9	1.90E-05	3.09E-05	-4.9		
Oversaturation	25	5.29	-3.7	3.55E-06	9.88E-03	-5.2	
		6.08	-4.0	5.47E-06	7.54E-04	-5.1	
	45	5.53	-4.1	3.89E-06	9.12E-03	-5.3	
		4.06	-3.1	5.21E-06	1.10E-02	-5.7	
	60	5.31	-3.8	1.76E-05	7.23E-03	-4.7	
		4.62	-3.3	8.91E-06	1.74E-02	-5.0	

\* 2.36E-01 is read as 2.36 x 10<sup>-1</sup>

**Figure 3: pH-pe diagrams for the system Se-O-H (a) and Se-Fe-O-H (b). The activities for dissolved species are  $\text{Se} = 10^{-6}$  ((a), (b)) and  $\text{Fe}^{2+} = 10^{-5}$  (b)**

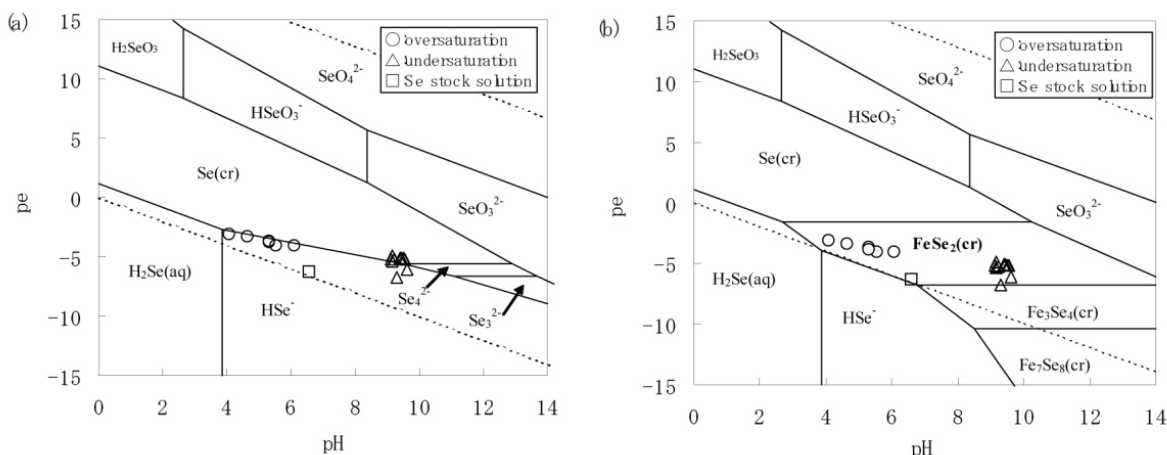
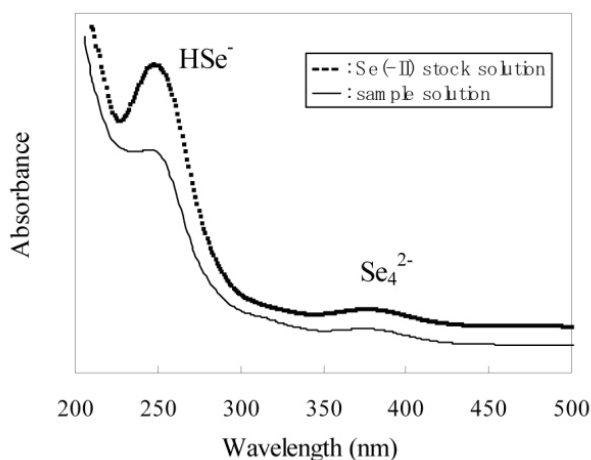


**Figure 4: UV-Vis spectra of the Se(-II) stock solution and sample solutions from the undersaturation direction after 240-day equilibration. The absorption band at 247 nm was assigned to  $\text{HSe}^-$  anion and the one at 377 nm to  $\text{Se}_4^{2-}$**



These values were 3 to 4 orders of magnitude higher than the value of  $K_1^0 = 10^{-8.6}$  calculated from the existing thermodynamic data of  $\Delta_f G_m^0(\text{FeSe}_2) = -101.3 \text{ kJ mol}^{-1}$  [14],  $\Delta_f G_m^0(\text{Fe}^{2+}) = -90.5 \text{ kJ mol}^{-1}$  [13] and  $\Delta_f G_m^0(\text{HSe}^-) = 43.471 \text{ kJ mol}^{-1}$  [14]. This disagreement indicates that  $\text{FeSe}_2$  with a solubility product of  $10^{-8.6}$  did not limit the solubility of selenium under the experimental conditions. On the other hand, the ion activity products could not be accurately calculated at 45°C and 60°C, because the data of pH, Eh and the selenium and iron concentration were obtained at room temperature, and because the data for temperature correction of the activities of  $\text{HSe}^-$  and  $\text{Se}_4^{2-}$  were not available. It is, however, not likely that the concentrations of selenium and iron limited by  $\text{FeSe}_2$  in the sample tubes increase remarkably during the cooling to room temperature, thus the ion activity products at 45°C and 60°C estimated from the data measured at room temperature are possible to compare with the value of  $K_1^0$  calculated from the existing thermodynamic data. Since the ion activity products at 45°C

and 60°C were similar to that at 25°C, it was not probable that FeSe<sub>2</sub> limit the solubility of selenium at also 45°C and 60°C.

To determine the solubility limiting solid of selenium, a slope analysis was performed for dissolution reactions of Fe<sub>n</sub>Se. The dissolution reaction can be described as



where solids with the n value of 0, 0.5, 0.75, 0.875 and 1.04 are known [14]. The relationship of  $a_{\text{HSe}^-}$ ,  $a_{\text{Fe}^{2+}}$ , pH and pe can be described as

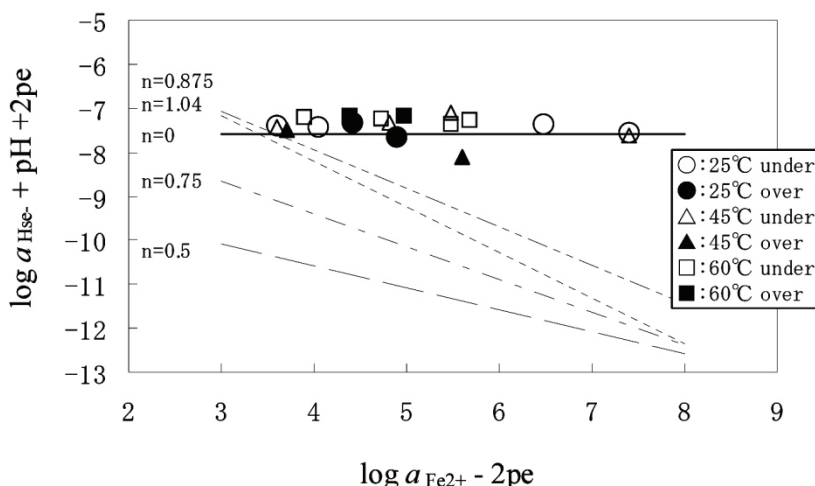
$$(\log a_{\text{HSe}^-} + \text{pH} + 2\text{pe}) = -n(\log a_{\text{Fe}^{2+}} - 2\text{pe}) + \log K_4^0 \quad (8)$$

Figure 5 shows the correlation between  $(\log a_{\text{HSe}^-} + \text{pH} + 2\text{pe})$  and  $(\log a_{\text{Fe}^{2+}} - 2\text{pe})$ . Using the least squares method, the slope was determined to be  $-0.05 \pm 0.07$  for 25°C, which virtually indicates  $n = 0$ .



is probably the predominant dissolution reaction. The plot of the data obtained from both the oversaturation and undersaturation experiments are identical, which assures the attainment of the equilibrium within 240 days.

**Figure 5** A plot of  $(\log a_{\text{HSe}^-} + \text{pH} + 2\text{pe})$  versus  $(\log a_{\text{Fe}^{2+}} - 2\text{pe})$ . The circles (○, ●), triangles (□, ■) and squares (△, ▲) represent the data obtained at 25°C, 45°C and 60°C, respectively. Open marks and closed marks represent the data obtained from the undersaturation and the oversaturation experiments, respectively. The lines represent the values for dissolution reactions calculated from existing thermodynamic data.



Applying a least-squares fitting on the experimental data obtained at 25°C to the equation (9) yields the equilibrium constants of  $\log K_5^0 = -7.46 \pm 0.11$ . This value agrees with the value of  $\log K^0 = -7.62 \pm 0.06$  for the reaction of  $\text{Se}(\text{cr}) + \text{H}^+ + 2\text{e}^- = \text{HSe}^-$  calculated from the existing

thermodynamic data of  $\Delta_f G_m^0(\text{Se}(\text{cr})) = 0 \text{ kJ mol}^{-1}$  and  $\Delta_f G_m^0(\text{HSe}^-) = 43.471 \text{ kJ mol}^{-1}$  [14] within errors. However,  $\text{Se}(\text{cr})$  was not identified in the most sample solids by XRD, which suggests that the solubility limiting solid of selenium would be amorphous or minor amount of crystalline selenium which can not be detected by XRD. This inference is supported by the knowledge that the primary selenium solid formed from aqueous solutions is in amorphous form, which crystallizes by heating [16].

The plots of the data obtained at 45°C and 60°C showed similar tendency to those at 25°C, as shown in Figure 2. The equilibrium constants were not strictly calculated at 45°C and 60°C, but the solution data measured at room temperature and XRD patterns suggested that the solubility limiting solid was amorphous or minor amount of crystalline selenium at also 45°C and 60°C. Further experimental studies will be required to elucidate the solubility of selenium at temperatures of deep underground.

## Conclusion

Dissolution experiments of selenium were performed in the presence of iron under anoxic conditions. Ferroselite which was the most thermodynamically stable solid phase under the experimental condition was identified in the solids by XRD. However, the ion activity products for the reaction of  $0.5\text{FeSe}_2 + \text{H}^+ + \text{e}^- = 0.5\text{Fe}^{2+} + \text{HSe}^-$ ,  $a_{\text{Fe}^{2+}}^{0.5} \cdot a_{\text{HSe}^-} \cdot a_{\text{H}^+}^{-1} \cdot a_{\text{e}^-}$ , obtained from both undersaturation and oversaturation directions were 3 to 4 orders of magnitude higher than the equilibrium constants calculated from existing thermodynamic data. The dominant dissolution reaction of selenium was determined as  $\text{Se}(\text{s}) + \text{H}^+ + 2\text{e}^- = \text{HSe}^-$  and its equilibrium constant was determined to be  $\log K^0 = -7.46 \pm 0.11$ . This value agrees with the value of  $\log K^0 = -7.62 \pm 0.06$  calculated from existing thermodynamic data of  $\text{Se}(\text{cr})$  within errors. However,  $\text{Se}(\text{cr})$  was not identified in the most sample solids by XRD, which suggests that the solubility limiting solid of selenium would be amorphous or minor amount of crystalline selenium which can not be detected by XRD.

We concluded that the solubility limiting solid of selenium is amorphous or crystalline selenium in the disposal environments even if the iron-selenium compounds are formed. Further experimental studies will be required to elucidate the solubility of selenium at temperatures of deep underground.

## Acknowledgement

The authors acknowledge Mr. T. Kawamura and Mr. K. Hotta for the experimental measurements.

## REFERENCES

- [1] Jiang, S.S., He, M., Diao, L.J., Guo, J.R. and Wu, S.Y., Remeasurement of the half-life of  $^{79}\text{Se}$  with the projectile X-ray detection method, *Chin. Phys. Lett.* 18, pp.746-749, 2001.
- [2] Japan Nuclear Cycle Development Institute, H12: Project to establish the scientific and technical basis for HLW disposal in Japan – Second progress report on research and development for the geological disposal of HLW in Japan, JNC TN 1410 2000-001, 2000.
- [3] Bruno, J., Cera, E., de Pablo, J., Duro, L., Jordana, S. and Savage, D., Determination of radionuclide solubility limits to be used in SR 97. Uncertainties associated to calculated solubilities, SKB TR-97-33, 1997.
- [4] Elkin E.M., Selenium and selenium compounds, In Kirk-Othmer, *Encyclopedia of chemical technology*, 3<sup>rd</sup> edition, vol. 20, John Wiley & Sons, New York, 1982.
- [5] Azuma, J., Shibata, M., Yui, M., Shibutani, T., Notoya, S. and Yoshida, Y., Solubility and speciation of radioactive elements of high-level radioactive waste disposal system, JNC TN8400 99-071, 1999 (in Japanese).
- [6] Shibutani, S., Yoshikawa, H. and Yui, M., Solubility measurement of Se in Se-H<sub>2</sub>O system under reducing condition, PNC TN8410 94-204, 1995(in Japanese).
- [7] Tachikawa, H., Kitao, H., Katsurai, K., Yanagisawa, I., Shibata, M., Suyama, T. and Yui, M., Experimental study on the solubility of selenium under simulated disposal conditions, JNC TN8400 99-068, 1999 (in Japanese).
- [8] Kitamura, A., Shibata, M. and Kitao, H., Solubility measurement of iron-selenium compounds under reducing conditions, *Mat. Res. Soc. Symp. Proc.* Vol. 807, pp. 609-614, 2004.
- [9] Syper, L. and Mlochowski, J., The convenient syntheses of organoselenium reagents, *Synthesis*, pp. 439-442, 1984.
- [10] Leussing, D.L. and Kolthoff, I.M., The solubility product of ferrous hydroxide and the ionization of the aquo-ferrous ion, *J. Am. Chem. Soc.* Vol.75, pp. 2476-2479, 1953.
- [11] Lyons, L. and Young, T., Alkaline selenide, polyselenide electrolytes: concentrations, absorption-spectra and formal potentials, *Aust. J. Chem.*, 39, 511, 1986.
- [12] Licht, S. and Forouzan, F., Speciation analysis of aqueous polyselenide solutions, *J. Electrochem. Soc.*, 142(5), 1546, 1995.

- [13] Japan Atomic Energy Research Institute, H17 Research on long-term safety assessment methodology for radioactive waste disposal, Japan Atomic Energy Research Institute, 2006 (in Japanese).
- [14] Olin, A., Nolang, B., Osadchii, E.G., Ohman, L.-O. and Rosen, E., Chemical thermodynamics of selenium, Elsevier, Amsterdam, 2005.
- [15] Stumm, W. and Morgan, J.J., Aquatic Chemistry, 3<sup>rd</sup> edition, John Wiley & Sons, Inc., New York, 1996.
- [16] The Chemical Society of Japan, Jikken Kagaku Kouza, 4<sup>th</sup> edition, vol. 15, Maruzen Co., Tokyo, 1991 (in Japanese).



## **IONS AT CLAY PARTICLE SURFACES AND IONIC EXCHANGE: A MOLECULAR DYNAMICS STUDY**

**Benjamin Rotenberg<sup>1,2</sup>, Virginie Marry<sup>1</sup>, Natalie Malikova<sup>3,4</sup>, Rodolphe Vuilleumier<sup>5</sup>,  
Jean-François Dufrêche<sup>1</sup>, Eric Giffaut<sup>2</sup> and Pierre Turq<sup>1</sup>**

<sup>1</sup>) Université P. et M. Curie-Paris6, Laboratoire LI2C, UMR CNRS 7612, France

<sup>2</sup>) Agence nationale pour la gestion des déchets radioactifs, France

<sup>3</sup>) Argonne National Laboratory, USA

<sup>4</sup>) Laboratoire Léon Brillouin, CEA Saclay, France

<sup>5</sup>) Université P. et M. Curie-Paris6, LPTMC, UMR CNRS 7600, France

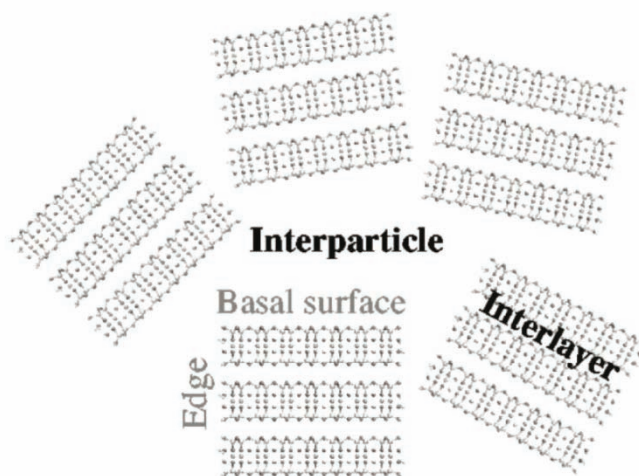
### **Abstract**

A microscopic description of ionic motion at the surface of clay particles is obtained via Molecular Dynamics simulations. Two types of surfaces are considered: basal and lateral (edges). In the first case, we provide a description of the ionic density profiles and the evolution of the diffusion coefficients as a function of the distance to the surface. In the second, we show that monovalent cations ( $\text{Na}^+$  and  $\text{Cs}^+$ ) can exchange within a few nanoseconds between interlayer and mesoporosity, while anions ( $\text{Cl}^-$ ) remain outside the interlayer at this timescale. This exclusion is confirmed by an estimation of the free energy penalty for the entrance of an ion in the interlayer (approximately  $12 k_{\text{B}}T$  at 298 K).

## Introduction

The mobility of radioactive ions, either cations (e.g.  $\text{Cs}^+$ ) or anions (e.g.  $\text{Cl}^-$ ), through geological barriers is greatly affected by their interactions with the mineral surfaces. In particular, it is now accepted that anions explore only a fraction of the porosity accessible to water, due to the electrostatic repulsion from the negatively charged clay surfaces [1]. This anionic exclusion, leading to the closure of diffusion pathways, explains to some extent the measured effective diffusion coefficients that are lower than that of water, and tend to increase with increasing ionic strength. On the contrary, cations are attracted by these surfaces and follow preferential diffusion pathways. This can increase their effective diffusion coefficient with respect to water. Furthermore, the negative charge born by clay minerals is the source of their cation exchange capacity: a radioactive cation may be exchanged with the natural compensating cations [2]. The fraction of the material explored by the cations can thus be different of that of anions, and exchange contributes to the retention properties of cations.

**Figure 1: Schematic representation of a clay particle aggregate in a compacted sample. Each particle contains interlayer porosity and exhibits two types of surfaces: basal and lateral (edges). Between particles, the porosity corresponds to larger pores. This picture is of course an idealized view. In particular, real particles are longer and thicker than the one represented here.**



These electrostatic interactions may be described using a continuum model within the framework of the Poisson-Boltzmann theory, if one considers only distances from the mineral surfaces that are (significantly) larger than the molecular size of the solvent. However, such a framework is not valid for the description of the ions at very short distances (typically of the order of nanometer), which is the one relevant for (a) adsorption of cation at the basal or lateral surfaces of clay particles and their possible entrance into the interlayers of clays via the lateral surfaces and (b) anion exclusion at very short distances from the surfaces and from the interlayers. The two types of surfaces are schematically represented in Figure 1.

We present a molecular dynamics study of these phenomena, with all species (clays, ions and water) resolved at the molecular scale. This allows for a precise description of the ionic

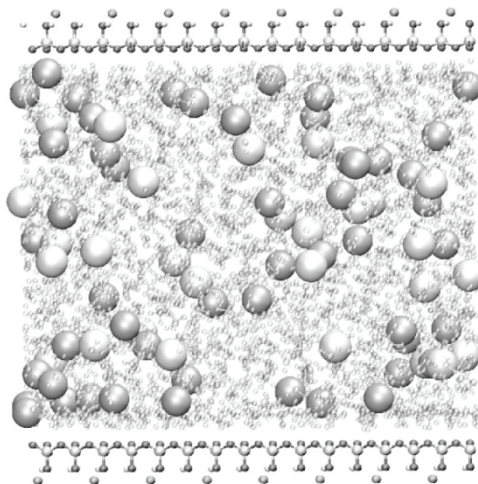
behaviour at basal and lateral surfaces of clays, and provides to our knowledge the first microscopic description of the elementary act of cation exchange. In particular, we show that a  $\text{Cs}^+$  ion near a lateral surface can enter into the interlayer within a few nanoseconds, and that water also exchanges between interlayer and interparticle pores at this timescale. On the contrary, no anion is seen to enter into the interlayer during these MD simulations. This exclusion is confirmed by an estimation of the free energy penalty for the entrance of an ion into the interlayer (approximately  $12 k_B T$  at 298 K). The next section is devoted to the study of basal surfaces, while section contains the results on the lateral surfaces.

## Basal surfaces

The first simulation box (Figure 2) contained a model montmorillonite layer described in previous publications [3], with 32 unit cells ( $41.44 \times 35.88$  Angströms), 24  $\text{Al}^{\text{III}}$  to  $\text{Mg}^{\text{II}}$  substitutions and 24 counterions ( $\text{Na}^+$  or  $\text{Cs}^+$ ). The substitutions were introduced at random, only excluding the possibility of adjacent Mg. Two half layers were separated by 1600 water molecules and 28 salt pairs ( $\text{NaCl}$  or  $\text{CsCl}$ ). This corresponds to an ionic strength of approximately 1M, higher than the experimental one in geological conditions (closer to 0.1M). Such a high value was chosen for two distinct reasons: first, it results in statistically more accurate data, because the number of particles involved is higher; second, the stronger electrostatic screening allows to treat the two surfaces as independent. This approach differs from that of Greathouse *et al.* for the study of uranyl(VI) adsorption on external clay surfaces, where special boundary conditions were employed to account for a semi-infinite pore facing the mineral surface [4,5]. Interactions between all atoms were introduced as Coulomb and Lennard-Jones potentials, with parameters given in [3]. In particular, we used the SPC/E water model [6], which is able to reproduce the water dielectric constant  $\epsilon_r^{\text{SPC/E}} = 81.5 \pm 5$  (close to the experimental value  $\epsilon_r^{\text{exp}} = 78.3 \pm 5$  at 298 K). The chosen parameters for ions, in conjunction with the SPC/E model, were shown by Koneshan *et al.* to accurately describe the structure and dynamics of bulk electrolyte solutions [7]. Periodic boundary conditions (PBC) in all directions were employed, and Ewald summation technique was used to compute the long-range electrostatic (Coulomb) part.

Prior to Molecular Dynamics (MD) simulation, the distance between the surfaces was first equilibrated using Monte Carlo (MC) simulations in the  $\text{NP}_z T$  ensemble. This distance was then fixed to its average value ( $42.9 \text{ \AA}$  between the center of the octahedral layers), and MD simulations were done in the NVT ensemble, i.e. at fixed number of particles, volume and temperature (298 K). All MD runs were performed using the DLPOLY simulation package. The timestep used was 1fs, and the temperature maintained around 298K using the Nosé-Hoover thermostat [8].

**Figure 2: Snapshot of the first simulation box.**  
**Between two basal surfaces, a pore contains 24 counterions and 28 salt pairs**  
**(approximately 1M).**  
**Na<sup>+</sup> are in silver, and Cl<sup>-</sup> in white.**

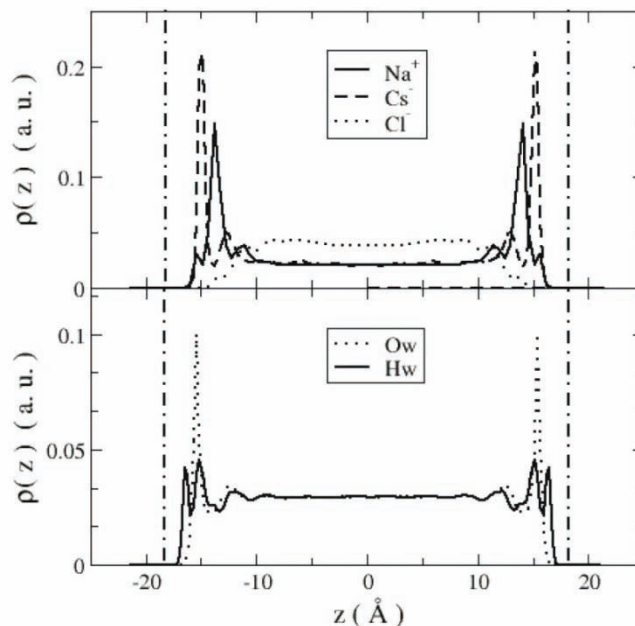


Density profiles across the pore were obtained on a succession of 328ps runs, separated by a simulated annealing [8] at 1 000K. Results are reported in Figure 3. All density profiles reach their bulk value within 1nm of the surfaces. Anions are excluded from the clay surface, with a depletion layer of approximately 7 Å in which the density is lower than in the bulk. This confirms the generally admitted anion exclusion. This effect is expected to be more pronounced at lower ionic strength.

On the contrary, cation densities are higher than in the bulk close to the surface. This is due to the excess of cations arising from the presence of counterions. Na<sup>+</sup> profiles display two maxima, the closer to the surface corresponding to Inner Sphere complexes (ISC), in which one or more surface oxygen atoms belong to the coordination shell of the ion, the second corresponding to Outer Sphere complexes (OSC), in which only water oxygen atoms coordinate the ion. For Cs<sup>+</sup>, almost only ISC are observed. This is in agreement with simulation results of clay interlayers [9,10,11].

Water profiles display oscillations only within 1nm of the surface. This shows that only a few (2 to 3) water layers are perturbed by the mineral surfaces, at least as far as density is concerned.

**Figure 3: Ions (top) and water (bottom) density profiles across the pore. The location of the oxygen surface atoms is indicated by vertical dashed-dotted lines. All profiles reach their bulk value within 1nm of the surface.**



Diffusion coefficients along the surfaces were determined from a linear fit of the Mean Square Displacement (MSD) of each species [8]. In order to compare the diffusion coefficient in the “bulk” and close to the clay surface, the pore was divided into slices. The width of the surface slice is chosen to include the density peaks (for the cations) and depleted region (anion). Thus we obtained one diffusion coefficient for ions in the vicinity of the surface ( $D_s$ ) and another for the ions in a region considered as not perturbed by the surfaces, or “bulk” ( $D_b$ ). Care was taken that the ions used to compute the MSD in each slice remained there during the sampling time.

Results for the “surface” and “bulk” diffusion coefficients are summarized in Table 1 ( $D_s$  and  $D_b$  respectively). They indicate that in the vicinity of the surface the ions diffuse significantly slower than in the rest of the pore. This decrease even exceeds 50% in the  $\text{Cs}^+$  case. Diffusion coefficients in the “bulk” are close to the diffusion at infinite dilution  $D_b^0$ , whose value for our simulation parameters is also given in Table 1. A value lower than the one at infinite dilution is not surprising because of steric hindrance. The chlorine diffusion coefficient is lower in the NaCl case. This indicates that the influence of the surfaces may be longer ranged in that case.

To draw conclusions on the long-term diffusion, one must keep in mind that the slower diffusion on the surface is balanced by the relatively short residence time near the surface. Therefore, the interplay between diffusion and exchange between slices results in an average value of the diffusion coefficient.

**Table 1: Surface and bulk diffusion coefficients.**  
**The value at infinite dilution obtained with our simulation parameters**  
**is also reported from [7].**

		$D_s$ ( $10^{-9}\text{m}^2.\text{s}^{-1}$ )	$D_b$ ( $10^{-9}\text{m}^2.\text{s}^{-1}$ )	$D_b^0$ ( $10^{-9}\text{m}^2.\text{s}^{-1}$ )
NaCl	Na <sup>+</sup>	$0.87 \pm 0.05$	$1.15 \pm 0.1$	$1.28 \pm 0.05$
	Cl <sup>-</sup>	$0.9 \pm 0.1$	$1.3 \pm 0.2$	$1.77 \pm 0.1$
CsCl	Cs <sup>+</sup>	$0.85 \pm 0.1$	$1.9 \pm 0.1$	$1.88 \pm 0.2$
	Cl <sup>-</sup>	$1.05 \pm 0.05$	$1.6 \pm 0.1$	$1.77 \pm 0.1$

## Lateral surfaces

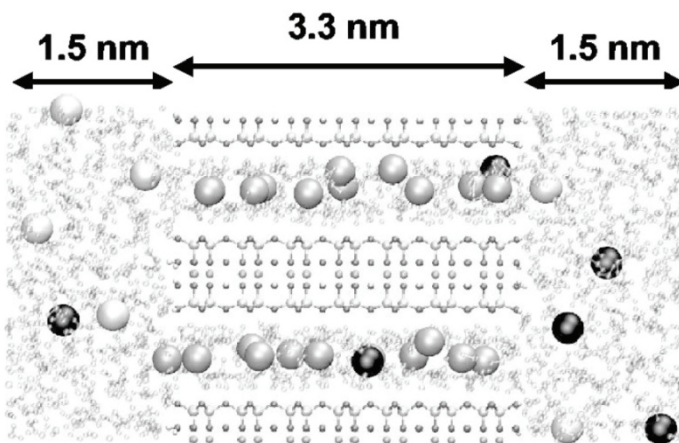
In contrast to basal surfaces, lateral surfaces provide an opening on the interlayers. This entrance offers a pathway for the ions inside the clay particles. However, the negative charge of the mineral layers tend to exclude the anions. Equilibrium of clays with a salt solution can result in the exchange of bulk cations with the clay counterions [1,2]. This exchange, quantified by the cation exchange capacity (CEC), is a possible source of retention for radioactive ions by clays, but it offers at the same time additional diffusion pathways compared to that in the pores. The presence of Cl<sup>-</sup> anions in the interlayer has recently been observed, and it is suspected that in this case, association with a divalent cation (Ca<sup>2+</sup>) is necessary [12]. The purpose of our microscopic simulations is to gain insight in the mechanisms leading to cation exchange and anion exclusion: how does Cs<sup>+</sup> ions penetrate in the interlayer from the pore, and why do Cl<sup>-</sup> ions remain in the interparticle pores?

In order to describe a lateral surface, one needs to cut the mineral layer along a given direction. The cut edge is then hydrated (possibly by dissociating water molecules) to complete the coordination shell of Al<sup>III</sup> in the octahedral sheet [13,14]. The partial charges of the edge sites were determined via *ab initio* simulations of the corresponding edge on a pyrophyllite fragment consisting of 72 atoms. Pyrophyllite has the same structure as montmorillonite, but without Al<sup>III</sup> to Mg<sup>II</sup> substitutions. The minimum energy configuration was first determined by constraining all but the edge atoms, leaving the latter free to rearrange. This was done using a modified version of the CPMD code. Once the atomic position and electronic density are determined, the electrostatic potential outside the clay fragment is evaluated. Partial charges on the edge sites are then adjusted to fit this electrostatic potential. In addition to the Coulomb interaction, a Lennard-Jones (LJ) potential was added for the edge oxygen atoms, with LJ parameters equal to that of the basal oxygen atoms. The details of the fitting procedure and the resulting partial charges are postponed to a futher publication.

We have chosen the surface referred to as (0,1,0) by Bickmore and Churakov, but as (1,-1,0) in the conventional indexing. This surface has a moderate surface energy and is one of the three commonly observed, resulting in the hexagonal shape of montmorillonite crystals [13]. Once the position and partial charges of the edge sites are known, the pyrophyllite fragment is cut and “completed” with bulk montmorillonite cells, and replicated along the edge direction. The Al<sup>III</sup> to Mg<sup>II</sup> substitutions were introduced as for the basal surfaces. The resulting clay layer contains 3x4 unit cells, with dimensions 33.0x20.72 Å. Note that the edge is overall neutral; no deprotonation was considered in this first study.

The simulation box, illustrated in Figure 4, contains two clay layers (and two interlayers) with interlayer distances of 15.4 Å, corresponding to two water layers, 22 Na<sup>+</sup> counterions, 898 water molecules and 6 CsCl pairs. Water fills the interlayers and the rest of the simulation box (3 nm in the direction perpendicular to the edge), which models a mesopore (= interparticle pore). The number of water molecules was chosen to ensure that the density is that of bulk water in the middle of the mesopore. The Cs<sup>+</sup> and Cl<sup>-</sup> ions are initially in the mesopore. The corresponding ionic strength is 0.52M, higher than the experimental one. The reason for this choice is again twofold: increased statistical accuracy (the smaller the pore, the faster it is sampled by the ions), and stronger electrostatic screening, that allows to consider the two edges as independent despite the relatively short distance (only 3nm).

**Figure 4: Snapshot of the second simulation box. A short (3.3 nm) clay particle faces a 3 nm pore containing salt. The colour code is the same as Figure 2, with Cs<sup>+</sup> in black. Initially, all Cs<sup>+</sup> were in the pore. It can exchange within nanoseconds with the interlayer Na<sup>+</sup>.**

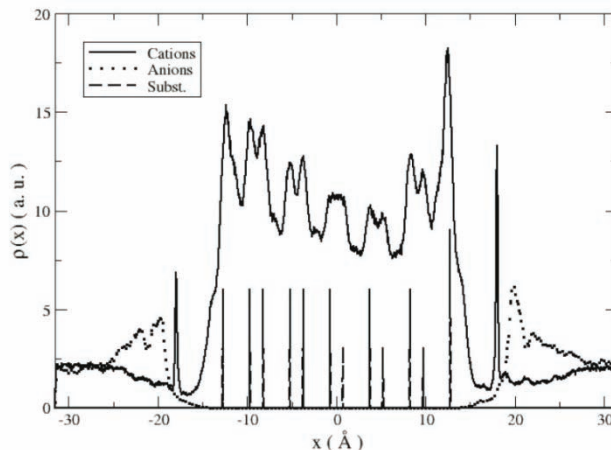


Simulations were done in the NVT ensemble, using a Nosé-Hoover thermostat. After equilibration, we checked that all Cs<sup>+</sup> were still in the mesopore. A 10 ns run was then performed. Within this short time (long however, from a computational cost point of view), 5 (out of 6) Cs<sup>+</sup> ions enter the interlayers, while as many Na<sup>+</sup> are released into the mesopore. This is to our knowledge the first simulation of the elementary act of ionic exchange in clays. Water molecules also exchange between the two porosities. The quantitative analysis of the exchange rates is under progress. Static properties are, nevertheless, already at hand. The density profiles for cations (average of Na<sup>+</sup> and Cs<sup>+</sup>) and anions are reported in figure 5, where the location and number of substitutions in the layer are also reported.

Anions are, as expected, excluded from the interlayer. Interestingly, the anion density displays a maximum at approximately 3.5 Å from the edges. This effect, which may seem counterintuitive, can be traced back to a correlation effect: cations are indeed attracted by the surface of the particle (although it is overall neutral, because of the counterions), as the two peaks at  $x=\pm 18$  Å reveal. This attraction is due to the presence of substitutions in the octahedral sheet near (but not on) the edge. The larger peak at  $x=\pm 18$  Å is consistent with the larger number

of substitutions near the right edge (dashed line in Figure 5). The high local cation density in turn attracts the anions. This structuring in the anionic density profile might be affected by the presence of negative charges on the edges.

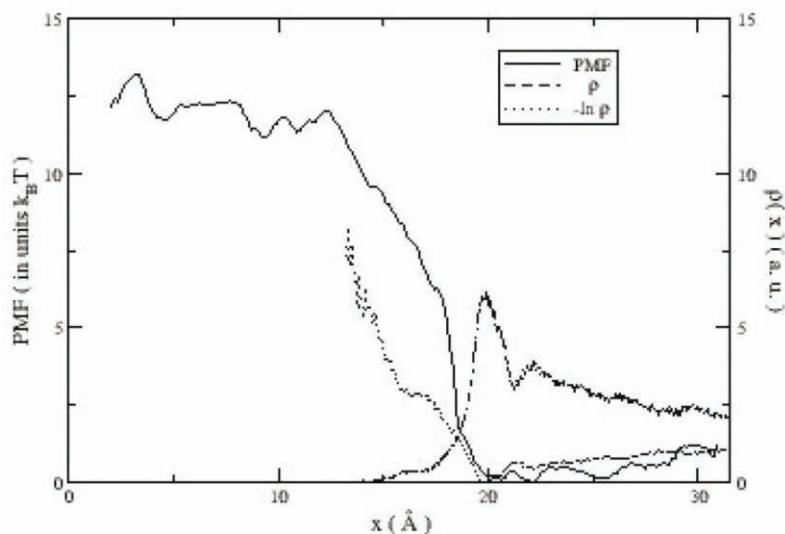
**Figure 5: Cation (solid) and anion (dotted) density across the simulation box (particle and pore). The cation density in the interlayer is modulated by the location of the  $\text{Al}^{\text{III}}$  to  $\text{Mg}^{\text{II}}$  substitutions (dashed lines). Anions are excluded from the interlayer porosity.**



In order to gain insight into anion exclusion from the interlayer, we evaluated the free energy barrier related to the entrance of an anion into the interlayer. This was achieved by a specific statistical analysis of biased simulations named Weighted Histogram Analysis Method (WHAM) [15]. A  $\text{Cl}^-$  ion is constrained around a fixed position  $x_0$  using a tethering potential  $1/2.k.(x-x_0)^2$ . The trajectory of this ion is collected during this biased simulation, and the sampling repeated for a set of  $x_0$  values (from 2 to 30 Å). WHAM then allows to recover the free energy profile from the analysis of the biased trajectories. The interested reader is referred to reference [15] for further details.

Results for the reconstructed potential, or Potential of Mean Force (PMF), are reported in Figure 6 divided by the thermal energy  $k_B T$ . This potential indicates that a very high energy barrier ( $12 k_B T$  at 298K) must be overcome to enter the interlayer. This result is in agreement with the extremely low concentration of anions in the interlayer (in fact zero concentration during the 10ns unbiased simulation). As an indication of the relevance of our approach, we also reported in figure 6 the opposite of the logarithm of the equilibrium density obtained from unbiased simulations. This quantity should by definition be equal to the PMF. The good agreement in the region where the equilibrium density is high indicates that the WHAM calculation provides a reasonable estimate of the PMF. In addition, the “natural” estimate ( $-\ln \rho$ ) is insufficient in the region of low density, because the latter is poorly sampled in unbiased simulations. This justifies the use of the more elaborate WHAM analysis to estimate the free energy barrier. The uncertainty on the PMF could not be evaluated properly. Therefore we consider that the result is only a qualitative confirmation of the anion exclusion, and that the value of  $12 k_B T$  must be taken with caution. The presence of a barrier of several times the thermal energy is nevertheless highly probable.

**Figure 6: Potential of Mean Force (solid line) for an anion entrance into the interlayer. The free energy penalty is as high as 12  $k_B T$  (at 298 K). The anion density is also reported ( $\rho$ , dashed line), together with another estimate of the free energy barrier ( $-\ln \rho$  pointed line).**



To conclude this study on the lateral surfaces, we have shown that cation exchange between  $\text{Na}^+$  and  $\text{Cs}^+$  can be observed on the nanosecond scale, and that the entrance of anions into the interlayer requires overcoming a substantial free energy barrier.

## Conclusion

We have presented a microscopic description of ionic motion at the surfaces of clay particles. Two types of surfaces were considered: basal and lateral (edges). For basal surfaces, it was shown that  $\text{Na}^+$  ions exhibit both inner sphere and outer sphere complexes, while  $\text{Cs}^+$  ions show mainly ISC. In addition,  $\text{Cl}^-$  ions are excluded from a 1nm layer in the vicinity of the surface. The diffusion coefficient of all ions is reduced near the surface; this reduction is as high as 50% for  $\text{Cs}^+$ .

For lateral surfaces, we have shown that  $\text{Na}^+$  and  $\text{Cs}^+$  can exchange within a few nanoseconds between interlayer and mesoporosity, while anions ( $\text{Cl}^-$ ) remain outside the interlayer at this timescale. This exclusion was confirmed by an estimation of the free energy penalty for the entrance of an ion in the interlayer (approximately 12  $k_B T$  at 298 K, that is 30 kJ/mol).

The study of these surfaces at lower ionic strength is under progress. We expect the conclusions of the present study to hold under these conditions, closer to the ones relevant for the geological storage of nuclear waste. In particular, the depletion layer for anions should be larger and the anion exclusion effect magnified. We are also considering a study of  $\text{CaCl}_2$  salt, which should allow the entrance of a  $\text{CaCl}^+$  ion pair into the clay interlayer, as well as the study of the effect of deprotonated edge sites on ion exchange and anion exclusion.

## Acknowledgements

B.R. acknowledges financial support from ANDRA (Agence nationale pour la gestion des déchets radioactifs). Financial support of GdR PARIS (Physico-chimie des actinides et autres radioéléments aux interfaces et en solution) is gratefully acknowledged. LI2C is part of the SFR Sciences chimiques pour l'analyse et la mesure de Paris-Centre.

## REFERENCES

- [1] ANDRA, Référentiel Matériaux, vol. 1 : Matériaux à base d'argiles gonflantes (2005)
- [2] M. Bradbury, B. Baeyens, Near Field Sorption Data Bases for Compacted MX-80 Bentonite for Performance Assessment of a High-Level Radioactive Waste Repository in Opalinus Clay Host Rock (2003)
- [3] V. Marry and P. Turq, *J. Phys. Chem. B* 107, 1832 (2003)
- [4] J.A. Greathouse and R.T. Cygan, *Phys. Chem. Chem. Phys.* 7, 3580 (2005)
- [5] J.A. Greathouse and R.T. Cygan, *Environ. Sci. Technol.* 40, 3865 (2006)
- [6] H.J.C. Berendsen, J.R. Grigera, and T.P. Straatsma, *J. Phys. Chem.* 91, 6269 (1987)
- [7] S. Koneshan, C. Rasaiah, R. Lynden-Bell, and S. Lee, *J. Phys. Chem. B* 102, 4193 (1998)
- [8] D. Frenkel, B. Smit, Understanding Molecular Simulations, From Algorithms to Applications (Academic Press, London, United Kingdom, 2002)
- [9] N.T. Skipper, G. Sposito, and F.C. Chang, *Clays Clay Miner.* 43, 294 (1995)
- [10] F.C. Chang, N.T. Skipper, G. Sposito, *Langmuir* 11, 2734 (1995)
- [11] E.S. Boek, P.V. Coveney, N.T. Skipper, *J. Am. Chem. Soc.* 117, 12608 (1995)
- [12] L. Charlet, C. Tournassat, *Aquatic Geochemistry* 11 (2), 115 (2005)
- [13] B.R. Bickmore, K.M. Rosso, K.L. Nagy, R.T. Cygan, and C.J. Tadanier, *Clays Clay Miner.* 51 (4), 359 (2003)
- [14] S.V. Churakov, *J. Phys. Chem. B* 110 (9), 4135 (2006)
- [15] B. Roux, *Comput. Phys. Comm.* 91 (1-3), 275 (1995)

## ACTIVATION ENERGIES OF DIFFUSION FOR I AND Cs IN INTERLAYER OF SMECTITE

**Haruo Sato**

Japan Atomic Energy Agency (JAEA), 432-2, Hokushin, Horonobe-cho,  
Hokkaido 098-3224, Japan

### Abstract

The apparent diffusivities ( $D_a$ ) and activation energies ( $\Delta E_a$ ) for  $\Gamma^-$  and  $\text{Cs}^+$  ions in compacted Na-smectite with an interlayer space of only 2 water layers were measured at a dry density of  $1.79 \text{ Mg/m}^3$ . In-diffusion experiments were carried out under the conditions that interlayer space, orientation of smectite stacks and dry density were controlled. Basal spacing was checked by X-ray diffractometry (XRD). All diffraction peaks to  $d_{(001)}$  indicated basal spacing, of which interlayer space was equal to 2 water layers. The  $\Delta E_a$  of  $\Gamma^-$  ions was at similar level as that for the ionic diffusivity of  $\Gamma^-$  ions in free water ( $D^0$ ) at a dry density of  $1.0 \text{ Mg/m}^3$ , but was  $35.24 \text{ kJ/mol}$  at a dry density of  $1.79 \text{ Mg/m}^3$ . The  $\Delta E_a$  for  $\text{Cs}^+$  ions was  $46.27 \text{ kJ/mol}$  which was higher than that for  $\Gamma^-$  ions, at a dry density of  $1.79 \text{ Mg/m}^3$ . Such high  $\Delta E_a$  for  $\Gamma^-$  ions in the interlayer of smectite could be explained by the lowering in the activity ( $a_{\text{H}_2\text{O}}$ ) of interlayer water. Since  $\text{Cs}^+$  ions sorb onto smectite by ion exchange, such high  $\Delta E_a$  for  $\text{Cs}^+$  ions could be explained by the combined effects of the  $\text{Cs}^+/\text{Na}^+$  ion exchange enthalpy ( $\Delta H^0$ ) in smectite and the lowering in the  $a_{\text{H}_2\text{O}}$  of interlayer water.

## Introduction

In the safety assessment of the geological disposal for a high-level radioactive waste in Japan, the role as a barrier function of the bentonite buffer composing the engineered barrier system is quite important to restrict the release of radionuclides (RN) from repository, and therefore several related studies have been reported so far [e.g., 1, 2]. Particularly, since RNs leached from vitrified wastes, enter the compacted bentonite, and diffuse through the bentonite towards the geosphere, it is clear that their diffusion properties in the bentonite are regarded as one of the most important characteristics in the safety assessment.

The rate of RN release as leached from the vitrified wastes depends on effective diffusivity ( $D_e$ ) and apparent diffusivity ( $D_a$ ). Particularly,  $D_a$  strongly depends on retardation factors such as distribution coefficients ( $K_d$ ) of RNs in the geological materials composing the bentonite and geosphere. These interactions occur at the solid-liquid interface, which makes it important to understand the reactions at the solid-liquid interface. The diffusion of RNs in compacted bentonite and in the rock matrix is mediated by the porewater. Thus, the nature of the porewater is considered to directly affect how the RNs are transported through the buffer materials and the host rock. Particularly, a potential distribution develops at the solid-liquid interface by contacting with porewater, and furthermore ionic concentration and viscosity distributions also develop simultaneously.

It is shown in previous studies that retardation in the diffusion process of RNs in compacted bentonite is affected by various physico-chemical properties such as porosity, bentonite's dry density [1, 3-6], sorption properties, interlayer cations of smectite [7], porewater chemistry [8, 9], additives to bentonite (e.g., silica sand) [10], initial bentonite grain size [10, 11], temperature [5, 12-17], etc. The author has reported in previous studies that clay particles oriented in the direction perpendicular to the direction of compaction for a bentonite with high-smectite content such as Kunipia-F bentonite which is almost 100 wt.% smectite [18-20]. Similarly, the  $D_e$  values of tritium (HTO) and deuterium (HDO) are entirely different between directions parallel and perpendicular to the orientation of clay particles [18-21]. It is also reported that the basal spacing of smectite changes depending on salinity [15, 22].

In terms of  $\Delta E_a$  for diffusion,  $\Delta E_a$  values for the  $D_a$  values of HTO,  $\text{Na}^+$ ,  $\text{Cs}^+$ ,  $\text{Sr}^{2+}$  and  $\text{Cl}^-$  in compacted Na-montmorillonite (Kunipia-F) [12-17] and those for Ni and  $\text{HSe}^-$  ions in compacted Na-bentonite (Kunigel-V1) which is ca. 50 wt.% smectite content have been reported [5, 23]. Particularly, for  $\text{Na}^+$  ions, the effects of silica sand mixture and salinity on  $\Delta E_a$  also have been studied. It is reported that the basal spacing of montmorillonite decreases with an increase of salinity [15, 22]. Even at the same montmorillonite partial density for a bentonite with silica sand, the  $\Delta E_a$  values for  $\text{Na}^+$  ions and the interlayer space of montmorillonite are different [15-17]. In a previous study, Suzuki *et al.* [21] have measured  $\Delta E_a$  values for the  $D_e$  of HDO in compacted smectite where the orientation of clay particles was controlled. The  $\Delta E_a$  values increased while rising with the smectite dry density and they were slightly higher than  $\Delta E_a$  of the ionic diffusivity in free water ( $D^0$ ) for HDO. This indicates that the nature of porewater near solid-liquid interfaces possibly differs from that of free water. The author and Miyamoto [23] also have discussed the nature of porewater in compacted bentonite based on the relative partial molar activation energies for hydroselenide ions ( $\text{HSe}^-$ ) and indicated the same

possibility as Suzuki *et al.* [21]. Furthermore, in recent studies, the author has measured the  $D_a$  values of  $\Gamma$  and  $\text{Cs}^+$  ions in compacted Na-smectite in the directions parallel and perpendicular to the orientation of smectite particles as a function of dry density ( $0.9\text{-}1.4 \text{ Mg/m}^3$ ), salinity ( $[\text{NaCl}] = 0.01, 0.51 \text{ M}$ ) and temperature, and discussed the diffusion pathways of both ions based on the anisotropies and the effect of salinity in the  $D_a$  and  $\Delta E_a$  values [9, 24-26]. Consequently, the  $\Delta E_a$  values of both ions increased with an increase of dry density, and the effect of the lowering in the  $a_{\text{H}_2\text{O}}$  of porewater was indicated. In contrast, it was interpreted that  $\Gamma$  ions predominantly diffused in external pores [9, 24-26]. However, it is still controversial whether anions such as iodide diffuse in interlayer which is quite narrow because of anionic exclusion.

This study was performed to discuss whether anions diffuse in the interlayer of smectite and to obtain  $\Delta E_a$  values of diffusion for ions in the interlayer, focusing on smectite which is a major clay mineral constituent of the bentonite buffer, one of the engineered barriers.

## Experimental

### *Preparation of Na-smectite*

Purified Na-smectite of which all interlayer cations were exchanged with  $\text{Na}^+$  ions and soluble salts were also removed, was prepared in this study. The preparation of the sample was carried out in the same way as previous diffusion experiments [9, 24-26]. As the starting material, Kunipia-P (Kunimine Industries Co. Ltd.) of which smectite content is approx. 100 wt.%, was used in this study. Since the smectite in Kunipia-P is almost montmorillonite, Kunipia-P can be said to be equivalent to montmorillonite. Incidentally, it is reported that Kunipia-F which is approx. the same as Kunipia-P in smectite content is a mixture of 83% Na- and 17% Ca-smectite [27]. The difference of interlayer cation affects basal spacing as well as external pore space. In addition, the  $D_a$  values of Cs in Na-smectite decrease with an increase of Ca-smectite content [7]. Thus, the mixture of Ca-smectite makes the  $D_a$  of Cs low. Therefore, preparation of interlayer cation and removal of soluble salts such as calcite were performed before diffusion experiments.

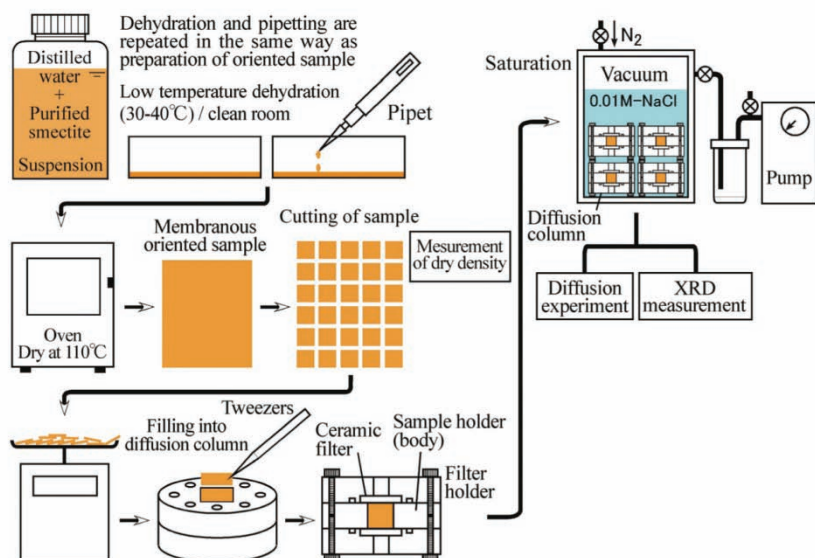
During a week to 61 d, bentonite powder was put in contact with a 1 M-NaCl solution at a solid-liquid ratio of 120 g/5 l. Then the bentonite was separated from the suspension. This operation was repeated 3 times. At the end of the third immersion with NaCl, the solid-liquid separation was made by centrifugation at 3 000 rpm for 20 mn. The bentonite was washed 3 times with 80% ethyl alcohol and was dried in air. Also in these washings, the solid-liquid separation was made by centrifugation. The washed bentonite was dispersed in distilled water and then only particles smaller than  $0.5 \mu\text{m}$  in diameter were collected by centrifugation at 3 000 rpm for 5 mn. By this classification, only clay minerals are collected. Next, the collected smectite was immersed in 1 M-NaCl, adjusted at pHs of 3 to 4 by  $\text{CH}_3\text{COOH}$ , to remove soluble salts. This operation was repeated until the pH becomes not to change. This operation was repeated 20 times. Finally, the smectite was washed 3 times with 80% ethyl alcohol.

Furthermore, the cation exchange capacity (CEC) measured by the ammonium ion exchange method was 122.8 meq/100 g. This CEC is at similar level as that (116.5 meq/100 g [7]) of montmorillonite (Kunipia-F). Incidentally, the CEC of Kunipia-F measured in this study was 111.2 meq/100 g, which was at similar level as reported value. In addition, the impurities of smectite were measured by XRD.

### *Preparation of compacted smectite sample which interlayer space was controlled*

Figure 1 illustrates the preparation procedure of a compacted smectite sample which interlayer space and orientation of the smectite stacks were controlled. A membranous oriented sample of the smectite was prepared in the same way as preparation of oriented sample which is generally used in XRD measurement. Purified smectite was firstly dispersed in distilled water and suspension was prepared. Next, the suspension was pipetted in a polypropylene vessel which has a plane bottom and was dehydrated at low temperature (30-40°C). This operation was repeated. After being approximately dehydrated, the membranous oriented sample was dried at 110°C. The thickness of the membranous oriented sample obtained ranged 0.4 to 1 mm. Next, the membranous oriented sample was cut into a square of 14 mm and then filled into an acrylic sample holder with a cubical space of 15 mm to obtain a target dry density of 1.8 Mg/m<sup>3</sup> (Figure 1).

**Figure 1: Preparation procedure of compacted smectite which interlayer space and orientation of smectite stacks were controlled**



After being filled, the smectite sample in the sample holder was saturated with 0.01 M-NaCl for 199 to 224 d. The saturation of the smectite sample was carried out in a vacuum chamber. Although the saturated state of the smectite sample can be checked by eye-measurement from the outside because an acrylic diffusion column was used in the experiments, it was checked by monitoring the water content. The homogeneity of the water distribution in the smectite sample was additionally checked in a separate experiment by the measurement of

the weight of the sliced sample after saturation. Basal spacing was also measured versus depth from the surface of the saturated smectite sample by XRD (0.5, 4 and 7.5 mm).

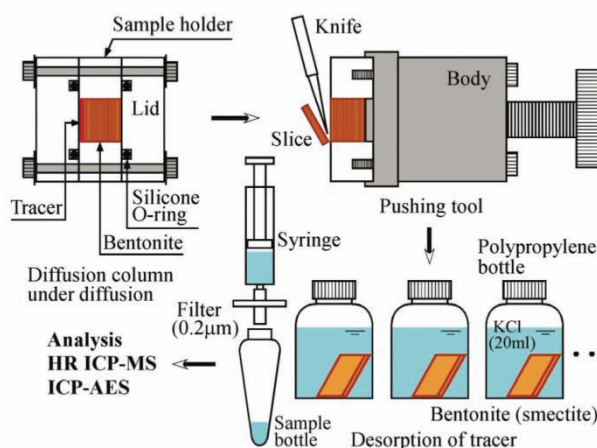
**Table 1: Experimental conditions for diffusion experiments**

Item	Method / Sample / Condition
Method	In-diffusion method (one side back-to-back)
Bentonite	Na-smectite (Kunipia-P of which interlayer cations were exchanged with Na <sup>+</sup> ions and soluble salts were removed)
Dry density	1.76-1.83 Mg/m <sup>3</sup> (average: 1.79 Mg/m <sup>3</sup> )(sample: cube of 15 mm)
Diffusion direction	Direction perpendicular to the orientation of smectite particles
Saturated solution	NaCl ([NaCl]=0.01 M)
Tracer solution	CsI ([CsI]=1.5E-2 M)
Spiked tracer quantity	50 µl/sample
Temperature	22-60°C
Atmosphere	Aerobic condition
Diffusion period	2-8 d (depending on temperature)

### Diffusion Experiments

The diffusion experiments were carried out by the in-diffusion method [e.g., 8, 23, 24]. Figure 2 illustrates the experimental procedure and Table 1 shows the experimental conditions. After the saturation by NaCl, a small amount of tracer solution (50 µl) was pipetted on the surface of one end of each smectite sample and was allowed to diffuse at temperatures of 22 to 60°C during 2 to 8 d (see Figure 2). The diffusion direction in this study is equivalent to the direction perpendicular to the orientation of smectite particles.

**Figure 2: Experimental procedure of diffusion experiments**



After respective diffusion periods, each smectite sample was cut with a knife into 1 mm-pitched slices. Each slice was immediately weighed to obtain the thickness of the slice and was immersed in a 20 ml KCl solution with 0.1 M to recover both ions from the slice. After being filtered through a 0.2 µm membrane filter for solid-liquid separation, the concentrations of I and Cs were analysed with an ICP-AES (Quantitative limit (QL): 0.1 ppm, ICPS-7000, Shimadzu,

Japan) and a High Resolution ICP-MS (QL: 0.01 ppb, Plasma Trace 2, Micromass, UK), respectively.

### ***Determinations of $D_a$ and $\Delta E_a$***

The  $D_a$  was determined based on Fick's 2nd law [28]. If  $D_a$  is a constant independent of distance (position) and tracer concentration, the diffusion equation for one-dimensional non-steady state in a sample of infinite length is generally expressed by the following equations:

$$\frac{\partial C}{\partial t} = \frac{\partial}{\partial X} \left( D_a \frac{\partial C}{\partial X} \right) = D_a \frac{\partial^2 C}{\partial X^2} = \left( \frac{D_e}{\alpha} \right) \frac{\partial^2 C}{\partial X^2} \quad (1)$$

where  $C$  is the concentration of tracer in unit smectite volume ( $\text{mg}/\text{m}^3$ ),  $t$  the diffusing time (s),  $X$  the distance from the tracer source (m),  $D_a$  the apparent diffusivity ( $\text{m}^2/\text{s}$ ),  $D_e$  the effective diffusivity ( $\text{m}^2/\text{s}$ ),  $\alpha$  the rock capacity factor ( $\alpha = n_p + \rho_d \cdot K_d$ ),  $n_p$  the porosity,  $\rho_d$  the smectite's dry density ( $\text{Mg}/\text{m}^3$ ), and  $K_d$  the distribution coefficient ( $\text{m}^3/\text{Mg}$ ).

The  $D_a$  was determined by the analytical solution of the diffusion equation shown above. Initially, all soluble tracer was at the origin of the system, leading to next initial and boundary conditions [28]:

$$C(X \geq 0, t=0) = 0$$

$$C(X \rightarrow \infty, t \geq 0) = 0$$

$$Q_0 = \int_0^{\infty} C(X, t=0) \delta(X) dX$$

where  $Q_0$  the total quantity of tracer per unit surface area in the system, and  $\delta(X)$  the delta-function.

The analytical solution of this problem is derived as below [28]:

$$C(X, t) = \frac{Q_0}{\sqrt{\pi D_a \cdot t}} \exp\left(-\frac{X^2}{4D_a \cdot t}\right) \quad (2)$$

The  $\Delta E_a$  was determined from Arrhenius plot as shown below [29]:

$$\frac{d \ln D_a}{dT} = \frac{\Delta E_a}{RT^2} \quad (3)$$

where  $T$  is the absolute temperature (K),  $R$  the gas constant ( $8.314 \text{ J}/\text{mol}/\text{K}$ ), and  $\Delta E_a$  the activation energy for  $D_a$  ( $\text{J}/\text{mol}$ ).

## Results and Discussion

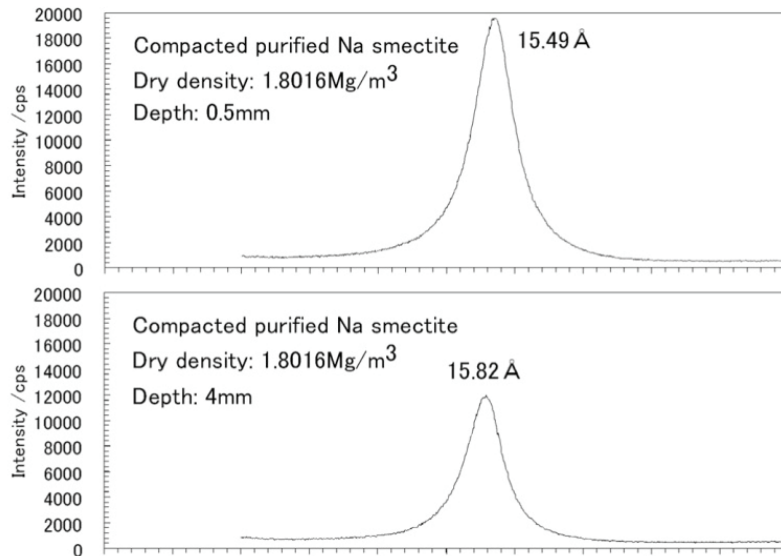
### *XRD measurements*

It was identified that purified Na-smectite, a homogeneously arranged Na-smectite, had no impurity and was a dioctahedral smectite from XRD profiles and peak positions for powder sample. Figure 3 shows XRD profiles versus  $2\theta$  (degree) for compacted smectite sample at a dry density of  $1.8 \text{ Mg/m}^3$ , measured at depths of 0.5, 4 and 7.5 mm from the surface of smectite sample. All diffraction peaks to  $d_{(001)}$  indicated only basal spacing (1.55-1.58 nm) of which interlayer space was equivalent to 2 water layers, and no heterogeneity on the basal spacing was found. In addition, pore space was also considered from a theoretical sideview based on the specific surface area of smectite. The specific surface area of smectite is known to be  $750\text{-}810 \text{ m}^2/\text{g}$  [30]. If all smectite sheets orient in the same direction and the surface area of the edge of smectite sheet is neglected, the average pore space can be approximately calculated by the following equations [e.g., 31]:

$$D_{\text{int}} = \frac{2n_p}{1E6S_{\text{sm}}(1-n_p)\rho_{\text{th}}} = \frac{\rho_{\text{th}} - \rho_{\text{d}}}{5E5S_{\text{sm}} \cdot \rho_{\text{th}} \cdot \rho_{\text{d}}} \quad (4)$$

where  $D_{\text{int}}$  is the average pore space (m),  $S_{\text{sm}}$  the specific surface area of smectite ( $\text{m}^2/\text{g}$ ),  $\rho_{\text{th}}$  the solid density of smectite ( $2.7 \text{ Mg/m}^3$ ), and  $\rho_{\text{d}}$  the smectite's dry density ( $\text{Mg/m}^3$ ).

**Figure 3: XRD profiles versus  $2\theta$  for compacted smectite at a dry density of  $1.8 \text{ Mg/m}^3$ , measured at depths of 0.5, 4 and 7.5 mm from the surface of smectite**



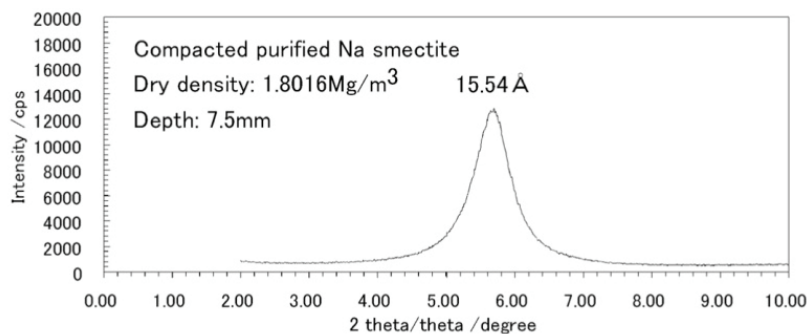
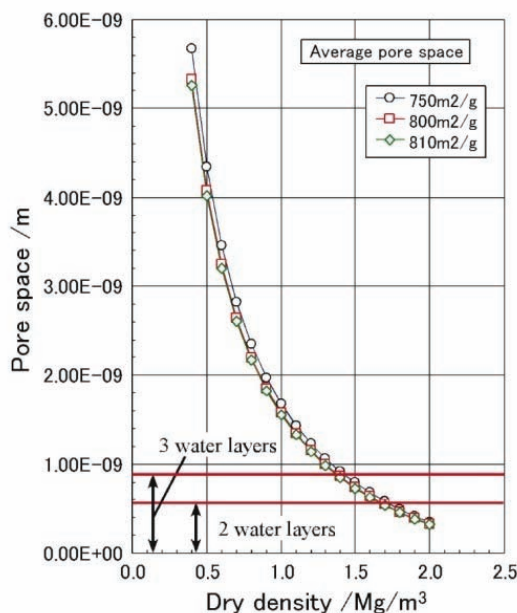


Figure 4 shows the calculated results of the average pore space of smectite versus dry density at specific surface areas of 750, 800 and 810 m<sup>2</sup>/g. The calculated results were approximately similar pore spaces for all specific surface areas. If the diameter of water molecule is 280 pm (=0.28 nm) [32], smectite's dry density where pore space is smaller than 2 water layers is approximately larger than 1.7 Mg/m<sup>3</sup>. Based on this, theoretically calculated pore space also indicates to be equivalent to 2 water layers.

**Figure 4: Calculated results of average pore space versus smectite's dry density at specific surface areas of 750, 800 and 810 m<sup>2</sup>/g**



### ***Diffusion of $\Gamma$ ions***

Figure 5 shows the measured  $D_a$  values for  $\Gamma$  ions in compacted smectite versus dry density at 22°C as well as the  $D_a$  data for  $\Gamma$  ions in Kunipia-F (saturated with distilled water: DW) [1] and  $\text{Cl}^-$  ions in Na-montmorillonite [14, 15] at 25°C. The author has reported in recent studies the  $D_a$  values of  $\Gamma$  ions in compacted smectite in the directions parallel and perpendicular to the orientation of smectite particles in a dry density range of 0.9 to 1.4 Mg/m<sup>3</sup>

[9, 24-26], and these results are also plotted together. The  $D_a$  values of  $\Gamma^-$  ions decreased with an increase of dry density, similarly to the trends reported before [1, 9, 14, 15, 24-26]. Comparing with  $D_a$  data of  $\Gamma^-$  ions reported in a previous study [1],  $D_a$  values obtained in this study are low at the same dry density. This might be because plane extension of smectite particles is larger in membranous oriented samples than in samples prepared by compaction and tortuosity for diffusion increased. It was indicated that  $\Gamma^-$  ions diffused in the interlayer of smectite.

**Figure 5: Measured  $D_a$  values for  $\Gamma^-$  ions in compacted smectite versus dry density (at 295.15 K) as well as  $D_a$  data for  $\Gamma^-$  ions in Kunipia-F [1] and  $\text{Cl}^-$  ions in Na<sup>-</sup> montmorillonite (at 298.15 K) [14, 15] (Parallel: parallel to the orientation of smectite particles, Perpendicular: perpendicular to the orientation of smectite particles)**

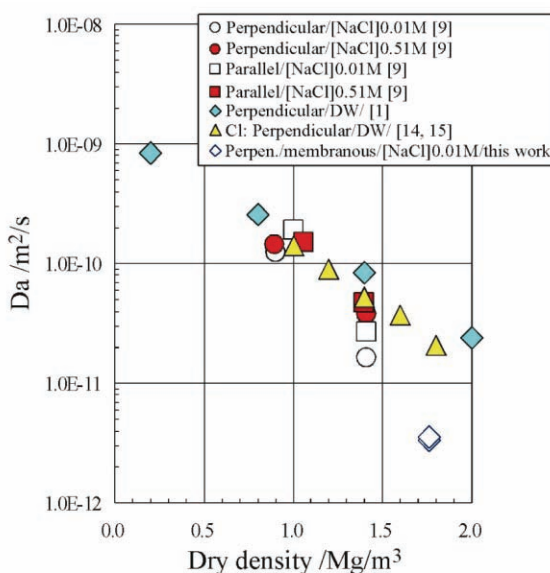
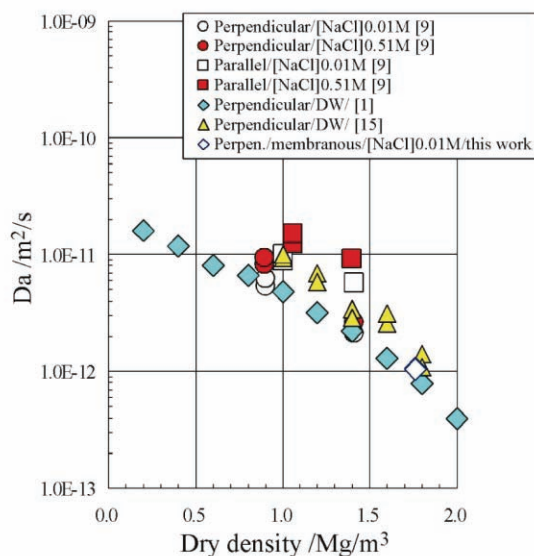


**Figure 6: Measured  $D_a$  values for  $\text{Cs}^+$  ions in compacted smectite versus the dry density for compacted smectite (at 295.15 K), Kunipia-F [1] and Na-montmorillonite (at 298.15 K) [15]**



### ***Diffusion of Cs<sup>+</sup> ions***

Figure 6 shows the measured  $D_a$  values of Cs<sup>+</sup> ions in compacted smectite versus dry density at 22°C, Kunipia-F [1] and Na-montmorillonite [15] at 25°C. The author has reported in recent studies the  $D_a$  values of Cs<sup>+</sup> ions in compacted smectite in the directions parallel and perpendicular to the orientation of smectite particles in a dry density range of 0.9 to 1.4 Mg/m<sup>3</sup> [9, 24-26]. The  $D_a$  values of Cs<sup>+</sup> ions decreased with an increase of dry density, similarly to the trends reported before [1, 9, 14, 15, 24-26], and were at similar levels as data reported before at the same dry density. In addition,  $D_a$  values increased with an increase of salinity [9, 24-26]. Since Cs<sup>+</sup> ions sorb onto smectite by ion exchange with interlayer cations in smectite, the increase in the  $D_a$  values at higher salinity is interpreted to be due to the decrease in sorption by competition with Na<sup>+</sup> ions. In contrast, similarly to  $\Gamma$  ions, tortuosity for diffusion is considered to increase due to the same effect as well. The reason that  $D_a$  values obtained in this study were however at similar levels as data reported before is considered to be that salinity of the porewater was higher than those in conventional studies.

### ***$\Delta E_a$ values of $\Gamma$ and Cs<sup>+</sup> ions***

Figures 7 and 8 show the dependences of the  $\Delta E_a$  values, calculated from Arrhenius plots, of  $\Gamma$  and Cs<sup>+</sup> ions on dry density, respectively. They concern the present results as well as those reported before [12, 14, 15]. The  $\Delta E_a$  values for  $\Gamma$  ions were at similar level ( $\Delta E_a=15.67\pm 0.37$  kJ/mol) as that ( $\Delta E_p=17.36$  kJ/mol) for the  $D^0$  of  $\Gamma$  ions at a low-dry density of ca. 1.0 Mg/m<sup>3</sup> [24], but was 35.24 kJ/mol at a dry density of 1.79 Mg/m<sup>3</sup> of which interlayer space was equivalent to 2 water layers. On the other hand, the  $\Delta E_a$  values for Cs<sup>+</sup> ions were clearly higher ( $\Delta E_a=24.66\pm 0.96$  kJ/mol) than that ( $\Delta E_p=16.47$  kJ/mol) for the  $D^0$  of Cs<sup>+</sup> ions even at low-dry density [24] and was 46.27 kJ/mol at a dry density of 1.79 Mg/m<sup>3</sup> prepared in this study.

It is reported that the  $a_{H_2O}$  of water on montmorillonite (smectite) surface is lower than that of free water [e.g., 33, 34]. It is also reported that the water near montmorillonite surface has a high-moisture potential and a high suction [35]. In these papers, one layer of water from montmorillonite surface is interpreted to be thermodynamically isostructural with ice at 0°C. Furthermore, the author has studied the thermodynamic properties of water on smectite surface [36] in parallel with this study, and has obtained similar results as Torikai *et al.* [33, 34] for the correlation between the  $a_{H_2O}$  of water and water content. If we think a pair of smectite sheets, this is equal to 2 water layers in the interlayer distance of smectite, and equals to the dry density of smectite prepared in this study.

**Figure 7:** A dependence of  $\Delta E_a$  values for  $I^-$  ions in compacted smectite on dry density obtained in this study together with  $\Delta E_a$  data of  $Cl^-$  ions in Na-montmorillonite [14, 15]

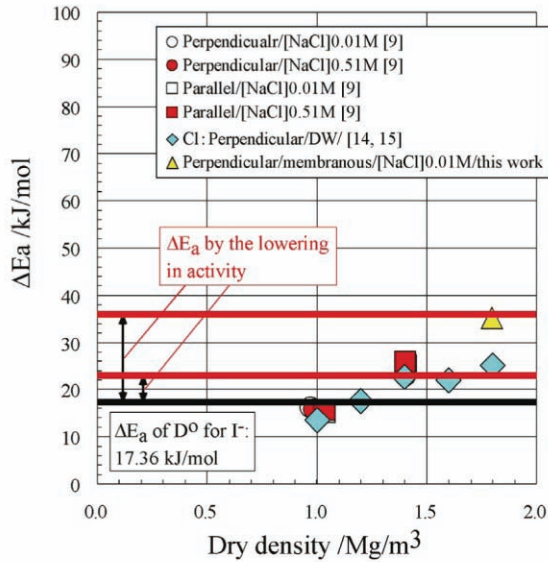
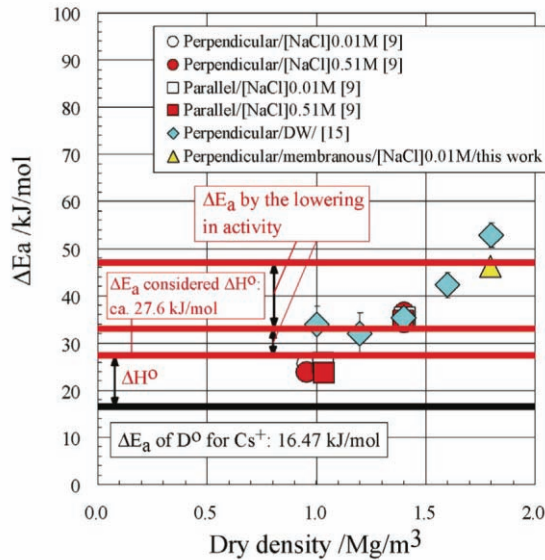


**Figure 8** A dependence of  $\Delta E_a$  values for  $Cs^+$  ions in compacted smectite on dry density obtained in this study together with  $\Delta E_a$  data of  $Cs^+$  ions in Na-montmorillonite [12, 15]



Suzuki *et al.* [21] have measured  $\Delta E_a$  values for the  $D_e$  of HDO, which is non-sorbing and not reactive, in compacted smectite, and the  $\Delta E_a$  values increased by ca. 5 kJ/mol with an increase of dry density in a dry density range of 0.9 to 1.35 Mg/m<sup>3</sup>. From the correlation between the  $a_{H_2O}$  of water and water content [33, 34], the  $a_{H_2O}$  of water decreased by 0.1 with an increase of dry density in this dry density range. That is to say, it was estimated that the decrease of 0.1 in the  $a_{H_2O}$  of water induced the increase of 5 kJ/mol in  $\Delta E_a$ . Water content at a dry density of 1.79 Mg/m<sup>3</sup> saturated with distilled water is ca. 20%, and the  $a_{H_2O}$  of water in this density is estimated to be ca. 0.6 [33, 34, 36]. From the correlation between the change in  $\Delta E_a$

and that in the  $a_{\text{H}_2\text{O}}$  of water, the  $\Delta E_a$  of  $\Gamma^-$  ions at a dry density of  $1.79 \text{ Mg/m}^3$  is estimated to be ca.  $37.4 \text{ kJ/mol}$ . This is in good agreement with the measured data. Therefore, such high  $\Delta E_a$  for  $\Gamma^-$  ions in the interlayer of smectite is considered to be attributed to the lowering in the  $a_{\text{H}_2\text{O}}$  of interlayer water.

On the other hand, the  $\Delta E_a$  values of  $\text{Cs}^+$  ions include enthalpy for sorption ( $K_d$ ) onto smectite. Since  $\text{Cs}^+$  ions sorb onto smectite by ion exchange between  $\text{Cs}^+$  and  $\text{Na}^+$  ions in the smectite interlayer, the  $\Delta E_a$  values of  $\text{Cs}^+$  ions can be thought to include both effects of the  $\Delta H^\circ$  between  $\text{Cs}^+$  and  $\text{Na}^+$  ions in the interlayer and  $\Delta E_a$  for the diffusion of  $\text{Cs}^+$  ions in the porewater of smectite ( $\Delta E_p$ ).

Assuming that the  $\Delta E_p$  of  $\text{Cs}^+$  ions is equivalent to  $\Delta E_a$  of its  $\text{D}^\circ$  and  $n_p$  can be regarded as much smaller compared with  $\rho_d \cdot K_d$ , the relationship between  $\Delta E_a$  and  $\Delta H^\circ$  can be approximately derived as follows:

$$\Delta E_a = \Delta E_p - \Delta H^\circ \quad (5)$$

where  $\Delta E_p$  is the  $\Delta E_a$  for  $\text{D}^\circ$  (J/mol) and  $\Delta H^\circ$  the ion exchange enthalpy (J/mol).

Since  $\Delta E_p = 16.47 \text{ kJ/mol}$  for  $\text{Cs}^+$  ions and  $\Delta H^\circ = -11.10 \text{ kJ/mol}$  for the  $\text{Cs}^+/\text{Na}^+$  ion exchange in a Na-smectite (Chambers montmorillonite) [37], expression (5) gives  $\Delta E_a = 27.57 \text{ kJ/mol}$ . This is relatively consistent with  $\Delta E_a$  values obtained at low-dry densities. In contrast, as discussed in  $\Gamma^-$  ions, the decrease of 0.1 in the  $a_{\text{H}_2\text{O}}$  of water induces the increase of  $5 \text{ kJ/mol}$  in  $\Delta E_a$ . Based on this empirical correlation for the increase of  $\Delta E_a$  with a decrease of the  $a_{\text{H}_2\text{O}}$  of water, the  $\Delta E_a$  of  $\text{Cs}^+$  ions at a dry density of  $1.79 \text{ Mg/m}^3$  is estimated to be ca.  $47.6 \text{ kJ/mol}$ . This value is in good agreement with the measured data. Therefore, such high  $\Delta E_a$  for  $\text{Cs}^+$  ions in the interlayer of smectite is considered to be due to the combined effects of  $\Delta H^\circ$  for the  $\text{Cs}^+/\text{Na}^+$  ion exchange in smectite as well as the lowering in the  $a_{\text{H}_2\text{O}}$  of interlayer water.

## Conclusions

The  $D_a$  and  $\Delta E_a$  values of  $\Gamma^-$  and  $\text{Cs}^+$  ions in compacted Na-smectite were measured at an average dry density of  $1.79 \text{ Mg/m}^3$  under the conditions that interlayer space and orientation of smectite stacks were controlled to be only 2 water layers and in the direction perpendicular to diffusion direction, respectively. Increasing dry density leads to smaller  $D_a$  values for both ions, compared with data obtained before. This is considered to be attributed to higher tortuosity. In contrast, the reason that  $D_a$  values for  $\text{Cs}^+$  ions were at similar levels as data reported before is considered to be that salinity of the porewater was higher than in conventional studies.

The  $\Delta E_a$  values of  $\Gamma^-$  and  $\text{Cs}^+$  ions obtained were  $35.24$  and  $46.27 \text{ kJ/mol}$  at a dry density of  $1.79 \text{ Mg/m}^3$ , and were clearly higher than those for the  $\text{D}^\circ$  values of individual ions. Since the decrease of 0.1 in the  $a_{\text{H}_2\text{O}}$  of water induces the increase of  $5 \text{ kJ/mol}$  in  $\Delta E_a$  and the  $a_{\text{H}_2\text{O}}$  of water at this dry density is about 0.6, the increase of the  $\Delta E_a$  for  $\Gamma^-$  ions in the interlayer of smectite is considered to be due to the effect of the lowering in the  $a_{\text{H}_2\text{O}}$  of interlayer water. In contrast,

since Cs<sup>+</sup> ions sorb onto smectite by ion exchange, the increase of the  $\Delta E_a$  for Cs<sup>+</sup> ions in the interlayer of smectite is considered to be due to the combined effects of the  $\Delta H^0$  of Cs<sup>+</sup> and Na<sup>+</sup> interchange in smectite as well as the lowering in the  $a_{H_2O}$  of interlayer water.

## REFERENCES

- [1] H. Sato, T. Ashida, Y. Kohara, M. Yui, N. Sasaki, Effect of Dry Density on Diffusion of Some Radionuclides in Compacted Sodium Bentonite, *J. Nucl. Sci. Technol.*, 29 (9), pp.873-882 (1992).
- [2] K. Idemitsu, H. Furuya, Y. Inagaki, Diffusion of Corrosion Products of Iron in Compacted Bentonite, *Mater. Res. Soc. Symp. Proc.*, Vol.294, pp.467-474 (1993).
- [3] H. Sato, T. Ashida, Y. Kohara, M. Yui, Study on Retardation Mechanism of <sup>3</sup>H, <sup>99</sup>Tc, <sup>137</sup>Cs, <sup>237</sup>Np and <sup>241</sup>Am in Compacted Sodium Bentonite, *Mater. Res. Soc. Symp. Proc.*, Vol.294, pp.403-408 (1993).
- [4] H. Sato, M. Yui, H. Yoshikawa, Diffusion Behaviour for Se and Zr in Sodium-Bentonite, *Mater. Res. Soc. Symp. Proc.*, Vol.353, pp.269-276 (1995).
- [5] H. Sato, M. Yui, Diffusion of Ni in Compacted Bentonite, *J. Nucl. Sci. Technol.*, 34 (3), pp.334-336 (1997).
- [6] H. Sato, Diffusion Behaviour of Se(-II) and Sm(III) in compacted sodium bentonite, *Radiochim. Acta*, 82, pp.173-178 (1998).
- [7] T. Kozaki, H. Sato, S. Sato, H. Ohashi, Diffusion Mechanism of Cesium Ions in Compacted Montmorillonite, *Eng. Geology*, 54, pp.223-230 (1999).
- [8] A. Murrinen, J. Rantanen, P. Penttiä-Hiltunen, *Mater. Res. Soc. Symp. Proc.*, Vol.50, pp.617-624 (1985).
- [9] H. Sato, Effects of the Orientation of Clay Particles and Ionic Strength on Diffusion and Activation Enthalpies of I<sup>-</sup> and Cs<sup>+</sup> Ions in Compacted Bentonite, *Mater. Res. Soc. Symp. Proc.*, Vol.824, pp.485-490 (2004).
- [10] H. Sato, The Effect of Pore Structural Factors on Diffusion in Compacted Bentonite, *Mater. Res. Soc. Symp. Proc.*, Vol.663, pp.605-615 (2001).
- [11] M. Nakajima, T. Kozaki, H. Kato, S. Sato, H. Ohashi, The Dependence of the Diffusion Coefficients of <sup>3</sup>H and Cs on Grain Size in Compacted Montmorillonite, *Mater. Res. Soc. Symp. Proc.*, Vol.506, pp.947-948 (1998).

- [12] T. Kozaki, H. Sato, A. Fujishima, S. Sato, H. Ohashi, Activation Energy for Diffusion for Cesium in Compacted Sodium Montmorillonite, *J. Nucl. Sci. Technol.*, 33 (6), pp.522-524 (1996).
- [13] T. Kozaki, H. Sato, A. Fujishima, S. Sato, H. Ohashi, Effect of Dry Density on Activation Energy for Diffusion of Strontium in Compacted Sodium Montmorillonite, *Mater. Res. Soc. Symp. Proc.*, Vol.465, pp.893-900 (1997).
- [14] T. Kozaki, N. Saito, A. Fujishima, S. Sato, H. Ohashi, Activation Energy for Diffusion of Chloride Ions in Compacted Sodium Bentonite, *J. Contam. Hydrol.*, 35, pp.67-75 (1998).
- [15] T. Kozaki, Fundamental Study on Corrosion of Overpack in Buffer Material and Nuclide Migration Behaviour in the Geological Disposal of High-Level Radioactive Waste, Doctoral Thesis, Hokkaido Univ. (1999) [in Japanese].
- [16] J. Liu, T. Kozaki, S. Sato, M. Horiuchi, Effects of Silica Sand and Salinity on Nuclide Migration Behaviour in Clay, Rep. 5<sup>th</sup> Information Exchange Meeting on the Geological Disposal of Radioactive Waste, Feb. 27-28, 2003, Hokkaido Univ., Japan, pp.23-34 (2003) [in Japanese].
- [17] J. Liu, N. Yamada, T. Kozaki, S. Sato, H. Ohashi, Effect of Silica Sand on Activation Energy for Diffusion of Sodium Ions in Montmorillonite and Silica Sand Mixture, *J. Contam. Hydrol.*, 61, pp.85-93 (2003).
- [18] H. Sato, A Study on the Effect of Clay Particle Orientation on Diffusion in Compacted Bentonite, Proc. 28<sup>th</sup> Symp. on HLW, LLW, Mixed and Hazardous Wastes and Environmental Restoration, Feb. 24-28, 2002, Tucson, AZ, USA, pp.1-15 (2002).
- [19] H. Sato, S. Suzuki, Fundamental Study on the Effect of an Orientation of Clay Particles on Diffusion Pathway in Compacted Bentonite, Reprints for Specialist Workshop on Clay Microstructure and Its Importance to Soil Behaviour, Oct. 15-17, 2002, Lund, Sweden, pp.87-96 (2002).
- [20] H. Sato, S. Suzuki, Fundamental Study on the Effect of an Orientation of Clay Particles on Diffusion Pathway in Compacted Bentonite, *Appl. Clay Sci.*, 23, pp.47-55 (2003).
- [21] S. Suzuki, H. Sato, T. Ishidera, N. Fujii, Study on Anisotropy of Effective Diffusion Coefficient and Activation Energy for Deuterated Water in Compacted Sodium Bentonite, *J. Contam. Hydrol.*, 68, pp.23-27 (2004).
- [22] S. Suzuki, S. Prayongphan, Y. Ichikawa, Insitu Observations of the Swelling Pressure of Bentonite Aggregates in NaCl solution for Interaction of Water Permeability in Compacted Bentonite, Proc. for Korea-Japan Joint Workshop on the Radioactive Waste Disposal 2004, Dec. 7, 2004, Daejeon, Korea, pp.103-118 (2004).
- [23] H. Sato, S. Miyamoto, Diffusion Behaviour of Selenite and Hydroselenide in Compacted Bentonite, *Appl. Clay Sci.*, 26, pp.47-55 (2004).

- [24] H. Sato, Effects of the Orientation of Clay Particles and Ionic Strength on Diffusion and Activation Enthalpies of  $\Gamma^-$  and  $\text{Cs}^+$  Ions in Compacted Bentonite (II), Mater. Res. Soc. Symp. Proc., Vol.932, pp.905-912 (2005).
- [25] H. Sato, Anisotropy in Diffusion and Activation Energies of  $\Gamma^-$  and  $\text{Cs}^+$  Ions in Compacted Smectite, Proc. 13<sup>th</sup> Int. Conf. on Nucl. Eng., May 16-20, 2005, Beijing, China, ICONE13-50313, pp.1-8 (2005).
- [26] H. Sato, Activation Energy of Diffusion for Iodine and Cesium in Compacted Smectite, Proc. 2<sup>nd</sup> Japan-Korea Joint Workshop on Radioactive Waste Disposal 2005: Interaction Between NBS and EBS, Oct. 6-7, 2005, Tokyo Inst. of Technol., pp.136-153 (2005).
- [27] M. Ito, M. Okamoto, M. Shibata, Y. Sasaki, T. Danbara, K. Suzuki, T. Watanabe, Mineral Composition of Bentonite, PNC TN8430 93-003 (1993) [in Japanese].
- [28] J. Crank, The Mathematics of Diffusion, 2<sup>nd</sup> ed., Pergamon Press, Oxford (1975).
- [29] Japan Nuclear Cycle Development Institute (JNC), 2<sup>nd</sup> Progress Report on Research and Development for the Geological Disposal of HLW in Japan – H12: Project to Establish the Scientific and Technical Basis for HLW Disposal in Japan – Supporting Report 3: Safety Assessment of the Geological Disposal System, JNC TN1410 2000-004 (2000).
- [30] H. Sato, A Study on Nuclide Migration in Buffer Materials and Rocks for Geological Disposal of Radioactive Waste, Doctoral Thesis, Akita University (1997) [in Japanese].
- [31] H. Sato, Effects of Orientation of Clay Particles and Ionic Strength on Diffusion and Activation Energies of  $\text{Cs}^+$  and  $\Gamma^-$  Ions in Compacted Bentonite, JNC TN1400 2003-016 (2004) [in Japanese].
- [32] H. Otaki, Ion-No-Suiwa (Ionic Hydration), Kyoritsu (1990) [in Japanese].
- [33] Y. Torikai, S. Sato, H. Ohashi, Thermodynamic Properties of Water in Compacted Bentonite under External Pressure-free Conditions, Mater. Res. Soc. Symp. Proc., Vol.353, pp.321-328 (1995).
- [34] Y. Torikai, S. Sato, H. Ohashi, Thermodynamic Properties of Water in Compacted Sodium Montmorillonite, Nucl. Technol., 115, pp.73-80 (1996).
- [35] T. Kanno, H. Wakamatsu, Moisture Adsorption and Volume Change of Partially Saturated Bentonite Buffer Materials, Mater. Res. Soc. Symp. Proc., Vol.294, pp.425-431 (1993).
- [36] H. Sato, Thermodynamic Data of Water on Smectite Surface and Those Application to Swelling Pressure of Compacted Bentonite, OECD/NEA Rep., Int. Workshop on Mobile Fission and Activation Products in Nuclear Waste Disposal, La Baule, France, Jan., 16-19, 2007 (these proceedings).
- [37] R. G. Gast, Alkali Metal Cation Exchange on Chambers Montmorillonite, Soil Sci. Soc. Amer. Proc., 36, pp.14-19 (1972).



# **THERMODYNAMIC DATA OF WATER ON SMECTITE SURFACE AND THOSE APPLICATIONS TO SWELLING PRESSURE OF COMPACTED BENTONITE**

**Haruo Sato**

Japan Atomic Energy Agency (JAEA), 432-2, Hokushin, Horonobe-cho,  
Hokkaido 098-3224, Japan

## **Abstract**

Swelling pressure was discussed focusing on the thermodynamic properties of water on smectite (montmorillonite) which is the major clay mineral constituent of the bentonite buffer. The thermodynamic data of the water on the smectite surface were obtained as a function of water content and temperature in a range of dry density 0.6-0.9 Mg/m<sup>3</sup>. Purified Na-smectite of which all interlayer cations were exchanged with Na<sup>+</sup> ions, was used. The activity ( $a_{\text{H}_2\text{O}}$ ) and the relative partial molar Gibbs free energy ( $\Delta G_{\text{H}_2\text{O}}$ ) of the water were obtained at 25°C. Both  $a_{\text{H}_2\text{O}}$  and  $\Delta G_{\text{H}_2\text{O}}$  decreased with a decrease of water content, and similar results were obtained to data reported for montmorillonite (Kunipia-F bentonite). Since the specific surface area of smectite is about 800 m<sup>2</sup>/g, water up to approximately 2 water layers from smectite surface is thermodynamically evaluated to be bound. Swelling pressure versus smectite partial density was calculated based on  $\Delta G_{\text{H}_2\text{O}}$  and compared to data experimentally obtained for various kinds of bentonites. The calculated results were in good agreement with the measured data over the range of smectite partial density between 1.0 and 2.0 Mg/m<sup>3</sup>.

## Introduction

In the safety assessment of the geological disposal for a high-level radioactive waste, radionuclides leached from vitrified wastes will migrate in the compacted bentonite buffer and the host rock. It may finally reach the biosphere through various pathways and processes after a long time. The rate of radionuclide release as leached from the vitrified wastes depends on the effective diffusivity and the apparent diffusivity. Particularly, apparent diffusivity strongly depends on retardation factors such as distribution coefficients of radionuclides in the geological materials composing the bentonite and geosphere. These interactions occur at the solid-liquid interface, which makes it important to understand these reactions.

The diffusion of radionuclides and ions in compacted bentonite and in the rock matrix is mediated by the porewater. Thus, the nature of the porewater directly affects how the radionuclides are transported through the buffer materials and the host rock. Geochemical predictions on the resulting porewater composition due to reactions on the solid-liquid interface assume that the porewater has the same properties as free water [1]. However, it has been reported that the activity of water near the surface of montmorillonite, a major constituent of bentonite, was lower than that of free water. It is also considered that part of the water had a low chemical potential [2, 3]. Moreover, it has also been reported that the water near the surface of montmorillonite has a high-moisture potential and a high suction [4, 5]. The author has also reported in a previous study that porewater on the surface of sandstone was weakly affected up to a distance of approximately 10 water layers from the solid surface and was strongly bound up to a distance of approximately 4 water layers [6]. Thus, in view of thermodynamics, porewater cannot be treated similar to free water.

The moisture potential of bentonite is closely related to swelling pressure. Kahr *et al.* [7] have predicted the swelling pressure for two kinds of bentonites (Montigel, MX-80) versus dry density. These were based on water vapour adsorption-desorption isotherms that were experimentally determined, and were consistent with obtained results. Kanno *et al.* [5] have also arrived at similar conclusions for the Japanese Na-bentonite (Kunigel-V1 bentonite).

With respect to the thermodynamic properties of porewater in bentonite, it has been reported by measuring its activity, the relative partial molar Gibbs free energy, the relative partial molar enthalpy and entropy of water in studies utilised vapour pressure measurements that the activity of water near the surface of montmorillonite is lower than free water and that its chemical potential is also low [2, 3]. Moisture potential measurements have previously been performed versus water content and temperature. In relation to studies regarding water diffusion behaviour in compacted bentonite, it is reported that the moisture potential and suction increased with a decrease of water content of bentonite [4, 5]. This indicates that water at the solid surface is thermodynamically different from free water.

In this study, swelling pressure of compacted bentonite, one of the fundamental properties, was discussed focusing on the thermodynamic data of water on the surface of smectite which is a major clay mineral constituent of the bentonite buffer. The vapour pressure method was utilised in this study to determine the thermodynamic data of the water on the smectite surface.

## Vapour pressure measurements

### *Material and experimental conditions*

Purified Na-smectite was prepared in this study. All interlayer cations were exchanged with Na<sup>+</sup> ions and soluble salts such as calcite were also removed. As the starting material, Kunipia-P bentonite (obtained from Kunimine Industries Co. Ltd.) was used, of which smectite content is approximately 100 wt.%.

**Table 1: Experimental conditions for the measurement of water vapour pressure**

Item	Method / Sample / Condition
Method	Vapour pressure method
Bentonite	Na-smectite (Kunipia-P of which interlayer cations were exchanged with Na <sup>+</sup> ions and soluble salts were removed) CEC: 122.8 meq/100 g
Dry density	0.6-0.9 Mg/m <sup>3</sup> (size: $\phi$ 10x5 mm) 3 samples
Water content	0-83 %
Temperature	15-40°C (temperature interval: 3-5°C)

During a week to 61 d, bentonite powder was put in contact with a 1 M-NaCl solution at a solid-liquid ratio of 120 g/5 liter. Then the bentonite was separated from the suspension. This operation was repeated 3 times. At the end of the third immersion with NaCl, the solid-liquid separation was made by centrifugation at 3 000 rpm for 20 mn. The bentonite was washed 3 times with 80% ethyl alcohol. Also in these washings, the solid-liquid separation was made by centrifugation. The washed bentonite was dispersed in distilled water and then only particles smaller than 0.5  $\mu$ m in diameter were collected by centrifugation at 3 000 rpm for 5 mn. Thus, purified Na-smectite was prepared.

The cation exchange capacity (CEC) measured by the ammonium ion exchange method was 122.8 meq/100 g. This CEC is at similar level as that (116.5 meq/100 g [8]) of montmorillonite (Kunipia-F bentonite). Incidentally, the CEC of the Kunipia-F bentonite measured in this study was 111.2 meq/100 g.

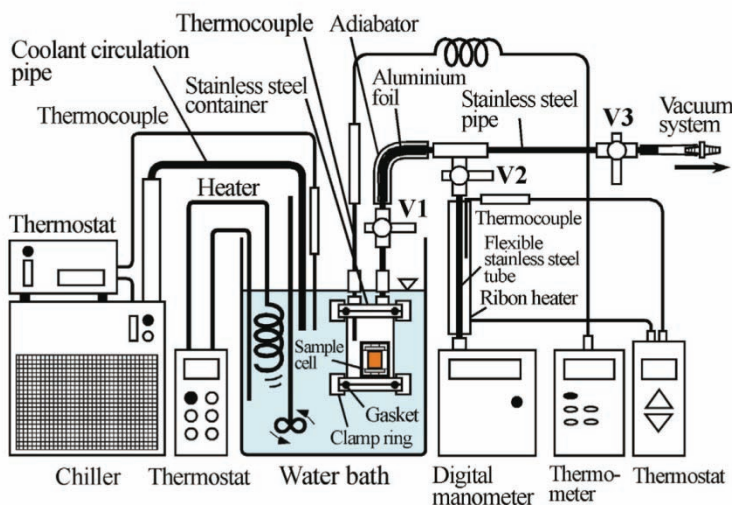
Table 1 shows the experimental conditions. Compacted smectite samples with a size of  $\phi$ 10x5 mm were used in all measurements.

### *Apparatus and procedure*

Figure 1 illustrates an experimental apparatus for the measurement of water vapour pressure. The apparatus consists of a digital manometer DM-2 (Shibata Scientific Technol. Ltd.) and a cylindrical stainless steel container, into which a thermocouple connected with a thermometer, was inserted. The top and bottom lids of the cylindrical container are secured with a clamp ring and gasket. The digital manometer is connected with a stainless steel pipe covered

with an adiadiator and a flexible stainless steel tube covered with a ribbon heater connected with a thermostat to maintain the temperature of the water vapour during the measurements.

**Figure 1: Experimental apparatus for the measurement of water vapour pressure**



Purified smectite powder dried at 110°C was filled into an acrylic sample holder in a sample cell to obtain dry densities of 0.6 to 0.9 Mg/m<sup>3</sup>. The smectite in the sample holder was initially moisturized with distilled water and the sample cell was disassembled. The surface of the sample holder was wiped off and then the sample cell was again assembled by using dried parts. This sample cell was put in a stainless steel container attached to a vacuum system. The container was sealed with clamp rings and gaskets to keep its air tightness. The container was then placed in a constant-temperature water bath, which can control the water temperature with an accuracy of 0.01°C. The inner diameter of the stainless steel pipe connected with the container is about 4 mm, which is substantially larger than the mean free path of water vapour ~0.05 mm at the low-pressure region of the water vapour pressure measurements (about 0.1 kPa) [3]. Valves 1, 2 and 3 were initially opened. The container was evacuated for about 10 min by a rotary pump, and then valve 3 closed. Water vapour pressure and temperature were periodically measured with accuracies of 0.1 kPa and 0.1 C, respectively. This operation was repeated until the water vapour pressure reaches a constant (water vapour pressure reaches equilibrium with porewater in smectite). Thus, the water vapour pressure in equilibrium with the porewater was measured at a temperature interval of 3 to 5°C as a function of water content. Three sets of containers were prepared and measurements were simultaneously performed in triplicate.

At the end of a series of water vapour pressure measurements, the sample cell was removed from the container and weighed. The sample cell was placed again in the container and was evacuated to lower the water content for a while. The aforementioned experimental procedure was repeated. Water vapour pressure during cooling was also measured to check for reversibility.

After all water vapour pressure measurements were performed, the smectite sample was dried at 110°C to obtain the dry weight. Incidentally, no water vapour pressure was detected for this dried sample over the range of temperature. The water content was determined from the difference in the dry weight and the moisturised weight of the samples used in each water vapour pressure measurement.

The water content ( $W_c$  (%)) is determined by the following relation:

$$W_c = \left( \frac{M_s - M_d}{M_d} \right) \times 100 \quad (1)$$

where  $W_c$  is the water content (%),  $M_s$  the moisturised weight of the sample (g), and  $M_d$  the dry weight of the sample (g).

The activity of porewater at a constant temperature is determined by the following relation:

$$a_{H_2O} = \frac{P_{H_2O}}{P_{H_2O}^o} \quad (2)$$

where  $a_{H_2O}$  is the activity of porewater,  $P_{H_2O}$  the water vapour pressure of poerwater at 25°C (Pa), and  $P_{H_2O}^o$  the water vapour pressure of pure water at 25°C (3.168 kPa [9]).

The relative partial molar Gibbs free energy is determined by the following relation:

$$\Delta G_{H_2O} = RT \ln \left( \frac{P_{H_2O}}{P_{H_2O}^o} \right) \quad (3)$$

where  $\Delta G_{H_2O}$  is the relative partial molar Gibbs free energy of porewater (J/mol), R the gas constant (8.314 J/mol/K), and T the absolute temperature (K).

The enthalpy of vaporisation is obtained from the temperature dependence of water vapour pressure as described by the following Clasius-Clapeyron equation:

$$\frac{d \ln P_{H_2O}}{d(1/T)} = \frac{\Delta H_V(s)}{RT} \quad (4)$$

The relative partial molar enthalpy is determined by the following equation:

$$\Delta H_{H_2O} = \Delta H_V^o(H_2O) - \Delta H_V(s) \quad (5)$$

where  $\Delta H_V(s)$  is the enthalpy of vaporisation of porewater (J/mol),  $\Delta H_{H_2O}$  the relative partial molar enthalpy of porewater (J/mol), and  $\Delta H_V^o(H_2O)$  the enthalpy of vaporisation of pure water (44.0 kJ/mol [9]).

Moreover, the relative partial molar entropy is determined from the following relation:

$$\Delta G_{\text{H}_2\text{O}} = \Delta H_{\text{H}_2\text{O}} - T \Delta S_{\text{H}_2\text{O}} \quad (6)$$

where  $\Delta S_{\text{H}_2\text{O}}$  is the relative partial molar entropy of porewater (J/mol/K).

## Results and Discussion

### *Activity and relative partial molar gibbs free energy of porewater*

Figure 2 shows an example of the measured results of  $\ln(P_{\text{H}_2\text{O}}/P^{\circ}_{\text{H}_2\text{O}})$  against  $1/T$ . As shown in Figure 2, both water vapour pressures to upward ( $\circ$ ) and downward temperatures ( $\bullet$ ) are in good agreement. This indicates that obtained water vapour pressures are all in equilibrium.

**Figure 2: An example of the correlations of  $\ln(P_{\text{H}_2\text{O}}/P^{\circ}_{\text{H}_2\text{O}})$  of porewater in smectite with  $1/T$**

$\circ$ : measured data for upward temperature,  
 $\bullet$ : measured data for downward temperature, water content: 78.6%

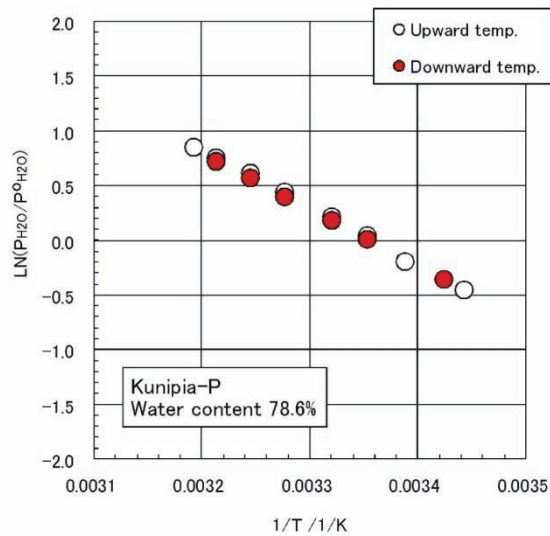
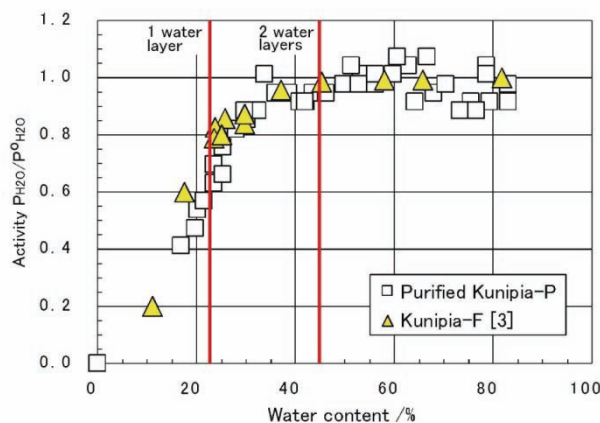


Figure 3 shows the activities of porewater in smectite obtained in this study and those of water in montmorillonite (Kunipia-F bentonite) [3] at 25°C as a function of water content.

**Figure 3: Activities of porewater in smectite obtained in this study (this work) and those of water in montmorillonite (Kunipia-F bentonite) [3] at 25°C as a function water content**



**Table 2: Representative data of the measured results of water vapour pressure, the calculated results of the activity and  $\Delta G_{H_2O}$  of porewater and the activities and  $\Delta G_{H_2O}$  values for some popular electrolytes at 25°C**

Solution/ $W_c$ (%)	$P_{H_2O}$ (kPa)	Activity	$\Delta G_{H_2O}$ (kJ/mol)
Pure water [9]	3.168	1.000	0.000
0.5 m NaCl		0.98355	-0.0411
5 m NaCl		0.8068	-0.5322
0.5 m NaNO <sub>3</sub>		0.92849	-0.1861
6 m NaNO <sub>3</sub>		0.44767	-1.992
0.5 m Na <sub>2</sub> SO <sub>4</sub>		0.86328	-0.3644
4 m Na <sub>2</sub> SO <sub>4</sub>		0.28242	-3.134
78.62	3.2	1.010	0.0247
59.86	3.2	1.010	0.0247
53.24	3.2	1.010	0.0247
49.68	3.1	0.978	-0.054
38.72	3.0	0.947	-0.135
35.91	3.0	0.947	-0.135
29.76	2.8	0.884	-0.306
28.09	2.6	0.821	-0.490
25.29	2.4	0.758	-0.688
23.65	2.2	0.694	-0.904
21.59	1.8	0.568	-1.402
20.11	1.7	0.537	-1.543
19.80	1.5	0.473	-1.854
16.78	1.3	0.410	-2.208

Table 2 shows representative data of the measured results of the water vapour pressure, the calculated results of the activity and  $\Delta G_{H_2O}$  of the porewater in smectite and the activities and  $\Delta G_{H_2O}$  values for some electrolytes at 25°C. The activities and  $\Delta G_{H_2O}$  values for those electrolytes were calculated based on their respective osmotic coefficients [10] from the following relations and Eq. (3);

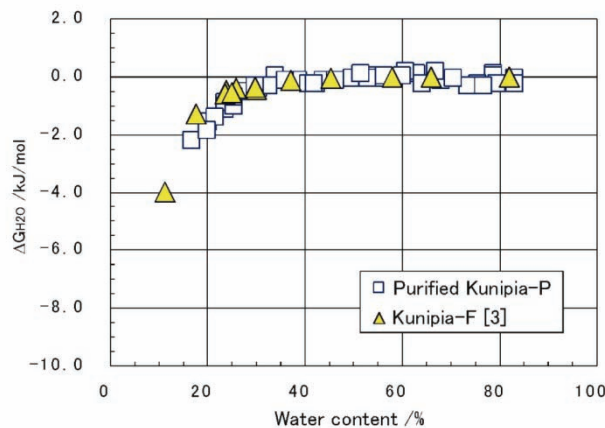
$$\ln a_{\text{H}_2\text{O}} = -\frac{m \gamma W}{1000} \phi = -\frac{M \gamma W}{1000 d d_0} \phi \quad (7)$$

where  $m$  is the concentration of the electrolyte in molality (mol/kg),  $\gamma$  the stoichiometric mole number of ions produced from the electrolyte of 1 mol (the number of ions produced by dissociation of 1 molecule),  $W$  the molecular weight of water (18.01528),  $\phi$  the osmotic coefficient,  $M$  the concentration of the electrolyte in molar (mol/dm<sup>3</sup>),  $d$  the specific gravity of the electrolyte at 25°C, and  $d_0$  the density of water at 25°C (0.997044 kg/dm<sup>3</sup>).

Some data scatterings are found in Figure 3, but the activities of porewater are approximately in unity at the region where water content is higher than about 40 %. The porewater can be regarded here as free water in the region of this water content. The activity of the porewater showed a tendency to gradually decrease with a lowering of water content in the region where water content is about 40%. Similar results were obtained to data reported for montmorillonite (Kunipia-F bentonite) of which smectite content was approximately 100 wt.% [3].

Figure 4 shows  $\Delta G_{\text{H}_2\text{O}}$  values obtained in this study and those of water in montmorillonite [3] at 25°C as a function of water content. The  $\Delta G_{\text{H}_2\text{O}}$  showed a tendency to gradually decrease with a lowering of water content in the region where water content is about 40%, similar to the trend of porewater activity. This indicates that the porewater changed into low-chemical potential, which is more stable in the region where water content is lower than about 40%.

**Figure 4:  $\Delta G_{\text{H}_2\text{O}}$  values obtained in this study (this work) and those of water in montmorillonite [3] at 25°C as a function water content**

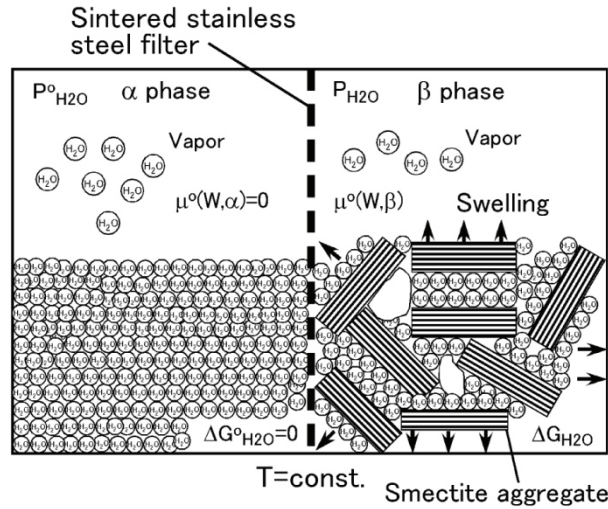


### *Region of porewater affected from smectite surface*

The region of porewater affected from smectite surface was deduced from the correlations of activity and  $\Delta G_{\text{H}_2\text{O}}$  versus water content. The diameter of water molecule at 25°C was assumed to be 280 pm (=0.28 nm) [11] in the estimation. Since there are 55.36 mol per 1 dm<sup>3</sup> of water molecules at 25°C based on water density, the surface area of 1 mol water molecule for a

mono-layer is estimated to be  $6.43E4 \text{ m}^2$ . Since the specific surface area of smectite is about  $800 \text{ m}^2/\text{g}$ , if the smectite surface is hydrated by a mono-layer of water molecules, the water weight per 1 g of smectite is 0.224 g. This corresponds to a water content of 22.4%. Since the decrease in chemical potential was found in the region where water content is lower than about 40%, porewater up to approximately 2 water layers from the surface of smectite is estimated to be somehow bound or affected. Bold lines in Figure 3 show water contents which correspond to 1 and 2 water layers from the surface of smectite.

**Figure 5 Concept of the chemical potential balance of water in equilibrium between free water and moisturised smectite at a constant temperature**



#### *Application of thermodynamic data of water to swelling pressure of compacted bentonite*

Figure 5 illustrates a concept of the chemical potential balance of water in equilibrium between free water and moisturised smectite through sintered stainless steel filter at a constant temperature. Where, the  $\alpha$  phase is the free water and the  $\beta$  phase is the moisturised smectite, and both phases contact through sintered stainless steel filter. If the  $\alpha$  and  $\beta$  phases reach equilibrium by penetration of the water to the smectite, the total chemical potentials in both phases are equivalent, and then the following relation makes good.

$$\mu^o(W, \alpha) = \mu^o(W, \beta) \quad (8)$$

Where,  $\mu^o(W, \alpha)$  is the total chemical potential of water in  $\alpha$  phase (J/mol), and  $\mu^o(W, \beta)$  the total chemical potential of water in  $\beta$  phase (J/mol).

In above system, since  $\mu^o(W, \alpha) = 0$  and the chemical potential of water in  $\beta$  phase is different from  $\alpha$  phase by  $\Delta G_{H_2O}$ , this different  $\Delta G_{H_2O}$  acts as swelling energy to take the energy balance in both phases. Therefore, the energy balance in  $\beta$  phase is expressed as below.

$$\mu^{\circ}(W, \beta) = RT \ln \left( \frac{P_{H_2O}}{P_{H_2O}^{\circ}} \right) + \int_{P_{ext}^{\circ}}^{P_{ext}} V_w dP = 0 \quad (9)$$

Where,  $P_{ext}^{\circ}$  and  $P_{ext}$  are the external pressure at dried condition (Pa) and the external pressure at saturated condition (Pa), respectively, and  $V_w$  is the volume of water per mol ( $m^3/mol$ ).

If  $V_w$  is a constant between  $P_{ext}^{\circ}$  and  $P_{ext}$ , swelling pressure is finally calculated from the following relations:

$$\Delta P_{ext} = P_{ext} - P_{ext}^{\circ} = -\frac{RT}{V_w} \ln \left( \frac{P_{H_2O}}{P_{H_2O}^{\circ}} \right) = -\frac{\Delta G_{H_2O}}{V_w} \quad (10)$$

where  $\Delta P_{ext}$  is the swelling pressure (Pa).

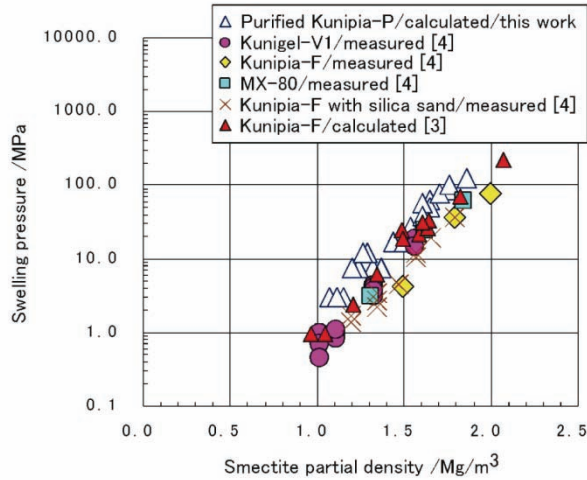
Based on Eq. (10) and  $\Delta G_{H_2O}$  determined in this study, swelling pressure versus smectite partial density (= montmorillonite partial density) was calculated and compared to data experimentally obtained for various kinds of bentonites (Kunigel-V1, MX-80, Kunipia-F, mixture of Kunipia-F and silica sand) [4]. The calculation was made assuming smectite contents of 48 wt.% for Kunigel-V1 bentonite, 75 wt.% for MX-80 bentonite and 99 wt.% for Kunipia-F bentonite, and was made for saturated condition. In addition, smectite partial density under saturated condition ( $\rho_{sm}$ ) was converted from water content obtained in this study. The  $\rho_{sm}$  was determined from the following relation:

$$\rho_{sm} = \frac{100\rho_{th} \cdot \rho_w}{W_c \cdot \rho_{th} + 100\rho_w} \quad (11)$$

where  $\rho_{sm}$  is the smectite partial density for saturated condition ( $Mg/m^3$ ),  $\rho_{th}$  the solid density of smectite ( $2.7 Mg/m^3$ ), and  $\rho_w$  the density of water ( $=0.997044 Mg/m^3$  at  $25^{\circ}C$ ).

The author also calculated swelling pressures based on the  $a_{H_2O}$  data of water on Kunipia-F bentonite of which data were reported by Torikai *et al.* [3]. Figure 6 shows the comparison of the calculated and measured swelling pressures. The calculated results are in good agreement with the measured data over the range of smectite partial density between  $1.0$  and  $2.0 Mg/m^3$ . This indicates that swelling pressure of compacted bentonite can be explained and calculated based on the thermodynamic data of water on smectite surface. Furthermore, this range of smectite partial density can cover almost all dry densities of compacted bentonite by considering smectite content.

**Figure 6: Comparison of calculated and measured [4] swelling pressures**  
**The author also calculated swelling pressures based on  $a_{H_2O}$  data of water**  
**on Kunipia-F bentonite [3]**



Although the effects of temperature and salinity on the swelling pressure were not discussed in this study, the change of the swelling pressure on temperature can be calculated based on Eq. (6) obtaining  $\Delta H_{H_2O}$  and  $\Delta S_{H_2O}$ . In addition, the effect of ionic strength such as salinity on the swelling pressure is also important, because it is reported that the swelling pressure decreases with an increase of ionic strength [e.g., 12]. These works will be done in the future.

## Conclusions

The activity and  $\Delta G_{H_2O}$  of porewater in smectite were obtained at 25°C as a function of water content in a range of dry density 0.6-0.9 Mg/m<sup>3</sup> by vapour pressure method. Both activity and  $\Delta G_{H_2O}$  of the porewater decreased with a decrease of water content in the region where water content is lower than about 40 %.

From the correlations of the activity and  $\Delta G_{H_2O}$  of the porewater with water content and the specific surface area of smectite, the porewater was deduced to be bound up to a distance of approximately 2 water layers from the surface of smectite. Swelling pressure versus smectite partial density under saturated condition was calculated based on the difference in the chemical potentials ( $\Delta G_{H_2O}$ ) of water in equilibrium between free water and moisturised smectite at a constant temperature, and compared to data experimentally obtained for various kinds and different smectite contents of bentonites. Both calculated and measured results were in good agreement over the range of smectite partial density between 1.0 and 2.0 Mg/m<sup>3</sup>. It was indicated that swelling pressure of compacted bentonite could be explained based on the thermodynamic data of water on smectite surface. However, the effects of temperature and salinity on the swelling pressure are the future work.

## REFERENCES

- [1] Japan Nuclear Cycle Development Institute (JNC), 2<sup>nd</sup> Progress Report on Research and Development for the Geological Disposal of HLW in Japan – H12: Project to Establish the Scientific and Technical Basis for HLW Disposal in Japan – Supporting Report 3: Safety Assessment of the Geological Disposal System, Tech. Rep., JNC TN1410 2000-004 (2000).
- [2] Y. Torikai, S. Sato, H. Ohashi, Thermodynamic Properties of Water in Compacted Bentonite under External Pressure-free Conditions, Mater. Res. Soc. Symp. Proc., Vol.353, pp.321-328 (1995).
- [3] Y. Torikai, S. Sato, H. Ohashi, Thermodynamic Properties of Water in Compacted Sodium Montmorillonite, Nucl. Technol., 115, pp.73-80 (1996).
- [4] H. Suzuki, T. Fujita, T. Kanno, Moisture Potential and Water Diffusivity for Buffer Materials, Tech. Rep., PNC TN8410 92-057 (1992).
- [5] T. Kanno, H. Wakamatsu, Moisture Adsorption and Volume Change of Partially Saturated Bentonite Buffer Materials, Mater. Res. Soc. Symp. Proc., Vol.294, pp.425-431 (1993).
- [6] H. Sato, Measurements on the Thermodynamic Properties of Porewater in Sandstone by Vapour Pressure Method, J. Nucl. Sci. Technol., 42 (4), pp.368-377 (2005).
- [7] G. Kahr, F. Bucher, P. A. Mayor, Water Uptake and Swelling Pressure in a Bentonite-based Backfill, Mater. Res. Soc. Symp. Proc., Vol.127, pp.683-689 (1989).
- [8] M. Ito, M. Okamoto, M. Shibata, Y. Sasaki, T. Danbara, K. Suzuki, T. Watanabe, Mineral Composition of Bentonite, Tech. Rep., PNC TN8430 93-003 (1993) [in Japanese].
- [9] R.A. Robinson, R.H. Stokes, Electrolyte Solutions, 2<sup>nd</sup> ed., Butterworths, London (1959).
- [10] Kagaku-Binran, Kisoheii (Handbook of Chemistry, Basic Version II), 2<sup>nd</sup> ed., Nihon-Kagakukai (Chem. Soc. Jpn.) (1975) [in Japanese].
- [11] H. Otaki, Ion-No-Suiwa (Ionic Hydration), Kyoritsu (1990) [in Japanese].
- [12] H. Kikuchi, K. Tanai, Basic Characteristic Test of Buffer / Backfill Material Under Horonobe Groundwater Condition, Tech. Rep., JNC TN8430 2004-005 (2005) [in Japanese].

# THE IMPORTANCE OF MATRIX DIFFUSION FOR THE TRANSPORT OF MOBILE RADIONUCLIDES IN GRANITIC ROCK – SUMMARY OF LABORATORY – SCALE EXPERIMENTS

**Pirkko Hölttä, Marja Siitari-Kauppi**

University of Helsinki, Laboratory of Radiochemistry, Department of Chemistry, Finland

**Antti Poteri**

Technical Research Centre of Finland, Finland

## Abstract

Crystalline rock has been considered as a host medium for the repository of high radioactive spent nuclear fuel in Finland. Radionuclide transport take place along water-carrying fractures and matrix diffusion has been indicated to be an important mechanism, which will retard the transport of mobile fission and activation products. Transport properties of mobile radionuclides in crystalline rock have been studied by means of different laboratory-scale methods using rock-fracture and rock-core columns and a rock-block having a horizontally planar natural fracture (0.9 m x 0.9 m). Objective of this study was to examine the processes causing retention in solute transport through rock fractures, especially focused on the matrix diffusion. Results of this work can be used to estimate importance of matrix diffusion as a retention process during transport in different scales and flow conditions.

Rock matrices of mica gneiss, unaltered, moderately altered and strongly altered tonalite and Kuru grey granite have been well characterised. Total porosity and the surface areas of mineral grains available for migration of species have been determined by the  $^{14}\text{C}$ -PMMA method. Pore apertures and geometry in mineral phases were analysed by field emission scanning electron microscopy (FESEM) and the minerals were quantified by energy dispersive X-ray micro analysis (EDX). The surface area of the solid rock was determined by the B.E.T. method. Hydrological properties of the columns or the natural fracture were characterised and flow paths were determined. Tracer experiments were performed using dye tracer uranine, and radioactive tracers HTO,  $^{36}\text{Cl}$ ,  $^{99}\text{Tc}$  and  $^{131}\text{I}$ .

Transport of tracers was modelled using modified migration models used in performance assessments, which were adapted for interpreting laboratory-scale experiments. The dominant matrix diffusion behaviour was demonstrated in porous ceramic columns. Demonstration of the effects of matrix diffusion in crystalline rock fracture column succeeded in a series of experiments where the experimental arrangements enabled very low water flow rates. Rock-block and rock-core column experiments could be modelled by applying consistent

parameterisation and transport processes. The effects of matrix diffusion were demonstrated on the slightly sorbing tracer breakthrough curves. Based on scoping calculations matrix diffusion begins to be significantly observable for a non-sorbing tracer when the flow rate is  $0.1 \mu\text{l}\cdot\text{min}^{-1}$  in the core column experiment and  $1 \mu\text{l}\cdot\text{min}^{-1}$  in the block experiment. This knowledge and understanding of the transport processes is transferable to different scales from laboratory to *insitu* conditions.

## Introduction

In Finland, the repository for spent nuclear fuel will be excavated at a depth of about 500 metres in the fractured crystalline bedrock in Olkiluoto at Eurajoki, the site proposed by Posiva Oy. Over very long time periods, radioactive substances may be released from a repository and then transported along water-conducting fracture zones. The fractures provide the most effective transport paths even though most of the porosity derives from the pores. Transport processes along the pores and fractures are very different; transport occurs in the fracture network, while the porous matrix act as a capacitor charged by exchange with adjacent fractures. The transport of radionuclides in the groundwater system is affected by various processes, such as advection, dispersion, channelling, matrix diffusion and sorption. The diffusion of mobile radionuclides into the micro fissures and pores are the main mechanisms retarding radionuclide transport in crystalline rock [1, 2].

In the case of crystalline rock, in short time scale laboratory experiments the residence times of tracers have been too short for matrix diffusion to occur, and hydrodynamic dispersion has dominated the transport behaviour of non-sorbing radionuclides. In laboratory-scale experiments, the effects of matrix diffusion have been demonstrated by Callahan *et al.* [3]. They investigated solute transport in fractured saturated volcanic tuff, which is significantly more porous than crystalline rock, allowing matrix diffusion to occur in a reasonable time. Only matrix diffusion can cause significant changes in the shape of a breakthrough curve as a function of either elution time or the diffusion coefficient. The water flow rate, the fracture dimensions and the porosity of fracture surfaces are the most important factors affecting the transport of solutes in fracture column experiments. The lower the flow rate is, the more important the effect of matrix diffusion becomes.

The elution times of non-sorbing tracers have been used usually to indicate the flow rate of the groundwater in the fracture. However, this knowledge and understanding of the transport and retention processes can be utilised to evaluate transport of mobile fission and activation products in the geosphere. Performance assessment is directly concerned with contribution of  $^{129}\text{I}$ ,  $^{36}\text{Cl}$ ,  $^{79}\text{Se}$ ,  $^{14}\text{C}$  and  $^{99}\text{Tc}$  in their long-term exposure risks. This paper is a summary of work in which transport properties of mobile radionuclides in crystalline rock have been studied by means of different laboratory-scale methods using fracture columns, rock-core columns and a rock-block having a horizontally planar natural fracture [4-8]. The objectives were to examine the processes causing retention in solute transport, especially matrix diffusion, and to estimate the importance of retention processes during transport in different scales and flow conditions.

## Experimental

All rock matrices used in these experiments have been well characterised. The total porosity and the surface areas of mineral grains available for sorption and migration of species were determined by the  $^{14}\text{C}$ -PMMA method [9]. The total bulk porosities of the rock matrices were also determined by means of water impregnation. The pore aperture distribution was evaluated on the basis of Hg-porosimetry determinations. Pore apertures and geometry in the mineral phases were analyzed also by scanning electron microscopy (SEM), and the minerals and sorbed tracer were quantified by energy dispersive X-ray microanalysis (EDX). The specific surface area of the solid rock was determined by the B.E.T. Hg impregnation method. The minerals were quantified by means of energy dispersive X-ray microanalysis.

First fracture columns were made out of tonalite drill core sections obtained from the Olkiluoto nuclear power plant site on the west coast of Finland. In order to demonstrate the effects of matrix diffusion in a breakthrough of non-sorbing solutes, a high porosity ceramic column with a narrow fracture width was introduced. The porosity of the material was determined by the water impregnation method to be  $30 \pm 1\%$  and was two orders of magnitude higher than the porosity of the rocks. Radionuclide migration in crystalline rock was studied systematically using rock samples obtained from hole SY-KR7 drilled in the Syyry area in Sievi in western Finland. The rock samples – mica gneiss, unaltered, moderately altered and strongly altered tonalite – represented different rock features and porosities, thereby making it possible to determine experimental boundary limit values for parameters describing both the transport and retardation of radionuclides and the rock matrix properties. Syyry was one of the five sites selected by Teollisuuden Voima Oy for preliminary investigations concerning the final disposal of spent nuclear fuel in Finland. Fracture flow and solute transport is studied now in a planar natural fracture using Kuru Grey granite block which was obtained from Kuru Quarry, Tampereen Kovakivi Oy, Finland. Rock-core column experiments were introduced to estimate the diffusion and sorption properties of Kuru Grey granite used in block-scale experiments.

### *Flow experiments*

In fracture flow experiments synthetic ground water was fed into the columns or through the natural block fracture at different flow rates of  $1\text{--}50 \mu\text{l}\cdot\text{min}^{-1}$  using a peristaltic pump to control water flow rate. A short tracer pulse (1 or 5  $\mu\text{l}$ ) was injected into the water flow using an injection loop and the out flowing tracer was collected using a fraction collector. In the very slow flow experiments, the water flow was controlled by hydrostatic pressure instead of by pumping. Fractions were collected by feeding the effluent into water in a sealed vial in order to avoid evaporation at the tip of the tube during the collection. The flow rate was monitored by weighing every fraction. The lowest flow rate obtained was  $0.02 \mu\text{l}\cdot\text{min}^{-1}$ .

The arrangement for the column experiments was constructed and tested using columns made of Olkiluoto tonalite drill core sections. One axial fracture was induced mechanically in each core by sawing or opening along the natural fracture. The cylindrical outer surfaces of the drill cores were sealed with urethane lacquer to prevent any water leakage from the rock except through the outlet end of the fracture. The ceramic column with a narrow fracture width and rock fracture columns of Syyry KR-7 were made of two rectangular slices, the surfaces were polished, and the

polished surfaces were set against each other. Inlet and outlet tubes were connected directly to the fracture, and the whole column was sealed from outside in order to prevent leaks.

Block-scale migration experiments were introduced to evaluate the simplified radionuclide transport concept used in assessing the safety of the under-ground waste repositories. Experimental set-up and instrumentation has been developed and tested using a granite block (0.9 m x 0.9 m x 0.7 m) having a horizontally planar natural fracture (Figure 1). Rock-block contains a natural hydraulically conducting fracture intersected by nine vertical boreholes. The drill holes were equipped with injection or sealing packers. The rock block was equipped with water pools that are installed at the vertical sides and top of the block in order to ensure saturation of the block and also to stabilise the hydraulic head around the vertical faces. A 5-mm wide water collection slit near the fracture was separated with a partition wall having openings at the bottom of the pool. The rock block was instrumented also at the outer vertical boundary of the block where the horizontal fracture intersects the faces of the block for the collection of the tracer. Hydrological properties of the fracture were characterized and flow paths were determined [5, 6]. In parallel with block-scale experiments rock-core column experiments were introduced to estimate the diffusion properties of Kuru Grey granite which was used in block-scale experiments. Rock-core columns were constructed from cores drilled to the fracture and were placed inside a tube to form flow channel in 0.5 mm gap between the core and the tube [8].

**Figure 1: Kuru Grey granite block having a natural hydraulically conducting natural fracture and local transmissivities determined from the water pumping tests.**

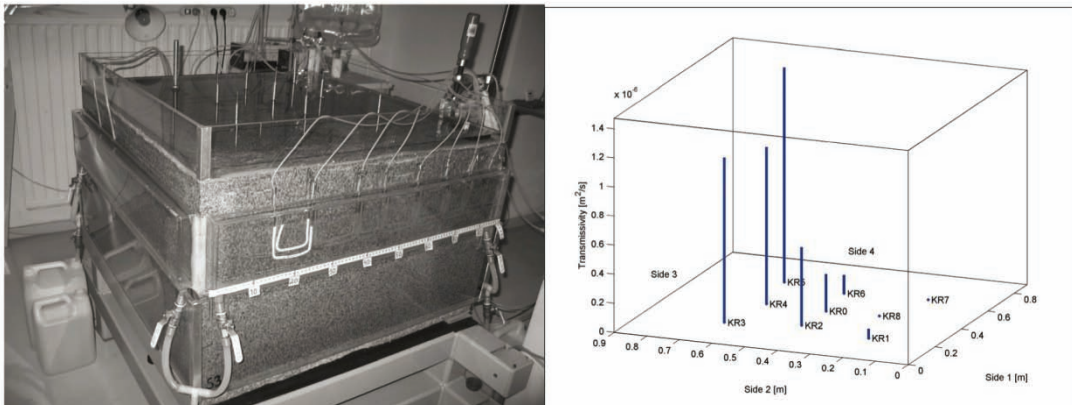


**Table I: Rock types, fracture dimensions, tracers and range of volumetric flow rate used in the experiments**

	Length (m)	Width (m)	Aperture (m)	Tracers	Flow rate ( $\mu\text{l}\cdot\text{min}^{-1}$ )
<b>Olkiluoto tonalite</b>					
Sawed fracture	0.068	0.035	$1\cdot 10^{-4}$	$^3\text{H}$ , $^{36}\text{Cl}$ , $^{99}\text{Tc}$	1 – 60
Natural fracture	0.083	0.035	$1\cdot 10^{-4}$	$^{22}\text{Na}$	0.8 – 11.5
				$^3\text{H}$ , $^{36}\text{Cl}$ , $^{99}\text{Tc}$	1 – 60
				$^{22}\text{Na}$	0.8 – 11.5
<b>Ceramic column</b>	0.145	$4\cdot 10^{-3}$	$1\cdot 10^{-5}$	$^3\text{H}$ , $^{36}\text{Cl}$ , $^{99}\text{Tc}$	1 – 16
<b>Syryy KR-7</b>					
Mica gneiss	0.190	0.01	$4\cdot 10^{-5}$	He	60 – 250
				$^3\text{H}$ , $^{36}\text{Cl}$	0.002 – 10
				$^{22}\text{Na}$ , $^{45}\text{Ca}$ , $^{85}\text{Sr}$	5 – 10
Unaltered tonalite	0.213	0.008	$5\cdot 10^{-5}$	$^3\text{H}$ , $^{36}\text{Cl}$	0.4 – 10
				$^{22}\text{Na}$ , $^{45}\text{Ca}$ , $^{85}\text{Sr}$	5 – 10
Moderately altered tonalite	0.085	0.015	$1\cdot 10^{-4}$	$^3\text{H}$ , $^{36}\text{Cl}$	1 – 10
				$^{22}\text{Na}$ , $^{45}\text{Ca}$ , $^{85}\text{Sr}$	5 – 10
Strongly altered tonalite	0.225	0.006	$1.7\cdot 10^{-4}$	He	80 – 360
				$^3\text{H}$ , $^{36}\text{Cl}$	0.7 – 10
				$^{22}\text{Na}$ , $^{45}\text{Ca}$ , $^{85}\text{Sr}$	5 – 10
<b>Kuru grey granite</b>					
Core column I	0.745	0.044	$5\cdot 10^{-4}$	Uranine, $^3\text{H}$	5 – 50
Core column II	0.685	0.044	$5\cdot 10^{-4}$	Uranine, $^3\text{H}$ , $^{36}\text{Cl}$ , $^{131}\text{I}$ , $^{22}\text{Na}$	0.7 – 20
Core column III	0.280	0.044	$5\cdot 10^{-4}$	Uranine, $^3\text{H}$ , $^{36}\text{Cl}$ , $^{22}\text{Na}$ , $^{85}\text{Sr}$	2 – 20
Block (0.9 m x 0.9 m x 0.7 m)					
Channel II	0.75	0.06	$6.5\cdot 10^{-4}$	Uranine,	
Channel III	0.8	0.035	$5\cdot 10^{-4}$	$^{99\text{m}}\text{Tc}$ , $^{131}\text{I}$ , $^{22}\text{Na}$	3 – 350

Experiments were performed using dye tracer uranine, HTO,  $^{36}\text{Cl}$ ,  $^{99\text{m}}\text{Tc}$ ,  $^{99}\text{Tc}$  and  $^{131}\text{I}$  as non-sorbing tracers and  $^{22}\text{Na}$  as a slightly sorbing tracer to increase the influence of the matrix diffusion. Fracture dimensions, tracers used in the experiments and range of the volumetric flow rate are presented in Table 1. The optical absorbance of uranine at 491 nm was measured by UV/VIS spectrophotometer, beta activities of HTO,  $^{36}\text{Cl}$  and  $^{99}\text{Tc}$  were determined by liquid scintillation counting and gamma activities of  $^{99\text{m}}\text{Tc}$ ,  $^{131}\text{I}$  and  $^{22}\text{Na}$  were detected by a Wizard gamma counter. Synthetic granitic groundwater equilibrated with crushed rock material was used in all experiments.

## Results and discussion

Transport of tracers was modelled using modified migration models used in performance assessments, which were adapted for interpreting laboratory-scale experiments. Solute mass flux through the transport channel was modelled by applying the assumption of a linear velocity profile and a molecular diffusion. Coupling of the advection and diffusion processes was based on the

model of generalised Taylor dispersion in the linear velocity profile. A detailed discussion of the problem and solution to the transport problem is given by Hautojärvi and Taivassalo [10].

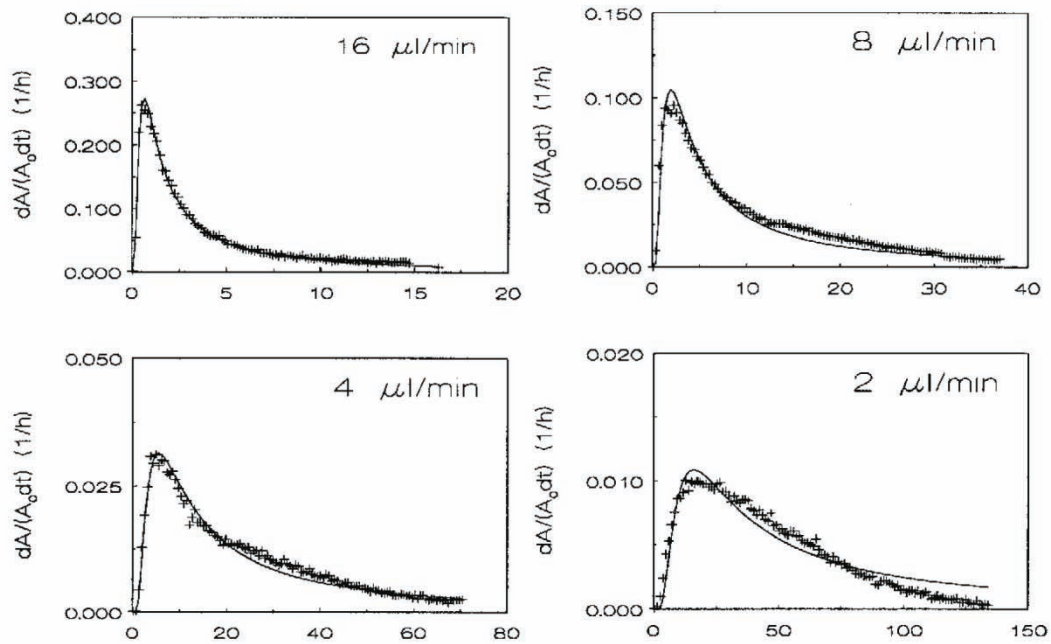
### ***Olkiluoto tonalite columns***

The experimental arrangement for the rock fracture column method was tested by using sawed and natural fracture columns made of Olkiluoto tonalite drill core sections. In the sawed fracture, the transport behaviour of non-sorbing tracers was explained using the calculation for dispersion only. Symmetrical elution curves and agreement between the experimental and calculated results showed that hydrodynamic dispersion dominated the transport of non-sorbing tracers. Estimations for the case of the effective diffusion coefficient determined for the Olkiluoto tonalite illustrated that the residence times were too short for matrix diffusion to occur. In the natural fracture column, the relative residence times of the tracers were longer and the elution peaks more spread than in the sawed fracture column. Tracer transport, including the diffusion of solutes from the fracture into the matrix, was interpreted. However, the required value of the effective diffusion coefficient,  $D_e$ , was unreasonably high for the crystalline rock matrix, suggesting solute diffusion into the fracture filling material or stagnant pore water areas near the uneven fracture surface. The change in the flow rate had no significant effect on the shapes of the elution curves, and it was impossible to extract the effects of matrix diffusion from other phenomena that cause dispersion.

### ***Ceramic column***

The effects of matrix diffusion in the elution curves of the non-sorbing tracers were demonstrated by the use of a high-porosity ceramic column [11]. A porosity of two orders of magnitude higher than the porosity of crystalline rock allowed matrix diffusion to occur with the use of routine volumetric flow rates. The transport of tritiated water and chlorine through the ceramic fracture column was interpreted using a widely known analytic solution to the advection-matrix diffusion problem, with semi-infinite boundary conditions in the matrix and a sudden release of the tracer at the inlet. Experimental and calculated elution curves for tritiated water and chloride from runs with different flow rates are shown in Figure 2. The consistency obtained between the experimental data and the calculated results showed that the transport of the non-sorbing tracers in the porous ceramic fracture column was affected by matrix diffusion. Longer rise time of the elution curve, lower peak height and increased tailing with lower flow rates are the main effects of matrix diffusion on the elution curves. With faster flow rates, the agreement between the calculated and experimental elution curves was good. As the flow rates decreased, there was increasing inconsistency between the curves. This disagreement was caused by limitation in matrix diffusion, which was a consequence of the shallow matrix depth of the column: 9 mm. With reflective boundary conditions, the tracer transport approach a steady state where, statistically, all the molecules experience the same velocities with equal column transport time within a Gaussian distribution. The existence of reflective boundaries in the limited matrix diffusion was confirmed by interpretation using a numerical code, FTRANS.

**Figure 2: Measured and calculated (solid line) breakthrough curves of chloride for the ceramic fracture column with different volumetric flow rates**



### **Syyry KR-7**

Radionuclide transport and retardation in a single crystalline rock fracture were studied systematically using mica gneiss and unaltered, moderately altered and strongly altered tonalite drill core samples from hole SY-KR7 [4]. Instead of analytical models, a numerical compartment model developed for near-field modelling, REPCOM [12] was modified to calculate the advection and hydrodynamic dispersion in the fracture columns. Owing to the limited dimensions of the columns, the boundary conditions have an important effect on the hydrodynamic dispersion of the transported tracer towards the end of the column. With decreasing flow rates, the longitudinal diffusion increases in importance, and it is no longer possible to model the tracer plume adequately using conventional approximate analytical models appropriate for longer distances and higher velocities. Based on the retention time distribution without matrix diffusion in the column, the effect of matrix diffusion was calculated for each short time interval by means of analytic expression of the matrix diffusion. These results were then summed up to give the final breakthrough curve (Figure 3).

**Figure 3: Measured and calculated elution curves of chloride for Syryy fracture columns. Solid lines are modelled results for advection and matrix diffusion; dotted lines are for the advection only. Left: unaltered tonalite, flow rates from left to right were 1.5, 0.95 and 0.43  $\mu\text{l}\cdot\text{min}^{-1}$ . Right: strongly altered tonalite, flow rates from left to right were 2.5, 1.9, 1.3 and 0.7  $\mu\text{l}\cdot\text{min}^{-1}$ .**

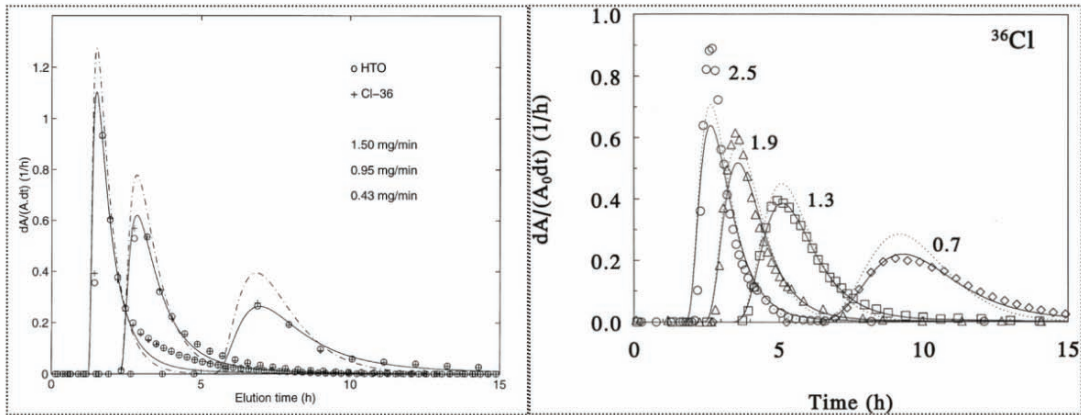
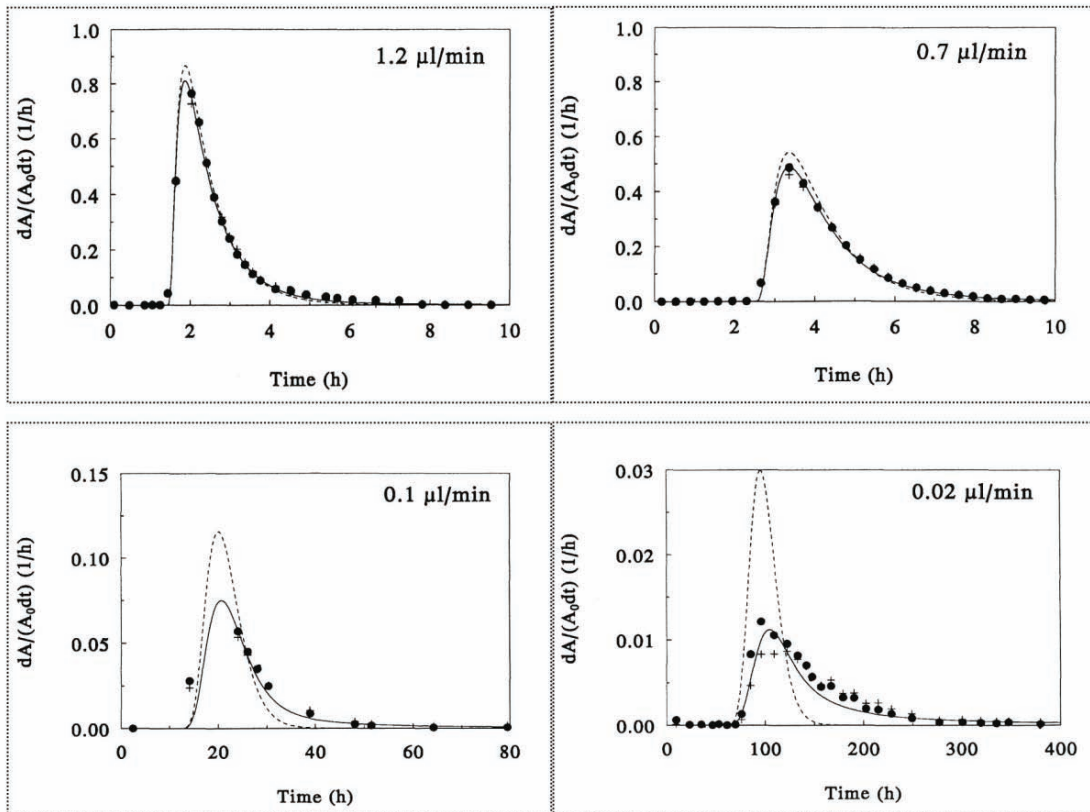


**Figure 4: Measured and calculated elution curves of tritiated water (+) and chloride (●) for the mica gneiss fracture column. Solid lines are modelled results for advection and matrix diffusion; dotted lines are for the advection only**



In order to demonstrate the effects of matrix diffusion in the elution curves for crystalline rock, a series of very low flow rate experiments was performed in the mica gneiss column. According to estimation from gas diffusion experiments, the lowest water flow rate of  $0.02 \mu\text{l}\cdot\text{min}^{-1}$  would enable demonstration of the dominating matrix diffusion behaviour in water flow experiments. Experimental and calculated elution curves of tritiated water and chloride for the mica gneiss column is shown in Figure 4. The transport of the tracers was calculated using a dispersion model with and without the inclusion of matrix diffusion. Each experiment was modelled using the same parameters throughout the flow rate range. In the experiments with the two fastest flow rates, 1.2 and  $0.7 \mu\text{l}\cdot\text{min}^{-1}$ , hydrodynamic dispersion dominated the transport of the tracers. Adding matrix diffusion gave a somewhat better fit with the experimental values but the difference was not significant. In an experiment with a flow rate of  $0.1 \mu\text{l}\cdot\text{min}^{-1}$  adjusted by hydrostatic pressure, the fraction collection frequency at the leading edge of the elution peak was sparse because of manual fraction collection. However, the experimental values at the trailing edge agree with the calculated curve that includes the effect of matrix diffusion. Scaling of the time axis and the mass flux values with the flow rates clearly reveals the change in the shape of the elution curve for the lowest flow rate of  $0.02 \mu\text{l}\cdot\text{min}^{-1}$ , indicating matrix diffusion behaviour.

### ***Kuru Grey granite***

In Kuru Grey rock-core columns solute mass flux through the transport channel was modelled by applying the assumption of a linear velocity profile and a molecular diffusion [7, 8]. Modelling work indicated that tests carried out with Core I had flow rates too high for clear indication of matrix diffusion. Tracer tests with the shortest core, Core III, were performed using a wide range of different tracers and flow rates. However, difficulties were faced in reproducing consistently the non-sorbing tracer breakthrough curves for different flow rates. Core II provided a consistent series of experimental results, for that reason the main modelling effort focused on experiments performed using Core II. Examples of the modelled and observed breakthrough curves for uranine and  $^{22}\text{Na}$  are presented in Figure 5. In the modelled curves clear differences in the tailings of uranine and  $^{22}\text{Na}$  was explained well by the stronger matrix diffusion effect in  $^{22}\text{Na}$  breakthrough curves due to the slight sorption of  $^{22}\text{Na}$  in the pore space of the rock matrix.

In a Kuru Grey block a set of tracer experiments were carried out applying flow fields and required flow conditions estimated on the basis of hydraulic characterisation and uranine tests [5-7]. Tracer experiments were performed for a maximum length of the flow path. In general higher flow rates led to broader spread of the tracer and lower flow rates led to a limited number of the shortest transport channels. The flow rate along the flow path that discharged to collection channels was quantified by measuring the recoveries. It was assumed that the tracer mass flux in the different parallel flow channels was proportional to the flow rates of these flow channels. A linear velocity profile over the channel was applied. This means that the tracer particles have an equal probability for any flow velocity between the minimum and the maximum values. The tracer tests performed in the natural fracture has been modelled using the same model used in the borehole cores. Parameters applied to model the fracture experiments were the same than used to model the borehole core experiments. Then sodium breakthrough curves were calculated using the same flow field but including the sorption properties of the sodium. The difference between uranine and sodium breakthrough curves was explained also well by matrix diffusion.

Scoping calculations were made for the core column and block fracture experiments. The basis of the scoping calculations was the geometrical dimensions and the evaluation data from existing tracer tests. These calculations showed that matrix diffusion begins to be observable for a non-sorbing tracer when the flow rate is below  $0.1 \mu\text{l}\cdot\text{min}^{-1}$  for the column experiment and below  $1 \mu\text{l}\cdot\text{min}^{-1}$  for the fracture experiment. Now several tracer tests have been performed using  $^{131}\text{I}$  as a non-sorbing tracer but modelling work is under way. Measured breakthrough curves for iodine are presented in Figure 6. Interpretation of these experiments is underway.

**Figure 5: Modelled and measured breakthrough curves for uranine (left) and  $^{22}\text{Na}$  (right) through the Core II column. Flow rates were  $20 \mu\text{l}\cdot\text{min}^{-1}$  (left),  $6 \mu\text{l}\cdot\text{min}^{-1}$  (middle) and  $3 \mu\text{l}\cdot\text{min}^{-1}$  (right). Solid lines are modelled results for advection and matrix diffusion. Dotted lines are for the advection only.**

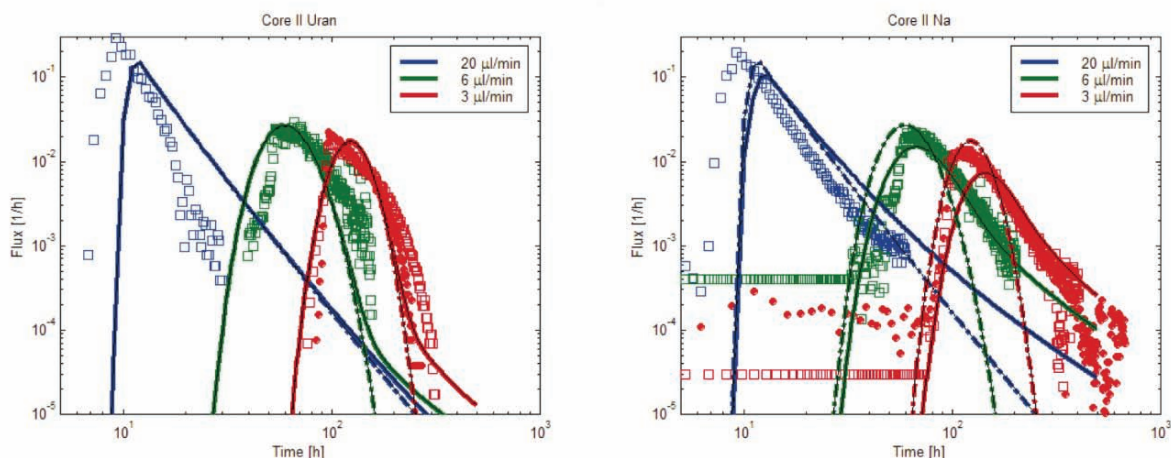
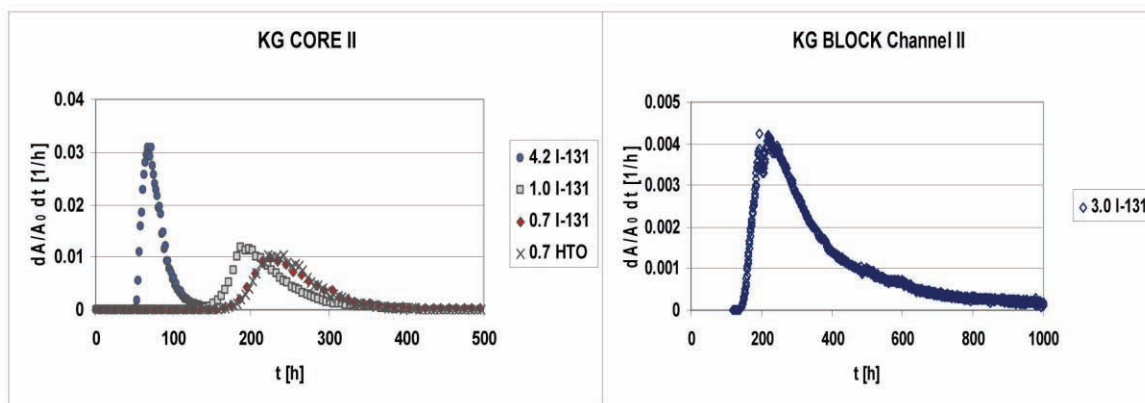


**Figure 6: Measured breakthrough curves for  $^{131}\text{I}$  with different flow rates through the Kuru Grey granite core column II (left) and block (right).**



## Conclusions

In this work, radionuclide transport in crystalline rock fractures was studied by means of laboratory-scale methods in order to gain a better understanding of different phenomena, particularly matrix diffusion, affecting the transport and retardation behaviour of radionuclides in fracture flow. Results of the experiments provide evidence that it is possible to investigate matrix

diffusion in the laboratory scale. The dominant matrix diffusion behaviour was demonstrated in porous ceramic columns. Demonstration of the effects of matrix diffusion in crystalline rock fracture column (0.2 m) succeeded in a series of experiments where the experimental arrangements enabled very low water flow rates (0.02  $\mu\text{l}/\text{min}$ ). Rock-block migration experiments were performed to evaluate the simplified radionuclide transport concept used in assessing the safety of the underground waste repositories. Rock-core column experiments were performed to estimate the diffusion and sorption properties of Kuru Grey granite used in block-scale experiments.

The experiments could be modelled by applying consistent parameterisation and transport processes. The processes, advection-dispersion and matrix diffusion, were conceptualised with sufficient accuracy to replicate the experimental results. The effects of matrix diffusion were demonstrated on the slightly sorbing sodium breakthrough curves. Based on scoping calculations matrix diffusion begins to be significantly observable for a non-sorbing tracer when the flow rate is  $0.1 \mu\text{l}\cdot\text{min}^{-1}$  in the core column experiment and  $1 \mu\text{l}\cdot\text{min}^{-1}$  in the block fracture experiment. The modelled experiments build confidence on the model predictions of the solute retention in groundwater flow. The experimental results presented here cannot be transferred directly to the spatial and temporal scales that prevail in the underground repository. However, this knowledge and understanding of the transport and retention processes is transferable to different scales from laboratory to *insitu* conditions.

## REFERENCES

- [1] Neretnieks, I., 1983. A Note on Fracture Flow Mechanisms in the Ground. *Water Resources Research*, vol. 19, 364-370.
- [2] Neretnieks, I., 2002. A stochastic multi-channel model for solute transport – analysis of tracer test in fractured rock. *J. Contam. Hydrol.* 55, 175-211.
- [3] Callahan, T.J., Reimus, P.W., Bowman, R.S. and Haga, M.J. 2000. Using multiple experimental methods to determine fracture/matrix interactions and dispersion of non-reactive solutes in saturated volcanic tuff. *Water Resources Research*, vol. 36, no. 12, 3547-3558.
- [4] Hölttä, P., 2002. Radionuclide migration in crystalline rock fractures–Laboratory study of matrix diffusion, Doctoral Thesis, University of Helsinki. Report Series in Radiochemistry 20/2002, 55 p. + Appendices (2002). (<http://ethesis.helsinki.fi>)
- [5] Hölttä, P., Poteri, A., Hakanen, M. and Hautojärvi, A., 2004. Fracture flow and radionuclide transport in block-scale laboratory experiments. *Radiochim. Acta* 92, 775-779.
- [6] Poteri, A. and Hölttä, P., 2005. Technical Research Centre of Finland Research Report. VTT/PRO1/1008/05, 37 p.
- [7] Poteri, A. and Hölttä, P., 2006. Technical Research Centre of Finland Research Report. VTT-R-03919–06, 25 p. (2006)
- [8] Hölttä, P., Siitari-Kauppi, M., Huittinen, N. and Poteri, A., 2007. Determination of Matrix Diffusion Properties of Granite. To be published in: *Scientific Basis for Nuclear Waste Management xxx*, Mater. Res. Soc. Proc., volume 985
- [9] Siitari-Kauppi, M., 2002. Development of <sup>14</sup>C-polymethylmethacrylate method for the characterisation of low porosity media. Doctoral Thesis, University of Helsinki, Helsinki. Report series in Radiochemistry 17/2002, 156 p. (<http://ethesis.helsinki.fi>)
- [10] Taivassalo, V., Hautojärvi, A., 1991. A Novel Conceptual Model for the Flow and Transport in Fractured Rock. In: *Scientific Basis for Nuclear Waste Management XIV* (T. Arbajano, Jr., L.H.Johnson, ed.) Mater. Res. Soc. Proc. 212, 831-838.
- [11] Hölttä, P., Hakanen, M., Hautojärvi, A., 1992. Transport and retardation of non-sorbing radionuclides in crystalline rock fractures. *Radiochim. Acta* 58/59, 285-290.
- [12] Nordman, H. and Vieno, T., 1994. Near-field model Repcom. Report YJT-94-14, Nuclear Waste Commission of Finnish Power Companies, 37 p.

# SORPTION AND DIFFUSION OF CS IN COMPACTED BENTONITE SATURATED WITH SALINE WATER UNDER TEMPERATURE RANGE OF 30 TO 60°C

Satoru Suzuki, Yoshimi Seida and Kazunori Suzuki

Nuclear Chemistry and Engineering Center, Institute of Research and Innovation, 1201 Takada, Kashiwa, 277-0861, Japan

## Abstract

Characteristics of sorption and diffusion of Cs in bentonite were investigated by a reservoir-depletion (RD) experiment. A crude bentonite was mixed with 30 wt.% of silica sand, and was compacted by a dry density  $1.6 \text{ Mg/m}^3$ . The specimens were saturated with simulated sea water. To identify a pair of the distribution coefficient  $K_d$  and the apparent diffusion coefficient  $D_a$  at temperatures 30, 40, 50 and 60°C, the depletion curve of Cs concentration in the stored solution was analyzed together with the concentration distribution in the bentonite specimen by a numerical calculation of Fick's diffusion equation. As an increase of temperature, the values of  $D_a$  increased from  $4.3 \times 10^{-12}$  to  $2.5 \times 10^{-11} \text{ m}^2/\text{s}$ , and the values of  $K_d$  decreased from 0.053 to 0.024  $\text{m}^3/\text{kg}$ . The calculated  $K_d$  values were comparable with those determined by batch sorption experiments, while the values of effective diffusion coefficient  $D_e$  calculated by  $D_a$  and  $K_d$  were also very close to the values determined by through-diffusion experiments. The temperature dependent characteristics were followed by an Arrhenius type equation. The activation energy  $Q_{De}$  estimated by  $D_e$  and the apparent enthalpy of sorption  $E_{Kd}$  were  $21.6 \pm 1.6 \text{ kJ/mol}$  and  $-21.6 \pm 3.0 \text{ kJ/mol}$ , respectively. The activation energy  $Q_{Da}$  estimated by  $D_a$  was  $46.3 \pm 4.0 \text{ kJ/mol}$ . The  $E_{Kd}$  value is theoretically equal to the difference of  $Q_{De}$  and  $Q_{Da}$ , and this was confirmed by the above experimental results as  $Q_{De} - Q_{Da} = -24.7 \text{ kJ/mol}$  and  $E_{Kd} = -21.6 \text{ kJ/mol}$ .

## Introduction

Sorption and diffusion properties of each radionuclide are essentially important for performance assessment of the bentonite buffer in high-level radioactive waste (HLW) disposal. In a site generic study we may assume that groundwater of a HLW repository is originated from sea water, and the temperature of the repository may be raised moderately high, e.g. up to 60°C in a Japanese scheme [1]. However, previous experimental studies of sorption and diffusion have mostly performed under conditions of room temperature using dilute solutions of a less amount of salt.

An example of performance assessment is shown in the H12 report [1] which gives a high release rate of Cs. In this example the activation energy is assumed to be 15 kJ/mol, which is determined in bulk solution, and the temperature dependence of  $K_d$  is not discussed in details.

It was found that the  $K_d$  values of dispersed bentonite are larger than those of compacted bentonite [2-4]. The reason has been discussed on a fact of accessibility of sorption sites [2] or pore water chemistry [4]. However, few experimental results of the sorption are found for compacted bentonite. In [3] the  $D_e$  and  $D_a$  values for compacted crude bentonite were determined as a function of temperature, and then the  $K_d$  value for compacted bentonite was calculated indirectly by using the  $D_e$  and  $D_a$  values as

$$D_e = (\varepsilon + \rho K_d) D_a \quad (1)$$

where  $\varepsilon$  and  $\rho$  are the porosity and dry density of compacted bentonite, respectively. In the present study the  $K_d$  values are directly determined for the compacted bentonite, and discuss the temperature dependent characteristics of sorption and diffusion of Cs in compacted bentonite comparing with the previous work.

## Experimental procedures

### *Materials*

The compacted bentonite used in this study was a mixture of silica sand and bentonite (with a mass fraction of 3:7) compacted to a dry density 1.6 Mg/m<sup>3</sup>, which is the same constitution as the candidate buffer material proposed in the H12 report [1]. The bentonite material was Kunigel V1<sup>®</sup>, which contains 46-49 wt. % of montmorillonite, 29-38 wt. % of quartz as chalcedony and small amount of other minerals [1]. Kunigel V1 was first treated by the simulated seawater whose chemistry is shown in Table 1. The silica sand mainly consisted of quartz and was a 1:1 mixture of coarse grains (the size 1-5 mm) and fine grains (the size 0.1-1 mm). This sand-bentonite mixture was compacted in a cylindrical sample holder (the inner diameter 16 mm and the height 10 mm), and then saturated with the simulated sea water during one month. Porosity of the specimens was approximately 0.4.

**Table 1: The chemical composition of the simulated sea water (Daigo Aquamarine®)**

Elements	Concentration [mmol/dm <sup>3</sup> ]
Na <sup>+</sup>	440–480
K <sup>+</sup>	10
Ca <sup>2+</sup>	8–10
Mg <sup>2+</sup>	48–55
Sr <sup>2+</sup>	0.0–0.2
Cl <sup>-</sup>	560–570
Br <sup>-</sup>	0.063–0.96
SO <sub>4</sub> <sup>2-</sup>	26–27
TOC	23–29 ppm

**Sorption-diffusion experiment**

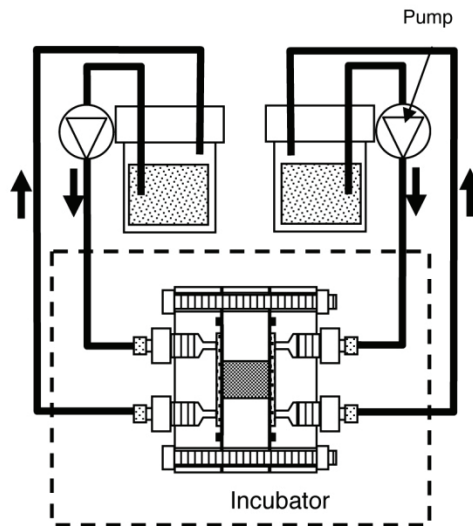
Fick’s diffusion equation for a porous medium with a linear sorption effect is given by

$$(\varepsilon + \rho K_d) \frac{\partial C_p}{\partial t} = \frac{\partial}{\partial x} \left( D_e \frac{\partial C_p}{\partial x} \right) \tag{2}$$

where  $C_p$  is the concentration of a chemical species in pore water,  $D_e$  is the effective diffusion coefficient, and  $\varepsilon$  is the porosity and  $\rho$  is the dry density. Note that  $D_e$ ,  $D_a$  and  $K_d$  are related by Eq. (1).

Reservoir depletion experiments [6-8] were performed in this study. Figure 1 shows a schematic diagram of the experiment. A detailed design of the diffusion cell can be found in [6]. The cell was kept in an incubator under a constant temperature 30, 40, 50 and 60°C, while the solution reservoirs were placed outside the incubator under a room temperature.

**Figure 1: Experimental system for the reservoir-depletion method**



A solution containing  $^{137}\text{Cs}$  (about  $500 \text{ MBq/m}^3$ ) on each side was circulated individually by a peristaltic pump through a porous plastic filter which was set alongside the bentonite specimen. The flow rate was approximately  $8 \text{ cm}^3/\text{hour}$ . The volume of solution of a reservoir was  $160 \text{ cm}^3$ . The pH of the solution was measured as 7.7 after equilibrating with the bentonite specimen. The Cs concentration in the solution was plotted with an elapse time, and a depletion curve was obtained. One experiment was performed during 2 to 4 weeks. After the experiment a distribution of Cs in the specimen was measured by cutting it into 1 mm thickness of slices and the radioactivity was measured by the  $\gamma$ -spectrometer with the NaI(Tl) scintillator.

To determine the sorption and diffusion coefficients, a one-dimensional finite difference analysis was performed for Eq.(2). Then the depletion curve and concentration distribution in the specimen were numerically calculated. The Cs concentration in a reservoir of each side was determined by

$$C(t) = C_0 - \frac{a}{V} \int_0^t J(t) \Big|_{x=0 \text{ or } L_b} dt \quad (3)$$

where  $a \text{ [m}^2\text{]}$  is the cross-sectional area of the specimen, and  $J(t) \Big|_{x=0 \text{ or } L_b} \text{ [Bq/m}^2\text{s]}$  is the diffusive flux at  $x=0$  or  $x = L_b$ . The concentration at each end surface of the specimen was determined by assuming the concentration in pore water was equal to that in a solution reservoir at each side. the concentration drop in the filter was calculated as

$$\Delta C_f = J \frac{l_f}{D_e^f} \quad (4)$$

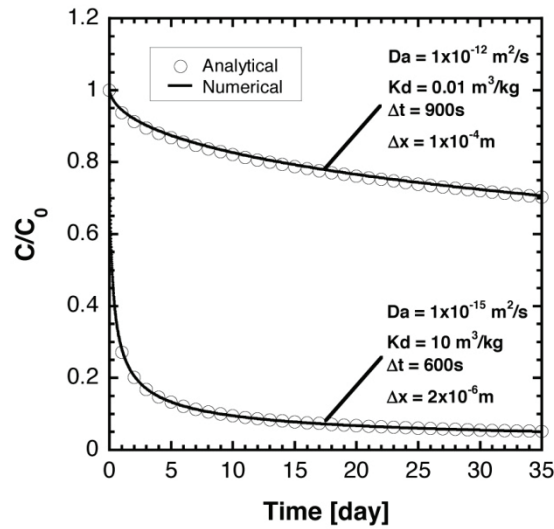
where  $J$  is the diffusive flux,  $l_f$  is the thickness of the membrane filter and  $D_e^f$  is the effective diffusion coefficient of the diffusant in the membrane filter. The  $D_e^f$  value was  $4 \times 10^{-10}$  at  $30^\circ\text{C}$  to  $8.4 \times 10^{-10} \text{ m}^2/\text{s}$  at  $60^\circ\text{C}$ . The diffusive flux  $J$  normalised by the concentration in the reservoir decreased from  $10^{-7}$  to  $10^{-9} \text{ m/s}$  in elapse time, the concentration drop in the membrane filter was calculated to be at most 2% of the concentration in the reservoir by our calculation, and thus negligible [6].

In order to validate the present numerical results we compared with the analytical solution for the infinite medium [6-8] given by:

$$C(t) = C_0 \exp\left(\frac{a^2 D_a \alpha^2 t}{V^2}\right) \text{erfc}\left(\sqrt{\frac{a^2 D_a \alpha^2 t}{V^2}}\right) \quad (5)$$

see Figure 2. The numerical calculations were performed for the sufficiently long medium, assumingly infinite. We agree that the numerical results are consistent to the analytical solutions. Then by fitting the numerical results for the medium with a finite domain to the experimental depletion curve and concentration profile, we can determine the  $D_a$  and  $K_d$  values of the compacted bentonite.

**Figure 2: Comparison of depletion curves calculated by the analytical and numerical solutions.  $\Delta t$  and  $\Delta x$  are the time and space intervals for the finite difference scheme**



## Results and discussion

Figure 3 shows a depletion curve and a concentration distribution under temperature 60°C. The original data of Figure 3 (a) and (b) are found in Suzuki *et al.* [6]. In the experiment the concentration of  $^{137}\text{Cs}$  in the circulated reservoir decreased with an elapse time and became constant after 10 days, which suggests a sorption equilibrium (Figure 3a). If the analytical solution for the infinite domain given by Eq.(5) is applied, the depletion curve does not reach constant after 9 days, which is not consistent with our experimental results. The concentration in the specimen is distributed within 10% error of the calculated value which is constant as shown in Figure 3 (b). This also suggests a state of sorption equilibrium. The reason why the concentration of Cs is partly lowered in the experimental data is due to a heterogeneous distribution of large size of silica grains (1 to 5 mm). These curves are consistent with the results of numerical calculation. Note that the  $D_a$  and  $K_d$  values are specified by the numerical analysis, and these values are close to the data reported by Suzuki *et al.* [6] in which the depletion curve was obtained by using the analytical solution for infinite medium (Table 2).

**Table 2: Experimental results for  $D_e$ ,  $D_a$  and  $K_d$  determined by various experimental methods. TD: through-diffusion method, ID: in-diffusion method, RD: reservoir-depletion method. B: Batch sorption experiment.**

$T$ [°C]	$D_a$ [ $\times 10^{-10}$ m <sup>2</sup> /s]	$D_e$ [ $\times 10^{-10}$ m <sup>2</sup> /s]	$K_d$ [m <sup>3</sup> /kg]
30	<b>0.043 (RD)</b> 0.055±0.001 (ID) <sup>*1</sup>	<b>3.7 (RD)</b> 3.2±0.1 (TD) <sup>*1</sup> 3.3±0.1 (TD) <sup>*1</sup> 3.9±0.1 (TD) <sup>*1</sup> 3.3±0.1 (TD) <sup>*1</sup>	<b>0.054 (RD)</b> 0.036 (ID/TD) <sup>*1</sup> 0.044 (ID/TD) <sup>*1</sup> 0.056±0.003 (B)
40	<b>0.062 (RD)</b> 0.091±0.001 (ID) <sup>*1</sup>	<b>5.2 (RD)</b> 4.3±0.1 (TD) <sup>*1</sup> 5.5±0.1 (TD) <sup>*1</sup>	<b>0.052 (RD)</b> 0.029 (ID/TD) <sup>*1</sup> 0.038 (ID/TD) <sup>*1</sup>
50	<b>0.12 (RD)</b> 0.14±0.01 (ID) <sup>*1</sup>	<b>5.2 (RD)</b> 5.9±0.1 (TD) 6.6±0.1 (TD)	<b>0.029 (RD)</b> 0.026 (ID/TD) <sup>*1</sup> 0.029 (ID/TD) <sup>*1</sup>
60	<b>0.25 (RD1)</b> 0.23±0.01 (ID) <sup>*2</sup> 0.19±0.01 (ID) <sup>*2</sup> 0.32±0.01 (TD) <sup>*2</sup> 0.25±0.01 (TD) <sup>*2</sup>	<b>7.5 (RD)</b> 7.6±0.1 (TD) <sup>*1</sup> 8.0±0.1 (TD) <sup>*1</sup> 7.2±0.1 (TD) <sup>*2</sup> 8.0±0.1 (TD) <sup>*2</sup>	<b>0.025 (RD, numerical)</b> 0.024±0.001 (TD) <sup>*2</sup> 0.014±0.001 (TD) <sup>*2</sup> 0.019 (ID/TD) <sup>*1</sup> 0.026 (ID/TD) <sup>*1</sup> 0.022 (RD, analytical) <sup>*2</sup> 0.021 (RD, analytical) <sup>*2</sup> 0.026±0.002 (B) <sup>*2</sup> 0.025±0.002 (B) <sup>*2</sup> 0.022±0.002 (B) <sup>*2</sup>

\*1: original data in Suzuki *et al.* [9]

\*2: referred from Suzuki *et al.* [6]. ‘ID/TD’ denoted the  $K_d$  values calculated by Eq.(1) using  $D_e$  of Cs.

The specified values of  $D_a$  and  $K_d$  are given in Table 2. The effective diffusion coefficient  $D_e$  is calculated by Eq.(1) using  $D_a$  and  $K_d$ . The  $D_a$  value determined by this reservoir-depletion experiment is consistent with the value determined by an in-diffusion experiment reported by Suzuki *et al.* [9]. The  $K_d$  value determined by this reservoir depletion is very close to the value which is indirectly estimated by using Eq.(1) under the known  $D_e$  and  $D_a$  values (see Suzuki *et al.* [9], denoted as “ID/TD”). This suggests that all the results of different experimental methods are consistent. It is reported that the  $K_d$  value of the compacted bentonite is lower than that of the dispersed bentonite [2-4]. In the present study we can conclude that the  $K_d$  value of the compacted bentonite is same as the value of the dispersed one at each temperature level.

Figure 3 (c) and (d) show the depletion curve and concentration distribution under temperature 40°C, which suggests a transient state is still kept. That is, a sorption equilibrium is not achieved within 28 elapse days, and the concentration in the specimen is profiled symmetrically. These curves are also well fitted by a numerical calculation.

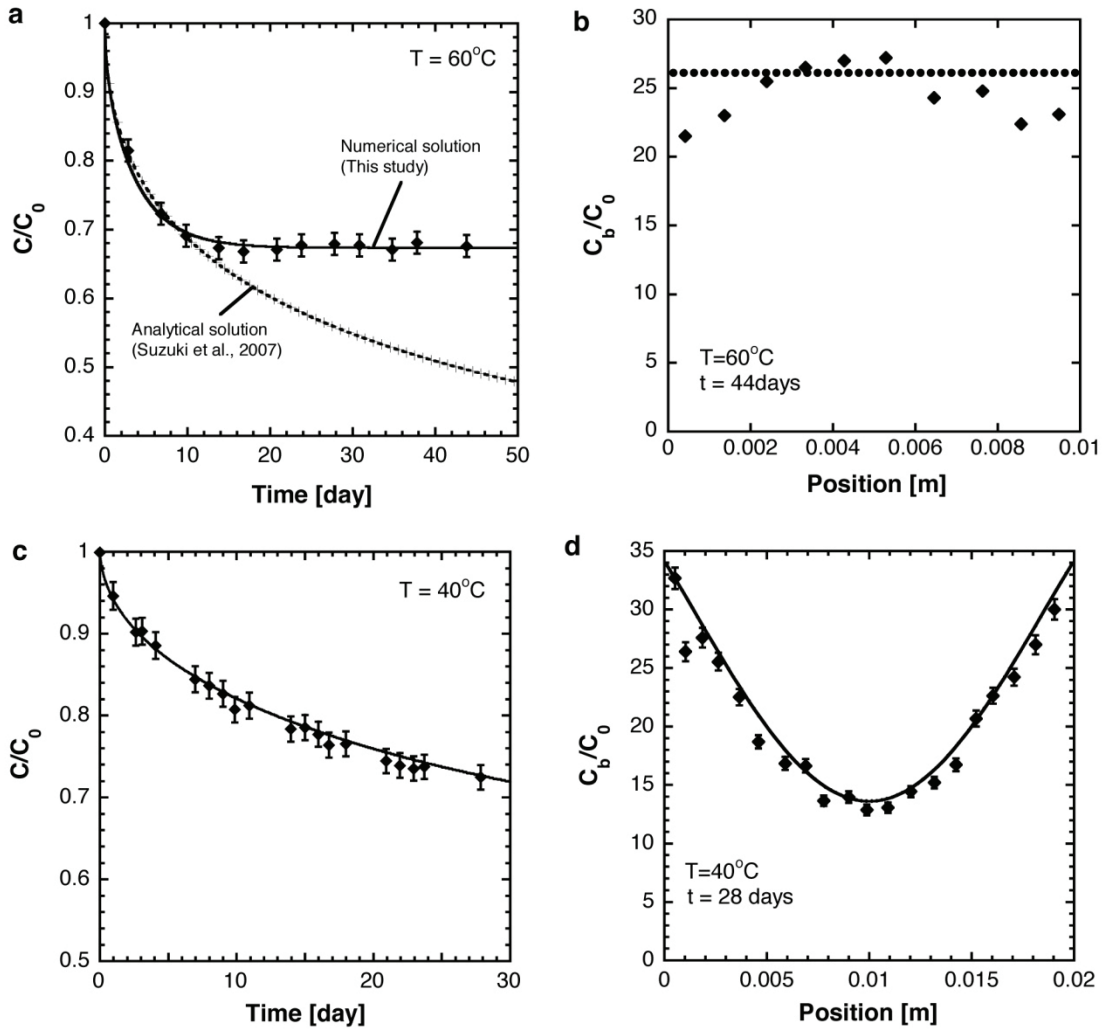
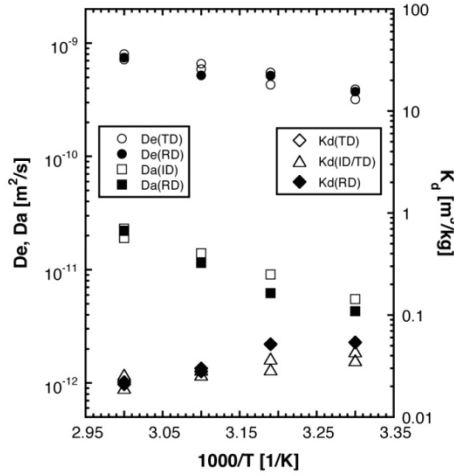


Figure 4 shows Arrhenius plots for  $C_s$  which give changes of  $D_e$ ,  $D_a$  and  $K_d$  as a function of  $1/T$  ( $T$ : temperature) in which the data reported in [6, 9] are also drawn. The results are consistent with the previously reported data within 25% errors, and we understand that the temperature dependence of  $D_e$ ,  $D_a$  and  $K_d$  follow an Arrhenius type relation. Therefore the activation energy can be calculated by using the data of Table 2 as  $46.3 \pm 4.0$  kJ/mol ( $Q_{Da}$ ), and  $Q_{De}$  is  $21.6 \pm 1.6$  kJ/mol. Assuming the van't Hoff formalism [10] the apparent energy  $E_{Kd}$  is equal to the enthalpy which is determined as  $-21.6 \pm 3.0$  kJ/mol. We have already reported the  $E_{Kd}$  value as  $-16.0 \pm 3.4$  kJ/mol [9]. This is because the  $K_d$  values of the reservoir-depletion method (RD) are larger than the values of the in-diffusion method (ID) and through-diffusion method (TD).

**Figure 4: Arrhenius plots for  $D_a$ ,  $D_e$  and  $K_d$  for Cs together with the data reported in Suzuki *et al.* [6, 9].**



The activation energy  $Q_{Da}=46.3\pm 4.0$  kJ/mol determined by  $D_a$  is about twice higher than the value  $Q_{De}=21.6\pm 1.6$  kJ/mol determined by  $D_e$ . This difference between  $Q_{De}$  and  $Q_{Da}$  may be caused by the temperature dependent characteristics of the distribution coefficient  $K_d$ . Note that based on the Arrhenius equation  $D_a$  can be expressed as

$$D_a = D_a^0 \exp\left(-\frac{Q_{Da}}{RT}\right) = \frac{D_e^0 \exp\left(-\frac{Q_{De}}{RT}\right)}{\varepsilon + \rho K_d^0 \exp\left(-\frac{E_{Kd}}{RT}\right)} \approx \frac{D_e^0}{\rho K_d^0} \exp\left(-\frac{(Q_{De} - E_{Kd})}{RT}\right) \quad (7)$$

where  $D_a^0$ ,  $D_e^0$  and  $K_d^0$  are material constants for  $D_a$ ,  $D_e$  and  $K_d$ , and  $E_{Kd}$  is the apparent energy describing temperature dependence of  $K_d$ . If  $\varepsilon$  (0.4) is small enough compared with  $\rho K_d$ ,  $E_{Kd}$  is equal to  $Q_{Da}-Q_{De}$  which is calculated as -24.7 kJ/mol. This indirectly determined value is close to the value determined directly by experiments (-21.6 kJ/mol) mentioned in the previous paragraph. In case of tritiated water the  $Q_{De}$  value (15.8±0.9 kJ/mol) [9] is close to  $Q_{Da}$  (15-20 kJ/mol) [10]. Because the sorption of HTO can be ignored,  $Q_{Da}$  of HTO is the almost same as  $Q_{De}$ . This observation also supported the above discussion of the difference between  $Q_{Da}$  and  $Q_{De}$  of Cs.

The apparent enthalpy of sorption  $E_{Kd}$  was reported to be -19±5 kJ/mol for MX80 bentonite under a low ionic strength condition ( $\text{NaClO}_4=0.025$  mol/dm<sup>3</sup>) [10]. However, because the reported data were largely scattered, the  $E_{Kd}$  value could not be determined under a high ionic strength condition ( $\text{NaClO}_4=0.5$  mol/dm<sup>3</sup>). We note that following the procedure studied here, the  $E_{Kd}$  value (-21.6 kJ/mol) can be specified uniquely in saline water where the ionic strength is changed up to 0.7. Although the solution contained Ca, Mg and K cations, Na was the major component and it may control the ionic exchange reaction. The  $E_{Kd}$  value of Cs thus seems to be independent of the ionic strength.

## Conclusion

We here discussed how the  $K_d$  and  $D_a$  values of Cs can be specified by the data of reservoir depletion experiments for compacted bentonite. We applied a finite difference scheme to interpret the experimental data. The obtained results are consistent with the values determined by conventional sorption and diffusion experiments. Furthermore the  $K_d$  values for compacted bentonite are almost same as those for dispersed bentonite. The temperature dependent characteristics of the diffusion and sorption of Cs are reevaluated by using the present and previously reported results. The activation energies of the Cs diffusion are specified as  $21.6 \pm 1.6$  kJ/mol ( $D_e$ ) and  $46.3 \pm 4.0$  kJ/mol ( $D_a$ ), while the apparent enthalpy  $E_{Kd}$  of the Cs sorption is  $-21.6 \pm 3.0$  kJ/mol. The difference  $Q_{Da} - Q_{De}$  is comparable to the  $E_{Kd}$  value.

## Acknowledgement

We acknowledge that this investigation was financed by the Ministry of Economy, Trade and Industry of Japan. The authors are grateful to Dr. H. Sato and Mr. M. Shibata for important comments on the presented results, and to Dr. Y. Ichikawa for critical review of the draft manuscript. The authors wish to thank an anonymous referee for constructive comments and suggestions.

## REFERENCES

- [1] Japan Nuclear Cycle Development Institute, JNC TN1410 2000-004 (2000).
- [2] D.W. Oscarson, H. B. Hume, and F. King, *Clays and Clay Minerals*, 42, 731 (1994).
- [3] M. Shibata, H. Sato, C. Oda and M. Yui, JNC TN8400 99-072 (1999).
- [4] M. Bradbury and B. Baeyens, PSI Bericht Nr. 03-02 (2003).
- [5] J.-W. Yu and I. Neretnieks, SKB TR97-12 (1997).
- [6] S. Suzuki, M. Haginuma, K. Suzuki, *J. Nucl. Sci. Tech.*, 44, 81-89 (2007).
- [7] D.A. Lever, Technical Report of the United Kingdom Atomic Energy Authority Harwell, AERE R 12321 (1982).
- [8] H. Sato, JNC TN8400 99-065 (1999).

- [9] S. Suzuki, K. Suzuki, MRS symp. proc. (in press).
- [10] E. Tertre, G. Berger, S. Castet, M. Loubet, E. Giffaut, *Geochim. Cosmochim. Acta*, 69, 4937 (2005).
- [11] T. Nakazawa, M. Takano, A. Nobuhara, Y. Torikai, S. Sato and H. Ohashi, *Radioactive Waste Management and Environmental Remediation-ASME* (1999).

## CHARACTERISATION OF HULL WASTE IN UNDERGROUND CONDITION

**Hiromi Tanabe, Tsutomu Nishimura, Masaaki Kaneko,  
Tomofumi Sakuragi, Yuji Nasu, Hidekazu Asano**

Radioactive Waste Management Funding and Research Center (RWMC), Japan

### **Abstract**

Hot tests using simulated hulls generated from reprocessing of PWR and BWR spent fuels have been conducted to evaluate  $^{14}\text{C}$  inventories in Zircaloy (Zry) metal and Zry oxide film, release property of  $^{14}\text{C}$  from them, chemical forms of released  $^{14}\text{C}$  into simulated underground water and distribution coefficients of  $^{14}\text{C}$  to cements. This paper described and discussed about the results of tests. Further tests are planned to evaluate long term behaviour of  $^{14}\text{C}$ .

## **Introduction**

A safe disposal concept of TRU wastes which are generated from reprocessing plants and MOX fuel fabrication plants has been studied in Japan by the Federation of Electric Power Companies of Japan (FEPC), Japan Atomic Energy Agency (JAEA) and Japan Nuclear Fuel Ltd. (JNFL) with support of research organizations. Based on the result of the safety assessment for TRU waste disposal,  $^{129}\text{I}$  in spent absorbent and  $^{14}\text{C}$  in hull waste are considered nuclides which contribute substantially to radiation exposure. In regard to  $^{14}\text{C}$ , hot tests using simulated hulls generated from reprocessing of PWR and BWR spent fuels have been conducted to evaluate inventories in Zircaloy (Zry) metal and Zry oxide film, release property of  $^{14}\text{C}$  from them, chemical forms of released  $^{14}\text{C}$  into simulated underground water and distribution coefficients of  $^{14}\text{C}$  to cements. This paper described and discussed about the results of tests. Further tests are planned to evaluate a long term behaviour of  $^{14}\text{C}$ .

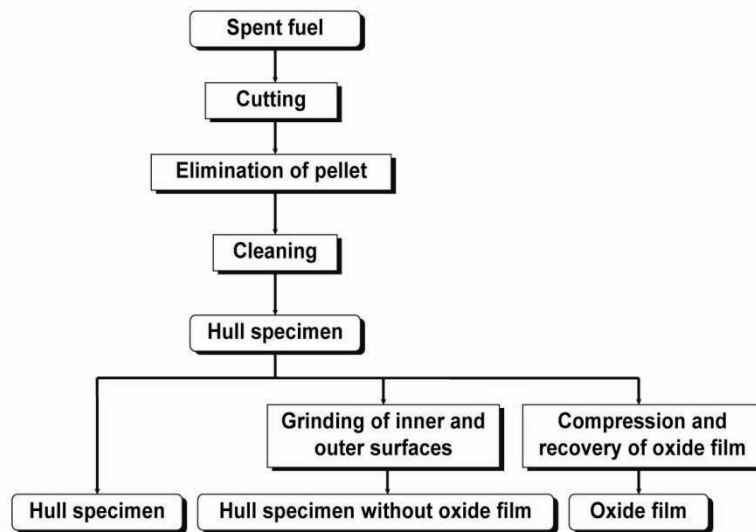
## **Test, data obtained and discussion**

### ***Preparation of hull specimens***

Irradiated Zry tubes from PWR spent fuel (burn-up: 47.9GWd/t, N content: 47ppm) and BWR spent fuel (burn-up: 39.4GWd/t, N content: 34ppm) have been used [1,4]. The treatment method of spent fuel was similar to the one in a reprocessing plant except a fuel pellet dissolution, which was first eliminated by a mechanical method, followed by the dissolution and cleaning of a small amount of attached pellet powder in the same dissolution conditions as in a reprocessing plant.

In the study, the following three types of specimen were prepared to examine differences in a radioactive inventory and a leaching behaviour between Zry metal and oxide film: 1) Hull specimen, 2) Hull specimen without oxide film and 3) Oxide film. The hull specimen without oxide film was prepared by mechanical scraping, and the oxide film was prepared by compressing the hull specimen. (see Figure 1).

Figure 1: Specimen preparation flow [1]



### *Inventory*

### *Method*

For conducting the analysis of radioactive inventory in hull, the whole hull specimen was dissolved by acid, and an analysis of radionuclides in the solution and the off-gas was carried out. The following three types of specimen were analysed: 1) Hull specimen, 2) Hull specimen without oxide film and 3) Oxide film. After the solution undergoes refining treatment and sodium hydrate trapping, which is the off-gas trap, the measurement of  $^{14}\text{C}$  and  $^{36}\text{Cl}$  is conducted by beta liquid scintillation counting. The measurement of gamma-ray emitting nuclides was also conducted by a gamma spectrometry of the solution [1].

### *Result*

Table 1 shows the inventory measurement results of PWR hull [1] and BWR hull [4].  $^{36}\text{Cl}$ ,  $^{60}\text{Co}$ ,  $^{134}\text{Cs}$ ,  $^{137}\text{Cs}$ ,  $^{154}\text{Eu}$ ,  $^{106}\text{Ru}/^{106}\text{Rh}$  and  $^{125}\text{Sb}$  were also detected.

**Table 1: Measurement results of  $^{14}\text{C}$  inventory in Zry metal and Zry oxide film [1,4,13]**

	thickness, $\mu\text{m}$		weight, %		activity, $10^4 \text{ Bq/g}$			C-14 distribution, %		note
	Zry metal	oxyde layer	Zry metal	oxide layer	Zry metal	oxide layer	oxide / metal	Zyr metal	oxide layer	oxide Layer
<b>PWR</b> 47.9 GWd/t N: 47 ppm	-	-	-	-	3.0	4.4 (5.9)*	1.5 (2.0)*	83	17	Inner + outer
<b>BWR</b> 39.4 GWd/t N: 34 ppm	752	20 outer Thin inner	97.8	2.2	1.9	3.3 (4.4)*	1.7 (2.3)*	96	4	Outer

\* In terms of metal weight

### Discussion

Table 2 shows the comparison of  $^{14}\text{C}$  inventory values between the measurement results and the calculation results by ORIGEN code. In the ORIGEN code calculation, the actual value of the impurity nitrogen, from which  $^{14}\text{C}$  was mainly generated, was used. In the case of PWR hull, the measurement result and the calculation result were almost same, however, in the case of BWR hull, the calculation result was 2.3 times higher than the measurement result. The reason is now under examined. Possible reason is guessed to be the much more uncertainty of neutron energy and flux distribution in BWR than in PWR.

Comparison of  $^{14}\text{C}$  inventories in Zry metal and oxide film shows the inventory in metal is two times lower than that of oxide film in both PWR and BWR cases as shown in Table 1. Possible reasons of the inventory increase are guessed to be  $^{16}\text{O}(n,\gamma)^{17}\text{O}(n,\alpha)\rightarrow^{14}\text{C}$  reaction in oxide film, diffusion of  $^{14}\text{C}$  from metal into oxide film and/or adsorption of  $^{14}\text{C}$  and nitrogen from coolant water into oxide film. Detailed examination is under discussion.

**Table 2: Comparison of inventory resulted from measurement and calculation [1,4,13]**

$^{14}\text{C}$  activity,  $10^4 \text{ Bq/g}$ , in the hull Zry metal.

	code	calculation	measured	calculation / measured
PWR	ORIGEN-2	4 *	3.0	1.3
BWR	ORIGEN-79	4.2 ~ 4.3 **	1.9	2.3

\* using an average burn-up for the fuel rod

\* burn-up values are set in a certain range in the fuel rod

### Release property from Zry metal and oxide film

#### Method

In the case of PWR hull, the conceptual plan of the leaching test is shown in Figure 2. A stainless steel container was placed in a hot cell and the hull specimen was put in the test container. After displacement of air by argon was conducted in the test container, simulated cement equilibrium groundwater prepared outside the hot cell was poured into the test container

through a tube. With the conditions of the immersion environment simulating those of groundwater environment, the test container was left to stand and stored for a certain period of time.  $^{14}\text{C}$  leached from Zry metal and/or oxide film was measured according to the leaching test sample analysis flow shown in Figure 3. For the  $^{14}\text{C}$  leaching test, the following two types of tests were planned: 1) Short-term test focusing on grasping the leached  $^{14}\text{C}$  chemical form, and 2) Long-term test focusing on leached volume. The composition of the test solution was decided from the calculation results using the geochemical calculation code PHREEQE by assuming a reaction between concrete and sea-water-derived groundwater, which is considered to provide conditions for the most advanced corrosion of hull. In the short-term test, the specimen was compressed in order to increase the surface area to volume ratio with the purpose of accelerating the leaching process. This was based on the prediction that the nuclide leaching behaviour from the hull waste differs from the leaching from oxide film and the leaching from Zry metal. A test was conducted on two types of specimen, the hull specimen and hull specimen without oxide film. The test conditions are shown in Table 3.

In the case of BWR hull, the same kind of leaching test apparatus was used. The test condition is shown in Table 3.  $^{14}\text{C}$  leached from Zry metal and/or oxide film was measured according to the leaching test sample analysis flow shown in Figure 3.

**Figure 2: Leaching test apparatus diagram [1]**

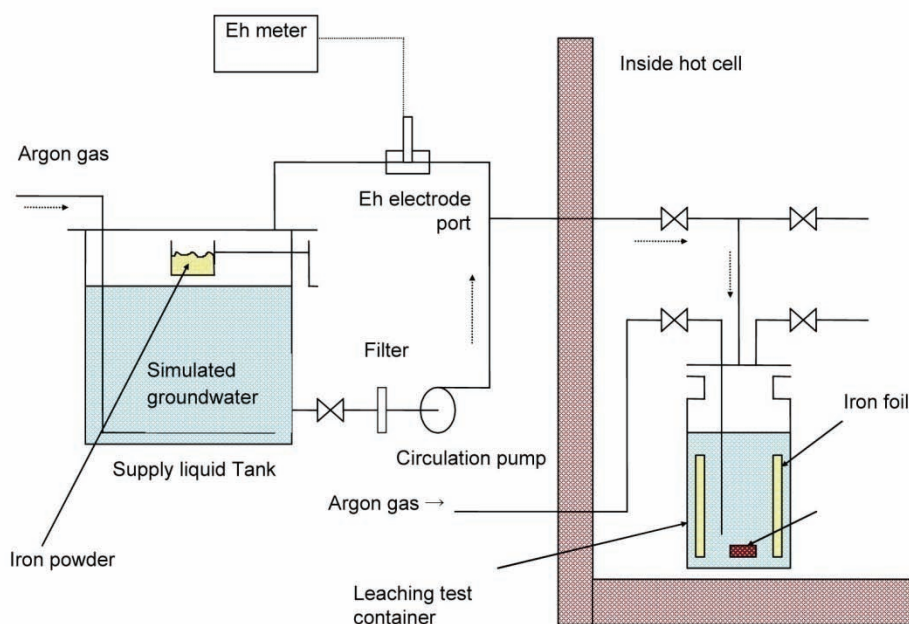


**Figure 3: Leaching test sample analysis flow [1]**

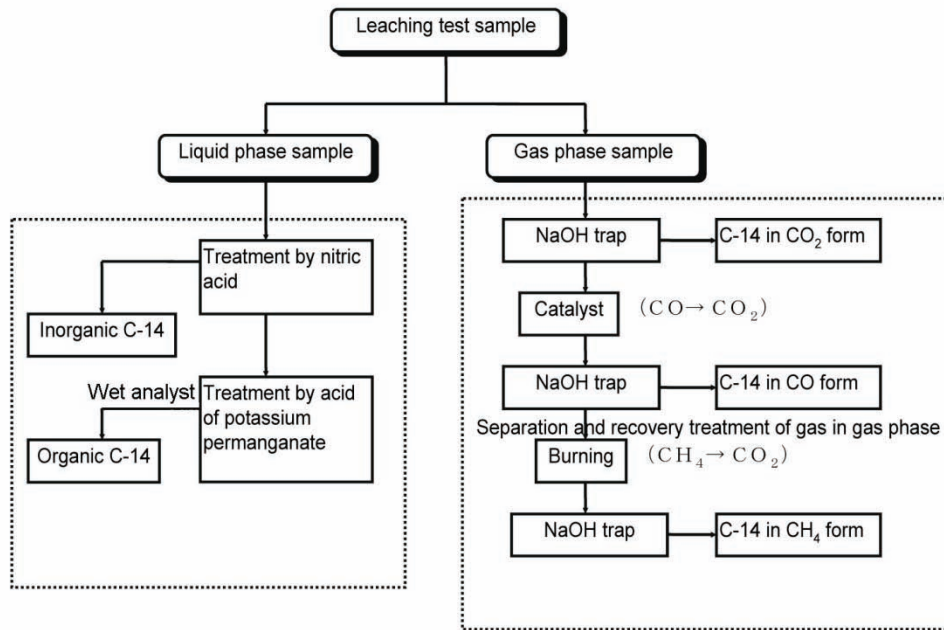


**Table 3: Leaching Test Conditions [1,4]**

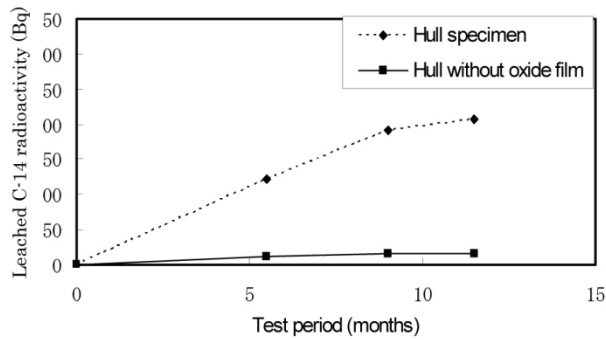
PWR

Item	Test specimen and test solution / batch					Test period
	Specimen en form	Specimen Size used	Test solution characteristics	Test Solution volume	Specimen surface area per unit volume	
Short term test	Hull specimen (compressed)	35mm x 2	Composition (m ol/L) SiO <sub>2</sub> ; 3.0E-5 H C O <sub>3</sub> <sup>-</sup> ; 1.4E-5 SO <sub>4</sub> <sup>2-</sup> ; 2.4E-4 Cl <sup>-</sup> ; 6.0E-1 Na <sup>+</sup> ; 6.0E-1 Ca <sup>2+</sup> ; 2.8E-2 Al <sup>3+</sup> ; 7.7E-6	1 liter	40 cm <sup>2</sup> / liter	3 months 5.5 months
Long term test	Hull specimen	35mm x 2		10 liters	10 cm <sup>2</sup> / liter	5.5 months 9 months 11.5 months
	Hull specimen Without oxide film	35mm x 5		10 liters	10 cm <sup>2</sup> / liter	5.5 months 9 months 11.5 months

BWR

Solid phase	Solide phase volume	Liquid phase	Liquid-to-solid ratio	Atmosphere	Temperature	Test period
Oxide film	0.5 g	NaOH pH 12.5	2ml/g	Reducing atmosphere (in a glove of nitrogen)	Room temperature	1 month
Hull specimen without oxide film	1.0g	NaOH ph 12.5	2ml/g	Reducing atmosphere (in a glove of nitrogen)	Room temperature	1 month

**Figure 4: Leaching test result of PWR hull**



### Result

Figure 4 shows the results of the leaching test of PWR hull with the radioactivity of  $^{14}\text{C}$  leached against time.  $^{14}\text{C}$  was detected in the liquid phase and not in the gas phase, and most of it in organic forms. The radioactivity of  $^{14}\text{C}$  leached from a hull specimen without oxide film was one order less compared to  $^{14}\text{C}$  leached from the hull specimen, showing an obvious difference of the existence or absence of oxide film. The leaching rate of  $^{14}\text{C}$  decreased with time. The leached nuclides that were detected were  $^{60}\text{Co}$ ,  $^{134}\text{Cs}$ ,  $^{137}\text{Cs}$ ,  $^{154}\text{Eu}$ ,  $^{106}\text{Ru}/^{106}\text{Rh}$  and  $^{125}\text{Sb}$  aside from  $^{14}\text{C}$ , but  $^{36}\text{C}$  was not detected. The leaching test of BWR hull is under test.

### Discussion

The leaching rate of  $^{14}\text{C}$  is defined as follows:

$$R = A_1 / A_0 \quad (1)$$

R: leaching rate (-)

$A_1$ : leached nuclide (Bq)

$A_0$ : nuclide inventory in hull (Bq)

Because there were differences in leaching behaviour, the “scenario” of  $^{14}\text{C}$  from its existence inside the hull to leaching was sorted out by identifying processes including the following as individual scenarios: 1) diffusion in metal 2) diffusion in oxide film 3) congruent dissolution with oxide film 4) corrosion of metal  $\rightarrow$  formation of oxide film 5) desorption of attached substances. From these scenarios, the leaching scenario of  $^{14}\text{C}$  was examined, with the oxide film and metal as the source for generation. Using reference data [5,6,7,8], a trial calculation of the leaching volumes in these scenarios was performed and the calculation results were compared with the long-term leaching test results, to evaluate the validity of these scenarios. For the diffusion coefficient, temperature correction was made to reference data for conversion to values at room temperature. The evaluation using diffusion coefficients from the

reference materials by Smith, *et al.* [5] matched well with the test results. For the hull specimen without oxide film, it became clear that the influence of the corrosion scenario is extensive.

Inventory analysis results confirmed that the  $^{14}\text{C}$  concentrations of Zry metal and of oxide film are almost same or rather the concentration of oxide film is larger than that of Zry metal. That means there is a possibility of a mechanism in which  $^{14}\text{C}$  is not released immediately by corrosion but is incorporated into the oxide film and then released by diffusion or by other mechanism.

Based on the results of the long-term leaching test, the period required for all  $^{14}\text{C}$  in hull to be leached out was calculated. From the conservative point of view, a linear leaching rate was assumed using 5.5 month and 11.5 month leaching data. Estimation results of  $^{14}\text{C}$  leaching period are shown in Table 4. From these results, it was evaluated that a minimum period of 20 000 years or longer is required for all of  $^{14}\text{C}$  to be released from the Zry metal and 400 years for oxide film. In estimating the leaching period of actual hulls, the increase of surface area according to the compaction treatment should be considered if high-compaction method is applied. As  $^{14}\text{C}$  has a half-life of 5 730 years, it became clear that there is a possibility that introducing the hull leaching model may reduce the dose rate caused by  $^{14}\text{C}$ . Long-term leaching test is now being pursued using BWR hull to obtain and evaluate more realistic leaching data.

**Table 4: Estimation of  $^{14}\text{C}$  leaching period [1,13]**

Hull	Zry metal	Oxide film
Estimation results of leaching period	5.5 month data: $2.2 \times 10^4$ y 11.5 month data: $3.4 \times 10^4$ y	5.5 month data: $4.0 \times 10^2$ y 11.5 month data: $5.0 \times 10^2$ y

### ***Chemical form***

#### *Method*

From references [9] and [10] concerning the chemical forms of  $^{14}\text{C}$  released from Zry, there is a possibility that the leached  $^{14}\text{C}$  may exist in the chemical forms of  $\text{CO}_2$  and  $\text{CO}/\text{CH}_4$  in gas phase. Therefore, a wet analysis was conducted to judge whether the  $^{14}\text{C}$  in liquid phase is organic or inorganic, as shown in the analysis flow in Figure 3.

In this method of analysis, inorganic carbon in the sample solution is brought into contact with inorganic acid to form carbon dioxide and discharged for a measurement as inorganic carbon. Next, oxidizing agent is added to the remaining sample to oxidize and discharge all carbon as carbon dioxide for its measurement as organic carbon. For the  $^{14}\text{C}$  in gas phase, the following method was employed for separation and recovery.  $^{14}\text{C}$  in  $\text{CO}_2$  form is first absorbed into sodium hydroxide solution, and then  $^{14}\text{C}$  in  $\text{CO}$  form is converted into  $\text{CO}_2$  by a catalyst and is absorbed into a sodium hydroxide solution. Finally,  $^{14}\text{C}$  in  $\text{CH}_4$  form is burned for conversion into  $\text{CO}_2$  and absorbed into the sodium hydroxide solution.

**Table 5: HPLC measurement system [2]**

Measurement conditions	
Column	Rspax KC-811*2
Mobile phase	1mM HClO <sub>4</sub>
Flow rate	0.8ml/min
Column temperature	40°C
UV detector	
Wavelength	210nm
Response	SLOW
Output	0.001AU/mV
RI detector	
Polarity	+
Response	SLOW
Output	0.5*10-6RIU/10mV
Injection	100 μ l

**Table 6: GC-MS measurement system**

Detections are made using β-counter for hot samples and IR or UV detectors for cold samples. Alcohol fractions that are found in preliminary tests are collected and C-14 presence in these fractions are confirmed. (practically, all fractions are measured for C-14)

**<apparatus>**

GC-MS:	Agilent Technologies
Column:	19091X-213 (HP-Wax, 30m, 0.3mm)

**<condition>**

carrier gas	He (flow rate: 2.0 ml/min)
injection	sprit injection volume: 1.0 μL, inlet temp.: 230 degrees C.
column temp.	260 degrees C. (Max)
Calibration curves	at conc. : 0, 1, 10, 100 ppm (targets are below 10 ppm)

In the test of reference [2], High Performance Liquid Chromatography (HPLC) and Gas Chromatography-Mass Spectrometer (GC-MS) were introduced to identify the chemical forms of leached <sup>14</sup>C. The leaching test was pursued using Fe<sub>3</sub>C and ZrC. The system and conditions of HPLC and GC-MS are shown in Tables 5 and 6 respectively.

In the case of BWR hull, HPLC with beta liquid scintillation counting is used.

*Result*

Table 7 shows the results of the short-term leaching test of PWR hull [1]. The leached <sup>14</sup>C was not detected in the chemical form of CO<sub>2</sub>, CO or CH<sub>4</sub> in the gas phase, and most of it in organic forms were detected in the liquid phase. Thus, most of the leached <sup>14</sup>C had to be presumed as organic compounds in the liquid phase. Filtering the leached liquid with an anion filter showed that most of the <sup>14</sup>C exists in the filtered liquid and that, as a result of this, there is a possibility of <sup>14</sup>C existing as a substance other than organic acid. However, the concentration of the leached <sup>14</sup>C was too small, with 0.1 Bq/ml, to identify the chemical species.

**Table 7: Results of leaching tests of PWR hulls [1]**

No	Test period	Liquid phase		Gas phase			Total
		Inorganic <sup>14</sup> C	Organic <sup>14</sup> C	CO <sub>2</sub>	CO	CH <sub>4</sub>	
RUN-1	3 months	<0.1 Bq (0.1%)	102.2 Bq (100%)	<0.1 Bq (0.1%)	<0.1 Bq (0.1%)	<0.1 Bq (0.1%)	102.2 Bq
RUN-2	5.5 months	18.5 Bq (21.1%)	69.5 Bq (78.9%)	<0.1 Bq (0.1%)	<0.1 Bq (0.1%)	<0.1 Bq (0.1%)	87.5 Bq

In the test of reference [2], the low-molecular weight organic carbons were detected. Organic carbon species were identified as low-molecular weight alcohols, carboxylic acids and aldehydes. The identified carboxylic acids by HPLC analysis were formic acid (HCOOH) and acetic acid (CH<sub>3</sub>COOH), and the aldehyde was formaldehyde (HCHO). Methanol (CH<sub>3</sub>OH) and ethanol (C<sub>2</sub>H<sub>5</sub>OH) were confirmed by GC-MS analysis as shown in Table 8.

**Table 8: Identification results of organic carbon leached from Fe<sub>3</sub>C and ZrC [2]**

Metal	pH	CH <sub>3</sub> OH	C <sub>2</sub> H <sub>5</sub> OH	HCHO	HCOOH	CH <sub>3</sub> COOH
Fe <sub>3</sub> C	p H 8	—	—	○	○	○
	p H 12.5	—	○	○	○	○
ZrC	p H 8	—	○	○	○	○
	p H 12.5	○	○	○	○	○

### Discussion

The results of the leaching test, confirmed that most of the <sup>14</sup>C released from the hull and existing in the leached liquid are in organic forms [1]. From a thermodynamic viewpoint, the disposal environment has reduction atmosphere conditions with oxidation-reduction potential at approximately -300mV. Further, it is estimated that the oxidation-reduction potential is even lower in the phase boundary in which the corrosion of Zry occurs, a region where methane and methanol exist in stable forms according to the Pourbaix chart [11]. Hydrogen is generated from the reduction condition oxidation of Zry. Thus, there is a high possibility that the released <sup>14</sup>C exist as those organic compounds.

The chemical form of <sup>14</sup>C in the hull is not clear, but there is a possibility that it may exist in graphite or carbon compounds forms including ZrC (zircaloy carbide). These forms are generally stable. Reference [12] reports that hydrocarbon compounds linking multiple carbon atoms are generated from iron carbide in an iron/water system containing carbon, which implies the possibility of carbon compounds that are contained in a metal becoming organic matters when released from the metal in a metal/water system.

The chemical form of <sup>14</sup>C leached from hull is important in determining the retention functions of the nuclide in the barrier material. Although the chemical species of the leached <sup>14</sup>C could not be identified due to its low concentration, obtaining data concerning its chemical

species, generation mechanism and migration in a disposal environment is considered important and are expected to be measured in the near future [4].

### ***Distribution coefficient to cement***

#### *Method*

To examine the migration behavior of leached  $^{14}\text{C}$  in engineered materials, an obtaining test of the distribution coefficient to hydrated ordinary portland cement (OPC) and OPC/blast furnace slag (BFS) cement using the leached solution obtained in the leaching test was conducted in the case of PWR hull [1]. In order to simulate the disposal environment, the test was conducted inside a glove box controlled by argon gas-displaced atmosphere. 1L leaching solutions were poured into polypropylene bottles, and after the oxidation-reduction potential was lowered by iron powder, 100g of cement was added and the solutions were left to stand for 7 days. After the immersing test, the solids and liquids were separated by filtering, and an analysis of  $^{14}\text{C}$  in the filtered liquid was conducted using wet analysis. The test conditions are shown in Table 9.

**Table 9: Measurement conditions of distribution coefficient [1]**

Item	Conditions
Cement	(1) OPC, (2)OPC/BFS(=1/9)
Test solution	Leached liquid obtained from the leaching test
Solid-to-liquid ratio	1:10
Test period	1 week
Test temperature	Room temperature

In the reference [2], the distribution coefficient of the organic carbon species identified in the leached solution to OPC was measured. The test conditions are shown in Table 10. After pH of the solution was adjusted to around 12.5 with sodium hydroxide, the solutions were contacted with the powdered hydrated cement (<250 micrometer) at a ratio of 40 cm<sup>3</sup> to 4 g. After 100 days the solutions were filtered through 0.45 micrometer filter. All operations were performed inside a glove box.

**Table 10: Measurement conditions of distribution coefficient [2]**

	OPC
Liquid phase	Purified water
Solid particle diameter	250 micrometer or less
Liquid-to-solid ratio	10ml/g
The organic materials covered	Methanol, Ethanol, Formaldehyde Formic acid, Acetic acid
Concentration of organic materials	10ppm
Temperature	Room temperature
Atmosphere	Reducing atmosphere (in a glove box of 3%nitrogen-hydrogen)

## Result

The distribution coefficient is expressed in the following equation:

$$K_d = (C_o / C_e - 1) V / W \quad (2)$$

$K_d$ : distribution coefficient

$C_o$ : initial concentration of  $^{14}\text{C}$  (Bq/ml)

$C_e$ : concentration of  $^{14}\text{C}$  after the test (Bq/ml)

$V$ : test solution volume (ml)

$W$ : cement weight (g)

Table 11 shows the concentration of  $^{14}\text{C}$  in the solutions before and after the test and the distribution coefficient obtained from the result. For the distribution coefficient of  $^{14}\text{C}$  for material, values were in the range of 1.9~8.8 ml/g. There was no significant difference in distribution coefficient according to the type of material between OPC and 1/9 (OPC/BFS) cement. There was also no significant difference in the liquid leached from the hull specimen and the hull specimen without the oxide film [1].

**Table 11: Results of the distribution coefficient measurement test [1]**

Barrier material	Test solution	$^{14}\text{C}$ concentration (Bq/ml)		Distribution coefficient (ml/g)
		Before test	After test	
OPC	Leached liquid from hull specimen	$1.9 \times 10^{-2}$	$1.6 \times 10^{-2}$	1.9
		$1.9 \times 10^{-2}$	$1.3 \times 10^{-2}$	4.6
	Leached liquid from hull without oxide film	$1.5 \times 10^{-3}$	$9.5 \times 10^{-4}$	5.8
		$1.5 \times 10^{-3}$	$1.2 \times 10^{-3}$	2.5
1/9 cement	Leached liquid from hull specimen	$1.9 \times 10^{-2}$	$1.4 \times 10^{-2}$	3.6
		$1.9 \times 10^{-2}$	$1.5 \times 10^{-2}$	2.7
	Leached liquid from hull without oxide film	$1.5 \times 10^{-3}$	$1.1 \times 10^{-3}$	3.6
		$1.5 \times 10^{-3}$	$8.0 \times 10^{-4}$	8.8

**Table 12: shows the distribution coefficients of the organic compounds to OPC obtained from tests in reference [2]**

Organic Compound	Distribution coefficient (ml/g)
Methanol ( $\text{CH}_3\text{OH}$ )	7.2
Ethanol ( $\text{C}_2\text{H}_5\text{OH}$ )	12
Formaldehyde ( $\text{HCHO}$ )	10
Formic acid ( $\text{HCOOH}$ )	4.1
Acetic acid ( $\text{CH}_3\text{COOH}$ )	9.5

## *Discussion*

The results show distribution coefficient values of  $^{14}\text{C}$  to cements are low and is consistent with the organic  $^{14}\text{C}$  leached. The distribution coefficient values obtained for leached  $^{14}\text{C}$  varies from 1.9 ml/g to 8.8 ml/g, hence the values for several organic materials identified in reference [2] varies from 4.1 ml/g to 12 ml/g. Further data will be obtained in BWR hull test and will be discussed further.

## ***Summary of the results and conclusion***

- a) Hull specimen was prepared from spent fuel to test inventory, leaching rate, chemical form and distribution coefficient of  $^{14}\text{C}$  released from Zry metal and oxide film.
- b) Inventory of PWR hull and BWR hull were obtained and compared with the calculation results using ORIGEN code. The inventory of Zry oxide film was larger than that of Zry metal.
- c) Leaching tests were conducted and leaching rate and chemical form of leached  $^{14}\text{C}$  were measured. Most of the leached  $^{14}\text{C}$  detected in the solution is in organic form, pointing the need for future research to understand its generating mechanism and migration in barrier material.
- d) Based on the leaching model, it was calculated that the period required to leaching all the  $^{14}\text{C}$  from the hull waste is 20 000 years or longer from Zry metal and 400 years or longer from an oxide film. The introduced leaching model shows clearly that the dose equivalent of  $^{14}\text{C}$  is reduced in the hull waste. In estimating the leaching period of actual hulls, the increase of surface area according to the compaction treatment should be considered if high-compaction method is applied.
- e) Long-term leaching test is now being pursued to obtain more realistic data regarding leaching rate, chemical form and distribution coefficient of  $^{14}\text{C}$  released from Zry metal and Zry oxide film.

## **REFERENCES**

- [1] Takashi Yamaguchi, Susumu Tanuma, Isamu Yasutomi, Tadashi Nakayama, Hiromi Tanabe, Kiyomichi Katsurai, Wataru Kawamura, Kazuto Maeda, Hideo Kitao, Moriyuki Saigusa, A Study on Chemical forms and Migration Behavior of Radionuclides in HULL

Waste, ICEM 1999, September, Nagoya, Japan, (1999).

\*This research was funded by the Japanese electric power utilities and JNFL.

- [2] Satoru Kaneko, Hiromi Tanabe, Michitaka Sasoh, Ryota Takahashi, Takayuki Shibano, Shinji Tateyama, A Study on the Chemical Forms and Migration Behavior of Carbon-14 Leached from the Simulated Hull Waste in the Underground Condition, MRS Fall Meeting 2002, December 2-6, Boston, MA, USA, (2002).

\*This research was funded by RWMC.

- [3] RWMC, Study on Carbon Migration Behavior Leached from Activated Metallic Wastes, (2004), (in Japanese).

\*This research was funded by Ministry of Economy, Trade and Industry(METI).

- [4] RWMC, Study on Carbon Migration Behavior Leached from Activated Metallic Wastes, (2005), (in Japanese).

\*This research was funded by METI.

- [5] H.D. Smith *et al.*, An Investigation of Thermal Release of Carbon 14 From PWR Zircaloy Spent Fuel Cladding, Journal of Nuclear Materials, 200, 128-137, (1993).

- [6] Japan Metal Society, Metal Data Book, (1984).

- [7] C.M. Hansson, The Corrosion of Zircaloy 2 in Anaerobic Synthetic Cement Pore Solution, SKB/KBS Technical Report, 84-13, (Dec.1984).

- [8] G. Plante *et al.*, Études de corrosion des matériaux de conteneurs pour le stockage des déchets radioactifs en sites granitiques, Communautés Européennes, EUR-8762FR (1984).

- [9] Lois *et al.*, Investigations into the Chemical Status of C-14 After Leaching of Cladding Material From Spent PWR and BWR Fuel Rods in a Salt Solution, SIEMENS U9414/88/001, (April 1988).

- [10] JAERI-M, 83-035, (1983).

- [11] Marcel Pourbaix, Atlas of Electrochemical Equilibria in Aqueous Solutions, (1974).

- [12] Baolin Deng *et al.*, Hydrocarbon Formation in Metallic Iron/Water System, Environ. Sc. Technol., 31.1185-1190, (1997).

- [13] Takashi Yamaguchi, Susumu Tanuma, Isamu Yasutomi, Tadashi Nakayama, Hiromi Tanabe, Kiyomichi Katsurai, Wataru Kawamura, Kazuto Maeda, Hideo Kitao, Moriyuki Saigusa *et al.*, A Study on Chemical forms and Migration Behavior of Radionuclides in HULL Waste, M45, M46, M7 of the proceedings of the Fall Meeting of the Atomic Energy Society of Japan, (1998). (in Japanese)

\*This research was funded by the Japanese electric power utilities and JNFL.

- [14] RWMC, Investigations into management and safekeeping measures for TRU wastes, (1998), (in Japanese).

\*This research was funded by METI.

## **DEVELOPMENT OF IMMOBILISATION TECHNIQUES FOR RADIOACTIVE IODINE FOR GEOLOGICAL DISPOSAL**

**Tsutomu Nishimura, Tomofumi Sakuragi, Yuji Nasu, Hidekazu Asano, Hiromi Tanabe**  
Radioactive Waste Management Funding and Research Center, JAPAN

### **Abstract**

Iodine-129 is predominantly contained in the silver adsorbents generated as waste during reprocessing plant operation. Cement kneaded solidification treatment is assumed to be the method of disposal for the waste. Because it has a half-life of as long as  $1.57 \times 10^7$  years and retardation by adsorption onto barrier materials is unlikely,  $^{129}\text{I}$  is recognised as one of the nuclides governing the exposure dose in geological disposal of TRU waste [1].

We are developing techniques for the immobilization of  $^{129}\text{I}$  that are able to flexibly adapt to the wide range of geological environments of Japan, with the aim of improving safety margins [1,2]. In developing these techniques, we are also developing iodine solidification treatment processes and assessing the capability of the waste form to control iodine release.

In this study, based on the results various immersion tests and investigations into the properties of three types of materials, the mechanisms of iodine release from the solidified substances were understood and long-term confinement performances were evaluated.

## **Introduction**

In nuclear reprocessing plants in Japan, radioactive iodine in the pretreatment process off-gas is collected using silver adsorbent. This waste silver adsorbent includes  $^{129}\text{I}$  and is categorized as TRU waste for geological disposal.

Iodine-129 has a long half-life ( $1.57 \times 10^7$  y) and is thought to exist in  $\text{I}^-$  chemical form in groundwater. Therefore, retardation of  $^{129}\text{I}$  by sorption onto barrier materials in the geological disposal environment is unlikely, and thus the peak exposure dose is easily affected by geological environmental conditions such as groundwater flow rates. Consequently, to flexibly meet the wide range of geological environmental conditions found in Japan, development of an iodine immobilization technique which aims to improve the performance of the solidified substance is desired to reduce the peak exposure dose.

The aim in this research is to develop iodine immobilisation techniques and propose effective solidifications for a variety of geological environments, from such viewpoints as reduction of  $^{129}\text{I}$  exposure dose, reliability of the long-term material performance evaluation, and feasibility of the iodine solidification treatment process.

Because  $^{129}\text{I}$  is a nuclide with a long half-life as noted above, radioactive decay by complete confinement with artificial barriers cannot be expected. Therefore, the development policy is to reduce the peak exposure dose by developing iodine immobilisation techniques able to delay the rate of iodine release from the waste form over long periods.

## **Relationship between iodine release period and exposure dose**

In order to set the desired iodine release delaying capability for the waste form, the relationship between the maximum  $^{129}\text{I}$  exposure dose and the iodine release period was assessed through calculations.

### ***Calculation analysis outline***

The disposal concept is based on a reference case in the 2<sup>nd</sup> TRU Report [2] in Japan. Thus, crystalline rock was assumed for the geological environmental conditions and 1 000 meters was adopted for the depth of the disposal facilities. In addition, the disposal facilities were assumed to be circular tunnels, which can be constructed even in crystalline rock with its relative abundance of cracks.

For the analysis code, the basic environmental nuclide concentration calculation code “FRONT” was used for the migration of nuclides which leach out from waste and pass through filling materials. This code handles advection-diffusion of multiple nuclides in the decay chain in a spatial one-dimensional system. For nuclide migration through host rock including cracks and faults around the repository, the natural barrier nuclide migration code “CRACK” was used. In this code, transmissibility in the host rock has a distribution and in faults is a fixed value. A

dose conversion coefficient of  $3.2 \times 10^{-15}$  (Bq/Sv) is used for a farmer based on the river water scenario.

### ***Analysis conditions***

The leaching periods from waste were set as instantaneous,  $10^4$ ,  $10^5$  and  $10^6$  years. The effective diffusion coefficients for iodine used were  $4 \times 10^{-11}$  in bentonite and  $3 \times 10^{-12}$  in the host rock. As in the case for 2<sup>nd</sup> TRU Report [2], the natural barrier was treated as a model of an accumulated fracture media with parallel flat-plate cracks. An average value of transmissibility was set  $10^{-9.99}$  in the reference case and one order of magnitude larger than that in variant case.

### ***Dose evaluation results***

Figures 1 and 2 show the relationship between  $^{129}\text{I}$  exposure dose and elapsed time after disposal when iodine release periods (instantaneous,  $10^4$ ,  $10^5$ , and  $10^6$  years). In the reference case (Figure 1), no noticeable difference was seen in the maximum exposure dose between instantaneous release and release period of  $10^4$  years. When the release period is  $10^5$  years or longer, the maximum exposure dose tended to decrease. In the variant case (Figure 2), the effect of  $^{129}\text{I}$  release period on the decrease in maximum exposure dose is larger than that in the reference case.

**Figure 1: Effect of leaching period on dose (Transmissibility range:  $10^{-13}$ – $10^{-7}$  m<sup>2</sup>/s)**

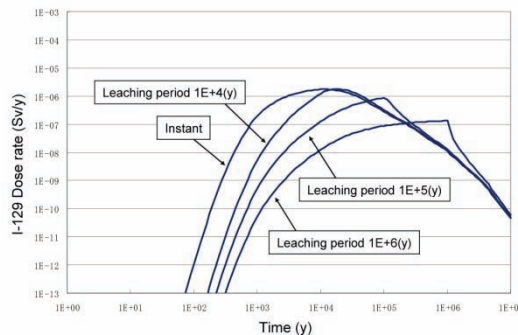


**Figure 2: Effect of leaching period on dose (Transmissibility range:  $10^{-12}$ – $10^{-6}$  m<sup>2</sup>/s)**

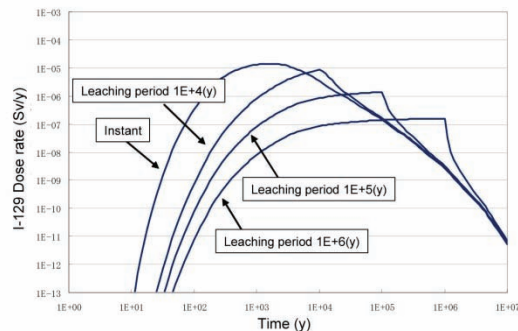
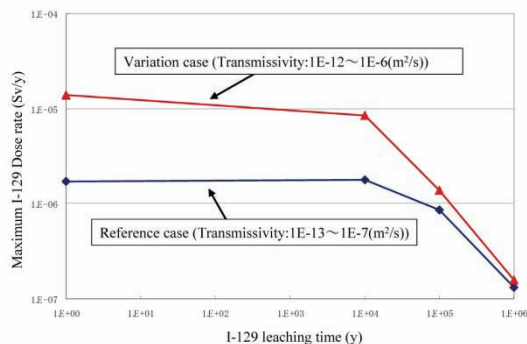


Figure 3 shows the relationship between the maximum exposure dose and release period. No noticeable reduction was observed in the maximum exposure dose when iodine release

period less than  $10^4$  years for either the reference case or the variant case. When the iodine release period was longer than  $10^5$  years, dose reduction is notable and the difference between reference and variant case is negligible. This result indicates that the controlling iodine release over  $10^5$  years reduces the effects of geologic conditions on the dose.

**Figure 3: Decreases in max. dose with I-129 leaching period at different transmissibilities**



In Japan, advances in engineering barrier systems for a variety of geological conditions are important in industrialising TRU waste disposal because disposal sites and the specific geologic environment have not yet been identified. Consequently, our goal is to develop waste forms that are able to suppress release for at least  $10^5$  years.

## Iodine immobilisation techniques

### *Features of iodine immobilisation techniques*

The techniques developed for the treatment and disposal of  $^{129}\text{I}$  can be classified into the following three types, according to iodine release mechanism.

- Leaching model (intergranular diffusion, congruent dissolution)
- Distribution equilibrium model
- Solubility equilibrium model

In the leaching model,  $^{129}\text{I}$  is physically sealed into intergranular solids and is released from the solid by diffusion through infiltrating groundwater. The iodine also leaches due to the surface dissolution of the solid. In the distribution equilibrium model, iodine is released depending on its sorptivity onto solid hydrates. In the solubility equilibrium model, iodine is fixed in an insoluble mineral as a component element. Five immobilisation techniques and the performance assessment models are listed in Table 1.

**Table 1: Iodine immobilisation techniques and performance assessment models**

Solidification technique	Immobilisation mechanism	Performance assessment model (assumption)
Synthetic rock	AgI is fixed in SiO <sub>2</sub> (quartz) grain boundaries	Diffusion through quartz intergranular
AgI vitrification	Immobilising I as a glass-forming component (3AgI-2AgI <sub>2</sub> O-P <sub>2</sub> O <sub>5</sub> )	Leaching model
BPI vitrification	Fixing I in a glass (6.5PbO-3B <sub>2</sub> O <sub>3</sub> -0.5ZnO) matrix	Leaching model
High performance cement	Sorption of IO <sub>3</sub> <sup>-</sup> onto ettringite and monosulphate	Distribution equilibrium model
Insoluble mineralization / synthetic sodalite	Immobilizing I in synthetic sodalite (Na <sub>8</sub> (AlSiO <sub>4</sub> ) <sub>6</sub> I <sub>2</sub> )	Solubility equilibrium model

The five waste forms were studied in experimental sizes with volumes of a few hundred milliliters through pretreatment and solidification. In addition, performance and modelling based on leaching properties were investigated for the three immobilisation techniques, using synthetic rock, AgI vitrification and high-performance cement, with results indicating that these wastes satisfy the requirements for performance. For the BPI vitrification and synthetic sodalite techniques, immersion tests were performed and experiments to test the effects of environmental conditions on performance are currently underway.

### *Synthetic rock technique*

#### *Iodine immobilisation principle*

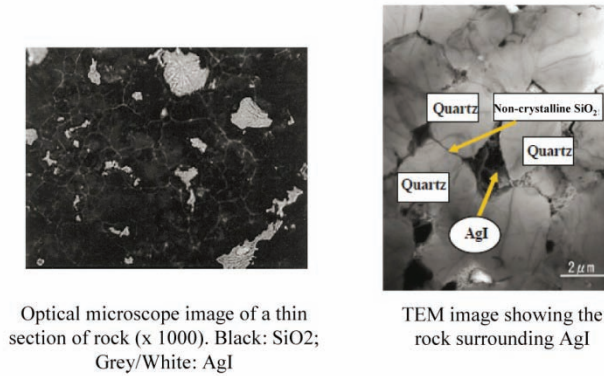
In synthetic rock, the iodine is held and fixed within densely solidified quartz grains in the form of silver iodide through hot isostatic pressing (HIP). Because natural hard rock such as granite provides long-term durability with a matrix that is difficult to dissolve and that does not easily allow water penetration, the chemical elements inside are not easily released. Therefore, it is assumed that the rocks changed to a crystalline material by HIP are stable and able to immobilize iodine over long periods.

#### *Solidification*

In HIP treatment, the waste silver adsorbent is pulverized and packed into a capsule, which is then heated at 750°C and 100 MPa for 1 hour [3,4]. This procedure generates very little secondary waste.

Figure 4 shows the optical photomicrograph (right) and TEM image (left) of the inside of the waste silver adsorbent immobilised in the synthetic rock. TEM observations show that SiO<sub>2</sub> in the matrix forms quartz crystals (several μm–10 μm in diameter) covered by a thin layer (30–50 nm) of amorphous SiO<sub>2</sub>. Iodine exists as AgI crystals, which are sealed into the matrix pore as aggregate of about 20 nm. Since the compressive strength of the rock is over 100 MPa, fracturing after disposal is thought to be unlikely and permeability was shown to be low.

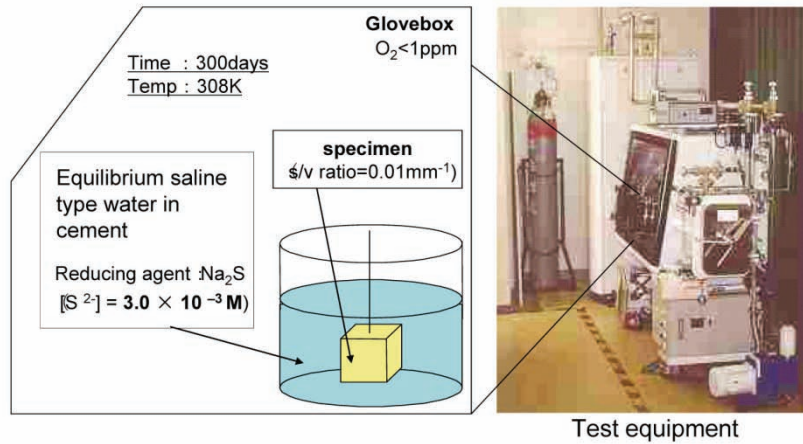
**Figure 4: Micrographs of AgI in rock**



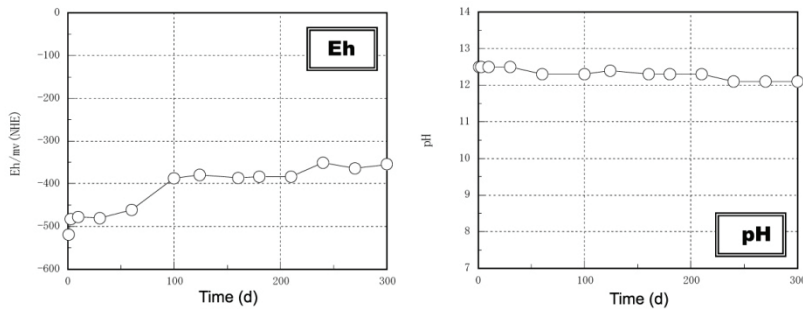
*Long-term durability of synthetic rock*

Figure 5 shows a schematic diagram of the apparatus and test conditions for the long-term immersion test [5]. The test was performed for 300 days, at the high-pH and under the reducing conditions assumed for the TRU repository environment. In Figure 6, the results of Eh and pH during the leaching test period are illustrated, while changes in iodine and silicon concentrations with time are shown in Figure 7.

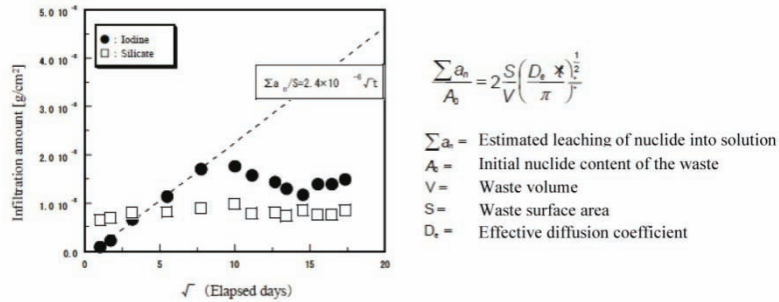
**Figure 5: Schematic representation of leaching test for HIP product**



**Figure 6: Changes in Eh and pH with test periods**

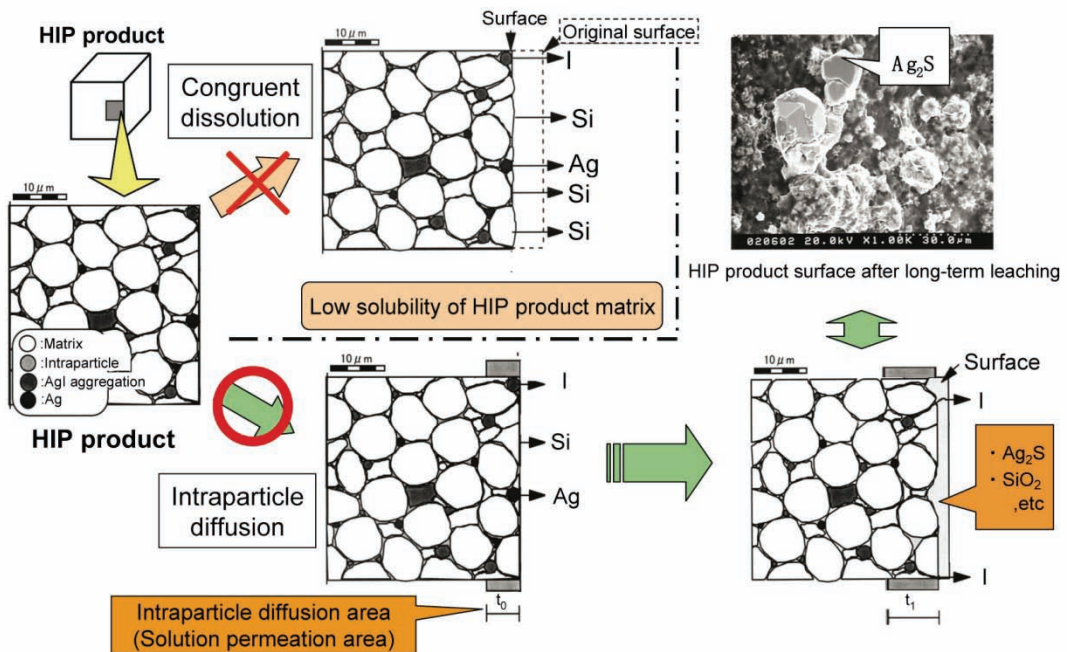


**Figure 7: Relationship between amount of iodine and silicate leached and  $\sqrt{t}$  (leaching period, t) for long-term leaching experiments**



It is assumed that the iodine release pathway from synthetic rock is the cavity between the grain boundary (about 50 nm) formed by the melting of amorphous  $\text{SiO}_2$ , which fills the area between the quartz matrix grains, and that iodine diffusion to the outside occurs through the cavities due to  $\text{AgI}$  being dissolved by the reducing agent present in the penetrating solution (Figure 8). A linear trend can be seen until about 60 days (Figure 7), which indicates diffusion. The diffusion coefficient calculated from the equation in Figure 7 is as small as  $D_e = 4.1 \times 10^{-20}$  ( $\text{m}^2/\text{s}$ ), but this trend decreases with time after 60 days. Based on these results, it is thought possible to immobilize the iodine over a long period of time because release from synthetic rock is controlled by diffusion, the rock provides high compression strength with low water permeability, and the quartz matrix provides low solubility even in a reducing environment.

**Figure 8: Schematic representation of leaching mechanisms from synthetic rock wastes**



## *AgI vitrification technique*

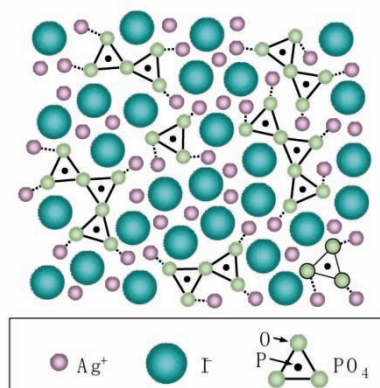
### *Iodine immobilisation principle*

The AgI vitrification technique consists of the chemical uptake of iodine into glass, immobilizing the AgI as a glass constituent. AgI glass has been developed as strong ion-conducting glass, with the composition  $\text{AgI-Ag}_2\text{O-M}_x\text{O}_y$ . This glass forms stably and is thought to immobilize the radioactive AgI. To form the glass matrix,  $\text{P}_2\text{O}_5$  was chosen by parametrically verifying its melting point when it is fabricated as a vitrified substance and its capability to confine iodine after vitrification [6,7].

### *AgI vitrification*

Using silver phosphate, a vitrification additive agent, a  $3\text{AgI-2Ag}_2\text{O-P}_2\text{O}_5$  composition is heated at  $500^\circ\text{C}$  for 6 hours to create the AgI vitrified substance. Figure 9 shows a structural drawing of the AgI vitrified material. Iodine itself is part of the glass structure and is homogeneously taken into the vitrified substance. Because the iodine content of AgI glass is as high as 30wt%, this method significantly reduces waste volume and reaches the compression strength of 90 MPa, sufficient for burial.

**Figure 9: Structure of AgI glass**

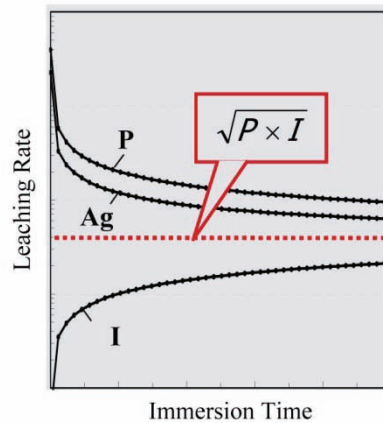


### *Long-term durability of AgI vitrified waste*

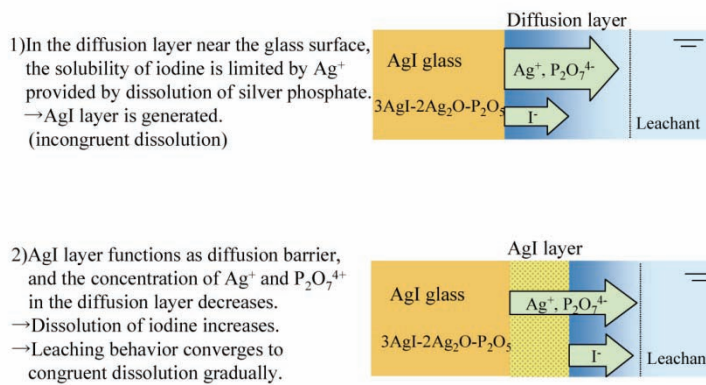
Figure 10 illustrates expected elemental leaching behaviour from AgI glass based on the hypothesis of leaching model (Figure 11). In the beginning, the leaching may be incongruent where the iodine leaching rate is extremely low compared with Ag and P, which is attributed to the formation of a stable AgI layer at the surface because of the high  $\text{Ag}^+$  concentration there. This AgI layer does not dissolve in the vicinity of the glass surface even in reducing conditions. Instead, it acts as a diffusion barrier that retards the diffusion of water into the glass matrix, causing Ag and P leaching to decrease with time. When the leaching is lowered to a certain point, the AgI layer begins to dissolve due to the decrease in the amount of  $\text{Ag}^+$  feeding the AgI

layer. Consequently, in the long term, the AgI layer is thought to converge to a certain thickness and approach congruent dissolution.

**Figure 10: Supposed behavior from AgI glass**



**Figure 11: Iodine leaching model from AgI glass**



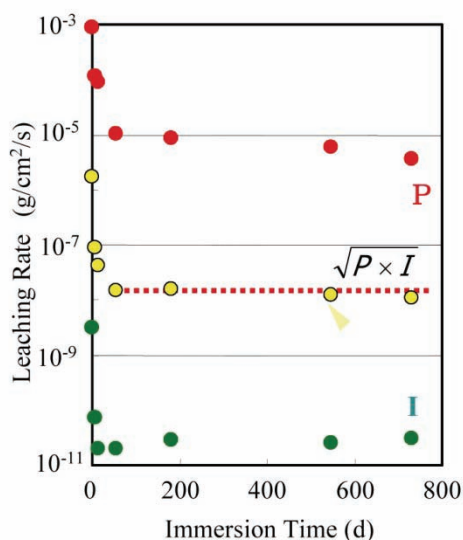
In the present model, the equilibrium leach rate at congruent dissolution can be found from the geometric mean of the transitional rates of P and I, which suggests that the equilibrium leaching rate is obtained from the experimental results, even if congruence is not reached within the experimental period.

Table 2 and Figure 12 show the experimental conditions and the results of the long-term leaching test (728 days) under high-pH and reducing conditions simulating the TRU repository environment. These results indicate that the geometric mean of the leaching rates for P and I is nearly constant except in the beginning, a trend which is seen in the results for other solutions such as deionized water and fresh groundwater below  $3 \times 10^{-7} \text{ g/cm}^2/\text{d}$ , suggesting the equilibrium leaching rate (Table 3).

**Table 2: Leaching test condition for AgI glass**

Size of specimen	13mm X 13mm X 13 mm
Type of leachant	Sea Water Equilibrated with Cement
pH of leachant	12
Leaching temperature	35°C
Reducing agent	Ferrous powder, 3% H <sub>2</sub> gas
Glass surface area to leachant volume ration	0.1 cm <sup>-1</sup>
Oxygen concentration in gaseous phase	< 1 ppm
Leaching period	728 days

**Figure 12: Leaching test results from AgI glass**



**Table 3: Leaching test results from AgI glass**

Immersion Water Type	Surface Layer Components	Equilibrated Leaching Rate [g/cm <sup>2</sup> /d]	Leaching Period* [y]
Rainfall	AgI, Ag(minor)	1.9 X 10 <sup>-7</sup>	1.4 X 10 <sup>6</sup>
Pure Water	AgI	2.3 X 10 <sup>-7</sup>	1.2 X 10 <sup>6</sup>
Sea Water Equilibrated with Cement	AgI, AgCl	1.6 X 10 <sup>-8</sup>	1.7 X 10 <sup>7</sup>
Na <sub>2</sub> S Soln. 10 <sup>-4</sup> mol/L	AgI, Ag <sub>2</sub> S(minor)	2.8 X 10 <sup>-7</sup>	9.4 X 10 <sup>5</sup>

\* Dimension of Waste: f43cm, H32.5cm, vol. ca.50L

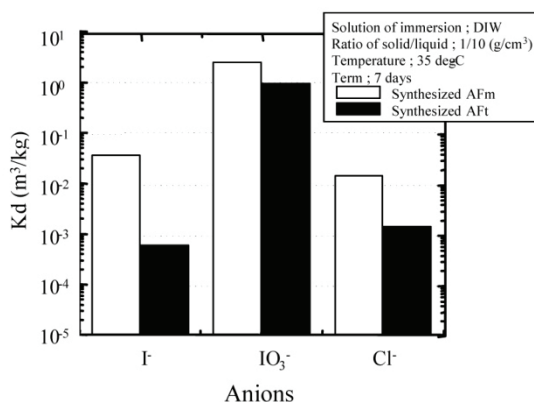
Consequently, the present leaching model can be adapted to different types of groundwater in the disposal environment. However, the leaching rate increases at sulfide ion concentrations greater than  $3 \times 10^{-4}$  mol/L, indicating that the sulfide concentration in groundwater is important in the disposal of AgI vitrified waste.

## High-performance cement technique

### Iodine immobilisation principle

Generally, iodine weakly adsorbs onto ordinary cementitious materials. However, some cement hydrates such as AFt (ettringite:  $\text{Ca}_6[\text{Al}(\text{OH})_6]_2 \cdot 24\text{H}_2\text{O}$ )  $(\text{SO}_4)_3 \cdot 2\text{H}_2\text{O}$ ) and AFm (monosulfate:  $[\text{Ca}_2\text{Al}(\text{OH})_6]_2(\text{SO}_4) \cdot 6\text{H}_2\text{O}$ ) easily adsorb anions. The high-performance cementitious technique uses high-performance cement enriched with aluminate sulfate based compounds (AFt and AFm). Iodine is fixed as a chemical form of  $\text{IO}_3^-$  due to its high affinity for the cementitious materials as shown in Figure 13 [8].

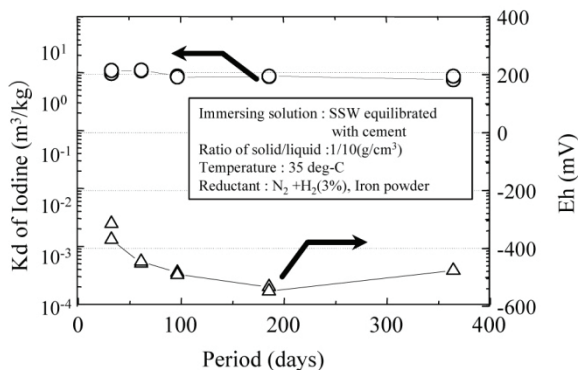
**Figure 13: Distribution coefficients of anions for cement materials**



### Cement solidification

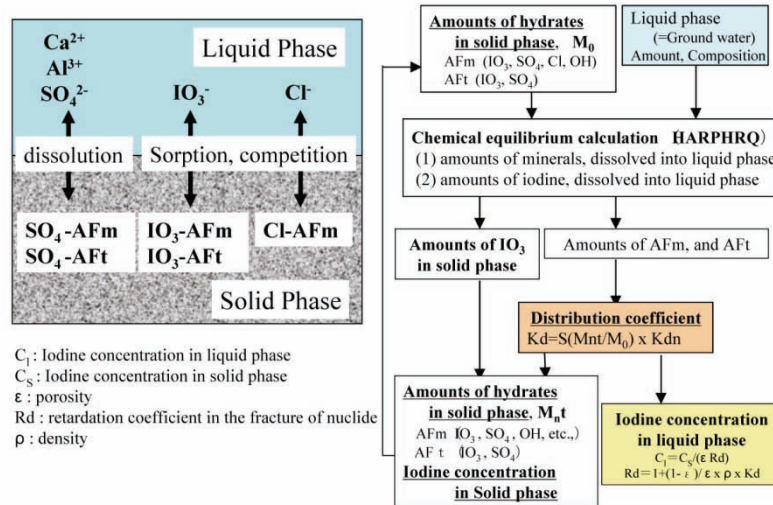
As a pretreatment, iodine is separated from the waste silver adsorbent in solution and converted into  $\text{IO}_3^-$  using ozone. The oxidized iodine is immobilised through kneading and solidification in a cementitious material with a highly affinity for anions. Because of the pretreatment in alkaline solutions, transition of iodine to the gas phase is rare, and the iodine recovery rate is extremely high, over 99.96%. Additionally, cementitious waste forms up to 20 L have been created.

**Figure 14: Results of long term leaching tests from cement materials**



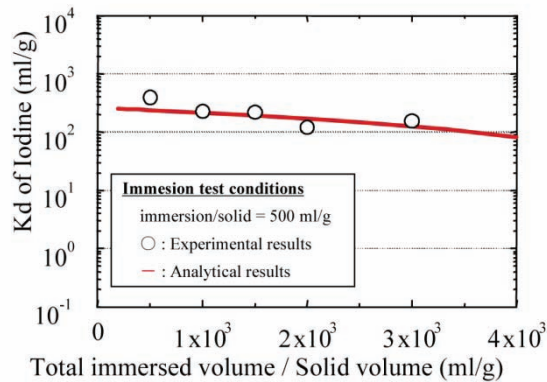
The sorption properties of iodine onto high-performance cement were evaluated through long-term leaching tests. Under reducing conditions, experiments were carried out in seawater-based cement equilibrium simulated groundwater [9]. Figure 14 shows the long-term immersion test results, which confirm that it is possible to maintain distribution coefficients at over 900 mL/g and that iodine is immobilized in AFt. Therefore, the distribution equilibrium model was thought to be applicable to this cemented substance and a long-term evaluation model (Figure 15) was formulated.

Figure 15: Leaching model of the components from cement materials



In order to confirm the long-term performance with accelerated experiments, liquid exchange tests were conducted, up to the maximum integrated liquid-to-solid ratio of 3 000 mL/g under reducing conditions in the seawater-based cement equilibrium simulated underground water (Figure 16). The distribution coefficient was over 100 mL/g even at the integrated liquid-to-solid ratio of 3 000 mL/g, suggesting that it is possible to evaluate experimental results using the model and the iodine release from the high-performance cement using the long-term evaluation model.

Figure 16: Distribution coefficients of iodine for cement material after liquid exchange



### ***Synthetic sodalite technique***

The synthetic sodalite technique is one type of insoluble mineralization to confine and immobilize iodine in a crystal structure. Sodalite is a kind of aluminosilicate and is naturally produced in Na-rich igneous rocks. The ideal chemical formula is expressed by  $\text{Na}_8(\text{AlSiO}_4)_6\text{X}_2$ , where halogen elements such as Cl or anions ( $\text{SO}_4^{2-}$  and  $\text{NO}_3^-$ ) can be substituted for X. It is assumed that homologous iodine is substituted for chlorine in the sodalite structure [10].

### ***BPI vitrification technique***

$\text{BiPbO}_2\text{NO}_3$  (BPN) is an inorganic ion exchanger developed to remove and immobilize various kinds of industrial waste liquids and negative ions, in particular, halogen generated as a result of nuclear power generation. The crystal structure of BPI ( $\text{BiPbO}_2\text{I}$ ) is similar to that of the natural mineral perite ( $\text{BiPbO}_2$ ) and is chemically stable. The BPI vitrified substance is formed by mixing BPI with  $\text{B}_2\text{O}_3$ -PbO based glass, a kind of lead glass used for radiation shielding, and then melting and solidifying the combination. Iodine is immobilized as a chemical form of  $\text{BiPbO}_2\text{I}$  in the matrix [11,12].

### **Summary**

A classification of the solidification products based on the iodine immobilization principles is below.

- Crystalline matrix: Iodine is fixed in the refractory matrix and leaching is suppressed; synthetic rock immobilised substance.
- Vitrification: Iodine leaching is suppressed by the surface layer formed by immersion in solution; AgI vitrified substance, BPI vitrified substance.
- High performance cement: Iodine is sorbed onto cement minerals.
- Synthetic mineral: Iodine leaching is controlled by mineral solubility equilibrium; synthetic sodalite.

Using the iodine leaching data for synthetic rock, AgI vitrification and high-performance cement solidification for evaluation on a practical scale (rock:  $\phi 25.5 \times 24$  (cm), AgI glass:  $\phi 43 \times 32.5$  (cm)), the time needed for complete iodine depletion from these waste forms was estimated to be  $10^5$  years or more.

This research is a part of “Development of immobilization techniques of radioactive iodine for geological disposal” under a grant from the Ministry of Economy, Trade and Industry (METI).

## REFERENCES

- [1] Progress Report on Disposal Concept for TRU Waste in Japan. 2000. Japan Nuclear Cycle Development Institute and The Federation of Electric Power Companies.
- [2] Progress Report on Disposal technology for TRU Waste in Japan. 2005. Japan Nuclear Cycle Development Institute and The Federation of Electric Power Companies. (in Japanese)
- [3] Wada, R., T. Nishimura *et al.* 1999. Fixation Radioactive Iodine by Hot Isostatic Pressing. The 7th International Conference Proceedings on Radioactive Waste Management and Environmental Remediation, Session 35 (L-7), No. 20 (ICEM 1999), Nagoya, Japan. (CD-ROM)
- [4] Wada, R., T. Nishimura *et al.* 2004. Manufacturing of Rock Solidified Waste by HIP. Publication of the Atomic Energy Society of Japan, 3 [2]: 165–173. (In Japanese)
- [5] Wada, R., T. Nishimura *et al.* 2004. Study on Iodine-Leaching Mechanism for HIP Rock Solidified Waste Form. Atomic Energy Society of Japan, 3 [2]: 174–184. (In Japanese)
- [6] Fujihara, H., T. Murase *et al.* 1999. Low Temperature Vitrification of Radioiodine Using AgI-Ag<sub>2</sub>O-P<sub>2</sub>O<sub>5</sub> Glass System. *Mat. Res. Soc. Symp. Proc.* Vol. 556: 375–382.
- [7] Noshita, K., T. Nishi *et al.* 1999. Vitrification Technique of Radioiodine Waste Using AgI-Ag<sub>2</sub>O-P<sub>2</sub>O<sub>5</sub> Glass System. The 7<sup>th</sup> International Conference Proceedings on Radioactive Waste Management and Environmental Remediation, Session 35 (L-7), No. 19 (ICEM 1999), Nagoya, Japan.
- [8] Tomita, F., K. Kaneko *et al.* 1999. Development of Iodine Immobilization Process with Cementitious Materials. Proc. of the 7<sup>th</sup> Int. Conf. on Radioactive Waste Management and Environmental Remediation.
- [9] Toyohara, M., M. Kaneko *et al.* 2000. Iodine Sorption onto Mixed Solid Alumina Cement and Calcium Compounds. *Journal of Nuclear Science and Technology*, Vol. 37, No. 11: 970.
- [10] Nakazawa, T. *et al.* 2001. Iodine Immobilization by Sodalite Waste Form. *Mat. Res. Soc. Symp. Proc.* Vol. 663: 51.
- [11] Amaya, T., A. Mukunoki, M. Shibuya and H. Kodama. Leaching of Iodine Ion from BiPbO<sub>2</sub>I under Reducing Conditions. ICEM 2001.
- [12] Amaya, T., A. Mukunoki and M. Shibuya. Study of BiPbO<sub>2</sub>NO<sub>3</sub> for I-129 Fixation under Reducing Conditions. MRS 2000.

## **BURN-UP EFFECT ON INSTANT RELEASE FROM AN INITIAL CORROSION OF UO<sub>2</sub> AND MOX FUEL UNDER ANOXIC CONDITIONS**

**J. Quiñones<sup>1</sup>, J. Cobos<sup>2</sup>, E. Iglesias<sup>1</sup>, S. van Winckel<sup>2</sup>, A. Martínez-Esparza<sup>3</sup>, J.P. Glatz<sup>2</sup>**

1. Ciemat. Avda. Complutense, 22. 28040-Madrid. Spain

2. ITU-JRC. Postfach 2340, D-76125 Karlsruhe. Germany

3. ENRESA. C/ Emilio Vargas, 7. 28043-Madrid. Spain

### **Abstract**

The objective of the work is to obtain instant release experimental values for different radionuclides as a function of spent fuel type (UO<sub>2</sub> and MOX) and burn-up (from 30 to 63 MWd/kgU) that will be useful for the performance assessment studies related to the behaviour of spent fuel under repository conditions or, in any case, spent fuel conditions in which labile radionuclides can be released.

To determine the instant release source terms, sets of leaching experiments were conducted with spent UO<sub>2</sub> and MOX fuel with burnups ranging from 30 to 63 MWd/kg U in presence of cladding as the container material. The fuels were leached in carbonated groundwater (CW) having a buffered pH of 7.5 at room temperature. Some observations are also made of the differences in matrix dissolution behaviour of the different fuels based on observed U, Pu and Np concentrations. The ultimate issue is to evaluate the differences in the “instant” inventory measurements for spent fuels in order to provide experimental data that allow to evaluate the source terms used in the safety-assessment calculations, and to improve the accuracy of such data for the future. It is important to remark that the quality of the experimental results obtained describes the influence of the spent fuel (SF) burn-up on fast release of inventory fraction (release under 200 days).

## Introduction

The fraction of SF radionuclides inventory undergoing fast release – in premature or normal failure under repository conditions – is one of the key issues necessary to describe in a performance assessment study because they govern the doses in SF storage under possible storage conditions. Nowadays, radionuclide release models used (ENRESA [1], SFS [2]) consider a conservative radionuclide inventory obtained from correlations with fission gas inventories.

Prediction of SF alteration rate is a difficult problem because of the sensitivity of uranium solubility to the redox conditions [3 and their references]. Although the SF matrix has a low solubility value ( $< 10^{-11} \text{ mol}\cdot\text{dm}^{-3}$ ) under reducing conditions, its solubility increases in some orders of magnitude under oxidizing conditions [2, 4]. Therefore, a prediction of the evolution of the SF alteration rate as a function of the conditions of the repository environment considered (groundwater composition, radiation field, etc.) is necessary.

The initial scenario, in most of the performance assessment studies, considers that contact between groundwater and the SF matrix reaches after the failure of the disposal containers, designed for a minimum safety lifetime of thousands years because the SF cladding is not considered from a performance assessment point of view. The behaviour of a failed canister is complex and depends on a large number of factors [5]. As a consequence of this contact (groundwater vs SF matrix) a fast initial radionuclide release will be observed due to the dissolution of soluble phases deposited in the gap region and the grain boundary during reactor operation. This behaviour was collective labelled as “Instant Release Fraction”. However, a new definition for the process has been propounded by Werme *et al.* [6]. They suggest for a repository situation the term “Rapid Release Fraction” as more appropriated for a better description since, “although it may be considerably faster than the release of matrix-bound radionuclides, the release from the grain boundaries may well continued for an extended period of time”[6].

From a safety point of view [2, 5-7] both are considered as an instant release from the SF matrix. Based on experimental evidences is possible to affirm that the SF source term (radionuclide release from matrix) is usually described as a combination of these processes: i) Rapid release of radionuclides (Instant Release Fraction or Rapid Release Fraction). Those radionuclides located in gap (gases or soluble precipitates) or in matrix grain boundaries; these areas are easy going leached when contact is reached; ii) Slow radionuclide release. This process is directly related to SF alteration rate (i.e., oxidation and dissolution rate of the matrix).

The initial release of radionuclide produced in the first stage of the alteration represents the highest contribution to the final doses arised from the fist instants of the disposal as it could be read in many of the published performance assessment calculations [2, 5-7]. For example, in the Spanish performance assessment, calculations performed assume that rapid release fraction of radionuclides will have the following composition: Cs, I, Rb, Cl, K, C, Kr. The release estimated is the 6% of the total inventory in the rod; in case of Se, Sn, Sr, Tc, Pd, Ag the release

considered is 3% of the total inventory in the rod. A clear controversial exists about the amount of each radionuclide needed to be considered in these type of exercises.

This document is focussed on to determine the radionuclides needed to be included as fast release and to explain their behaviour in leaching experiments. In order to clarify the aforementioned controversy in relation to the amount of each radionuclide, the paper discuss the experimental results measured in leaching experiments performed with SF (UO<sub>2</sub> & MOX with different levels of burn-up) under simulated repository conditions. The paper provides and evaluates the differences in the radionuclide release obtained during the first stage of the leaching process. These experimental data will be useful to define a more conservative scenario and source terms to be used in future performance assessment studies; in order to improve the reliability of the results from both, the scientific point of view and the public opinion.

## Materials and methods

Four types of PWR fuels – with a different burn-up after irradiation in a commercial power reactor – were studied. The corresponding fuel parameters, specimen designation, burn-ups as well as technical specifications of the materials used for the SF leaching tests, are given in Table 1.

**Table 1: Summary of some properties of the materials used for the spent fuel leaching tests**

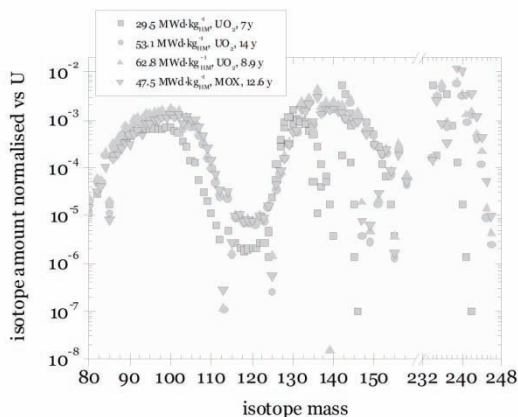
Label	Reactor type	Fuel type	Burn-up (MWd·kg <sup>-1</sup> U)	Fission gas Release (%)	<sup>235</sup> U enrichment (%)	Pu total (%)
PWR-UO2-1	PWR	UO <sub>2</sub>	62.8	9*	3.8	
PWR-UO2-2	PWR	UO <sub>2</sub>	29.5	0.36	6.85	
PWR-UO2-3	PWR	UO <sub>2</sub>	53.1	3	3.19	
PWR-MOX-4	PWR	MOX	44.4	7*	0.71	5

Two samples of each specimen were prepared for the leaching experiments: whole disc, approximately 1 mm thick, cut from the rods together with the SF cladding were obtained. Special attention in order to minimize the damage of the fuel and to get discs in pellet form was taken into account. The discs used in the experiments were all of a similar shape and size as shown in Table . One of the faces of the discs was used to perform surface characterisation before and after leaching tests. Fines produced during sample preparation were removed by appropriate washing of the samples. The samples manufacture, the experimental procedures and laboratory setup were similar for all the materials. Some degree of preoxidation cannot be excluded when the contact period with water begins. Therefore, possible changes among the different burn-up samples, in terms of pre-oxidized surface layer forming process must be ascribed to different storage times.

Commercial carbonated groundwater, Volvic (CW), was used for the leaching tests. Its composition is given in Table in equilibrium with air at room temperature. The pH of the leachate after the beginning of the leaching experiments was measured to be ~7.0. In order to

investigate the dissolution of the SF in presence of the cladding material, three SF  $\text{UO}_2$  with 30, 53, 63  $\text{MWd}\cdot\text{kg}^{-1}$  U burn-ups (labelled PWR- $\text{UO}_2$ -1, PWR- $\text{UO}_2$ -2 and PWR- $\text{UO}_2$ -3 respectively) and one SF MOX with a burn-up of 44  $\text{MWd}\cdot\text{kg}^{-1}$  HM (labelled PWR-MOX-40) were leached (Table). The values of the fission gas release were obtained by puncturing tests indicating the Xe and Kr isotopes released to the free volume. However those values corresponded to PWR- $\text{UO}_2$ -1 and PWR-MOX-4 were estimated from the the results obtained by Manzel and Johnson [7, 8].

**Figure 1: SF compositions as a function of burn-up and fuel type ( $\text{UO}_2$  and MOX)**



Static batch leaching experiments were performed on with 2 g samples of each SF discs in 70 ml volume borosilicate glass vessels. All tests were carried out at room temperature, in a hot-cell with air atmosphere; the leachant was 50 ml of CW water (Table). This was deaerated by purging with inert gas for several hours prior to the start of the leaching. During the whole of the contact period, the vessels remained sealed. The leaching experiments (same sample increasing leaching times) were performed by taking aliquots of leachate (1 ml) without replacement from the reaction vessel. The duration of single contact periods ranged from 0.1, 0.2, 1, 7, 12, 16, 30 to 500 days for IRO 1, 2, 7, 8 tests and from 0.1, 0.3, 1, 6, 13, 30 to 600 days for IRO 3, 4, 5, 6 (Table 2). The total timeframe of the experiments was about the order of 3 years.

**Table 2: Summary of the dimensions of SFs used for the leaching experiments**

	Exp. label	Height (mm)	Diameter (mm)	Total weight (g)	Cladding weight (g)	Fuel weight (g)
PWR- $\text{UO}_2$ -1	IRO1	3.50	9.95	2.06	0.52	1.54
	IRO2	3.50	10.03	2.83	0.52	2.31
PWR- $\text{UO}_2$ -2	IRO3	3.10	9.90	2.59	0.46	2.13
	IRO4	3.00	9.95	2.49	0.45	2.04
PWR- $\text{UO}_2$ -3	IRO5	4.20	9.85	2.63	0.63	2.03
	IRO6	3.10	9.91	2.47	0.46	2.01
PWR-MOX-4	IRO7	3.20	10.05	2.61	0.48	2.13
	IRO8	3.80	10.10	2.69	0.57	2.12

The solutions were analysed by Inductively Coupled Plasma – Mass Spectrometry (ICP-MS). The analyses were performed with a nuclearised ELEMENT 2 instrument (*Thermo Electron GmbH* Bremen, Germany) [8].

**Table 3: Composition of the CW used in the leaching experiments.**

	Conc. / mol.kg <sup>-1</sup> H <sub>2</sub> O)
Na <sup>+</sup>	4.09·10 <sup>-4</sup>
K <sup>+</sup>	1.46·10 <sup>-4</sup>
Mg <sup>2+</sup>	2.51·10 <sup>-4</sup>
Ca <sup>2+</sup>	2.47·10 <sup>-4</sup>
Cl <sup>-</sup>	2.37·10 <sup>-4</sup>
Si	4.99·10 <sup>-4</sup>
SO <sub>4</sub> <sup>2-</sup>	7.19·10 <sup>-5</sup>
HCO <sub>3</sub> <sup>-</sup>	1.07·10 <sup>-3</sup>
F <sup>-</sup>	1.05·10 <sup>-5</sup>
PO <sub>4</sub> <sup>3-</sup>	1.04·10 <sup>-7</sup>
Al <sup>3+</sup>	1.85·10 <sup>-7</sup>
U <sub>total</sub>	2.32·10 <sup>-9</sup>

It is important to remark that these results allow to evaluate the influence of burn-up and the difference existing between MOX or UO<sub>2</sub> on the final radionuclide release observed. As it is well known, the level of burn-up has a strong influence on the final isotopic compositions. Figure shows the composition of the SFs as a function of burn-up – these data are those used in the document aforementioned [8]. The results showed in the figure are normalised to the amount of U. The increase of burn-up is associated to an increase in the amount of fission products, activation products and actinides formed. This fact will have a strong influence in the final results obtained. Fraction of inventory in the aqueous phase (FIAP) for each element were previously explained in the base document [8] but this is not the objective of this document. The experimental results used in this document are those presented in the work from Cobos *et al.* [8].

## Results and discussions

As a difference between the previous report and this document, the concentration will be presented as “mol·dm<sup>-3</sup>”. These units are more useful for modelling the results with thermodynamical or kinetic approaches. Giving an example, Figure 2 to Figure 5, represent the evolution of the U, Pu and Np concentration as a function of the leaching time, type of SF and burnup. In these figures the U, Pu and Np concentrations data are represented as squares, circles and triangles, respectively. Furthermore, it is pointed out that with independence of the material considered – and/or the burn-up – achieved in the initial periods (lower than 1 day), the concentration in solution reached, approximately, the final value obtained. This fact evidence that, probably, for these elements the concentrations achieved is close to their own solubility value.

**Figure 2: Evolution of the U, Pu and Np conc. in leaching experiments performed with  $\text{UO}_2$  SF (burn-up  $\approx 30 \text{ MWd}\cdot\text{kg}^{-1}$  U) under simulated CW.**

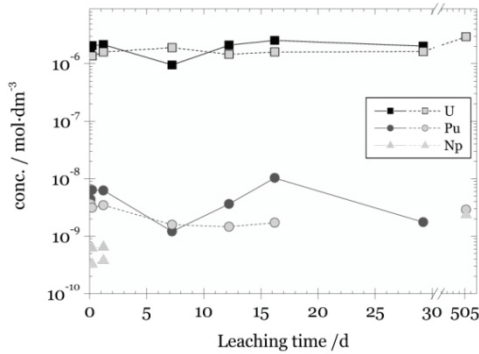


**Figure 3: Evolution of the U, Pu and Np conc. in leaching experiments performed with  $\text{UO}_2$  SF (burn-up  $\approx 53 \text{ MWd}\cdot\text{kg}^{-1}$  U) under simulated CW.**

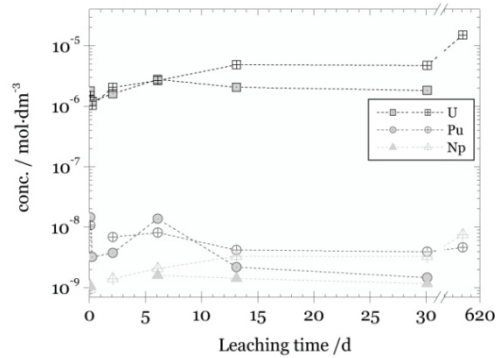


**Figure 4: Evolution of the U, Pu and Np conc. in leaching experiments performed with  $\text{UO}_2$  SF (burn-up  $\approx 63 \text{ MWd}\cdot\text{kg}^{-1}$  U) under simulated GW.**

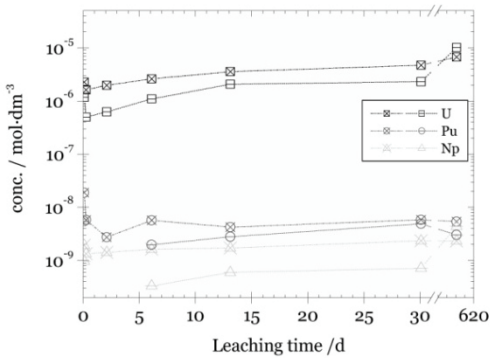
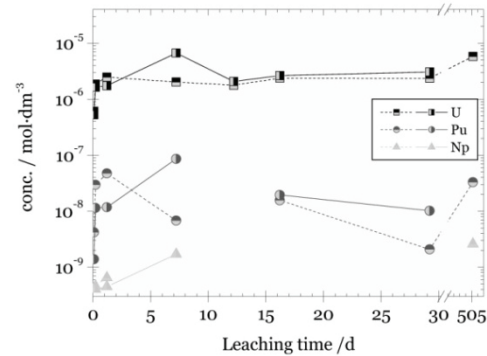


**Figure 5: Evolution of the U, Pu and Np conc. in leaching experiments performed with MOX SF (burn-up  $\approx 44 \text{ MWd}\cdot\text{kg}^{-1}$  U) under simulated GW.**



### ***Influence of burn-up***

Hereafter, for each element of interest, the data plotted is the mean concentration in solution obtained as a function of burn-up (Figure 6 to Figure 9). In the following figures the shape and colour are in concordance with those before presented. The data marked with a rectangle are those values obtained from MOX fuel leaching. As can be observed in Figure, the mean U concentration obtained for the low burn-up  $\text{UO}_2$  fuel ( $30 \text{ MWd}\cdot\text{kg}^{-1}$ ) in comparison with high burn-up fuels ( $53$  and  $63 \text{ MWd}\cdot\text{kg}^{-1}$ ) shows a clear dependence of the leached (SF). Since the experiments were performed at “initially” reducing conditions a clear effect of water radiolysis is observed between the low and high burn-up groups of experiments. The increase of the concentration with burn-up is due to higher radiation fields, in those experiments performed with higher burn-up. However, in the case of Pu and Np, the tendency observed is clearly different. In the case of Np, with independence of the burn-up or fuel type, the concentration value obtained is close to  $10^{-9} \text{ mol}\cdot\text{dm}^{-3}$ , whereas for the Pu ( $\text{UO}_2$  fuel), with independence of the burn-up, the concentration value obtained is close to  $10^{-9} \text{ mol}\cdot\text{dm}^{-3}$ [9]. This fact infers to

think that the concentration is controlled by solubility. Furthermore, in case of Pu, the tendency shows dependence with the type of SF  $\text{UO}_2$  or MOX.

**Figure 6: Influence of the SF burn-up on the final conc. in solution value achieved on leaching experiments under GW conditions.**

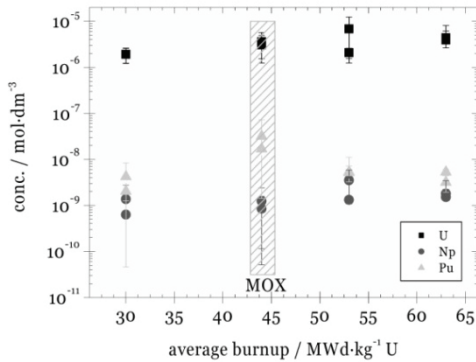


**Figure 7: Influence of the SF burn-up on the final conc. in solution value achieved on leaching experiments under GW conditions.**

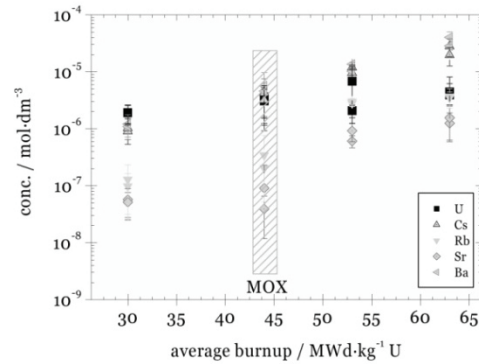


**Figure 8: Influence of the SF burn-up on the final concentration in solution value achieved on leaching experiments in granite conditions and under initially reducing conditions. Square point represents the U conc. in solution, whereas Mo, Tc, Cd, Ru, Rh and Pd are plotted with the same nomenclature than before.**

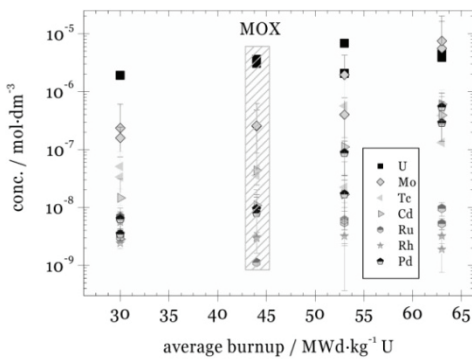
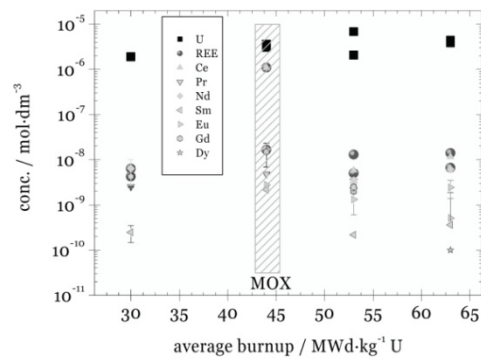


**Figure 9: Influence of the SF burn-up on the final concentration in solution value achieved on leaching experiments in granite conditions and under initially reducing conditions.**

Square point represents the U conc. in solution, whereas Ce, Pr, Nd, Sm, Eu, Gd and Dy are plotted with the same nomenclature than before. REE represents the total amount of trivalent elements.



Due to the different structure and composition of the MOX fuel, the concentration of Pu in solution observed during the leaching experiments showed a much higher value than those performed with  $\text{UO}_2$  fuels. The Pu-island observed in the MOX pellet structure would be the reason of this behaviour, due to: i) increasing of Pu concentration in these areas and ii) the higher alpha radiation field that could promote a higher oxidation state. Figure would be a good approach for justifying the behaviour of monovalent (Cs & Rb) and bivalent element (Sr & Ba). Both cases show a clear dependence on the concentration in solution with the burn-up of the fuel; fact related to the amount of element in the solid, i.e., with the increase of burnup the ratio of the element is higher. Focused on the bivalent element no clear solubility control is observed, so a thermodynamical model of the results obtained will be propounded. Figure 8 shows the

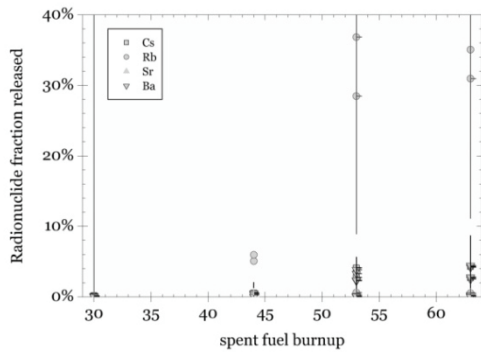
dependence of Mo and Tc (sensitive redox element) and noble elements such as Ru, Rh and Pd. Mo and Tc concentration in solution increase with burn-up and no clear dependence on the type of material used is observed; however, no influence with burn-up and/or type of fuel for the noble elements was measured. The increase in the concentration observed (for leached with higher burn-up) can not be explained as a consequence of the increase of fission products (Figure), otherwise the U concentration controlled by secondary phase formation is presented.

Figure 9 summarises the influence of burn-up on the rare earth element (REE) or trivalent element. In this figure the circle (REE) represents remainder rest elements present in this plot. With an exception of Ce, the rest of the elements did not show any influence on the burn-up in the final mean concentration obtained. This behaviour could be expressed as a consequence of solubility control due to coprecipitation of trivalent actinide and formation of a mixture secondary phase  $\text{REE}(\text{OH})_3(\text{s})$  as it is mentioned in the literature [10]. From the data obtained it is possible to extrapolate several remarks that could be of interest for performance assessment studies. Taking as starting hypothesis that “the amount of each radionuclide is the contribution of fast release (gap and grain boundary release) and matrix release, and expecting that matrix release of each radionuclide is congruent to U release to leachant”, it is possible to calculate the amount of radionuclide (% total inventory) that is consequence of a fast release process.

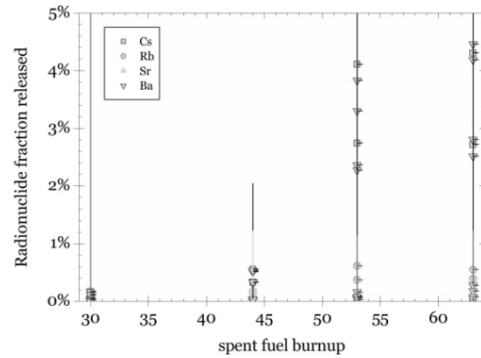
The following figures (Figure 10 to Figure 17) show the release of the radionuclides measured which have a contribution on the fast release process. In these figures, the influence of burn-up in the amount of radionuclide released are plotted. In all figures the mean values obtained for each element is plotted as symbols and the lines of the same colour represent the maximum and minimum values observed; the radionuclides were linked in different plots as a function of their chemical behaviour. Cs, Rb, Sr and Ba elements (mono- and bivalent element) show a clear increasing on the fast release process with the burn-up increase of the SF specimen (Figure 10 & Figure 11). The large scatter is observed in case of Rb. For this element, the amount released achieved the 30% in case of burn-up  $> 50 \text{ MWd}\cdot\text{kg}^{-1} \text{ U}$ . However, in case of Cs, a proportional increase of the amount released with burn-up is observed. The higher mean value obtained is  $\approx 4.5\%$ . In case of bivalent elements (Sr & Ba, see Figure) the value achieved is always lower than 1%. This behaviour is related with the distribution of these elements in the SF (as matrix solid solution and/or oxide precipitate phase [11]).

Figure 12 and 13 show the results obtained for the redox sensitive elements (Mo and Tc). In whole cases an increase of fast release with burn-up is observed; although the Mo amount released is always higher than Tc. Both average values are lower than 0.4% (with a maximum values up to 1.5%). As it was aforementioned, the chemical state of these fission products in the SF can justify the behaviour observed [11]. In case of those elements – constituents of metallic particles in the SF– (Figures 14 and 15) showed a similar dependence with burn-up, as the previous elements explained. Only in the case of Pd amount released, the mean values achieved are higher than 2%. For the rest of the elements could be considered that not fast released must be taken into account. Other elements that have shown a contribution of fast release is Cd, Sn and Te (see Figure). The total amount released for each element is around 1%. In case of MOX SF specimens higher values were obtained, i.e., in case of Sn & Te released average values of 6% were achieved. However in case of Cd amount released the value achieved due to fast release process is 5%.

**Figure 10: Amount of Cs, Rb, Sr and Ba released as a consequence of fast release process and in function of the SF burnup**



**Figure 11: Amount of Cs, Rb, Sr and Ba released as a consequence of fast release process and in function of the SF burn-up (zoom of Figure 10)**



**Figure 12: Amount of Mo and Tc released as a consequence of fast release process and in function of the SF burnup**

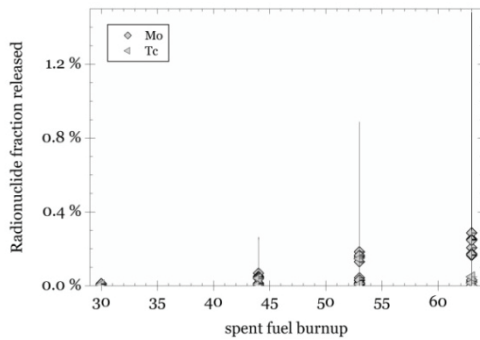


**Figure 13: Amount of Mo and Tc released as a consequence of fast release process and in function of the SF burn-up (zoom of Figure 12)**

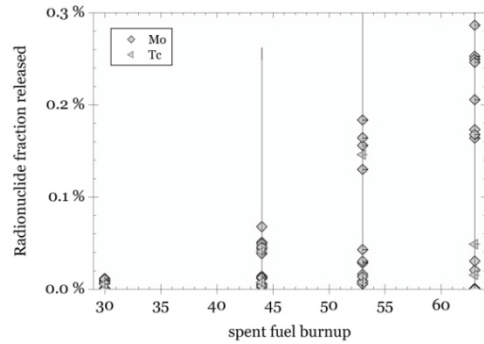


**Figure 14: Amount of Ru, Rh, Pd and Ag released as a consequence of fast release process and in function of the SF burnup**

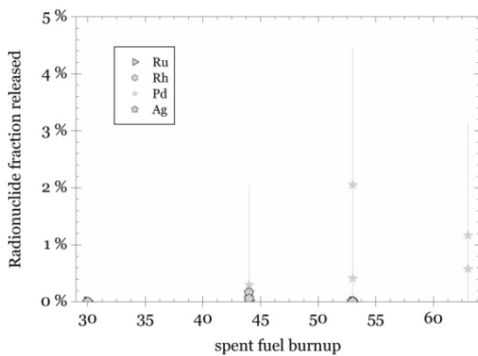


**Figure 15: Amount of Ru, Rh, Pd and Ag released as a consequence of fast release process and in function of the SF burn-up (zoom of Figure 14)**

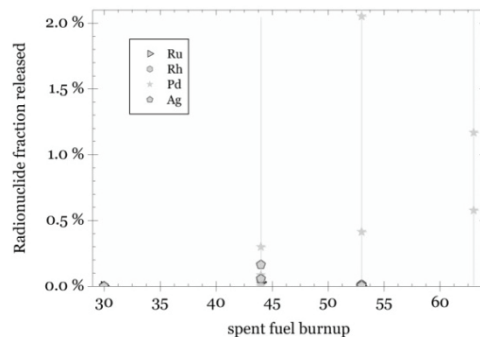


**Figure 16: Amount of Cd, Sn and Te released as a consequence of fast release process and in function of the SF burn-up**

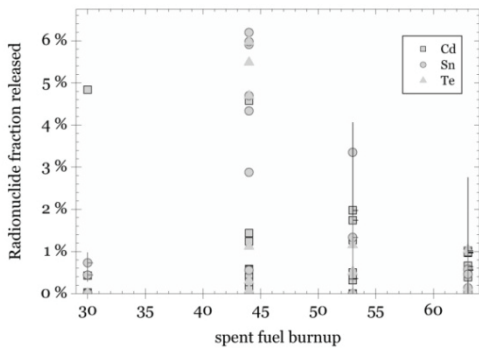
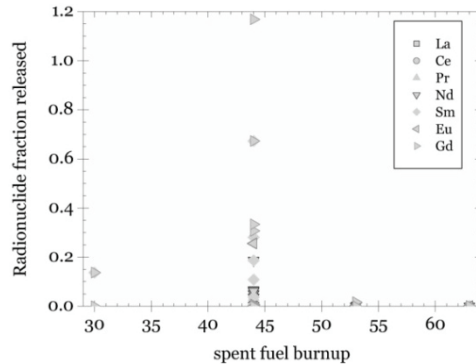


**Figure 17: Amount of La, Ce, Pr, Nd, Sm, Eu and Gd released as a consequence of fast release process and in function of the SF burn-up**



## Conclusions

It was shown that the investigated instant release of spent fuel depends on the level of burn-up producing the water radiolysis that has governed the spent fuel alteration process due to the oxidants generation – for surface oxidation process – and ulterior dissolution process by different species, modifying the redox conditions in the neighbourhoods of the spent fuel specimens. The present study confirms the high stability of spent fuel (UOX or MOX) under leaching conditions (two years of leaching time).

The experimental results obtained show that at higher burnup, higher is the alteration of the SF, besides an increasing in the mean concentration value of the radionuclides is observed. The higher differences observed between MOX and UOX SF specimens are related to the Pu concentration in solution. The highest Pu concentration was measured with MOX specimens, whereas, in case of UOX, not influence in the Pu concentration with burn-up was measured. The different behaviour and concentration in solution of Pu measured would be related to the microstructure of the specimens. This one could induce to produce a higher Pu dissolution rate in case of MOX than UOX SF.

The concentration evolution in solution of these different radionuclides specimens suggests the following explanation: i) U concentration in solution had not show any influence, neither with burn-up nor type of fuel. The U concentration in solution is controlled by secondary phase formation, i.e., studtite. ii) In case of Np a slight increase of the concentration in solution is observed. The concentration in solution measured is always lower than the solubility of the pure phase iii) Focused on the behaviour of the monovalents (Cs, Rb) and bivalents elements (Sr, Ba) in whole cases an increase of the concentration in solution with burn-up was observed. This behaviour justified the presence in the system of a precipitation process (U secondary phase, i.e., studtite). iv) The concentrations in solution measured for redox sensitive elements (as Mo, Tc) show a clear increase with burnup. The type of fuel studied had not developed any influence for the radionuclides studied. It is important to remark that the concentration values measured were always lower than the solubility of the pure phases. Furthermore, the same as mono and

bivalent elements, this behaviour increase the confidence on the studtite precipitation process in all experiments had been produced.

The experimental procedure done and the time of leaching (more than 2 years) allow to write that in all the radionuclides measured, the behaviour observed indicates that after the first two days of leaching process the release of radionuclide are congruent with the matrix alteration process. Furthermore, if the U concentrations achieve the studtite solubility value, the release of radionuclides remains with the same tendency without any interference of the U secondary phase precipitation process. Furthermore, these data could be used as experimental evidence that the performance assessment studies are overestimating the real contribution of the fast radionuclide release on the repository safety.

### *Acknowledgements*

The work was performed under the CIEMAT – ENRESA agreement (ACACIAS). This work was performed in the frame of the EC-funded “Spent Fuel Stability” project, and as part of a framework agreement between ITU and ENRESA/CIEMAT. We thank J. Serrano-Agejas, E. Toscano, J. Spino, S. Birck and D. Botoomley.

## **REFERENCES**

- [1] ENRESA, 2003. Evaluación del comportamiento y de la seguridad de un almacén geológico profundo de residuos radiactivos de alta actividad en arcilla. Proceso de selección del elemento combustible de referencia, in: ENRESA, Madrid, 2003.
- [2] C. Poinssot, C. Ferry, M. Kelm, B. Grambow, A. Martínez Esparza, L. Johnson, Z. Andriambololona, J. Bruno, C. Cachoir, J.M. Cavedon, H. Christensen, C. Corbel, C. Jegou, K. Lemmens, A. Loida, P. Lovera, F. Miserque, J. De Pablo, A. Poulesquen, J. Quiñones, V.V. Rondinella, K. Spahiu, D. Wegen, Final report of the european project Spent Fuel Stability under repository conditions, Saclay, 2005.
- [3] S. Sunder, D.W. Shoesmith, M. Kolar, D.M. LeNeveu, From laboratory experiments to geological disposal vault: Calculation of used nuclear fuel dissolution rates, in: I.G. McKinley, C. McCombie (Eds.), Scientific Basis for Nuclear Waste Management XXI, vol 506, Materials Research Society, Warrendale, Pennsylvania, 1998, pp. 273-280.
- [4] J.A. Serrano, J. Quiñones, J. Cobos, P. Díaz, V.V. Rondinella, J.P. Glatz, H. Matzke, A. Martínez Esparza, J.A. Esteban, Radioactive Waste Management and Environmental Remediation - ASME (2001).

- [5] ENRESA, Evaluación del comportamiento y de la seguridad de un almacén geológico profundo de residuos radiactivos de alta actividad en arcilla. Criterios seguidos para la selección del inventario genérico de radionucleidos para ENRESA 2003, in: ENRESA, 2003, p. 13.
- [6] L.O. Werme, L.H. Johnson, V.M. Oversby, F. King, K. Spahiu, B. Grambow, D.W. Shoesmith, Spent fuel performance under repository conditions: A model for use in SR-Can, in: Technical Report, vol TR-04-19, SKB, Stockholm Sweden, 2004.
- [7] ENRESA, Evaluación del comportamiento y de la seguridad de un almacén geológico profundo de residuos radiactivos de alta actividad en arcilla. Criterios seguidos para la selección del inventario genérico de radionucleidos para ENRESA 2003, in: ENRESA, 2003, p. 13.
- [8] J. Cobos, J.A. Serrano, D. Papaioannou, S. van Winckel, S. Brick, J.P. Glatz, Instant release dissolution on spent nuclear fuel, in: European Commission. Directorate-General JRC. Joint Research Centre. Institute for Transuranium Elements, Karlsruhe, 2005, p. 36.
- [9] R. Guillaumont, T. Fanghänel, J. Fuger, I. Grenthe, V. Neck, D.A. Palmer, M.H. Rand, Update on the Chemical Thermodynamics of Uranium, Neptunium, Plutonium, Americium and Technetium, Elsevier B.V., Amsterdam. Boston. Heilderberg. London. New York. Oxford. Paris. San Diego. San Francisco. Singapore. Sydney. Tokyo, 2003, p. 960.
- [10] J. Quiñones, J.A. Serrano, P.P. Díaz Arocas, J. Nucl. Mater. 298 (2001).
- [11] H. Kleykamp, J. Nucl. Mater. 131 (1985) 221-246.

## THE LEACHING OF SE, SN, ZR, PD FROM VITRIFIED HIGH-LEVEL WASTE IN CLAY SLURRIES

**Pierre Van Iseghem, Karel Lemmens, Véra Pirlet\***

SCK•CEN, Boeretang 200, B-2400 Mol, Belgium

\*now: University of Liège, B-4000 Liège (Sart-Tilman), Belgium

### Abstract

We report the results of the leaching of Se, Zr, Pd and Sn from reference high-level waste glasses in a reducing clay slurry, simulating a clay based disposal medium. In the Belgian disposal design, Se-79, Zr-93, Pd-107 and Sn-126 strongly contribute to the dose-to-man in the biosphere. Inactive isotopes were used to simulate the radionuclides, and the element concentrations in the soluble phase of the slurries were measured. The presence of the glass does not lead to an increase of these elements in solution, compared with the situation where only clay slurry is used. Relatively steady state concentrations are achieved,  $\sim 10^{-7}$  M for Se, and  $\sim 10^{-8}$  M for Sn, Pd, Zr. Se in solution is probably present as a mixture of Se VI (selenate,  $(\text{SeO}_4)^{2-}$ ), Se IV (selenite,  $(\text{SeO}_3)^{2-}$ ), and Se (0). There are arguments to interpret our results in terms of solubility control, but the data did not allow to interpret the element speciation in solution. We further compare the results with the results from studies in far field conditions in Boom Clay, speciation calculations, and data used in performance assessment

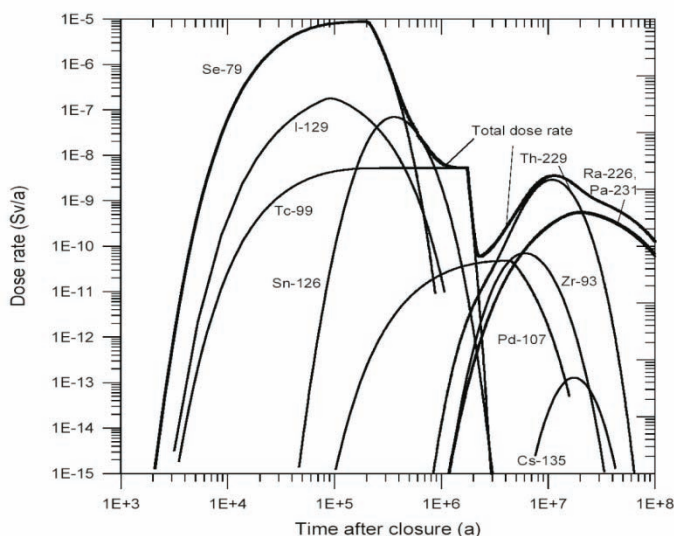
## Introduction

Belgium is considering the geological disposal in Boom Clay of the high-level waste resulting from its nuclear energy production. The conditioned high-level waste basically consists of the vitrified HLW generated by the former Eurochemic reprocessing plant located in Mol, the vitrified HLW produced by Cogema upon the reprocessing of part of the spent fuel issued by the Belgian nuclear power plants, and non-reprocessed spent fuel from the operation of the Belgian nuclear power plants.

Since some 25 years, SCK•CEN has been conducting R&D on the dissolution behaviour of HLW glasses, and since more than 10 years also the corrosion behaviour of spent fuel is being studied. The R&D has been conceived in a parametric way, aiming on the one hand to understand the basic dissolution behaviour of these waste forms (typically in pure water), and on the other hand to identify and understand the dissolution behaviour in conditions representative for the geological disposal conditions (see [1,2] for some overviews).

The starting point of the work presented in this paper is the result of the safety assessment calculation performed around 2000 for the geological disposal of HLW glass in Boom Clay, considering the Safir disposal design [3,4]. A typical result of the calculation of the dose rate-to-man in the biosphere assuming a normal evolution scenario is shown in Figure 1. Unlike the safety assessment calculations made before, this result shows that certain long-living fission products (Se-79, I-129, Tc-99, Sn-126, *etc.*) dominate the long-term safety, rather than the actinides. Some of the reasons are explained in [5]. This is why we decided to investigate the leaching behaviour of radionuclides such as Se-79, Zr-93, Pd-107 and Sn-126 from HLW glass in clay slurries, representative for potential near-field media contacting the HLW glass. We did not insert I-129 in our study, because its inventory in the HLW glass is very uncertain [5]. The release of Tc-99 from HLW glass has been studied in detail [6].

**Figure 1: Calculated total dose rate and dose rates due to the different radionuclides for the well pathway (reference case), for the vitrified high-level waste (glass SON68) [3,4]**



## Experimental

We performed leach tests on two reference high-level waste glasses (SON68, SM539 – see further below) in a medium with physicochemical characteristics simulating the near field potentially contacting the glass once the canister and overpack would have corroded. The medium (called “Int-RIC”) consisted of a mixture of the candidate backfill material (FoCa clay mixed with sand and graphite), iron oxide powder and (uncorroded) stainless steel powder, and Boom Clay, with real interstitial Boom Clay pore water (“RIC”). The relative weight fractions are listed in Table I. These materials were mixed and equilibrated during 11 months before glass was added. By performing the tests in an Argon purged glove box, we managed to reproduce the (reducing) redox conditions prevailing in our underground repository.

Further test parameters were temperature (40°C – slightly above the temperature expected once the overpack has corroded) and glass surface to solution volume (2500 m<sup>-1</sup>, achieved by using a powdered glass of 125-250 µm size). Different test cups were used for the different test durations.

**Table I: Summary of the leach test conditions**

Medium	Glass	T (°C)	SA/V (m <sup>-1</sup> )	Duration (days)
Int-RIC	SON68 SM539	40	2500	90, 180, 365, 540, 720

Int-RIC: 712,5 g M2 + 712,5 g Boom Clay + 37,5 g Fe<sub>3</sub>O<sub>4</sub> + 37,5 g stainless steel powder (AISI 316 L) per liter RIC; M2: reference backfill mixture (65% FoCa-clay, 30% sand, 5% graphite)

The analysis of the leach tests was focused on the determination of the mobile Se, Sn, Zr, Pd concentration in the leachates obtained by ultrafiltration over membranes of 100 000 and 10 000 MWCO. 100 000 MWCO corresponds to a particle size of a 5 nm, which is considered as the upper limit for migration in Boom Clay. 10 000 MWCO corresponds to a particle size of ~2nm, which is considered as the dissolved (non-colloidal) concentration. pH and Eh were measured at the end of each leach test.

Two glasses were investigated: the COGEMA R7T7 reference glass SON68 and the DWK/PAMELA reference glass SM539 HE 540-12 with 22,5 weight% of waste oxides, further called glass SM539 (see Table II). SON68 was selected to immobilise reprocessed PWR spent fuel, and SM539 to immobilise high enriched waste concentrates from MTR spent fuel. SM539 has relatively large Al<sub>2</sub>O<sub>3</sub> content, and low fission product – actinide concentrations.

**Table II: Main constituents of the two HLW glasses studied**

(wt%)	SON68	SM539
SiO <sub>2</sub>	45.48	35.28
B <sub>2</sub> O <sub>3</sub>	14.02	25.58
Na <sub>2</sub> O	9.86	9.21
Li <sub>2</sub> O	1.98	3.49
Al <sub>2</sub> O <sub>3</sub>	4.91	19.83
CaO	4.04	5.05
TiO <sub>2</sub>	/	0.003
FP oxides	13.38	0.96
Balance	6.33	0.6

For SON68, we compared the nominal concentration of SeO<sub>2</sub>, SnO<sub>2</sub>, ZrO<sub>2</sub> and PdO (both radioactive and inactive) in the glasses, as declared by the producer, with the composition of the as received reference glass samples. Then we doped the glass till the nominal concentration was achieved. Only SeO<sub>2</sub> and PdO was added. The concentration of ZrO<sub>2</sub> and SnO<sub>2</sub> in the reference SON68 glass was sufficiently high. The doping was performed by melting crushed SON68 reference glass together with the required amounts of SeO<sub>2</sub> and PdO in oxidising atmosphere. We verified the composition of the doped glass by ICP-MS analysis, and we observed that microwave dissolution before analysis provided a higher yield than a borax melt [7]. Some details for SON68 are given in Table III (full details: see [7]). The SM539 reference glass was used as such, although it did not contain any SnO<sub>2</sub>. We did not use radioactive isotopes, merely because we were essentially interested in the total element concentration in the soluble phase of the leaching medium, since only total element solubility is a parameter in the performance assessment calculation.

**Table III: Weight percentages of SeO<sub>2</sub>, ZrO<sub>2</sub>, PdO, SnO<sub>2</sub> in glass SON68 (wt %)**

	Wt % in active glass [8]	Nominal Wt % in as received	Nominal Wt % as doped (by SCK•CEN)	Measured Wt % (analysis SCK•CEN)
SeO <sub>2</sub>	0.03	0.00	0.038	0.02
ZrO <sub>2</sub>	1.70 (+ 0.54% inactive)	2.65	2.65	1.96
PdO	0.38	0.00	0.35	0.033
SnO <sub>2</sub>	0.02	0.02	0.02	0.016

Valence states in the as molten glass are expected to be II-fold for Pd and IV-fold for Sn and Zr. For Se, a mixture of IV and VI is likely, because Se was added as Se(IV) (SeO<sub>2</sub>), but the glass was molten under oxidizing conditions. For Se, Sn and Zr the assumed valence state by the producer is IV [9]. However, SeO<sub>2</sub> and SnO<sub>2</sub> are known to be redox sensitive, and they

are often used as redox additives in glass melting in glass industry [10]. Pd (metal) is assumed in the industrial HLW glass, as Pd is part of the insoluble fines [9].

## Results and discussion

The results of the evolution of the concentrations of Se, Sn, Pd and Zr in the liquid fraction (< 10 000 MWCO) of the clay slurries in function of the duration are shown in Figures 2 (a-d). Both the data in the absence of glass (“blank tests” with only the clay slurry) and in the presence of glass are shown. Each data point corresponds to a single experiment. The concentration ranges in the figures correspond to the highest and lowest value measured for the blanks (we ran blanks for one and two years).

From these figures we can observe that the concentrations of Se, Sn, Pd, Zr in solution (particle size smaller than ~2 nm) upon glass dissolution are relatively stable with time. Many of the analytical data are below the detection limit, as indicated in Figure 2. For Sn only the two years data point was a precise measurement (an ICP-MS with lower detection limit was used for the two years test data). The most remarkable observation is that the concentrations of Se, Sn, Pd, Zr in solution in the test with or without glass are of the same order of magnitude (the uncertainty of the analytical data is large – errors are at the minimum 50% close to the detection limit). This would mean that the presence (and consequent dissolution) of glass would **not** increase the concentrations of these elements in the clay water. This should not be surprising however, because the concentration of Se, Sn, Pd, Zr in the solid phase of the clay slurry was measured to be about the same as the corresponding concentrations in the glass! Additionally the concentrations measured in solutions without or with glass present might suggest that these concentrations are solubility controlled, as the effect of the glass dissolution (and leaching of Se, Sn, Pd, Zr) does not result in higher concentrations in solution.

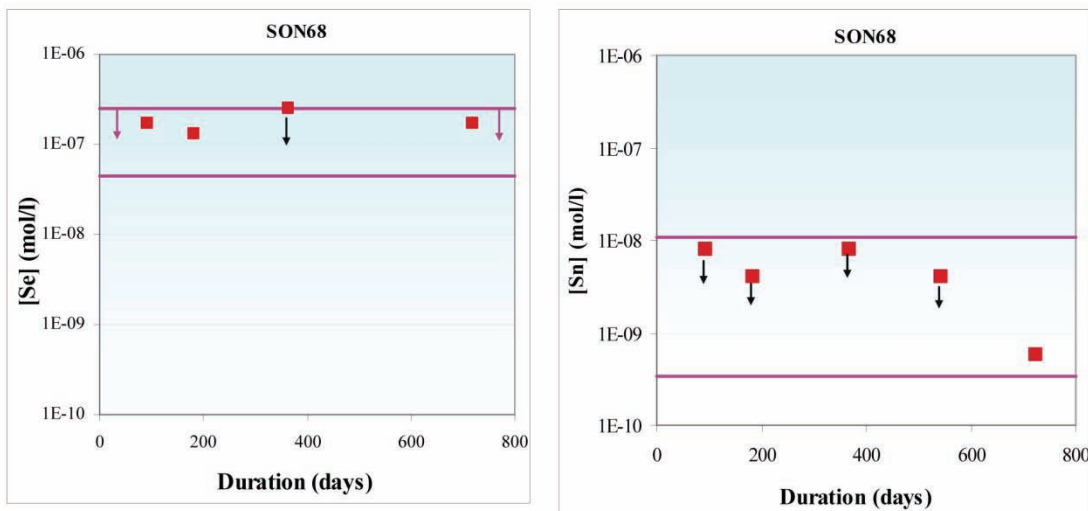
The results for glass SM539, which has a nominal SeO<sub>2</sub>, ZrO<sub>2</sub> and PdO content about 10 times or more smaller than glass SON68, and which did not contain any Sn, were nevertheless very similar! This confirms the dominating role of the clay slurry medium towards the concentration in solution of these elements and provides an additional argument to interpret the nearly stable Se, Sn, Pd, Zr concentrations in solution for both glasses as due to solubility control.

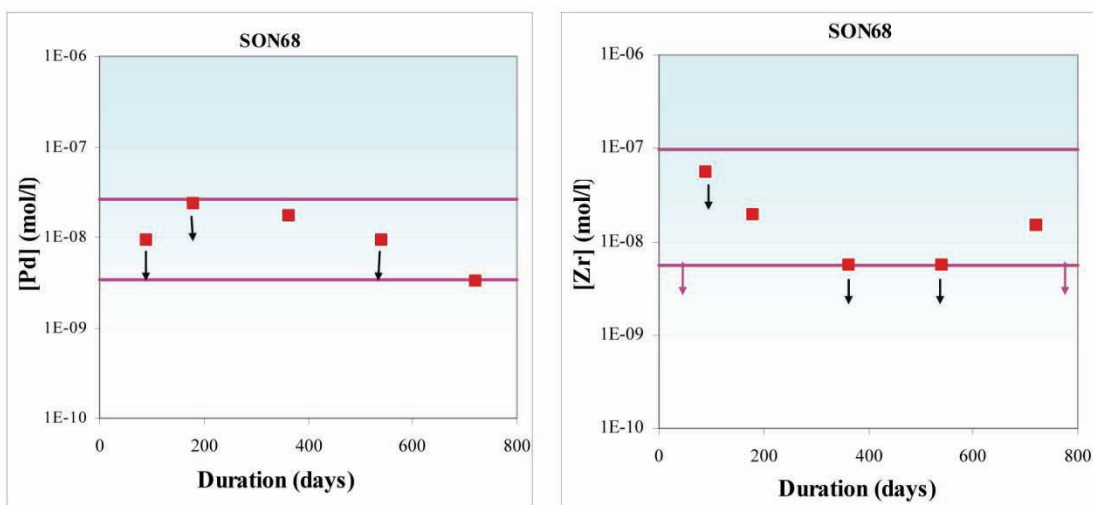
We can't make a mass balance of the leaching of Se, Sn, Pd and Zr from the glass. Indeed, we can't distinguish between these elements as whether they belong to the glass or to the clay, since we doped the glass with inactive isotopes. We can't therefore measure the inventory of these elements sorbed onto the solid fraction of the clay slurry. On the other hand we can be sure that the glass does dissolve in our test. The dissolution of glass in clay slurries proceeds to a further extent than in pure water because of the sorption onto clay, and is well documented – see e.g. [11]. Based on similar tests on inactive glass, we can expect total mass loss of glass SON68 after two years interaction of ~10 g.m<sup>-2</sup> [12], which corresponds to a dissolved glass thickness of about 4 μm (the mass loss for SM539 is up to four times larger). To help to interpret this data: a mass loss of 10 g.m<sup>-2</sup> corresponds to the dissolution that would occur within 10 days in pure water at low S/V at 90°C – a standard condition to measure the glass durability in pure, non-saturated water [13]

We compared the average values of the element concentrations in our test with predicted values according to potential solubility controlling solid phases [14] – see Table IV. We also compared with the steady state concentrations measured in radionuclide migration tests in Boom Clay [15] and with element concentrations measured in natural Boom Clay porewater [16]. The last column lists the best estimate radionuclide solubility values that are used by performance assessment calculation of the geological disposal [5]. We observe the following:

- The solubility controlling phases mentioned are those that can occur in the pH-E<sub>h</sub> range considered in our tests (pH range 8.0 to 8.4, Eh range -100 to -200 mV<sub>SHE</sub>). Only in case of Se one of the solid phases (Se(cr)) matches. None of the phases predicted for the other elements matches with our results (near field condition).
- Comparison with the data obtained with radionuclide migration tests on natural Boom Clay (“far-field”) shows a good fit for Pd, whereas Se in our tests generates a 10 times higher “steady state” concentration in solution. The same is true when comparing our data on Se with Se concentration in natural Boom Clay porewater. There are no data available for Zr and Sn from migration tests.

**Figure 2: Average concentrations of Se, Sn, Pd and Zr in the leachates after ultrafiltration for the SON68 glass. The pink dashed lines show the background concentrations in the medium. Concentrations reported as “lower than” (for the leach tests and for the blank tests) are indicated with a downward arrow.**





The data for Zr, Pd and Sn selected in the performance assessment studies (last column) are much higher than the average values from our tests. They currently refer to “far-field” conditions, and correspond to best-estimate data from migration tests or to literature data. The data for Se selected in the performance assessment studies account for the different Se valence possible in the reducing condition in Boom Clay. In case Se remains oxidized (VI) one assumes no solubility limitation in solution. We compare the data from our tests with the other data further below.

We will spend special attention to the results for Se, because of its predominant importance in the safety assessment results (see Figure 1). The main reason for the deviation between our results and the data from other sources is probably the valence state of Se. A priori we assume that Se in the glass is in the IV or VI state, although no analytical evidence is available. It is known that the reduction kinetics of Se VI (selenate;  $(\text{SeO}_4)^{2-}$ ) in a (reducing) clay medium are slow but unknown [17], and that Se (VI) is stable even in presence of pyrite  $\text{FeS}_2$  [21]. In addition selenate is not solubility limited [18,19]. This situation could fit with the relatively high Se concentrations we measured. If Se would have been tetravalent (IV) in the glass, it is known that  $(\text{SeO}_3)^{2-}$  (selenite) is reduced to Se (0) readily under the reducing conditions in our test [17]. Its solubility would become much lower than the value we recorded. However, the following arguments may lead to another hypothesis:

- Our hypothesis of Se being as VI-fold in the glass is anyhow conflicting with observations in coloured "commercial" glasses, where Se was found mainly in IV and 0-fold state [10].
- The solubility of selenium Se(0) in clay water increases with decreasing Eh, from a value of  $2.4 \cdot 10^{-8}$  M (reference Boom clay pore water) till values between  $10^{-8}$ - $10^{-7}$  M for
- Eh  $\sim$  250 mV<sub>SHE</sub> [20]. The difference with the steady state values in our tests of  $\sim 2.5 \cdot 10^{-7}$  M becomes very small.

- We therefore argue that Se in our HLW glasses will be in various valence states, but only to a minor extent as VI-fold, preferentially as IV-fold. We also argue that different Se species (selenate, selenite and elemental Se control the (solubility limited) Se concentration in soluble form in our tests, even if selenate would be present only to a very minor extent. Any direct evidence of the Se valence state in the glasses or speciation in solution is missing however so far. The sorption coefficient of selenite (or selenate) onto the clay minerals in our study is not well known either, but we can assume that e.g. selenite will sorb onto pyrite (FeS<sub>2</sub>) present in the clay.

We can't really correlate the steady state concentrations of Pd, Sn or Zr (our results) to any of the predicted solid phases. Our results for Pd agree well with those from the migration tests in natural Boom Clay (see Table IV). This may suggest that the valence state is the same in both tests (II or 0). There are almost no data available of migration tests or concentration in natural porewater for Zr or Sn. The steady state concentrations we measured are much smaller than the best-estimate values used in performance assessment studies. We can't provide arguments for other solubility data to use in performance assessment studies however, because our tests were not designed to provide data on radionuclide solubility, and they do not relate to far field (Boom Clay) conditions.

**Table IV: Comparison of the near-field concentrations obtained from our leach tests with the far-field concentrations**

Element	[element] (near-field)	Solubility limiting Solid phase	[RN] (far-field)	[element] (in natural porewater)	[RN] (best estimate PA values)
	(mol/l)	(mol/l)	(mol/l)	(mol/l)	(mol/l)
Se	$2.5 \times 10^{-7}$	FeSe $1.9 \times 10^{-9}$ Se (cr) $2.9 \times 10^{-7}$	$1 - 0.3 \times 10^{-8}$	$2.4 \times 10^{-8}$	- $5 \times 10^{-8}$ (Se 0, -II) - No solubility limitation (Se VI)
Zr	$5.5 \times 10^{-9}$	ZrO <sub>2</sub> $6.7 \times 10^{-10}$ ZrSiO <sub>4</sub> $1.3 \times 10^{-13}$	/ (no data)	$6.4 - 34 \times 10^{-7}$	$1 \times 10^{-6}$
Pd	$9.4 \times 10^{-9}$	Pd poorly soluble	$1.6 - 1.9 \times 10^{-8}$	/	$1 \times 10^{-7}$
Sn	$4.2 \times 10^{-9}$	SnO <sub>2</sub> $2.7 \times 10^{-8}$	/ (no data)	/	$5.5 \times 10^{-7}$

The uncertainty on the valence state Se in the HLW glass, and subsequently in the leachate has a direct relationship with the safety assessment calculations for the geological disposal design [5]. Selenate in solution (from Se-VI in the glass) is not solubility limited, and the radioactivity flux leaving the geological disposal site in Boom Clay due to Se-79 would be proportional to the Se inventory in the glass. But neither the Se valence, nor the concentration (Se-79 and total Se) in the glass are precisely known. We therefore strongly recommend that these properties should be better characterised. The same argument can be used for the other radionuclides considered in this paper, as the inventory in the HLW glass of Zr-93, Pd-107, Sn-126 is not fully qualified as well. But as there is stronger evidence that their concentration in the pore water of the far field (Boom Clay) is solubility limited [3,15], the inventory of these radionuclides in the glass would not affect the result of the safety assessment study.

## Conclusions

In the tested clay medium the release of Se, Zr, Pd and Sn from the reference HLW glasses SON68 and SM539 (inactive isotopes simulating the radionuclides Se-79, Zr-93, Pd-107 and Sn-126, respectively) did **not** increase their element concentration in the contacting solution. This is because these elements have a natural (non-radioactive) abundance in the clay medium, and because their leaching appears to be limited. Yet, we can't conclude for sure if their leaching from the glass is limited by solubility, and whether the concentration of their stable isotopes in the clay medium will affect the radionuclide leaching behaviour (e.g. due to isotope dilution), because we only considered the concentration in the aqueous phase of the clay medium. We can expect a similar behaviour in other (clay-based) near field environments with similar characteristics. The solubility limitation would imply that the diffusion of the radioisotopes through the near field will be retarded by isotopic dilution with the inactive, naturally occurring isotopes.

It is difficult to formulate straightforward conclusions for the Se-leaching. The initial hypothesis was that Se would be in its oxidized form (VI) in the glass, and that the concentration of Se in the aqueous phase of the clay medium would not be solubility limited. However, we rather believe that Se is present as Se(IV) in the glass, and its concentration in the aqueous phase might be solubility limited. We believe that different Se species (selenate, selenite, selenium) control the concentration in solution.

The leaching of Zr, Pd and Sn in the clay medium is proceeding in a similar way as for Se, characterized by rather steady state concentrations in the aqueous phase, which are interpreted as solubility controlled. These concentrations are much smaller than the corresponding radionuclide solubilities used in the safety assessment study.

Yet there are a number of limitations and uncertainties in our approach and interpretation:

The amount of tests done was only limited, and we did not perform any speciation measurements of the solutions.

We used inactive isotopes of Se, Sn, Zr, Pd, so we could not differentiate between element leaching from the glass or from the clay. We could neither determine the sorption of the elements onto the solids (clay, container).

We strongly recommend to investigate some characteristics of the radionuclides considered (Se-79, Zr-93, Pd-107, Sn-126) in the HLW glasses of interest. In particular, the valence state of Se and the radioactive and total element inventory of all four radionuclides have not been verified. This is especially relevant for Se, as it is a predominant radionuclide in the safety assessment evaluation, and because there are strong uncertainties with respect to its speciation in the glass and in the solutions of the leaching tests.

## Acknowledgements

The authors gratefully acknowledge the financial support of NIRAS/ONDRAF (the Belgian agency for the management of radioactive waste) and of the European Commission (GLASTAB project). They also acknowledge helpful discussions with L. Wang, C. Bruggeman, N. Maes, P. De Cannière and M. De Craen.

## REFERENCES

- [1] P. Van Iseghem, M. Aertsens, K. Lemmens, P. Lolivier, V. Pirlet, E. Valcke, Wei Jiang, “Long-term behaviour of high-level waste forms in clay repository conditions” Final report for IAEA agreement No 6795/CF, 1997
- [2] P. Van Iseghem, K. Lemmens, M. Aertsens, C. Cachoir, D. Jacques, V. Pirlet, S. Salah, E. Valcke, “Chemical durability of vitrified high-level waste and spent fuel under simulated repository conditions of a Boom Clay formation”. Final report to IAEA for the CRP programme 1998-2004. to be published by IAEA
- [3] SAFIR 2. Safety Assessment and Feasibility Interim Report 2. NIROND 2001-06 E, december 2001
- [4] D. Mallants, J. Marivoet, X. Sillen, “Performance assessment of the disposal of vitrified high-level waste in a clay layer”. *Journal of Nuclear Materials* 298 (2001), 125-135
- [5] J. Marivoet, E. Weetjens, “The importance of mobile fission products for long-term safety in the case of disposal of vitrified high-level waste and spent fuel in a clay formation”. This conference.
- [6] V. Pirlet, K. Lemmens, P. Van Iseghem, “Influence of the near-field conditions on the mobile concentrations of Np and Tc leached out from vitrified HLW”. *Scientific Basis for Nuclear Waste Management XXVIII, Mat. Res. Soc. Symp. Proc. Vol 824 (2004)*, 385-390.
- [7] V. Pirlet and K. Lemmens, “The importance of the glass composition and the near-field for the mobile concentrations of radionuclides”. Thematical report for WP4 of RP.WD.008 for the period January 2000 – June 2003. Characterization and compatibility with the disposal medium of Cogema and Eurochemic reprocessing waste forms. Tasks VM-6 and GV8 of NIRAS/ONDRAF contracts CCHO-90/123-1 and CCHO-90/123-2 (vitrified waste).
- [8] Personal communication by Thierry Advocat (CEA).

- [9] Personal communication by N Godon (CEA).
- [10] C. Stalhandske, T. Bring and B. Jonson, "Gold ruby glasses: influence of iron and selenium on their colour". *Glass Technology: Eur. Journal of Glass Science Technology A*, August 2006, Vol 47 (4), 112-120
- [11] K. Lemmens, The effect of clay on the dissolution of nuclear waste glass. *Journal of Nuclear Materials* 298 (2001), 11-18
- [12] K. Lemmens, M. Aertsens, P. Lolivier, N. Malengreau, V. Pirlet, P. Van Iseghem, Characterization and compatibility with the disposal medium of Cogema and Eurochemic reprocessing waste forms. Final report 1996-2000 for NIRAS/ONDRAF. R- 3644, 2002
- [13] ASTM C 1220 – 92. Standard Test Method for Static Leaching of Monolithic Waste Forms for Disposal of Radioactive Waste, 1993.
- [14] L. Wang, A. Dierckx, P. De Cannière, "Speciation and solubility of radionuclides in Boom Clay". SCK•CEN report R-3508, 2000
- [15] N. Maes, personal communication
- [16] M. De Craen, L. Wang, E. Weetjens, Natural evidence on the long-term behaviour of trace elements and radionuclides in the Boom Clay. R-3926 (2004)
- [17] C. Bruggeman, this conference.
- [18] F.J. Mompean and H. Wanner, The OECD Nuclear Energy Agency thermochemical Database Project. *Radiochimica Acta*, 2003, vol. 91, no11, pp. 617-621.
- [19] [www.oecdnea.org/html/dbtdb](http://www.oecdnea.org/html/dbtdb).
- [20] C. Bruggeman, Assessment of the geochemical behaviour of Selenium oxyanions under Boom clay geochemical conditions. PhD thesis, Katholieke Universiteit Leuven, 2006.
- [21] T. Beauwens, P. De Cannière, H. Moors, L. Wang, N. Maes, Studying the migration behaviour of selenate in boom clay by electromigration. *Engineering Geology*, vol 77, no 3-4 (2005), 285-293.



## **LIST OF PARTICIPANTS**



NAME	EMAIL
ABDELOUAS, Abdesselam	abdesselam.abdelouas@subatech.in2p3.fr
ALBRECHT, Achim	achim.albrecht@andra.fr
BREYNAERT, Eric	eric.breynaert@biw.kuleuven.be
BRUGGEMAN, Christophe	christophe.bruggeman@biw.kuleuven.be
BRUNO, Jordi	jbruno@enviroz.biz
CATALETTE, Hubert	hubert.catalette@edf.fr
CHARLET, Laurent	laurent.charlet@obs.ujf-grenoble.fr
CROVISIER, Jean-Louis	jlc@illite.u-strasbg.fr
CUI, Daqing	daging.cui@cec.eu.int
CZERWINSKI, Ken	czerwin2@unlv.nevada.edu
DE PABLO, Joan	joan.de.pablo@upc.edu
DESCOSTES, Michael	michael.descostes@cea.fr
DEWONCK, Sarah	sarah.dewonck@andra.fr
DIERCKX, Ann	a.dierckx@nirond.be
DURO PEREZ, Lara	lduro@enviros.biz
EVANS, Nick	n.d.e.m.evans@lboro.ac.uk
FACHINGER, Johannes	j.fachinger@fz-juelich.de
FALCK, Eberhard	eberhard.falck@jrc.nl
FATTAHI, Massoud	fattahi@subatech.in2p3.fr
FERRY, Cécile	cecile.ferry@cea.fr
FLOCARD, Hubert	flocard@csnsm.in2p3.fr
GECKEIS, Horst	geckeis@ine.fzk.de
GIFFAUT, Eric	eric.giffaut@andra.fr
GLAUS, Martin	martin.glaus@psi.ch
GOUTELARD, Florence	florence.goutelard@cea.fr
GRAMBOW, Bernd	grambow@subatech.in2p3.fr
HERNAN, Pedro	pher@enresa.es
HOLTTA, Pirkko	piholtta@mappi.helsinki.fi
HUMMEL, Wolfgang	wolfgang.hummel@psi.ch
IIDA, Yoshihisa	iida.yoshihisa@jaea.go.jp
IVANOV, Peter	peter.ivanov@manchester.co.uk
JOHNSON, Lawrence	lawrence.johnson@nagra.ch
JORDAN, Norbert	norbert.jordan@unice.fr
KANEKO, Masaaki	masaaki.kaneko@toshiba.co.jp
KIENZLER, Bernhard	kienzler@ine.fzk.de
KIM, Won-Ho	whkim@kaeri.re.kr
KOLARIKOVA, Irena	jaro@natur.cuni.cz
LANDAIS, Patrick	patrick.landais@andra.fr
LANDESMAN, Catherine	landesman@subatech.in2p3.fr
LARSSON, Peter	peter.larsson@skb.se
LARTIGUE, Jean-Eric	jean-eric.lartigue@cea.fr
LECLERC, Elisabeth	elisabeth.leclerc@andra.fr
LE HECHO, Isabelle	isabelle.lehecho@univ-pau.fr
LIU, Xiaolan	xiaolan.liu@subatech.in2p3.fr
LLORENS, Isabelle	isabelle.llorens@subatech.in2p3.fr

MACE, Nathalie	nathalie.mace@cea.fr
MAES, André	andre.maes@biw.kuleuven.be
MARCOS, Nuria	nuria.marcos@sroy.fi
MARIVOET, Jan	jmarivoe@sckcen.be
MARMIER, Nicolas	nicolas.marmier@unice.fr
MARSAL, François	francois.marsal@irsn.fr
MOLNAR, Mihaly	mmol@atomki.hu
MOMPEAN, Federico	mompean@nea.fr
MONTAVON, Gilles	montavon@subatech.in2p3.fr
MULLER, John	muller@subatech.in2p3.fr
NISHIMURA, Tsutomu	t-nishimura@rwmc.or.jp
PIPON, Yves	y.pipon@ipnl.in2p3.fr
PITTOIS, Aurélien	aurelien.pittois@manchester.ac.uk
PLAS, Frédéric	frederic.plas@andra.fr
POINEAU, Frédéric	freder29@unlv.nevada.edu
POINSSOT, Christophe	christophe.poinssot@cea.fr
PUIGDOMENECH, Ignasi	ignasi@skb.se
QUINONES, Javier	javier.quinones@ciemat.es
REILLER, Pascal	pascal.reiller@cea.fr
RIBET, Isabelle	isabelle.ribet@cea.fr
ROTENBERG, Benjamin	rotenberg@ccr.jussieu.fr
RUBEL, André	andre.ruebel@grs.de
SATO, Haruo	sato.haruo@jaea.go.jp
SCHWYN, Bernhard	bernhard.schwyn@nagra.ch
SAVOYE, Sébastien	sebastien.savoye@irsn.fr
SEBY, Fabienne	fabienne.seby@univ-pau.fr
SEKOKO, Isarel	isekoko@necsa.co.za
SIITARI-KAUPPI, Marja	marja.siitari-kauppi@helsinki.fi
SLADOV, Vladimir	sladov@ipno.in2p3.fr
SMALL, Joe	joe.S.small@nexasolutions.com
SMIDTS, Olivier	osm@avn.be
SMITH, Graham	graham.smith@enviros.com
SPAHIU, Kastriot	kastriot.spahiu@skb.se
SUZUKI, Satoru	kakusuzuki@iri.or.jp
TAKAHASHI, Hiroaki	hiro-ta@iri.or.jp
TANABE, Hiromi	tanabe@rwmc.or.jp
TOURNASSAT, Christophe	c.tournassat@brgm.fr
UMEKI, Hiroyuki	umeki.hiroyuki@jaea.go.jp
VAN ISEGHEM, Pierre	pviseghe@sckcen.be
VUORINEN, Ulla	ulla.vuorinen@vtt.fi
WANG, Xiangke	xkwang@ipp.ac.cn
WIELAND, Erich	erich.wieland@psi.ch
WITTERBROODT, Charles	

OECD PUBLICATIONS, 2 rue André-Pascal, 75775 PARIS CEDEX 16  
Printed in France.